PRESERVATION AND SEDIMENT CYCLING BENEATH "GHOST GLACIERS": HOW COLD-BASED ICE DICTATES ARCTIC LANDSCAPE EVOLUTION

A Dissertation Presented

by

Lee Corbett

to

The Faculty of the Graduate College

of

The University of Vermont

In partial Fulfillment of the Requirements
for the Degree of Doctor of Philosophy
Specializing in Natural Resources

May, 2016

Defense Date: March 17, 2016

Dissertation Examination Committee:
Paul Bierman, PhD, Advisor
Andrea Lini, PhD, Chairperson
Jeffrey Hughes, PhD
Shelly Rayback, PhD
Cynthia J. Forehand, PhD, Dean of the Graduate College

ABSTRACT

Constraining past episodes of climate change and glacial response is critical for understanding future impacts of climate change, especially in the high latitudes where warming is expected to be rapid and most of Earth's glaciers exist. Many studies of past glacier size utilize rare isotopes called cosmogenic nuclides to perform surface exposure dating. Since most areas of Earth's surface that were previously glaciated were covered by erosive ice, which stripped away pre-existing cosmogenic nuclides, surface exposure dating yields the timing of the most recent deglaciation. However, in some high latitude areas where glacial ice is cold-based and non-erosive (so-called "ghost glaciers"), the assumptions of surface exposure dating are violated. Alternate approaches are required to constrain the complex histories of such landscapes.

My doctoral dissertation focuses on both developing and employing alternative approaches to studying glacial history in the high latitudes, where glacial ice is non-erosive and dating rock surfaces with a single cosmogenic nuclide does not yield exposure ages. Here, I utilize optimized laboratory methods, paired analyses of two cosmogenic isotopes (^{10}Be and ^{26}Al), numerical models to assess possible exposure/burial histories, and Monte Carlo simulations to constrain uncertainties. To study the exposure and burial history of long-preserved landscapes in the Arctic, I investigate landscapes in two high-latitude locations: Thule, northwestern Greenland; and Cumberland Sound, southern Baffin Island, Canada.

Bedrock surfaces, sampled on Baffin Island, exhibit evidence of long-lived subaerial weathering and have simple ^{10}Be exposure ages up to 160,000 yr, despite being glaciated until ~10,000 yr. Simple exposure ages tend to increase with elevation, suggesting more effective erosion in the fjords and longer-term preservation of the uplands. Minimum limiting total histories calculated with ^{26}Al/^{10}Be range up to several million years, with periods of exposure representing ~20% of the total history, describing surfaces that have been alternately preserved beneath non-erosive glacial ice and weathered subaerially over many glacial/interglacial cycles.

Boulders, sampled at both sites, have simple ^{10}Be exposure ages up to 78,000 yr in Thule and 79,000 yr on Baffin Island, and yield multi-modal age distributions. Simple exposure ages of boulders tend to under-estimate bedrock ages in the cases of paired bedrock/boulder samples. Minimum limiting total histories calculated with ^{26}Al/^{10}Be range up to 700,000 yr in Thule and several million years on Baffin Island, with periods of exposure representing only a small portion of the total history. Forward numerical models suggest that boulders have been repeatedly reworked, likely experiencing partial or complete shielding during interglacial periods because of rotation and/or burial by till.

The landscapes I assess here preserve histories of hundreds of thousands to millions of years, and represent a complex interplay of interglacial exposure, subglacial preservation beneath cold-based ice, periglacial processes, and subaerial weathering. Although such landscapes represent methodological challenges, they contain valuable information about long-term variations in glacial extent and climate.

CITATIONS

Material from this dissertation has been published in the following form:

Corbett, L.B., Bierman, P.R., Lasher, G.E., and Rood, D.H.. (2015). Landscape chronology and glacial history in Thule, northwest Greenland. Quaternary Science Reviews, 109, 57-67.

Corbett, L.B., Bierman, P.R., and Rood, D.H.. (2016). An approach for optimizing in situ cosmogenic ^{10}Be sample preparation. Quaternary Geochronology, DOI 10.1016/ j.quageo.2016.02.001.

***

Material from this dissertation has been accepted for publication in the following form:

Corbett, L.B., Bierman, P.R., and Rood, D.H.. (2016). Constraining multi-stage exposure-burial scenarios for boulders preserved beneath cold-based glacial ice in Thule, northwest Greenland. Earth and Planetary Science Letters.

Corbett, L.B., Bierman, P.R., and Davis, P.T.. (2016). Glacial history and landscape evolution of southern Cumberland Peninsula, Baffin Island, Canada, constrained by cosmogenic ^{10}Be and ^{26}Al. Geological Society of America Bulletin.

DEDICATION

To my parents, for teaching me the importance of education and for supporting me unconditionally from first grade through twenty-fifth grade.

ACKNOWLEDGEMENTS

I would likely be running a bakery instead of finishing a PhD if not for the unfailing support of my advisor, Paul Bierman. Thank you for welcoming me back to UVM when my academic future looked dark and for the endless opportunities and encouragement over the near-decade of my graduate school career. The enthusiasm with which you approach research, teaching, and life is inspiring, and I am incredibly grateful for all the lessons I have learned from you over the years.

Thank you also to my committee members Jeff Hughes, Andrea Lini, and Shelly Rayback. Your diverse ideas and backgrounds have provided valuable insight to my research and I enjoyed working with you throughout my academic journey.

Funding for this work was provided primarily by the National Science Foundation through a Graduate Research Fellowship, a Doctoral Dissertation Research Improvement Grant (BCS-1433878), and several grants through the ARC and IGERT programs. Additional analytical support was provided by the Geological Society of America Quaternary Geology and Geomorphology Division J. Hoover Mackin Award and an International Association of Geochemistry Student Research Grant. The Rubenstein School of Environment and Natural Resources and the Department of Geology offered further support for salary, conference travel, and sample preparation and analysis.

Sample analysis was performed at Lawrence Livermore National Laboratory in partnership with Bob Finkel and at Scottish Universities Environmental Research Centre in partnership with Dylan Rood, both of whom were thoughtful collaborators and helped

to see these projects from inception to completion. Thom Davis and Everett Lasher provided additional insight for the Baffin and Thule projects, respectively.

Throughout my dissertation work, I was fortunate to be affiliated with both the Rubenstein School of Environment and Natural Resources and the Department of Geology. Faculty, staff, and students from both departments served as mentors and collaborators in endeavors ranging from teaching to publishing. Thank you especially to the Cosmo team and Stephen Wright for being such supportive colleagues.

Thank you also to the Middlebury College Geology faculty for your continued support of my career and for passing on your wisdom long beyond my time as a student. I enjoyed being part of your department during the fall of 2015 and will continued to be inspired by your dedication to teaching wherever my future paths lead.

I have a wonderful group of family (especially my parents, Pam and Pat Corbett) and friends who served as cheerleaders for me throughout the long and somewhat meandering path I wove through graduate school. Thank you for celebrating my successes, supporting me through challenges, and reminding me of what is truly important in life.

Finally, my path through science and through life has been inextricably and thoroughly entangled with Dave. Over a dozen years ago, you converted me from an architect into a geologist and have been an unconditional supporter over the progression of my career. Having the roles of teacher, mentor, collaborator, best friend, and husband all rolled into a single relationship has tied us together in many deep and intricate ways that I am grateful for every day. Thank you for being my better half and for helping me to follow my dreams.

TABLE OF CONTENTS

Chapter 3: Landscape Development Beneath Non-Erosive Glacial Ice In Thule, Greenland, Part II of II

Chapter 4: Landscape Development Beneath Non-Erosive Glacial Ice On Baffin Island, Canada

CHAPTER 1. INTRODUCTION AND COMPREHENSIVE LITERATURE REVIEW

1. Motivations and Overview

Earth's high latitudes hold most of the planet's glacial ice, and thus have the potential to be significant contributors to sea level rise during times of warming climate (Alley et al., 2010; Alley et al., 2005). These same high-latitude areas are also forecasted to experience the greatest warming in the future due to anthropogenic climate change (IPCC, 2013). The Greenland Ice Sheet alone contains seven meters of sea level equivalent, and in recent years outlet glaciers there have thinned and their flow rate has increased (Csatho et al., 2008; Joughin et al., 2008). There has been widespread surface melt (Nghiem et al., 2012), and net mass loss (Wouters et al., 2008), all signs of ice sheet instability in a warming world.

For these reasons, it is particularly important to understand the response of the high-latitude cryosphere to past episodes of climate change in order to provide insight about possible future change (Long, 2009). For example, constraining the extent of ice loss during past warm periods, particularly the previous interglacial period (the Eemian, ~130,000 years ago), may illustrate possible future ice extent (Cuffey and Marshall, 2000; Letréguilly et al., 1991; Otto-Bliesner et al., 2006; Overpeck et al., 2006). Constraining the rate of ice margin retreat at the end of the last glacial period (~10,000 years ago) may provide insight about possible ice retreat rates to expect in the future (Briner et al., 2009; Corbett et al., 2013; Hughes et al., 2012). Field-based evidence collected from high latitude regions will further inform models of future ice behavior (Huybrechts et al., 1991; Lecavalier et al., 2014; Simpson et al., 2009).

However, the high latitudes are also some of the most difficult areas for studying glacial history because the presence of cold-based, non-erosive glacial ice violates key assumptions of cosmogenic exposure dating, a technique widely used to reconstruct past glacial extent and chronology (Balco, 2011; Fabel and Harbor, 1999; Nishiizumi et al., 1989). Cosmogenic isotopes, including ^{10}Be and ^{26}Al, form at known rates in rock surfaces bombarded by high-energy cosmic rays (Lal, 1988). Thus, determining the nuclide concentration in a rock surface has the potential to provide insight about when the sample site was exposed from beneath retreating glacial ice (Gosse and Phillips, 2001; Phillips et al., 1990). Interpretation of a cosmogenic measurement in glacial terrain as a "simple" exposure age relies upon a critical assumption: that the surface of interest contained no nuclides inherited from previous periods of exposure before being uncovered from beneath retreating glacial ice. Since cosmogenic nuclide production decreases exponentially with depth, erosion (e.g. by subglacial abrasion or plucking) of at least several meters of rock is required to strip most pre-existing nuclides from a surface and make this assumption valid (Balco, 2011).

Landscapes that have been preserved beneath non-erosive glacial ice (Kleman and Borgstrom, 1994) violate the assumption of no inherited nuclides because they have experienced alternating periods of exposure and burial without sufficient erosion during periods of glaciation to remove nuclides produced during earlier periods of exposure. Such landscapes are therefore a product of numerous glacial-interglacial cycles and can be preserved subglacially for hundreds of thousands to millions of years (Sugden, 1977, 1978; Sugden and Watts, 1977). Surfaces preserved through multiple glacial/interglacial cycles beneath non-erosive "ghost glaciers" yield multi-modal simple exposure age

distributions (Briner et al., 2005) and paired-isotope cosmogenic isotope data that can be interpreted in numerous, non-unique ways (Bierman et al., 1999), making the extraction of ice behavior information challenging.

In the face of modern climate change, it is important to refine methods for constraining the timing of glacial events in areas preserved for long durations beneath non-erosive glacial ice because these old, multi-genetic surfaces are archives of valuable long-term climatic and glacial information. The goals of my doctoral thesis is to develop new approaches to using cosmogenic nuclides to constrain past glacier behavior in high-latitude areas characterized by non-erosive glacial ice, and to use these new techniques to make inferences about past ice sheet behavior in Greenland and on Baffin Island, Canada (Fig. 1).

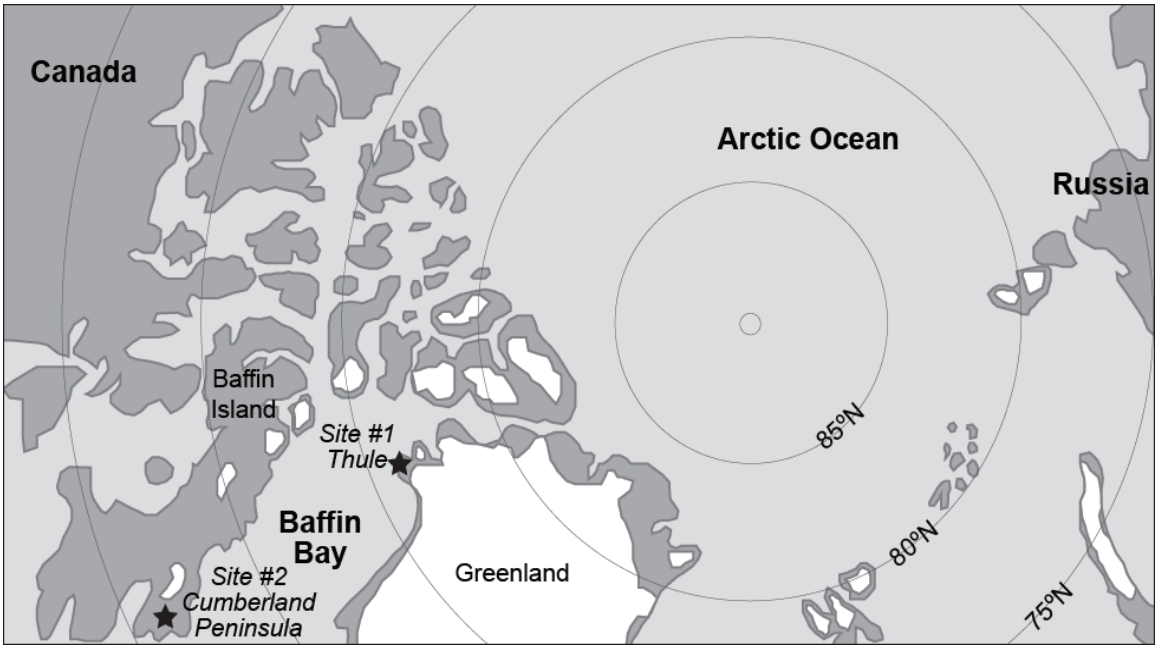

Figure 1. Map of the Arctic, showing the two study sites investigated by the work described here: Thule, Northwest Greenland and Cumberland Peninsula, Southern Baffin Island, Canada.

2. History of Glaciation in the Arctic

2.1. The Onset of Glaciation

Although the Arctic cryosphere is an important player in Earth's climate system, the onset of Arctic glaciation is not well-constrained. The oldest widespread ice-rafted debris found in North Atlantic marine sediment cores dates to ~7.3 Ma (Larsen et al., 1994; St John and Krissek, 2002), indicating that glaciers became large enough to reach the coast near the drill site (southeastern Greenland) during the Late Miocene. The texture of quartz from the same sediments suggests at least limited glaciation as early as 11 Ma (Helland and Holmes, 1997). However, high Arctic glaciation, at least in isolated areas such as those surrounding the Norwegian Sea, may have begun as early as ~40 Ma (Eldrett et al., 2007; Tripati et al., 2008). Regardless, multiple IRD records indicate expansive Greenland glaciation by 2.7 Ma (Flesche-Kleiven et al., 2002).

2.2. Variations in Quaternary Ice Extent

Few paleoclimate records exist that provide information about ancient glacial advances and retreats, primarily because any land-based evidence of glacial retreat gets erased when the ice re-advances. Based on the marine record, pulses of ice-rafted debris at 3.1, 2.7, 2.6, and 2.4 Ma may be indicators of periods of heightened Arctic glacial activity (Larsen et al., 1994; St John and Krissek, 2002). Similarly, debris flow deposits in marine cores off of East Greenland indicate major shelf-edge glaciations ~5 and 2.6 Ma (Butt et al., 2001). Only five major shelf-edge glaciations appear to have occurred off of southern Greenland since the inception of glaciation, with the oldest being ~4.6 Ma and the youngest ~160 ka (Nielsen and Kuijpers, 2013). At the GISP2 coring site in

central Greenland, meteoric ^{10}Be data from silt at the base of the ice core suggest near continuous cover by cold-based, non-erosive ice for millions of years (Bierman et al., 2014), supporting the presence of a long-lived, stable ice sheet.

Ancient interglacial deposits containing diagnostic fauna and flora may indicate warm Arctic conditions during the late Pliocene or early Pleistocene, after the initial onset of glaciation (Funder et al., 2001; Matthews and Ovenden, 1990). Such interglacial sediments have been found in both Greenland (Bennike et al., 2002; Bennike et al., 2010; Feyling-Hanssen, 1990; Feyling-Hanssen et al., 1983; Funder et al., 1985; Funder et al., 2001; Funder and Simonarson, 1984; Simonarson et al., 1998) and Arctic Canada (Andrews et al., 1972; Balkwill and Bustin, 1975; Davies et al., 2014; Hills and Bustin, 1976; Hills and Matthews, 1974; Kuc, 1973, 1974; Matthews, 1977; Terasmae et al., 1966; Thorsteinsson, 1961; Vaughan et al., 2014; Vincent et al., 1984). Although many of these deposits are insecurely dated, they may point to times in the Late Pliocene or Early Pleistocene when Arctic climate was significantly warmer, sedimentation was non-glacial, and warmer species assemblages dominated.

Evidence for warm-Arctic conditions is especially prevalent during Marine Isotope Stage 11, likely one of the warmest interglacial periods in the Quaternary (Lisiecki and Raymo, 2005). Analysis of bedrock at the bottom of the GISP2 ice core suggests that significant melting of the Greenland Ice Sheet occurred at 500 ± 200 ka, thereby exposing the underlying land surface (Nishiizumi et al., 1996). Ice at the base of the Dye 3 ice core, which contains pollen indicative of boreal forest cover, indicates warm conditions ~800-500 ka (Steig and Wolfe, 2008; Willerslev et al., 2007). Spruce pollen from marine sediment cores (De Vernal and Hillaire-Marcel, 2008) and sediment

provenance studies (Reyes et al., 2014) also suggest significantly warmer conditions and reduced ice cover during Marine Isotope Stage 11.

The last interglacial period (the Eemian, Marine Isotope Stage 5e, ~130-120 ka), another warm interglacial period (Lisiecki and Raymo, 2005), may have been characterized by significant ice loss in the Arctic. Modeling efforts suggest that ice cover in Greenland during the Eemian was significantly reduced in relation to its present-day extent (Cuffey and Marshall, 2000; Letréguilly et al., 1991; Otto-Bliesner et al., 2006; Overpeck et al., 2006). Additionally, chemical and physical properties of Eemian-age ice from Greenland indicate a smaller, thinner ice sheet at lower elevation which may have originally accumulated in a snowfield during the initial stages of ice sheet re-growth (Koerner, 1989). Global sea level at this time was ~6-9 m higher than present, supporting a significantly warmer Arctic and reduced glacial cover (Vasskog et al., 2015).

2.3 The Last Glacial-Interglacial Cycle

Arctic ice was again extensive during the Last Glacial Maximum ~25-20 ka. The Greenland Ice Sheet expanded to cover virtually all of Greenland (Håkansson et al., 2011; Håkansson et al., 2007), while the Laurentide Ice Sheet expanded to cover much of northern North America, including all of Baffin Island (Balco et al., 2002; Ives, 1978; Sugden, 1977). Ice from Greenland and Arctic Canada coalesced at the highest latitudes, spanning northwestern Greenland and Ellesmere Island to form the Innuitian Ice Sheet (England, 1998, 1999; England et al., 2006). There is considerable evidence that Arctic ice cover during the last glacial period and previous glacial periods had at least certain areas that were cold-based and non-erosive, allowing areas in both Greenland (Corbett et

al., 2013; Håkansson et al., 2008; Hakansson et al., 2007) and Baffin Island (Bierman et al., 1999; Briner et al., 2006a; Briner et al., 2003; Briner et al., 2005, 2006b; Miller et al., 2006) to be preserved subglacially for numerous glacial-interglacial cycles.

The chronology of the last deglaciation in the Arctic is more closely constrained than older events because ice has not over-run the land-based evidence. Greenland's coastal regions remained glaciated until the Latest Pleistocene or early Holocene, with ice melting first on the southern peninsula and latest on the northern tip, although there is substantial local variability (Bennike and Björck, 2002). The margin if the Laurentide Ice Sheet retreated slowly across North America, beginning ~23 ka (Balco et al., 2002; Ridge et al., 2012), and ultimately exposing Baffin Island in the early Holocene. Analysis of cosmogenic nuclides in bedrock and/or boulder surfaces has been widely used to refine the timing and rates deglaciation in along both the western (Corbett et al., 2013; Corbett et al., 2011; Kelley et al., 2013; Larsen et al., 2014; Levy et al., 2012; Rinterknecht et al., 2009; Young et al., 2013; Young et al., 2011) and eastern (Hughes et al., 2012; Kelly et al., 2008; Roberts et al., 2009; Roberts et al., 2008) Greenland Ice Sheet margins as well as on Baffin Island (Briner et al., 2009; Briner et al., 2006a; Kaplan and Miller, 2003; Kaplan et al., 2001; Marsella et al., 2000). However, the existence of nuclides inherited from previous periods of exposure has complicated attempts to determine deglacial chronology in some areas.

Although the Holocene period has been relatively stable climatically in comparison to glacial-interglacial cycles over the Quaternary, variations in the size of the Greenland Ice Sheet have still occurred. Retreat likely occurred during the Holocene climatic optimum ~8-5 ka (Briner et al., 2010; Goldthwait, 1960; Larsen et al., 2015;

Weidick et al., 1990), while re-advance may have occurred during the Neoglacial ~1.5 ka (Winsor et al., 2014) and the Little Ice Age ~1300-1850 CE (Briner et al., 2010; Young et al., 2015). Glacier extent during the Medieval Warm Period ~950-1250 CE was not significantly reduced (Young et al., 2015). Since the end of the Little Ice Age, ice extent has slowly shrunk due to warmer temperatures, a phenomenon that has been especially pronounced at Jakobshavn Isbræ on the west coast of Greenland (Csatho et al., 2008) but less pronounced along land-terminating margins (Kelley et al., 2012).

3. Study Sites

3.1. Thule, Northwest Greenland

The Greenland Ice Sheet occupies about 1.7 x 10^6 km^2 of land area and is the second largest ice sheet in the world after the Antarctic Ice Sheet. It covers ~80% of Greenland, with the unglaciated areas found predominately around the coast and in the southwestern region. Although the thickness of the ice sheet near the coast is only 10's of meters, it increases to roughly 3,400 m at the center (Huybrechts et al., 1991). Because of Greenland's polar climate, the ice sheet is frozen to the bed in certain locations but reaches the pressure melting point in the areas of thicker ice and/or higher geothermal heat flux (Greve, 2005; Huybrechts, 1996).

The work described in my thesis focuses on the Thule region of northwestern Greenland (~69°W, 77°N), located on the coast at the margin of the Greenland Ice Sheet (Fig. 1). Thule, an American Air Base, is bordered on the east by TUTO Ice Dome and on the north by the Harald Moltke Bræ outlet glacier. Little bedrock is exposed in the study area, although Late Proterozoic basin sediments of the Thule Supergroup (including

shale and redbeds) crop out in the areas of high topography lying to the north and northeast of Thule Air Base (Dawes, 2006). Archaean basement orthogneises and paragneises are exposed to the east of the study area between TUTO Ice Dome and Harald Moltke Bræ, as well as across the fjord on the north side of Harald Moltke Bræ (Dawes, 2006).

3.2. Cumberland Peninsula, Southern Baffin Island, Canada

Baffin Island, Canada, is a NW-SE elongate island almost 1500 km in length, extending north to above 73°N. The island parallels the western coast of Greenland, which is ~500 km to the east across Baffin Bay. Although Baffin Island was once glaciated by the Laurentide Ice Sheet, at present it has only several small ice caps (Penny Ice Cap and Barnes Ice Cap, both ~6 x 10^3 km^2) as well as icefields and alpine glaciers, particularly along the northeast coast where higher topography exists.

The work described in my thesis focuses on Cumberland Peninsula, southern Baffin Island, an area that extends from ~65°N to ~67.5°N and borders Cumberland Sound (Fig. 1). The study area is primarily underlain by Paleoproterozoic crystalline rocks of the Canadian Shield (Hamilton et al., 2012; Jackson and Taylor, 1972). One of the most prominent landscape features bordering Cumberland Sound is Pangnirtung Fiord, which is 43 km long, averages 2.5 km wide, and has a maximum water depth of 160 m (Gilbert, 1978). Pangnirtung Fiord is flanked by highlands with elevations up to ~400 m a.s.l. on both its northwest and southeast sides, with the Penny Ice Cap located on the highlands directly to northwest of the fjord.

4. Cosmogenic Nuclide Dating: Technique and Approach

4.1. Theoretical Overview

In order to constrain past ice sheet behavior, I employ analysis of cosmogenic nuclides (Balco, 2011; Fabel and Harbor, 1999; Gosse and Phillips, 2001). These isotopes, including ^{10}Be and ^{26}Al, build up slowly in rock surfaces over time as they are exposed to bombardment by high-energy cosmic radiation (Lal, 1988) and decay radioactively. Since production rates of these isotopes are well constrained (Balco et al., 2009; Briner et al., 2012), determining their inventory in a rock's surface provides information about the exposure history of that surface. Cosmogenic nuclide production in rock surfaces decreases exponentially with depth (Lal, 1988); therefore, significant erosion of several meters of material, such as by glacial ice, strips away most of these nuclides.

In the simplest case, a surface is exposed to cosmic radiation from beneath retreating glacial ice and the concentration of cosmogenic nuclides in material collected from that surface can be used to determine when exposure occurred (Balco, 2011). This method, which relies on the assumption that the surface was deeply eroded and all nuclides from prior interglacial periods were removed, has been used widely in Greenland (Corbett et al., 2011; Håkansson et al., 2007; Hughes et al., 2012; Kelley et al., 2013; Levy et al., 2012; Rinterknecht et al., 2009; Young et al., 2011) and on Baffin Island (Briner et al., 2009; Marsella et al., 2000). Ages derived with a single cosmogenic isotope assuming no erosion and no inherited nuclides from previous periods of exposure are referred to as "simple" exposure ages.

However, certain areas of the world, especially those at high latitude, violate the assumption that the surface of interest contains no nuclides inherited from previous periods of exposure. Most forms of subglacial erosion require basal ice to be at its melting point; this enables processes such as basal sliding, regelation, and freeze-on of rock and sediment to operate (Herman et al., 2011). Warm-based glaciers, for which the basal temperature is at the pressure melting point, can erode their beds. But under cold-based glaciers, where the basal temperature does not reach the pressure melting point, little erosion occurs (Sugden, 1978; Sugden and Watts, 1977). Although exceptions have been noted (Atkins et al., 2002; Cuffey et al., 2000; Waller et al., 2012), episodes of burial caused by cold-based glacial ice are usually incapable of removing sufficient material to expose fresh rock surfaces after glaciation. The presence of non-erosive ice therefore violates the assumption of no inherited nuclides since surfaces contain nuclides from one or numerous past interglacial periods (Bierman et al., 1999).

When the assumptions of "simple" exposure dating are violated, an alternative approach known as burial dating can be employed that relies on using multiple cosmogenic isotopes with different half-lives. Analysis of two isotopes in tandem can provide information about more complex histories that involve periods of both exposure and burial (Granger and Muzikar, 2001; Nishiizumi et al., 1991; Nishiizumi et al., 1989). Using the $^{26}Al/^{10}Be$ system as an example, ^{26}Al is produced ~6.75 times as rapidly as ^{10}Be (Balco et al., 2008). Over time, because its half-life is less (0.71 million years), a greater percentage of ^{26}Al will be lost to decay than ^{10}Be (half-life 1.36 million years) and the $^{26}Al/^{10}Be$ ratio will drop from 6.75 as exposure continues and the sample ages. In the event of complete burial, production of both nuclides ceases and ^{26}Al decays more

quickly than ^{10}Be. If a sample is exposed again, production resumes. Two-isotope data are plotted on a diagram (Fig. 2) that contains different zones corresponding to different sample histories (Klein et al., 1986). Measuring multiple isotopes in a single sample enables the calculation of minimum limiting exposure durations, burial durations, and total histories (Klein et al., 1986). This information allows minimum limits to be placed on the landscape's age, how long it has spent buried and preserved beneath glacial ice, and how effectively glacial ice erodes underlying surfaces.

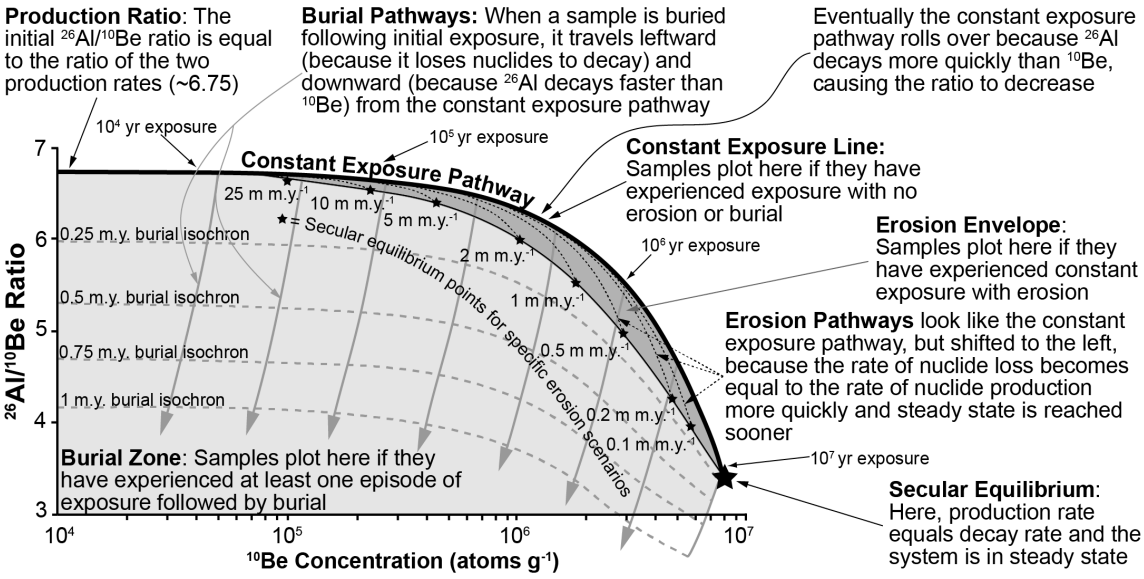

Figure 2. Schematic depiction of a cosmogenic two-isotope plot, from Corbett et al. (2013).

4.2. Using the Cosmogenic Multi-Isotope Approach to Study Non-Erosive Glacial Ice

The burial dating approach with ^{26}Al/^{10}Be has been utilized in areas with non-erosive glacial ice to constrain landscape history. Isotopic evidence for non-erosive glacial ice has been found in Baffin Island, Canada (Bierman et al., 1999; Briner et al., 2003; Briner et al., 2006b), Newfoundland, Canada (Gosse et al., 1993; Gosse et al.,

1995), Scotland (Phillips et al., 2006), and western Greenland (Corbett et al., 2013). Exposed land surfaces are hundreds of thousands of years old despite being covered by glacial ice up until ~10,000 years ago. This complex land surface history is indicated by discordant ^{10}Be and ^{26}Al ages and ^{26}Al/^{10}Be ratios that fall below the constant exposure pathway (Fig. 2). Surfaces preserved beneath cold-based, non-erosive glacial ice record a history of at least several glacial-interglacial periods, indicating that glacial ice can be an ineffective agent of geomorphic change under certain conditions.

In the simplest model of burial dating, a surface is exposed to cosmic radiation for an amount of time much shorter than the half-lives of the cosmogenic nuclides, and then buried deeply enough to halt all production (Granger and Muzikar, 2001). In the two-isotope diagram (Fig. 2), this would equate to traveling along the curved "constant exposure" line for a certain amount of time proportional to the duration of cosmic ray exposure, and then traveling perpendicularly to that path across the burial isochrones for an amount of time proportional to the duration of burial. As shown by the path described above, the ^{26}Al/^{10}Be ratio decreases with burial because the half-life of ^{26}Al is less than that of ^{10}Be.

The burial dating model can become increasingly complex if multiple periods of exposure and burial are involved, since any point on the two-isotope diagram represents a non-unique solution (Granger and Muzikar, 2001). Using two nuclides together can yield information about minimum exposure and burial durations, but additional isotopes (Miller et al., 2006) and/or numerical models (Bierman et al., 1999) are required to constrain histories involving more than two stages.

5. Thesis Outline

Understanding past changes in the cryosphere is important for constraining potential future changes, especially in high-latitude areas that hold most of the planet's glacial ice. Overall, the goal of my work is twofold. First, I seek to refine existing techniques and develop new techniques, both in the laboratory and in terms of data analysis, for employing analysis of cosmogenic nuclides in landscapes that violate a critical assumption of the method. Second, I employ these new techniques to gain insight about landscape development and glacial chronology in the Arctic. This manuscript-based doctoral thesis includes four scientific papers detailed below that have been published or are currently under review.

My work focuses on two regions of the Arctic: Thule, Northwest Greenland and Cumberland Sound, Southern Baffin Island, Canada (Fig. 1). At both sites, I employ analysis of paired cosmogenic isotopes (^{10}Be and ^{26}Al) to investigate subglacial erosion, landscape development, and glacial chronology. My work in Thule is described in Chapters 2 and 3. Chapter 2, which was published in *Quaternary Science Reviews* in 2015, focuses primarily on surficial geologic mapping and recent glacial chronology established with radiocarbon dating of marine organic material and ^{10}Be analysis in glacially-deposited boulders. Chapter 3, which is currently in review at *Earth and Planetary Science Letters*, focuses on subglacial systematics and numerical modeling with the paired ^{26}Al/^{10}Be cosmogenic nuclide system. My work on Baffin Island is described in Chapter 4, which is currently in review at *Geological Society of America Bulletin*, and uses paired analysis of ^{26}Al and ^{10}Be in bedrock surfaces and glacially-

deposited boulders. Both projects seek to develop new approaches for understanding the history of cold-based ice landscapes.

A key aspect of my work involved performing methodological optimization in the Cosmogenic Nuclide Laboratory at University of Vermont in order to achieve improved accuracy and precision. The methodological advances made focus on tracing beryllium and aluminum throughout the extraction process, producing high-yield and high-purity samples, minimizing background levels, and increasing sample processing efficiency. Methodological optimization is described in Chapter 5, which is currently in review at *Quaternary Geochronology.*

The four scientific manuscripts described above represent contributions to the fields of glacial geology, geomorphology, and paleoclimate studies both because they detail methodological developments and describe the application of those new approaches to Arctic landscapes. My findings from these separate studies are synthesized in Chapter 6. There, I also provide ideas for possible future work that would continue to constrain landscape history in high-latitude areas preserved beneath non-erosive glacial ice.

References

Alley, R., Andrews, J., Brigham-Grette, J., Clarke, G., Cuffey, K., Fitzpatrick, J., Funder, S., Marshall, S., Miller, G., Mitrovica, J., 2010. History of the Greenland Ice Sheet: paleoclimatic insights. Quaternary Science Reviews 29, 1728-1756.

Alley, R., Clark, P., Huybrechts, P., Joughin, I., 2005. Ice-sheet and sea-level changes. Science 310, 456-460.

Andrews, J., Barry, R., Bradley, R., Miller, G., Williams, L., 1972. Past and present glaciological responses to climate in eastern Baffin Island. Quaternary Research 2, 303-314.

Atkins, C., Barrett, P., Hicock, S., 2002. Cold glaciers erode and deposit: evidence from Allan Hills, Antarctica. Geology 30, 659-662.

Balco, G., 2011. Contributions and unrealized potential contributions of cosmogenic-nuclide exposure dating to glacier chronology, 1990-2010. Quaternary Science Reviews 30, 3-27.

Balco, G., Briner, J., Finkel, R., Rayburn, J., Ridge, J., Schaefer, J., 2009. Regional beryllium-10 production rate calibration for late-glacial northeastern North America. Quaternary Geochronology 4, 93-107.

Balco, G., Stone, J., Lifton, N., Dunai, T., 2008. A complete and easily accessible means of calculating surface exposure ages or erosion rates from ^{10}Be and ^{26}Al measurements. Quaternary Geochronology 3, 174-195.

Balco, G., Stone, J., Porter, S., Caffee, M., 2002. Cosmogenic-nuclide ages for New England coastal moraines, Martha's Vineyard and Cape Cod, Massachusetts, USA. Quaternary Science Reviews 21, 2127-2135.

Balkwill, H., Bustin, R., 1975. Stratigraphic and structural studies; central Ellesmere Island and eastern Axel Heiberg Island, District of Franklin. Geological Survey of Canada Paper 75-1A, 513-517.

Bennike, O., Abrahamsen, N., Bak, M., Israelson, C., Konradi, P., Matthiessen, J., Witkowski, A., 2002. A multi-proxy study of Pliocene sediments from Ile de France, North-East Greenland. Palaeogeography, Palaeoclimatology, Palaeoecology 186, 1-23.

Bennike, O., Björck, S., 2002. Chronology of the last recession of the Greenland Ice Sheet. Journal of Quaternary Science 17, 211-219.

Bennike, O., Knudsen, K., Abrahamsen, N., Bocher, J., Cremer, H., Wagner, B., 2010. Early Pleistocene sediments on Store Koldewey, northeast Greenland. Boreas 39, 603-619.

Bierman, P., Marsella, K., Patterson, C., Davis, P., Caffee, M., 1999. Mid-Pleistocene cosmogenic minimum-age limits for pre-Wisconsinan glacial surfaces in southwestern Minnesota and southern Baffin Island: a multiple nuclide approach. Geomorphology 27, 25-39.

Briner, J., Bini, A., Anderson, R., 2009. Rapid early Holocene retreat of a Laurentide outlet glacier through an Arctic fjord. Nature Geoscience 2, 496-499.

Briner, J., Gosse, J., Bierman, P., 2006a. Applications of cosmogenic nuclides to Laurentide Ice Sheet history and dynamics. Geological Society of America Special Papers 415, 29-41.

Briner, J., Miller, G., Davis, P., Bierman, P., Caffee, M., 2003. Last Glacial Maximum ice sheet dynamics in Arctic Canada inferred from young erratics perched on ancient tors. Quaternary Science Reviews 22, 437-444.
Briner, J., Miller, G., Davis, P., Finkel, R., 2005. Cosmogenic exposure dating in arctic glacial landscapes: implications for the glacial history of northeastern Baffin Island, Arctic Canada. Canadian Journal of Earth Sciences 42, 67-84.
Briner, J., Miller, G., Davis, P., Finkel, R., 2006b. Cosmogenic radionuclides from fjord landscapes support differential erosion by overriding ice sheets. Geological Society of America Bulletin 118, 406-420.
Briner, J., Stewart, H., Young, N., Phillips, W., Losee, S., 2010. Using proglacial-threshold lakes to constrain fluctuations of the Jakobshavn Isbrae ice margin, western Greenland, during the Holocene. Quaternary Science Reviews 29, 3861-3874.
Briner, J., Young, N., Goehring, B., Schaefer, J., 2012. Constraining Holocene ^{10}Be production rates in Greenland. Journal of Quaternary Science 27, 2-6.
Butt, F., Elverhoi, A., Forsberg, C., Solheim, A., 2001. Evolution of the Scoresby Sund Fan, central East Green land - evidence from ODP Site 987. Norweigan Journal of Geology 81, 3-15.
Corbett, L., Bierman, P., Graly, J., Neumann, T., Rood, D., 2013. Constraining landscape history and glacial erosivity using paired cosmogenic nuclides in Upernavik, northwest Greenland. Geological Society of America Bulletin 125, 1539-1553.
Corbett, L., Young, N., Bierman, P., Briner, J., Neumann, T., Graly, J., Rood, D., 2011. Paired bedrock and boulder 10Be concentrations resulting from early Holocene ice retreat near Jakobshavn Isfjord, western Greenland. Quaternary Science Reviews 30, 1739-1749.
Csatho, B., Schenk, T., Van der Veen, C., Krabill, W., 2008. Intermittent thinning of Jakobshavn Isbræ, West Greenland, since the Little Ice Age. Journal of Glaciology 54, 131-144.
Cuffey, K., Conway, H., Gades, A., Hallet, B., Lorrain, R., Severinghaus, J., Steig, E., Vaughn, B., White, J., 2000. Entrainment at cold glacier beds. Geology 28, 351-354.
Cuffey, K., Marshall, S., 2000. Substantial contribution to sea-level rise during the last interglacial from the Greenland ice sheet. Nature 404, 591-594.
Davies, N., Gosse, J., Rybczynski, N., 2014. Cross-bedded woody debris from a Pliocene forested river system in the high Arctic: Beaufort Formation, Meighen Island, Canada. Journal of Sedimentary Research 84, 19-25.
Dawes, P., 2006. Geological map of Greenland, 1:500,000, Thule, Sheet 5, Geological Survey of Denmark and Greenland Map Series 2. Geological Survey of Denmark and Greenland, Danish Ministry of the Environment.
De Vernal, A., Hillaire-Marcel, C., 2008. Natural variability of Greenland climate, vegetation, and ice volume during the past million years. Science 320, 1622-1625.
Eldrett, J., Harding, I., Wilson, P., Butler, E., Roberts, A., 2007. Continental ice in Greenland during the Eocene and Oligocene. Nature 466, 176-179.
England, J., 1998. Suport for the Innutian Ice Sheet in the Canadian High Arctic during the Last Glacial Maximum. Journal of Quaternary Science 13, 275-280.

England, J., 1999. Coalescent Greenland and Innuitian ice during the Last Glacial Maximum: revising the Quaternary of the Canadian High Arctic. Quaternary Science Reviews 18, 421-456.
England, J., Atkinson, N., Bednarski, J., Dyke, A., Hodgson, D., Cofaigh, C., 2006. The Innutian Ice Sheet: configuration, dynamics, and chronology. Quaternary Science Reviews 25, 689-703.
Fabel, D., Harbor, J., 1999. The use of in-situ produced cosmogenic radionuclides in glaciology and glacial geomorphology. Annals of Glaciology 28, 103-110.
Feyling-Hanssen, R., 1990. Foraminiferal stratigraphy in the Plio-Pleistocene Kap Kobenhavn Formation, North Greenland. Meddelelser om Gronland 24, 1-32.
Feyling-Hanssen, R., Funder, S., Petersen, K., 1983. The Lodin Elv Formation; a Plio-Pleistocene occurrence in Greenland. Bulletin of the Geological Society of Denmark 31, 81-106.
Flesche-Kleiven, H., Jansen, E., Fronval, T., Smith, T., 2002. Intensification of Northern Hemisphere glaciations in the circum Atlantic region (3.5–2.4 Ma) – ice-rafted detritus evidence. Palaeogeography, Palaeoclimatology, Palaeoecology 184, 213-223.
Funder, S., Abrahamsen, N., Bennike, O., Feyling-Hanssen, R., 1985. Forested arctic: evidence from north Greenland. Geology 13, 542-546.
Funder, S., Bennike, O., Bocher, J., Israelson, C., Petersen, K., Simonarson, L., 2001. Late Pliocene Greenland- The Kap Kobenhavn Formation in North Greenland. Bulletin of the Geological Society of Denmark 48, 117-134.
Funder, S., Simonarson, L., 1984. Bio- and aminostratigraphy of some Quaternary marine deposits in West Greenland. Canadian Journal of Earth Sciences 21, 843-852.
Gilbert, R., 1978. Observations on oceanography and sedimentation at Pangnirtung Fiord, Baffin Island. Maritime Sediments 14, 1-9.
Goldthwait, R., 1960. Study of ice cliff in Nunatarssuaq, Greenland. U.S. Army Snow, Ice, and Permafrost Research Establishment Technical Report 39, 106 p.
Gosse, J., Grant, D., Klein, J., Klassen, R., Evenson, E., Lawn, B., Middleton, R., 1993. Significance of altitudinal weathering zones in Atlantic Canada, inferred from in situ produced cosmogenic radionuclides. Geological Society of America Abstracts with Programs 25, A394.
Gosse, J., Grant, D., Klein, J., Lawn, B., 1995. Cosmogenic ^{10}Be and ^{26}Al constraints on weathering zone genesis, ice cap basal conditions, and Long Range Mountain (Newfoundland) glacial history. CANQUA-CGRG conference abstracts CA19.
Gosse, J., Phillips, F., 2001. Terrestrial in situ cosmogenic nuclides: theory and application. Quaternary Science Reviews 20, 1475-1560.
Granger, D., Muzikar, P., 2001. Dating sediment burial with in situ-produced cosmogenic nuclides: theory, techniques, and limitations. Earth and Planetary Science Letters 188, 269-281.
Greve, R., 2005. Relation of measured basal temperatures and the spatial distribution of the geothermal heat flux for the Greenland ice sheet. Annals of Glaciology 42, 424-432.

Håkansson, L., Alexanderson, H., Hjort, C., Moller, P., Briner, J., Aldahan, A., Possnert, G., 2008. Late Pleistocene glacial history of Jameson Land, central East Greenland, derived from cosmogenic ^{10}Be and ^{26}Al exposure dating. Boreas 38, 244-260.

Håkansson, L., Briner, J., Aldahan, A., Possnert, G., 2011. ^{10}Be data from meltwater channels suggest that Jameson Land, east Greenland, was ice-covered during the last glacial maximum. Quaternary Research 76, 452-459.

Håkansson, L., Briner, J., Alexanderson, H., Aldahan, A., Possnert, G., 2007. ^{10}Be ages from central east Greenland constrain the extent of the Greenland ice sheet during the Last Glacial Maximum. Quaternary Science Reviews 26, 2316-2321.

Hakansson, L., Graf, A., Strasky, S., Ivy-Ochs, S., Kubik, P., Hjort, C., Schluchter, C., 2007. Cosmogenic 10Be ages from the Store Koldewey Island, NE Greenland.

Hamilton, B., Pattison, D., Sanborn-Barrie, M., Young, M., 2012. Preliminary characterization of metamorphism on Cumberland Peninsula, Baffin Island, Nunavut. Geologic Survey of Current Research 2012-9, 17 pp.

Helland, P., Holmes, M., 1997. Surface Textural Analysis of Quartz Sand Grains from ODP Site 918 Off the Southeast Coast of Greenland Suggests Glaciation of Southern Greenland at 11 Ma. Palaeogeography, Palaeoclimatology, Palaeoecology 135, 109-121.

Herman, F., Beaud, F., Champagnac, J., Lemieux, J., Sternai, P., 2011. Glacial hydrology and erosion patterns: A mechanism for carving glacial valleys. Earth and Planetary Science Letters 310, 498-508.

Hills, L., Bustin, R., 1976. Picea banksii from Axel Heiberg Island, District of Franklin. Geological Survey of Canada Paper 76-1B, 61-63.

Hills, L., Matthews, J., 1974. A preliminary list of fossil plants from the Beaufort Formation, Meighen Island, District of Franklin. Geological Survey of Canada Paper 74-1B, 224-226.

Hughes, A., Rainsley, E., Murray, T., Fogwill, C., Schnabel, C., Xu, S., 2012. Rapid response of Helheim Glacier, southeast Greenland, to early Holocene climate warming. Geology 40, 427-430.

Huybrechts, P., 1996. Basal temperature conditions of the Greenland ice sheet during the glacial cycles. Annals of Glaciology 23, 226-236.

Huybrechts, P., Letreguilly, A., Reeh, N., 1991. The Greenland ice sheet and greenhouse warming. Global and Planetary Change 3, 399-412.

IPCC, 2013. Climate Change 2013: The Physical Science Basis. Working Group I Contribution to the Fifth Assessment Report of the Intergovernmental Panel on Climate Change. Cambridge University Press.

Ives, J., 1978. The maximum extent of the Laurentide Ice Sheet along the east coast of North America during the last deglaciation. Arctic 32, 24-35.

Jackson, G., Taylor, F., 1972. Correlation of major Aphebian rock units in the northern Canadian Shield. Canadian Journal of Earth Sciences 9, 1650-1669.

Joughin, I., Das, S., King, M., Smith, B., Howat, I., Moon, T., 2008. Seasonal speedup along the western flank of the Greenland Ice Sheet. Science 320, 781-783.

Kaplan, M., Miller, G., 2003. Early Holocene delevelling and deglaciation of the Cumberland Sound region, Baffin Island, Arctic Canada. Geological Society of America Bulletin 115, 445-462.

Kaplan, M., Miller, G., Steig, E., 2001. Low-gradient outlet glaciers (ice streams?) drained the Laurentide ice sheet. Geology 29, 343-346.
Kelley, S., Briner, J., Young, N., 2013. Rapid ice retreat in Disko Bugt supported by 10Be dating of the last recession of the western Greenland Ice Sheet. Quaternary Science Reviews 82, 13-22.
Kelley, S., Briner, J., Young, N., Babonis, G., Csatho, B., 2012. Maximum late Holocene extent of the western Greenland Ice Sheet during the late 20th century. Quaternary Science Reviews 56, 89-98.
Kelly, M., Lowell, T., Hall, B., Schaefer, J., Finkel, R., Goehring, B., Alley, R., Denton, G., 2008. A ^{10}Be chronology of lateglacial and Holocene mountain glaciation in the Scoresby Sund region, east Greenland: implications for seasonality during lateglacial time. Quaternary Science Reviews 27, 2273-2282.
Klein, J., Giegengack, R., Middleton, R., Sharma, P., Underwood, J., Weeks, R., 1986. Revealing histories of exposure using *in situ* produced 26Al and 10Be in Libyan desert glass. Radiocarbon 28, 547-555.
Kleman, J., Borgstrom, I., 1994. Glacial land forms indicative of a partly frozen bed. Journal of Glaciology 40, 255-264.
Koerner, R., 1989. Ice core evidence for extensive melting of the Greenland ice sheet in the last interglacial. Science 244, 964-968.
Kuc, M., 1973. Fossil flora of the Beaufort Formation, Meighen Island, NWT, Canada. Canadian-Polish Research Institute Biology and Earth Sciences Series A No. 1, 1-41.
Kuc, M., 1974. The interglacial flora of Worth Point, western Banks Island. Geological Survey of Canada Paper 74-1B 227-231.
Lal, D., 1988. In situ-produced cosmogenic isotopes in terrestrial rocks. Annual Review of Earth and Planetary Sciences 16, 355-388.
Larsen, H., Saunders, A., Clift, P., Beget, J., Wei, W., Spezzaferri, S., 1994. Seven million years of glaciation in Greenland. Science 264, 952-955.
Larsen, N., Funder, S., Kjaer, K., Kjeldsen, K., Knudsen, M., Linge, H., 2014. Rapid early Holocene ice retreat in West Greenland. Quaternary Science Reviews 92, 310-323.
Larsen, N., Hjaer, K., Lecavalier, B., Bjork, A., Colding, S., Huybrechts, P., Jakobsen, K., Kjeldsen, K., Knudsen, K., Odgaard, B., Olsen, J., 2015. The response of the southern Greenland ice sheet to the Holocene thermal maximum. Geology 43, 291-294.
Lecavalier, B., Milne, G., Simpson, M., Wake, L., Huybrechts, P., Tarasov, L., Kjeldsen, K., Funder, S., Long, A., Woodroffe, S., Dyke, A., Larsen, N., 2014. A model of Greenland ice sheet deglaciation constrained by observations of relative sea level and ice extent. Quaternary Science Reviews 102, 54-84.
Letréguilly, A., Reeh, N., Huybrechts, P., 1991. The Greenland ice sheet through the last glacial-interglacial cycle. Global and Planetary Change 4, 385-394.
Levy, L., Kelly, M., Howley, J., Virginia, R., 2012. Age of the Ørkendalen moraines, Kangerlussuaq, Greenland: constraints on the extent of the southwestern margin of the Greenland Ice Sheet during the Holocene. Quaternary Science Reviews 52, 1-5.

Lisiecki, L., Raymo, M., 2005. A Plio-Pleistocene stack of 57 globally distributed benthic ^{18}O records. Paleoceanography 20, 522–533.
Long, A., 2009. Back to the future: Greenland's contribution to sea-level change. GSA Today 19, 4-10.
Marsella, K., Bierman, P., Davis, P., Caffee, M., 2000. Cosmogenic ^{10}Be and ^{26}Al ages for the last glacial maximum, eastern Baffin Island, Arctic Canada. Geological Society of America Bulletin 112, 1296-1312.
Matthews, J., 1977. Coleoptera fossils: their potential value for dating and correlation of late Cenozoic sediments. Canadian Journal of Earth Sciences 14, 2339-2347.
Matthews, J., Ovenden, L., 1990. Late Tertiary plant macrofossils from localities in Arctic/Subarctic North America: A review of the data. Arctic 43, 384-392.
Miller, G., Briner, J., Lifton, N., Finkel, R., 2006. Limited ice-sheet erosion and complex exposure histories derived from in situ cosmogenic 10Be, 26Al, and 14C on Baffin Island, Arctic Canada. Quaternary Geochronology 1, 74-85.
Nghiem, S., Hall, D., Mote, T., Tedesco, M., Albert, M., Keegan, K., Shuman, C., DiGirolamo, N., Neumann, G., 2012. The extreme melt across the Greenland Ice Sheet in 2012. Geophysical Research Letters 39, L20502.
Nielsen, T., Kuijpers, A., 2013. Only 5 southern Greenland shelf edge glaciations since the early Pliocene. Scientific Reports 3, 1-5.
Nishiizumi, K., Finkel, R., Ponganis, K., Graf, T., Kohl, C., Marti, K., 1996. *In situ* produced cosmogenic nuclides in GISP2 rock core from Greenland summit. EOS Transactions of the American Geophysical Union 77, Abstract 06945142.
Nishiizumi, K., Kohl, C., Arnold, J., Klein, J., Fink, D., Middleton, R., 1991. Cosmic ray produced ^{10}Be and ^{26}Al in Antarctic rocks: exposure and erosion history. Earth and Planetary Science Letters 104, 440-454.
Nishiizumi, K., Winterer, E., Kohl, C., Klein, J., Middleton, R., Lal, D., Arnold, J., 1989. Cosmic ray production rates of ^{10}Be and ^{26}Al in quartz from glacially polished rocks. Journal of Geophysical Research 94, 17907.
Otto-Bliesner, B., Marshall, S., Overpeck, J., Miller, G., Hu, A., 2006. Simulating Arctic climate warmth and icefield retreat in the last interglaciation. Science 311, 1751-1753.
Overpeck, J., Otto-Bliesner, B., Miller, G., Muhs, D., Alley, R., Kiehl, J., 2006. Paleoclimatic evidence for future ice-sheet instability and rapid sea-level rise. Science 311, 1747-1750.
Phillips, F., Zreda, M., Smith, S., Elmore, D., Kubik, P., Sharma, P., 1990. Cosmogenic chlorine-36 chronology for glacial deposits at Bloody Canyon, eastern Sierra Nevada. Science 248, 1529-1532.
Phillips, W., Hall, A., Mottram, R., Fifield, L., Sugden, D., 2006. Cosmogenic 10Be and 26Al exposure ages of tors and erratics, Cairngorm Mountains, Scotland: Timescales for the development of a classic landscape of selective linear glacial erosion. Geomorphology 73, 222-245.
Reyes, A., Carlson, A., Beard, B., Hatfield, R., Stoner, J., Winsor, K., Welke, B., Ullman, D., 2014. South Greenland ice-sheet collapse during Marine Isotope Stage 11. Nature 510, 525-528.

Ridge, J., Balco, G., Bayless, R., Beck, C., Carter, L., Cean, J., Voytek, E., Wei, J., 2012. The new North American varve chronology: A precise record of southeastern Laurentide Ice Sheet deglaciation and climate 18.2-12.5 kyr BP, and correlations with Greenland Ice Core records. American Journal of Science 312, 685-722.

Rinterknecht, V., Gorokhovich, Y., Schaefer, J., Caffee, M., 2009. Preliminary ^{10}Be chronology for the last deglaciation of the western margin of the Greenland Ice Sheet. Journal of Quaternary Science 24, 270-278.

Roberts, D., Long, A., Schnabel, C., Davies, B., Xu, S., Simpson, M., Huybrechts, P., 2009. Ice sheet extent and early deglacial history of the southwestern sector of the Greenland Ice Sheet. Quaternary Science Reviews 28, 2760-2773.

Roberts, D., Long, A., Schnabel, C., Freeman, S., Simpson, M., 2008. The deglacial history of southeast sector of the Greenland Ice Sheet during the Last Glacial Maximum. Quaternary Science Reviews 27, 1505-1516.

Simonarson, L., Petersen, K., Funder, S., 1998. Molluscan palaeontology of the Pliocene-Pleistocene Kap Kobenhavn Formation, North Greenland. Meddelelser om Gronland, Geoscience 36, 1-104.

Simpson, M., Milne, G., Huybrechts, P., Long, A., 2009. Calibrating a glaciological model of the Greenland Ice Sheet from the last glacial maximum to present-day using field observations of relative sea level and ice extent. Quaternary Science Reviews 28, 1631-1657.

St John, K., Krissek, L., 2002. The late Miocene to Pleistocene ice-rafting history of southeast Greenland. Boreas 31, 28-35.

Steig, E., Wolfe, A., 2008. Sprucing Up Greenland. Science 320, 1595-1596.

Sugden, D., 1977. Reconstruction of the morphology, dynamics, and thermal characteristics of the Laurentide Ice Sheet at its maximum. Arctic and Alpine Research 9, 21-47.

Sugden, D., 1978. Glacial erosion by the Laurentide ice sheet. Journal of Glaciology 20, 367-391.

Sugden, D., Watts, S., 1977. Tors, felsenmeer, and glaciation in northern Cumberland Peninsula, Baffin Island. Canadian Journal of Earth Sciences 14, 2817-2823.

Terasmae, J., Webber, P., Andrews, J., 1966. A study of late Quaternary plant-bearing beds in north-central Baffin Island, Canada. Arctic 19, 296-318.

Thorsteinsson, R., 1961. History and geology of Meighen Island. Geological Survey of Canada Bulletin 75, 1-19.

Tripati, A., Eagle, R., Morton, A., Dowdeswell, J., Atkinson, N., Bahe, Y., Dawber, C., Khadun, E., Shaw, R., Shorttle, O., Thanabalasundaram, L., 2008. Evidence for glaciation in the Northern Hemisphere back to 44 Ma from ice-rafted debris in the Greenland Sea. Earth and Planetary Science Letters 265, 112-122.

Vasskog, K., Langebroek, P., Andrews, J., Nilsen, J., Nesje, A., 2015. The Greenland Ice Sheet during the last glacial cycle: Current ice loss and contribution to sea-level rise from a palaeoclimatic perspective. Earth-Science Reviews 150, 45-67.

Vaughan, J., England, J., Evans, D., 2014. Glaciotectonic deformation and reinterpretation of the Worth Point stratigraphic sequence: Banks Island, NT, Canada. Quaternary Science Reviews 91, 124-145.

Vincent, J., Morris, W., Ochietti, S., 1984. Glacial and nonglacial sedimens of Matuyama paleomagnetic age on Banks Island, Canadian Arctic Archipelago. Geology 12, 139-142.

Waller, R., Murton, J., Kristensen, L., 2012. Glacier–permafrost interactions: processes, products and glaciological implications. Sedimentary Geology 255-256, 1-28.

Weidick, A., Oerter, H., Reeh, N., Thomsen, H., Thorning, L., 1990. The recession of the Inland Ice margin during the Holocene climatic optimum in the Jakobshavn Isfjord area of West Greenland. Global and Planetary Change 2, 389-399.

Willerslev, E., Cappellini, E., Boomsma, W., Nielsen, R., Hebsgaard, M., Brand, T., Hofreiter, M., Bunce, M., Poinar, H., Dahl-Jensen, D., 2007. Ancient biomolecules from deep ice cores reveal a forested southern Greenland. Science 317, 111-114.

Winsor, K., Carlson, A., Rood, D., 2014. 10Be dating of the Narsarsuaq moraine in southernmost Greenland: evidence for a late-Holocene ice advance exceeding the Little Ice Age maximum. Quaternary Science Reviews 98, 135-143.

Wouters, B., Chambers, D., Schrama, E., 2008. GRACE observes small-scale mass loss in Greenland. Geophysical Research Letters 35, L20501.

Young, N., Briner, J., Rood, D., Finkel, R., Corbett, L., Bierman, P., 2013. Age of the Fjord Stade moraines in the Disko Bugt region, western Greenland, and the 9.3 and 8.2 ka cooling events. Quaternary Science Reviews 60, 76-90.

Young, N., Briner, J., Stewart, H., Axford, Y., Csatho, B., Rood, D., Finkel, R., 2011. Response of Jakobshavn Isbrae, Greenland, to Holocene climate change. Geology 39, 131-134.

Young, N., Schweinsberg, A., Briner, J., Schaefer, J., 2015. Glacier maxima in Baffin Bay during the Medieval Warm Period coeval with Norse settlement. Science Advances 1, e1500806.

CHAPTER 2. LANDSCAPE DEVELOPMENT BENEATH NON-EROSIVE GLACIAL ICE IN THULE, GREENLAND, PART I OF II

(PUBLISHED IN QUATERNARY SCIENCE REVIEWS IN 2015, V. 109, P. 57-67)

LANDSCAPE CHRONOLOGY AND GLACIAL HISTORY IN THULE, NORTHWEST GREENLAND

Lee B. Corbett*[a], Paul R. Bierman[a], G. Everett Lasher[b], and Dylan H. Rood[c]

*Corresponding Author: Ashley.Corbett@uvm.edu, (802) 380-2344
[a]Department of Geology and Rubenstein School of Environment and Natural Resources, University of Vermont, Burlington, VT 05405 USA
[b]Department of Earth and Planetary Sciences, Northwestern University, Evanston IL 60208 USA
[c]Department of Earth Science and Engineering, Imperial College London, South Kensington Campus, London SW7 2AZ, UK & Scottish Universities Environmental Research Centre (SUERC), East Kilbride G75 0QF, UK

Abstract

Constraining past responses of ice sheets to changes in climate enhances our ability to predict future changes in ice extent and sea level. Here, we employ surficial geologic mapping, stratigraphic analysis, radiocarbon dating of marine mollusks, and analysis of cosmogenic ^{10}Be in glacially-deposited boulders to make inferences about past ice extents in Thule, northwest Greenland. Our work shows the existence of two distinct diamict units in the Thule area; we infer that one diamict was deposited by the main Greenland Ice Sheet while the second was deposited by a subsequent outlet glacier re-advance. Boulders in the two diamicts (n = 13 and n = 15, respectively) have similar bimodal distributions of cosmogenic ^{10}Be ages. Both diamicts have a group of younger ^{10}Be ages as well as a more diffuse group of considerably older ^{10}Be ages (~20-30 ka). Many of the boulders likely contain nuclides inherited from previous periods of exposure, suggesting that glacial ice in the Thule region has been cold-based and non-erosive in the past. The landscape chronology we develop suggests that deglaciation after the Last Glacial Maximum occurred ~10.8 ka and was later followed by a re-advance of outlet glaciers, possibly in concert with the 9.3 ka or 8.2 ka cold events.

1. Introduction

Northwest Greenland has long been the center of debate regarding the extent of past glacial advances (for a thorough review, see England (1999) and England et al. (2006)). Some evidence was interpreted to suggest a limited extent of the ice sheet in northwestern Greenland during the Last Glacial Maximum (LGM), including reconstruction of postglacial isobases (England, 1976), old radiocarbon ages of shells in raised marine sediments (Weidick, 1976), and detailed study of stratigraphic units (Houmark-Nielsen et al., 1990). Proponents of this "little ice" theory argued that the Greenland Ice Sheet did not coalesce with ice in Arctic Canada. Other evidence suggested that the northwestern Greenland Ice Sheet grew significantly during the LGM; this evidence included glacial striations and erratics on islands in the strait between northwest Greenland and Arctic Canada (Nichols, 1969), glacial landforms on the sea floor in Baffin Bay (Blake, 1970), reconstructions of paleo-ice thickness from early to middle Holocene marine limits (Blake, 1970), and young radiocarbon ages of mollusks from raised marine sediments (England, 1998, 1999). Proponents of this "big ice" theory contended that the Greenland Ice Sheet coalesced with ice in Arctic Canada to form the Innuitian Ice Sheet (England et al., 2006).

Although this debate has been settled in favor of the "big ice" argument and the existence of the Innuitian Ice Sheet (England et al., 2006), the decades of inquiry provided important insights into past glacial extents in northwest Greenland, which in turn yield information about the response of the ice sheet to climate change. Thermal reconstructions from Greenlandic ice cores demonstrate that mean annual temperatures over Greenland's center varied by as much as ~20 °C over the course of the last

glacial/interglacial cycle (Buizert et al., 2014; Vinther et al., 2009). Further, studies of past ice extent show that the ice sheet responds to climatic forcing (Carlson and Winsor, 2012), resulting in significant changes in ice sheet extent over time (Cuffey and Marshall, 2000; Letréguilly et al., 1991; Otto-Bliesner et al., 2006; Overpeck et al., 2006). Being able to link well-studied climatic conditions with an evidence-based reconstruction of ice sheet extent (for example, the LGM configuration of the Innuitian Ice Sheet) provides an important constraint on the relationship between climate forcing and ice sheet response.

Investigating the past sensitivity of ice extent to climatic forcing provides constraints for models of ice sheet behavior (Lecavalier et al., 2014; Simpson et al., 2009). This is especially relevant because certain areas of the Greenland Ice Sheet margin have demonstrated the ability to change rapidly. An episode of sudden ice loss in Upernavik, northwest Greenland, occurred 11.3 ± 0.5 ka when a marine-terminating outlet glacier retreated ~100 km in what was likely several centuries and not more than a millennium (Corbett et al., 2013). A similar and possibly synchronous event occurred in East Greenland when the Helheim Glacier retreated 80 km in less than one thousand years at 10.8 ± 0.3 ka (Hughes et al., 2012). Correlating past ice extents with a well-studied climate record, such as from the nearby Camp Century ice core from northwest Greenland (Dansgaard et al., 1969), informs models of future ice retreat and sea level rise (Long, 2009).

Here, we use surficial mapping, stratigraphic analysis, radiocarbon dating of marine mollusks, and analysis of cosmogenic ^{10}Be in quartz extracted from boulders to study past ice sheet behavior in Thule, northwest Greenland (Fig. 1). We investigate the extent of ice cover during the LGM and the timing of the last deglaciation. We also study

a deposit formed by a more recent outlet glacier re-advance to shed light on changes in early Holocene ice extent.

2. Study Site, Previous Work, and Surficial Mapping

2.1. The Thule Region: Overview and Previous Work

Thule, a United States Air Base, is located at ~68.6°W, 76.5°N on the coast of northwestern Greenland (Fig. 1). The study area is bordered on the south and east by TUTO Ice Dome, which is physically connected to, but glaciologically independent from, the Greenland Ice Sheet, and on the north and east by the Harald Moltke Bræ outlet glacier and Wolstenholme Fjord (Fig. 1). A small coastal ice cap, North Ice Cap, lies to the north of Thule on the opposite side of Wolstenholme Fjord. The landscape around the Air Base is mantled in boulder-rich sediments and little bedrock is exposed except for southeast-dipping black shale beds exposed on a high plateau to the east side of the mapping area (Fig. 1). The bedrock in the Thule region is dominantly Late Proterozoic basin sediments of the Thule Supergroup (redbeds, shales, etc.), underlain by Archaean basement gneisses (Dawes, 2006). These Archaean orthogneises and paragneises are the primary lithologies we sampled for cosmogenic isotope analysis.

Much scientific research was conducted in Thule in the early decades of the Air Base's history. The earliest work focused on understanding regional glaciological conditions so that the nuclear-powered base at Camp Century, as well as the ice ramps and ice road leading to it, could be constructed and maintained (Bishop, 1957; Davis, 1967; Goldthwait, 1960, 1971; Griffiths, 1960; Nobles, 1960; Waterhouse et al., 1963).

Later work focused on developing a chronology of past glacial events. We have recalibrated the following radiocarbon ages using the online Calib program (version 7.0) in order to standardize the data, employing the MARINE13 calibration curve with a -400 yr global marine reservoir correction for marine material and the INTCAL13 calibration curve for terrestrial material. We report uncorrected and uncalibrated ages in units of "^{14}C yr BP" and corrected and calibrated ages in units of "cal yr BP". Radiocarbon ages of mollusk shells in raised marine material from either side of Wolstenholme Fjord are reported as 8200-9300 ^{14}C yr BP (Morner and Funder, 1990) and 9000 ^{14}C yr BP (Goldthwait, 1960), which calibrate to 8720-10100 cal yr BP (Table 1). These ages provide a minimum constraint for the timing of retreat of Harald Moltke Bræ through the fjord. There is also evidence for further mid-Holocene retreat of outlet glaciers, including a radiocarbon age of 6980 ^{14}C yr BP (or 7480 cal yr BP) on marine material embedded in a Harald Moltke Bræ shear plane (Morner and Funder, 1990) (Table 1). Farther north, shear planes in North Ice Cap preserve fossilized organic material dating to 4760 ^{14}C yr BP (5460 cal yr BP), suggesting mid-Holocene ice cap retreat followed by re-advance (Goldthwait, 1960) (Table 1). A stable isotope study of ice margins near Thule by Reeh et al. (1990) determined that no or little ice from the Last Glacial Period is exposed in the area; instead, only Holocene ice was found, which Reeh et al. (1990) interpreted to have resulted from a shrinking of the ice sheet during the mid-Holocene.

Mapping and stratigraphic analysis suggests that the Thule region preserves a geologic record of numerous ice margin positions, possibly over multiple glacial/interglacial cycles. The existence of such a long record is supported by old thermoluminescence ages (up to ~135 ka) of marine sediments exposed in Wolstenholme

Fjord thought to represent Marine Isotope Stage 5 (Kronborg et al., 1990). Both Houmark-Nielsen et al. (1990) and Kelly et al. (1999) argue that four pre-Holocene glacial advances can be identified in Thule, with each phase being less extensive than the previous. As proponents of the previously-described "little ice" argument, Houmark-Nielsen et al. (1990) and Kelly et al. (1999) identified the inner-most extent (the Wolstenholme Fjord Stage) as representing the LGM, suggesting that the LGM ice extent in Thule was barely larger than the present ice extent. They mapped moraines east of Thule Air Base as representing the LGM extent of Harald Moltke Bræ; these are the moraines that we revisit in our study (Fig. 2).

In addition to focusing on past ice margin positions, prior work in Thule has investigated the post-glacial marine limit. Beach ridges were mapped up to 40 m a.s.l. near Thule Air Base (Nichols, 1953). Similarly, mollusks were sampled from marine sediments in Wolstenholme Fjord up to ~40 m a.s.l. for radiocarbon dating, as discussed previously (Morner and Funder, 1990). Regional models of post-glacial isostatic depression indicate a marine limit of ~40-60 m a.s.l. in Wolstenholme Fjord (England and Bednarski, 1986) and ~40-80 m for the Thule region as a whole (Funder and Hansen, 1996; Lecavalier et al., 2014; Simpson et al., 2009).

2.2. Surficial Mapping

We conducted surficial mapping using satellite imagery, air photographs, and field studies, revealing the existence of two distinct diamict units (Fig. 2). Most of the landscape in the study area is covered by a clay-rich diamict that is gray, dense, highly-cohesive, has no sorting or internal stratigraphy, and contains a range of subrounded to

angular cobbles and boulders of varying lithologies (Fig. 3a). This unit has a smooth subaerial surface that is evident on the ground and in the aerial imagery (Fig. 1). Much of this unit exhibits periglacial features such as sorted circles and solifluction lobes. It contains boulders up to 5-6 m in diameter, and these boulders exhibit varying degrees of weathering.

A small area of land (~20 km^2) in a valley near Wolstenholme Fjord contains a different and distinct diamict with a sandy matrix (Fig. 2). The valley has a half-bowl shape that opens towards Wolstenholme Fjord; this bowl slopes down to sea level at its base and is surrounded by land ~400-800 m in elevation. Like the clay-rich diamict, the sandy diamict is unsorted, has no internal stratigraphy, and contains abundant subrounded to angular cobbles and boulders (Fig. 3b). However, it has low cohesion and its matrix is composed of medium to coarse sand with little finer material (Fig. 3b), making it distinctive in the field. The sandy diamict has an uneven, hummocky surface that is clearly visible both from the ground and with aerial imagery (Fig. 1). The sandy diamict does not typically exhibit periglacial features, and the boulders contained within it are generally smaller than those in the clay-rich diamict, only 1-3 m in diameter. Similar to the clay-rich diamict, the boulders in the sandy diamict have differing degrees of weathering. The sandy diamict contains numerous moraines that curve around the valley, opening towards Wolstenholme Fjord (Fig. 2). The lower extent of the moraines begins around ~70 m a.s.l. and they reach up to over 200 m a.s.l. at the upper extent of the deposit – all above the previously mapped marine limit (Morner and Funder, 1990; Nichols, 1953). Individual moraine ridges are well defined, sharp-crested, and up to ~10-20 m in height (Fig. 3c).

The contact between the clay-rich diamict and the sandy diamict can be clearly traced on aerial imagery based on the differing surface morphologies (the clay-rich diamict has a smooth surface while the sandy diamict is hummocky and uneven, Figs. 1 & 2). The contact is less readily observed in the field since the surface patterns are not as evident from the ground, although the clay-rich diamict generally has a wetter surface and different vegetation due to its low capacity for infiltration. Along the contact, the sandy diamict appears to extend over the flat-lying clay-rich diamict in mounded lobes (Figs. 1&2), suggesting that the sandy diamict was deposited after and on top of the clay-rich diamict.

Close to Wolstenholme Fjord, at elevations below ~50 m a.s.l., the sandy diamict's surface is reworked (Fig. 2). Fine material has been removed, causing the surface to appear deflated and armored. This armoring effect is only superficial, extending downward several cm and transitioning gradationally into the sandy diamict characteristics as described above. At low elevations where it has been reworked, the surface of the sandy diamict preserves numerous wave-cut benches that form near-continuous ridges parallel to the shore (Fig. 3d). These benches have flat tops and steep fronts; large boulders (1-2 m) often rest on their tops (Fig. 3e).

3. Methods

3.1. Experimental Design and Field Methods

In the Thule region, we conducted surficial mapping using air photographs, satellite imagery, and field observation. We studied the sedimentology of both diamict units throughout the mapping area by digging numerous shallow soil pits. In July 2013,

near Wolstenholme Fjord, we excavated four stratigraphic sections in the walls of a stream channel cut into (and through) the reworked sandy diamict (Fig. 4), described the sedimentary units, and constructed stratigraphic logs. From the lower-most sedimentary unit exposed in these sections, we collected four marine bivalve shells, which we later dated using radiocarbon (Table 1).

To study the chronology and history of the Thule landscape, during 2011-2013 we sampled 28 glacially-deposited boulders for analysis of *in situ* cosmogenic ^{10}Be (Table 2; Figs. 3f & 4). Thirteen of the boulders are scattered across the Thule landscape, spanning ~20 km from east to west and stretching from the present-day ice margin to the coast. These boulders all cropped out from the clay-rich diamict. We collected another 15 boulders from moraine crests in the sandy diamict near the Harald Moltke Bræ outlet glacier and Wolstenholme Fjord. We tried to avoid boulders that had been subjected to post-glacial and periglacial reworking by not sampling boulders that appeared frost-shattered or were on steep slopes; we avoided sampling near patterned ground in the clay-rich diamict and tried to sample directly from the moraine crests in the sandy diamict. To minimize the likelihood of post-glacial reworking, we sampled the tallest and largest boulders available (boulder heights ranged from 0.3-3 m, see data repository).

3.2. Laboratory Methods

Radiocarbon preparation and analysis were conducted at the W.M. Keck Carbon Cycle Accelerator Mass Spectrometry (AMS) Laboratory at University of California Irvine (Southon and Santos, 2004, 2007; Southon et al., 2004). We pre-treated shell samples with weak hydrochloric acid, extracted carbon dioxide, graphitized the carbon

dioxide on an iron catalyst, and analyzed the samples for $^{14}C/^{12}C$ via AMS. Sample ages were calibrated using the online Calib program (version 7.0) with the MARINE13 calibration curve (Reimer et al., 2013) that incorporates a -400 yr global marine reservoir correction (Table 1). This is the marine correction traditionally used in northwestern Greenland (Bennike, 2008; Bennike and Björck, 2002; Morner and Funder, 1990).

Cosmogenic samples were prepared at the University of Vermont as described in Corbett et al. (2011). We isolated quartz from the rock using a series of both physical and chemical processes, and Be from the quartz through a series of chemical processes. We used a low $^{10}Be/^{9}Be$ beryl carrier made at the University of Vermont for all samples, adding ~250 μg of ^{9}Be to each sample as a spike. Samples were prepared in four separate batches, with each batch containing one fully-processed blank.

One of the samples in the dataset (GT019) contained native ^{9}Be, as identified through inductively coupled plasma optical emission spectrometry (ICP-OES) analysis. To identify and correct for the contribution of native ^{9}Be, we used replicate analysis of small aliquots removed from the sample directly following digestion (Portenga et al., *In Press*). These aliquots represented ~2% and 4% of the sample, respectively. ICP-OES measurements indicate that the sample contained 304 μg of total ^{9}Be, instead of the 241 μg added through carrier; all further calculations use the measured ^{9}Be value for this sample.

3.3. Isotopic Analysis

We measured $^{10}Be/^{9}Be$ ratios by AMS at Scottish Universities Environmental Research Centre (Xu et al., 2010). Blank-corrected $^{10}Be/^{9}Be$ sample ratios ranged from

$6.6 \cdot 10^{-14}$ to $5.6 \cdot 10^{-13}$ (see data repository); these ratios have been normalized to the NIST standard with an assumed $^{10}Be/^{9}Be$ ratio of $2.79 \cdot 10^{-11}$ (Nishiizumi et al., 2007). We used a background value of $2.7 \pm 1.1 \cdot 10^{-15}$ for $^{10}Be/^{9}Be$, which is the average and standard deviation of the four blanks included in the four sample batches. We subtracted this background from sample ratios and propagated blank uncertainties in quadrature. AMS measurement precisions (1σ) are 2.8 ± 0.6% (mean ± 1SD; see data repository).

3.4. Exposure Age Calculations

We calculated ^{10}Be exposure ages (Table 2) with the online CRONUS Earth calculator (Balco et al., 2008) using main calculator version 2.1 and constants version 2.2.1. We used the northeastern North American sea-level production rate of 3.93 ± 0.19 atoms g^{-1} yr^{-1} (Balco et al., 2009) and the Lal/Stone constant production rate model and scaling scheme (Lal, 1991; Stone, 2000). In CRONUS, we made corrections for latitude/longitude, elevation, sample thickness (2-5.5 cm) and topographic shielding (0.98-1.00). We assumed a density of 2.7 g cm^{-3}, which is representative of the granites and gneisses we sampled.

Because we have no reliable erosion rate estimates for these boulder surfaces, we cannot correct cosmogenic exposure ages for erosion; thus, assuming no inheritance from prior exposure and zero erosion, all presented ^{10}Be ages are apparent exposure ages. For these apparent exposure ages, we report external uncertainties as calculated by CRONUS Earth, which include AMS measurement error as well as uncertainty in production rates, elevation corrections, and latitude corrections. We use external uncertainties, which account for scaling model uncertainty, so that our cosmogenic ages can be compared to

radiocarbon ages from Thule and cosmogenic data sets from elsewhere in Greenland that have different latitudes and elevations.

4. Results

Our work in Thule addresses both the chronology and the glacial history of the landscape. Surficial mapping documents the existence of two distinct diamicts (see Section 2.2): a clay-rich diamict covering the majority of the landscape and a sandy diamict in the bowl-shaped valley adjacent to Wolstenholme Fjord (Fig. 2). The sandy diamict appears to overlie the clay-rich diamict at the contact between the two units. Close to Wolstenholme Fjord, at elevations below ~50 m, the surface of the sandy diamict has been wave-washed and reworked.

4.1. Stratigraphy and Radiocarbon Chronology

Stratigraphic analysis of sections excavated into (and through) the reworked sandy diamict in stream channel walls (locations shown in Figure 4) reveals that the sandy diamict is underlain by two different sedimentary units (Fig. 5). A dark gray, silty, finely laminated unit was exposed at the bottom of three of the four sections; this unit contains abundant marine bivalves that are sometimes disarticulated. In two of the four sections, this unit is overlain by a thick (up to 2 m) sequence of fine to medium sand that ranges from unstratified to well-stratified. The sand unit contains occasional shell fragments as well as tilted layers and small folds that are likely a product of soft-sediment deformation. The upper-most unit of these sections (except section B, which was excavated in a modern fluvial point bar) comprises a thin layer of sandy diamict. As

described in Section 2.2, the sandy diamict is unsorted, has little cohesion, and contains angular boulders ~1-2 m in diameter that directly overlie our stream channel sections. The top surface of the sandy diamict near the sections appears deflated and armored, and abundant boulders protrude from the armored surface.

Four marine bivalves from the bottom-most unit were radiocarbon dated in order to provide a maximum limit for the depositional age of the sandy diamict (Table 1; Fig. 5). These bivalves were identified as *Mya truncata*, which are commonly found and dated in the Arctic (Bennike and Björck, 2002; Funder and Hansen, 1996). Non-reservoir corrected radiocarbon ages range from 9110-9340 ^{14}C yr BP with uncertainties of ~20 ^{14}C yr. Corrected (assuming a global marine reservoir correction of -400 yr) and calibrated ages range from 9840-10180 cal yr BP with uncertainties of ~50 cal yr (Table 1; Fig. 5).

4.2. Cosmogenic ^{10}Be Chronology

Measured ^{10}Be concentrations in samples from boulder surfaces range from $5.3 \cdot 10^4$ to $4.4 \cdot 10^5$ atoms g^{-1} and calculated apparent ^{10}Be exposure ages range from 10.7 to 78.4 ka (Table 2). The distribution of apparent exposure ages for boulders collected from the surface of the clay-rich diamict is similar to that of boulders collected from the surface of the sandy diamict. For both sample sets, there is a small group of young sample ages that overlap within uncertainty, as well as a more diffuse group of sample ages that form a wide, older, overlapping distribution (Table 2; Fig. 6). For the clay-rich diamict, the young samples are 10.7 ± 0.6, 10.8 ± 0.6, and 10.9 ± 0.7 ka, while the older samples range from 18.9-29.7 ka with uncertainties of 1.1-1.7 ka. There is a single outlier with a ^{10}Be age of 78.4 ± 4.1 ka. For the sandy diamict, the two overlapping young

samples are 12.2 ± 0.7 and 12.4 ± 0.7 ka. The population of older samples ranges from 16.8-28.6 ka with uncertainties of 0.9-1.6 ka.

5. Discussion

The landscape in Thule, northwest Greenland, preserves a record of diverse glacial processes and events. Here, we utilize apparent cosmogenic exposure ages of 28 boulders to make inferences about the age and depositional history of two distinct diamict units: the clay-rich diamict that covers the majority of the Thule landscape and the sandy diamict that covers the bowl-shaped valley adjacent to Wolstenholme Fjord (Fig. 2). We infer that the clay-rich diamict was deposited by the main Greenland Ice Sheet while the sandy diamict was deposited during a subsequent re-advance of Harald Moltke Bræ. We employ surficial mapping, stratigraphic analysis, and interpretations of radiocarbon ages to reconstruct the sequence of glacial events recorded on the Thule landscape, including the re-advance of Harald Moltke Bræ.

5.1. Age of the Thule Landscape

The Thule landscape has a complex chronology that is likely the product of more than one glacial/interglacial cycle. Most of the landscape is mantled in a clay-rich diamict that contains boulders with ^{10}Be ages of 10.7-29.7 ka (excluding one outlier). Similarly, the sandy diamict near Wolstenholme Fjord, which we infer was deposited by a post-glacial re-advance of Harald Moltke Bræ, contains boulders with ^{10}Be ages of 12.2-28.6 ka.

The three youngest ages from the clay-rich diamict (GT023, 10.7 ± 0.6 ka; GT022, 10.8 ± 0.6 ka; and GT055, 10.9 ± 0.7 ka; Table 2) are consistent with other estimates of post-LGM deglaciation timing in northwestern Greenland based on radiocarbon chronology and modeling (Bennike and Björck, 2002; Lecavalier et al., 2014). Further, the characteristics of these three boulders make us confident that they record true exposure ages. The boulders are large (~2-3 m in diameter) and are therefore unlikely to have been altered by post-depositional movement due to periglacial processes. They range in height from 0.6-3 m (see data repository). Burial by snow is possible, although the effect is insignificant (<2%) due to the low density of snow and the dry, windy climate in northwestern Greenland (Corbett et al., 2013). Exhumation from beneath till cover is also possible for the smaller boulders, but this is unlikely given that all three young boulders were on flat ground where erosion potential would be low and none of the boulder surfaces had residual gravel or clasts on them. The fresh boulder surfaces and close coincidence of ages suggests that the three young boulders contain little if any ^{10}Be produced during pre-Holocene exposure. These three ages suggest that the Thule area was exposed from beneath the retreating Greenland Ice Sheet in the earliest Holocene (10.8 ± 0.6 ka, average), likely in response to post-glacial warming as recorded in Greenland ice cores (Buizert et al., 2014).

The majority of boulders on the Thule landscape, however, record at least some pre-Holocene exposure. These older cosmogenic ages likely reflect ^{10}Be inherited from previous periods of exposure. The presence of inherited nuclides is evidenced by the fact that mollusks with ages of ~10 ka (Fig. 5) stratigraphically underlie the sandy diamict, from which the youngest boulders are ~12 ka (Fig. 6). This age reversal violates

stratigraphic principles, indicating that inherited ^{10}Be is present in many of the boulder samples. Inherited nuclides may have formed during previous interglacial periods such as during Marine Isotope Stage 5e (Cuffey and Marshall, 2000; Letréguilly et al., 1991; Otto-Bliesner et al., 2006; Overpeck et al., 2006) and/or Marine Isotope Stage 11 (Reyes et al., 2014), when global ice cover decreased (Lisiecki and Raymo, 2005) and Greenland's coastal landscapes were deglaciated (Willerslev et al., 2007).

The existence of old boulders with a variety of pre-LGM exposure histories suggests that glacial ice in Thule was non-erosive or weakly-erosive during at least the LGM and potentially other previous glacial periods as well. Significant erosion of rock surfaces (~1-2 m) would have removed the surface material containing most nuclides from prior periods of exposure. The presence of inherited ^{10}Be in most Thule boulders indicates that glacial ice was likely frozen to the bed and incapable of eroding even a few meters of rock from most surfaces over which it flowed. Similarly old boulders and bedrock surfaces have been documented using ^{10}Be in high-latitude areas of low mean annual temperature including ~600 km south in Upernavik, northwest Greenland (Corbett et al., 2013), in central-eastern Greenland (Håkansson et al., 2008), and at lower latitudes on Baffin Island, Canada (Bierman et al., 1999; Briner et al., 2003; Briner et al., 2005, 2006), in northeastern Quebec and Labrador, Canada (Marquette et al., 2004), and in northern Sweden (Harbor et al., 2006; Stroeven et al., 2002). Cold-based, non-erosive ice also existed in areas previously covered by the margin of the Antarctic Ice Sheet (Lilly et al., 2010; Sugden et al., 2005).

5.2. Boulder Source and History

The exposure history of boulders in the clay-rich diamict is very similar to that of boulders in the sandy diamict with a small, clustered group of young samples and a more diffuse group of older samples (Fig. 6). Because we infer the clay-rich diamict to have been deposited by the main Greenland Ice Sheet and the sandy diamict to have been deposited by Harald Moltke Bræ, the close match between boulder exposure histories indicates that the two ice bodies were sourcing boulders from the same or related deposits. This observation suggests that the diamicts we sampled were recycled from an older, spatially extensive diamict that covered the landscape during the last interglacial period.

Because most of our boulder ages indicate that glacial ice in Thule was non-erosive or weakly-erosive during its recent history, it is unlikely that the boulders we sampled were directly plucked from bedrock outcrops. Instead, these boulders were likely part of a recycled till that mantled the landscape during one or more past interglacial periods. The boulders were transported and rotated during glaciation, but surface erosion was minimal. Our ability to understand the exact history of this recycled till is uncertain, but a noteworthy observation is that there is a cluster of ages from ~20-30 ka and only a single older age (GT021, 78.4 ka; Fig. 6). This population distribution is not typical of inheritance-bearing landscapes, where cosmogenic age distributions often have a young peak and a broad tail (see Figure 5 in Briner et al. (2003); Figure 7 in Corbett et al. (2013); and Figure 7 in Håkansson et al. (2008)).

The age distribution of boulders in Thule, however, is similar to the age distribution of boulders sampled from certain areas of eastern Baffin Island. Marsella et

al. (2000) dated 14 boulders from the Duval moraine system near Pangnirtung in southeastern Baffin Island; they found two distinct age populations, ~9-12 ka and ~20-22 ka (Table 1, Marsella et al. (2000)). Ten additional boulders from outside the moraine had two age populations of ~9-12 ka and ~21-23 ka, with a single outlier of 66 ka (Table 3, Marsella et al. (2000)). Similarly, working in the Clyde Foreland area of central eastern Baffin Island, Briner et al. (2005) found modal age distributions, even in landscapes that appeared to be glacially-scoured. Twenty-one erratics from the scoured Kogalu River valley have two distinct age modes of ~15 and ~23 ka, as well as two older outliers (Fig. 6, Briner et al. (2005)). Non-scoured areas showed more complex modal distributions, but 11 erratics from the uplands near Patricia Bay also fall into two distinct clusters of ~12 ka and ~19 ka, with a single older outlier (Fig. 6, Briner et al. (2005)). Erratics from Thule and eastern Baffin Island, therefore, exhibit similar modal age distributions, possibly indicating that areas on either side of Baffin Bay were subjected to the same erosive processes.

We suspect there is a geomorphic mechanism that systematically limits the exposure history of the Thule boulders (and potentially those from Baffin Island described above), allowing them to carry only small and generally consistent concentrations of inherited nuclides. For example, rock surfaces may have been deeply eroded during a previous glacial period when global ice volume was high (Lisiecki and Raymo, 2005) and glacial ice in Thule was thicker and warm-based. A period of deep erosion would remove most previously-formed cosmogenic nuclides from rock surfaces, resetting the ^{10}Be clock in all boulders simultaneously. Subsequently, these rock surfaces would have experienced the same exposure/burial history as the till was recycled one or

numerous times. Such a scenario would cause the boulders to record generally similar exposure histories, with some spread due to burial and/or rotation as the till was reworked.

5.3. Timing of Glacial Re-Advance

Although retreat of the main Greenland Ice Sheet likely occurred in the early Holocene (10.8 ± 0.6 ka, the average of the young boulder ages from the clay-rich diamict), we infer that a later re-advance deposited the sandy diamict and moraines found near Wolstenholme Fjord (Fig. 2). This assertion is supported by the surficial mapping work, which documents that the sandy diamict appears to overlie the clay-rich diamict at the contact between the two units (see Section 2.2) and was thus deposited subsequently. Therefore, the depositional age of the clay-rich diamict (10.8 ± 0.6 ka) should serve as a maximum limit for the timing of Harald Moltke Bræ readvance. Similarly, because marine sediments underlie the sandy diamict in areas near the coast (Fig. 5), radiocarbon ages of marine bivalves (9840-10180 cal yr BP) also serve as a maximum limit for the timing of re-advance.

None of the cosmogenic ages of boulders in the sandy till appear to record the timing of this re-advance. There are only two young ^{10}Be ages from this deposit (GT039, 12.2 ± 0.7 ka; and GT038, 12.4 ± 0.7 ka; Fig. 6). Both violate the maximum limiting age constraints provided by ^{10}Be ages from the underlying clay-rich diamict and radiocarbon ages from shells in the underlying marine sediments. Therefore, these two ~12 ka boulders likely contain inherited nuclides, albeit at a lower concentration than the majority of boulders in the dataset.

Based on the maximum age constraints detailed above, we conclude that Harald Moltke Bræ re-advanced more recently than ~10 ka, perhaps coincident with the 9.3 and/or 8.2 ka cooling events (Alley and Ágústsdóttir, 2005; Alley et al., 1997; Fleitmann et al., 2008; Rasmussen et al., 2007), the most prominent cooling events in the Holocene. These events were relatively short in duration (several decades for the 9.3 ka event and ~150 yr for the 8.2 ka event, Rasmussen et al. (2007)), which may explain why the sandy diamict is confined to the boundaries of Harald Moltke Bræ and is not found along the margins of TUTO Ice Dome (Fig. 1). The moraines in Thule may be correlative with the Fjord Stade moraines in central-western Greenland near Ilulissat (Kelly, 1985; Long and Roberts, 2002; Long et al., 2006; Weidick, 1968; Weidick and Bennike, 2007), which have been dated to ~9.3 ka (for the outer "Marrait" moraine system) and ~8.2 ka (for the inner "Tasiussaq" moraine system) using ^{10}Be (Young et al., 2013; Young et al., 2011). The chronology we present here does not allow us to decide which if any of these alternatives is most likely.

The sandy diamict near Wolstenholme Fjord is unique in its composition (Fig. 3b) and was not found elsewhere on the Thule landscape. The sand in this deposit must have had a different source that was spatially restricted, probably just to the fjord. Perhaps the source of this sand was a pro-glacial deposit, such as a delta, which would have formed when Harald Moltke Bræ had retreated up the fjord in the earliest Holocene. The thick sequence of stratified sands underlying the diamict (Fig. 5) could be part of this pro-glacial deposit since the sands are well-sorted and were likely deposited in standing water near a significant sediment source. Subsequent re-advance of the outlet glacier would

have incorporated this sandy material and transported it down the fjord and up into the bowl-shaped valley, depositing it as sand-rich unstratified diamict (Fig. 2).

5.4. Post-Glacial Marine Limit

The Thule landscape preserves a record of a post-glacial marine highstand interrupted by glacial re-advance. After the Greenland Ice Sheet retreated following the LGM, the land surface was isostatically depressed (Funder and Hansen, 1996). This would have led to deposition of marine sediments, which are visible at the bottom of our stratigraphic sections in the form of gray, silty, finely laminated deposits containing abundant marine bivalves (Fig. 5). Our radiocarbon ages of 9840-10180 cal yr BP on shells in this deposit agree well with shells dated elsewhere along Wolstenholme Fjord (Table 1) that range from 8720-10100 cal yr BP (Goldthwait, 1960; Morner and Funder, 1990)).

The post-glacial marine transgression in Wolstenholme Fjord was interrupted by a re-advance of Harald Moltke Bræ; as discussed above, this re-advance overran and incorporated some of the marine sediments. However, we also see evidence that the marine high-stand persisted after Harald Moltke Bræ retreated back up the fjord. Below ~50 m a.s.l., the sandy diamict deposited during the readvance has been reworked; much of the fine material has been removed from the upper-most ~5-10 cm, creating an armored surface. There are numerous parallel wave-cut benches (Figs. 3d & 3e), showing evidence of a progressively lowering shoreline. The highest extent of the reworked diamict in our study area (~50 m) agrees with previous estimates of post-glacial marine limit in Thule of ~40 m from mapping (Morner and Funder, 1990; Nichols, 1953) and

~40-80 m from modeling (England and Bednarski, 1986; Funder and Hansen, 1996; Lecavalier et al., 2014; Simpson et al., 2009). The lack of moraine forms below about 70 m a.s.l. suggests that storm surges may have gone to higher elevations just after deglaciation. We did not find any marine sediments deposited on top of the sandy diamict, indicating that little marine deposition occurred following outlet glacier retreat, possibly because this phase was short-lived. While the first phase of marine highstand seems to have been largely characterized by deposition, the second phase seems to have been dominated by erosion and reworking as local, relative sea level fell rapidly.

5.5. Constraining Past Extent of the Northwestern Greenland Ice Sheet

Our work in Thule helps to constrain the past extent of the northwestern Greenland Ice Sheet over the last glacial/interglacial cycle. The existence of early Holocene cosmogenic exposure ages is consistent with an extensive advance of the northwestern Greenland Ice Sheet during the LGM (England, 1999; England et al., 2006). Further, our ages suggest that initial deglaciation of the Thule landscape occurred ~10.8 ± 0.6 ka. Coupled with climatic information from the nearby Camp Century ice core in northwest Greenland (Dansgaard et al., 1969), the data from Thule provide a link between reconstructed climate and observed ice extent. Our ^{10}Be and radiocarbon ages also provide maximum limiting constraints for the deposition of the sandy diamict, allowing us to infer that the Harald Moltke Bræ outlet glacier re-advanced in the early Holocene. If the moraines we sampled are indeed coincident with the 9.3 or 8.2 ka Events (Alley and Ágústsdóttir, 2005), this coincidence would provide another link between a recent, well-studied climatic event and an observation of glacier response. Since the

Greenland Ice Sheet is likely to change in size and be an important contributor to sea level rise in the future (Alley et al., 2005), establishing relationships between climatic forcings and ice sheet response will enhance our ability to predict future change.

6. Conclusions

The Thule landscape is complex, preserving history from not only the Holocene but also one or more preceding interglacial periods. Most boulder surfaces contain inherited cosmogenic nuclides suggesting that glacial ice in Thule was cold-based and non-erosive. The systematic distribution of these boulder ages suggests that the material we sampled is till recycled from an earlier interglacial period. After the LGM, ice retreated from the Thule landscape ~10.8 ± 0.6 ka, based on the average age of the youngest boulders in the clay-rich diamict. Our data are consistent with LGM ice in northwestern Greenland being considerably more extensive than today. A re-advance of the Harald Moltke Bræ outlet glacier occurred in the early Holocene, perhaps in response to the 9.3 or 8.2 ka cold events.

Acknowledgements

Support for this research was provided by a National Science Foundation Doctoral Dissertation Research Improvement Grant to Corbett (BCS-1433878), a National Science Foundation Graduate Research Fellowship to Corbett, a National Science Foundation IGERT Grant to R. Virginia (DGE-0801490), and National Science Foundation grants to E. Osterberg (ARC-1107411) and R. Hawley (ARC-0909265). Additional analytical support was provided to Corbett by the Geological Society of America Quaternary Geology and Geomorphology Division J. Hoover Mackin Award, an International Association of Geochemistry Student Research Grant, the Rubenstein School of Environment and Natural Resources at University of Vermont, and a Dartmouth College Graduate Alumni Research Award. Field support was provided by CH2MHILL, particularly J. Hurley and K. Derry. We thank J. Southon, C. Bertrand, and H. Martinez for assistance in preparing and analyzing radiocarbon samples; E. Osterberg and M. Kelly for help in project design; and Y. Axford for supporting and facilitating fieldwork. We thank two anonymous reviewers for greatly improving the manuscript.

References

Alley, R., Ágústsdóttir, A., 2005. The 8k event: cause and consequences of a major Holocene abrupt climate change. Quaternary Science Reviews 24, 1123-1149.

Alley, R., Clark, P., Huybrechts, P., Joughin, I., 2005. Ice-sheet and sea-level changes. Science 310, 456-460.

Alley, R., Mayewski, P., Sowers, T., Stuiver, M., Taylor, K., Clark, P., 1997. Holocene climatic instability: a prominent, widespread event 8200 yr ago. Geology 25, 483-486.

Balco, G., Briner, J., Finkel, R., Rayburn, J., Ridge, J., Schaefer, J., 2009. Regional beryllium-10 production rate calibration for late-glacial northeastern North America. Quaternary Geochronology 4, 93-107.

Balco, G., Stone, J., Lifton, N., Dunai, T., 2008. A complete and easily accessible means of calculating surface exposure ages or erosion rates from ^{10}Be and ^{26}Al measurements. Quaternary Geochronology 3, 174-195.

Bennike, O., 2008. An early Holocene Greenland whale from Melville Bugt, Greenland. Quaternary Research 69, 72-76.

Bennike, O., Björck, S., 2002. Chronology of the last recession of the Greenland Ice Sheet. Journal of Quaternary Science 17, 211-219.

Bierman, P., Marsella, K., Patterson, C., Davis, P., Caffee, M., 1999. Mid-Pleistocene cosmogenic minimum-age limits for pre-Wisconsinan glacial surfaces in southwestern Minnesota and southern Baffin Island: a multiple nuclide approach. Geomorphology 27, 25-39.

Bishop, B., 1957. Shear moraines in the Thule area, Northwest Greenland. U.S. Army Snow, Ice, and Permafrost Research Establishment Research Report 17, 47 p.

Blake, W., 1970. Studies of glacial history in Arctic Canada: Pumice, radiocarbon dates, and differential postglacial uplift in the eastern Queen Elizabeth Islands. Canadian Journal of Earth Sciences 7, 634-664.

Briner, J., Miller, G., Davis, P., Bierman, P., Caffee, M., 2003. Last Glacial Maximum ice sheet dynamics in Arctic Canada inferred from young erratics perched on ancient tors. Quaternary Science Reviews 22, 437-444.

Briner, J., Miller, G., Davis, P., Finkel, R., 2005. Cosmogenic exposure dating in arctic glacial landscapes: implications for the glacial history of northeastern Baffin Island, Arctic Canada. Canadian Journal of Earth Sciences 42, 67-84.

Briner, J., Miller, G., Davis, P., Finkel, R., 2006. Cosmogenic radionuclides from fjord landscapes support differential erosion by overriding ice sheets. Geological Society of America Bulletin 118, 406-420.

Buizert, C., Gkinis, V., Severinghaus, J., He, F., Lecavalier, B., Kindler, P., Leuenberger, M., Carlson, A., Vinther, B., Masson-Delmotte, V., White, J., Liu, Z., Otto-Bliesner, B., Brook, E., 2014. Greenland temperature response to climate forcing during the last deglaciation. Science 345, 1177-1180.

Carlson, A., Winsor, K., 2012. Northern Hemisphere ice-sheet responses to past climate warming. Nature Geoscience 5, 607-613.

Corbett, L., Bierman, P., Graly, J., Neumann, T., Rood, D., 2013. Constraining landscape history and glacial erosivity using paired cosmogenic nuclides in Upernavik, northwest Greenland. Geological Society of America Bulletin 125, 1539-1553.
Corbett, L., Young, N., Bierman, P., Briner, J., Neumann, T., Graly, J., Rood, D., 2011. Paired bedrock and boulder 10Be concentrations resulting from early Holocene ice retreat near Jakobshavn Isfjord, western Greenland. Quaternary Science Reviews 30, 1739-1749.
Cuffey, K., Marshall, S., 2000. Substantial contribution to sea-level rise during the last interglacial from the Greenland ice sheet. Nature 404, 591-594.
Dansgaard, W., Johnsen, S.J., Moller, J., Langway, C., 1969. One thousand centuries of climate record from Camp Century on the Greenland Ice Sheet. Science 166, 377-381.
Davis, R., 1967. Ice surface movemebt on the Tuto Ramp in North Greenland. Cold Regions Research and Engineering Laboratory Technical Report 164, 16 p.
Dawes, P., 2006. Geological map of Greenland, 1:500,000, Thule, Sheet 5, Geological Survey of Denmark and Greenland Map Series 2. Geological Survey of Denmark and Greenland, Danish Ministry of the Environment.
England, J., 1976. Postglacial isobases and uplift curves from the Canadian and Greenland high Arctic. Arctic and Alpine Research 8, 61-78.
England, J., 1998. Suport for the Innutian Ice Sheet in the Canadian High Arctic during the Last Glacial Maximum. Journal of Quaternary Science 13, 275-280.
England, J., 1999. Coalescent Greenland and Innuitian ice during the Last Glacial Maximum: revising the Quaternary of the Canadian High Arctic. Quaternary Science Reviews 18, 421-456.
England, J., Atkinson, N., Bednarski, J., Dyke, A., Hodgson, D., Cofaigh, C., 2006. The Innutian Ice Sheet: configuration, dynamics, and chronology. Quaternary Science Reviews 25, 689-703.
England, J., Bednarski, J., 1986. Postglacial isobases from northern Ellesmere Island and Greenland: new data. Geographie physique and Quaternaire 40, 299-305.
Fleitmann, D., Mudelsee, M., Burns, S., Bradley, R., Kramers, J., Matter, A., 2008. Evidence for a widespread climatic anomaly at around 9.2 ka before present. Paleoceanography 23, PA1102.
Funder, S., Hansen, L., 1996. The Greenland ice sheet-a model for its culmination and decay during and after the last glacial maximum. Bulletin of the Geological Society of Denmark 42, 137-152.
Goldthwait, R., 1960. Study of ice cliff in Nunatarssuaq, Greenland. U.S. Army Snow, Ice, and Permafrost Research Establishment Technical Report 39, 106 p.
Goldthwait, R., 1971. Restudy of red rock ice cliff, Nunatarssuaq, Greenland. Cold Regions Research and Engineering Laboratory Report, 29 p.
Griffiths, T., 1960. Glaciological investigations in the TUTO area of Greenland. U.S. Army Snow, Ice, and Permafrost Research Establishment Report 47, 63 p.
Håkansson, L., Alexanderson, H., Hjort, C., Moller, P., Briner, J., Aldahan, A., Possnert, G., 2008. Late Pleistocene glacial history of Jameson Land, central East Greenland, derived from cosmogenic ^{10}Be and ^{26}Al exposure dating. Boreas 38, 244-260.

Harbor, J., Stroeven, A., Fabel, D., Clarhäll, A., Kleman, J., Li, Y., Elmore, D., Fink, D., 2006. Cosmogenic nuclide evidence for minimal erosion across two subglacial sliding boundaries of the late glacial Fennoscandian ice sheet. Geomorphology 75, 90-99.

Houmark-Nielsen, M., Kelly, M., Landvik, J., Sorby, L., 1990. The pre-Holocene Quaternary: Lithostratigraphic and geomorphic evidence. Meddelelser om Gronland 22, 8-18.

Hughes, A., Rainsley, E., Murray, T., Fogwill, C., Schnabel, C., Xu, S., 2012. Rapid response of Helheim Glacier, southeast Greenland, to early Holocene climate warming. Geology 40, 427-430.

Kelly, M., 1985. A review of the Quaternary geology of western Greenland, In: Andrews, J. (Ed.), Quaternary Environments; Eastern Canadian Arctic, Baffin Bay and Western Greenland. Allen and Unwin, Boston, pp. 461-501.

Kelly, M., Funder, S., Houmark-Nielsen, M., Knudsen, K., Kronborg, C., Landvik, J., Sorby, L., 1999. Quaternary glacial and marine environmental history of northwest Greenland: a review and reappraisal. Quaternary Science Reviews 18, 373-392.

Kronborg, C., Mejdahl, V., Sejrup, H., 1990. Thermoluminescence dating and amino acid analysis. Meddelelser om Gronland 22, 33-39.

Lal, D., 1991. Cosmic ray labeling of erosion surfaces: in situ nuclide production rates and erosion models. Earth and Planetary Science Letters 104, 424-439.

Lecavalier, B., Milne, G., Simpson, M., Wake, L., Huybrechts, P., Tarasov, L., Kjeldsen, K., Funder, S., Long, A., Woodroffe, S., Dyke, A., Larsen, N., 2014. A model of Greenland ice sheet deglaciation constrained by observations of relative sea level and ice extent. Quaternary Science Reviews 102, 54-84.

Letréguilly, A., Reeh, N., Huybrechts, P., 1991. The Greenland ice sheet through the last glacial-interglacial cycle. Global and Planetary Change 4, 385-394.

Lilly, K., Fink, D., Fabel, D., Lambeck, K., 2010. Pleistocene dynamics of the interior of the East Antarctic ice sheet. Geology 38, 703-706.

Lisiecki, L., Raymo, M., 2005. A Plio-Pleistocene stack of 57 globally distributed benthic ^{18}O records. Paleoceanography 20, 522–533.

Long, A., 2009. Back to the future: Greenland's contribution to sea-level change. GSA Today 19, 4-10.

Long, A., Roberts, D., 2002. A revised chronology for the 'Fjord Stade' moraine in Disko Bugt, West Greenland. Journal of Quaternary Science 17, 561-579.

Long, A., Roberts, D., Dawson, S., 2006. Early Holocene history of the West Greenland Ice Sheet and the GH-8.2 event. Quaternary Science Reviews 25, 904-922.

Marquette, G., Gray, J., Gosse, J., Courchesne, F., Stockli, L., Macpherson, G., Finkel, R., 2004. Felsenmeer persistence under non-erosive ice in the Torngat and Kaumajet mountains, Quebec and Labrador, as determined by soil weathering and cosmogenic nuclide exposure dating. Canadian Journal of Earth Sciences 41, 19-38.

Marsella, K., Bierman, P., Davis, P., Caffee, M., 2000. Cosmogenic ^{10}Be and ^{26}Al ages for the last glacial maximum, eastern Baffin Island, Arctic Canada. Geological Society of America Bulletin 112, 1296-1312.

Morner, N., Funder, S., 1990. C-14 dating of samples collected during the NORDQUA 86 expedition, and notes on the marine reservour effect. Meddelelser om Gronland 22, 57-63.

Nichols, R., 1953. Geomorphologic observations at Thule, Greenland and Resolute Bay, Cornwallis Island, N.W.T. American Journal of Science 251, 268-275.

Nichols, R., 1969. Geomorphology of Inglefield Land, North Greenland. Meddelelser om Gronland 188, 3-105.

Nishiizumi, K., Imamura, M., Caffee, M., Southon, J., Finkel, R., McAninch, J., 2007. Absolute calibration of ^{10}Be AMS standards. Nuclear Instruments and Methods in Physics Research Section B: Beam Interactions with Materials and Atoms 258, 403-413.

Nobles, L., 1960. Glaciological investigations, Nunatarssuaq ice ramp, northwestern Greenland. U.S. Army Snow, Ice, and Permafrost Research Establishment Technical Report 66, 57 p.

Otto-Bliesner, B., Marshall, S., Overpeck, J., Miller, G., Hu, A., 2006. Simulating Arctic climate warmth and icefield retreat in the last interglaciation. Science 311, 1751-1753.

Overpeck, J., Otto-Bliesner, B., Miller, G., Muhs, D., Alley, R., Kiehl, J., 2006. Paleoclimatic evidence for future ice-sheet instability and rapid sea-level rise. Science 311, 1747-1750.

Portenga, E., Bierman, P., Duncan, C., Corbett, L., Kehrwald, N., Rood, D., *In Press*. Erosion rates of the Bhutanese Himalaya determined using in situ-produced 10Be. Geomorphology.

Rasmussen, S., Vinther, B., Clausen, H., Andersen, K., 2007. Early Holocene climate oscillations recorded in three Greenland ice cores. Quaternary Science Reviews 26, 1907-1914.

Reeh, N., Thomsen, H., Frich, P., Clausen, H., 1990. Stable isotope studies on ice margins in the Thule area, In: Funder, S. (Ed.), Meddelelser om Gronland, Geoscience, pp. 47-63.

Reimer, P., Bard, E., Bayliss, A., Beck, J., Blackwell, P., Ramsey, C., Buck, C., Cheng, H., Edwards, R., Friedrich, M., Grootes, P., Guilderson, T., Haflidason, H., Hajdas, I., Hatte, C., Heaton, T., Hoffman, D., Hogg, A., Hughen, K., Kaiser, K., Kromer, B., Manning, S., Niu, M., Reimer, R., Richards, D., Scott, E., Southon, J., Staff, R., Turney, C., van der Plicht, J., 2013. IntCal13 and Marine13 radiocarbon age calibration curves 0–50,000 years cal BP. Radiocarbon 55, 1869-1887.

Reyes, A., Carlson, A., Beard, B., Hatfield, R., Stoner, J., Winsor, K., Welke, B., Ullman, D., 2014. South Greenland ice-sheet collapse during Marine Isotope Stage 11. Nature 510, 525-528.

Simpson, M., Milne, G., Huybrechts, P., Long, A., 2009. Calibrating a glaciological model of the Greenland Ice Sheet from the last glacial maximum to present-day using field observations of relative sea level and ice extent. Quaternary Science Reviews 28, 1631-1657.

Southon, J., Santos, G., 2004. Ion source development at KCCAMS, University of California, Irvine. Radiocarbon 46, 33-39.

Southon, J., Santos, G., 2007. Life with MC-SNICS part II: Further ion source development at the Keck carbon cycle AMS facility. Nuclear Instruments and Methods in Physics Research B 259, 88-93.
Southon, J., Santos, G., Druffel-Rodriguez, K., Druffel, E., Trumbore, S., Xu, X., Griffin, S., Ali, S., Mazon, M., 2004. The Keck carbon cycle AMS Laboratory, University of California, Irvine: Initial operation and a background surprise. 46 1.
Stone, J., 2000. Air pressure and cosmogenic isotope production. Journal of Geophysical Research 105, 23753-23759.
Stroeven, A., Fabel, D., Hattestrand, C., Harbor, J., 2002. A relict landscape in the centre of Fennoscandian glaciation: cosmogenic radionuclide evidence of tors preserved through multiple glacial cycles. Geomorphology 44, 145-154.
Sugden, D., Balco, G., Cowdery, S., Stone, J., Sass III, L., 2005. Selective glacial erosion and weathering zones in the coastal mountains of Marie Byrd Land, Antarctica. Geomorphology 67, 317-334.
Vinther, B., Buchardt, S., Clausen, H., Dahl-Jensen, D., Johnsen, S., Fisher, D., Koerner, R., Raynaud, D., Lipenkov, V., Andersen, K., 2009. Holocene thinning of the Greenland ice sheet. Nature 461, 385-388.
Waterhouse, R., Tobiasson, W., Scott, B., 1963. Camp Century movement record, Cold Regions Research and Engineering Laboratory Technical Report, p. 79 p.
Weidick, A., 1968. Observations on some Holocene glacier fluctuations in West Greenland, Meddelelser om Gronland, p. 194 pp.
Weidick, A., 1976. Glaciations of Northern Greenland- New evidence. Polarforschung 46, 26-33.
Weidick, A., Bennike, O., 2007. Quaternary glaciation history and glaciology of Jakobshavn Isbrae and the Disko Bugt region, west Greenland: a review. Geologic Survey of Denmark and Greenland Bulletin 14, 1-13.
Willerslev, E., Cappellini, E., Boomsma, W., Nielsen, R., Hebsgaard, M., Brand, T., Hofreiter, M., Bunce, M., Poinar, H., Dahl-Jensen, D., 2007. Ancient biomolecules from deep ice cores reveal a forested southern Greenland. Science 317, 111-114.
Xu, S., Dougans, A., Freeman, S., Schanbel, C., Wilcken, K., 2010. Improved 10Be and 26Al - AMS with a 5 MV spectrometer. Nuclear Instruments and Methods in Physics Research B 268.
Young, N., Briner, J., Rood, D., Finkel, R., Corbett, L., Bierman, P., 2013. Age of the Fjord Stade moraines in the Disko Bugt region, western Greenland, and the 9.3 and 8.2 ka cooling events. Quaternary Science Reviews 60, 76-90.
Young, N., Briner, J., Stewart, H., Axford, Y., Csatho, B., Rood, D., Finkel, R., 2011. Response of Jakobshavn Isbrae, Greenland, to Holocene climate change. Geology 39, 131-134.

Table 1. Radiocarbon ages of previously-published samples from the Thule area and of marine bivalves from stratigraphic sections excavated through the reworked diamict (this study; see Figure 5 for stratigraphic locations).

Source	Lab ID	Location*	Stratigraphic Section	Depth (cm)	Uncorrected Age (^{14}C yr BP)	Corrected & Calibrated Age (yr BP)**
Morner and Funder, 1990	GC68-001	Wolstenholme Fjord	--	--	8200 ± 85	8720 ± 100
Morner and Funder, 1990	GC68-013	Wolstenholme Fjord	--	--	9150 ± 200	9900 ± 210
Morner and Funder, 1990	GC68-021	Wolstenholme Fjord	--	--	9150 ± 95	9910 ± 110
Morner and Funder, 1990	GC68-088	Wolstenholme Fjord	--	--	9295 ± 100	10100 ± 110
Morner and Funder, 1990	GC68-094	Wolstenholme Fjord	--	--	9005 ± 85	9700 ± 100
Morner and Funder, 1990	GC68-095	Wolstenholme Fjord	--	--	8965 ± 85	9650 ± 100
Morner and Funder, 1990	GC68-096	Wolstenholme Fjord	--	--	8760 ± 180	9420 ± 190
Morner and Funder, 1990	GC68-097	Wolstenholme Fjord	--	--	8570 ± 95	9210 ± 110
Morner and Funder, 1990	GC68-161	Wolstenholme Fjord	--	--	9040 ± 95	9750 ± 110
Morner and Funder, 1990	GC68-172	Harald Moltke Brae	--	--	6980 ± 85	7480 ± 100
Goldthwait, 1960	--	Wolstenholme Fjord	--	--	9000 ± 350	9740 ± 360
Goldthwait, 1960	--	North Ice Cap	--	--	4760 ± 220	5460 ± 230
This study	UCIAMS#136301	Wolstenholme Fjord	A	222	9110 ± 20	9840 ± 50
This study	UCIAMS#136302	Wolstenholme Fjord	B	13	9340 ± 20	10180 ± 50
This study	UCIAMS#136303	Wolstenholme Fjord	B	26	9285 ± 20	10140 ± 50
This study	UCIAMS#136300	Wolstenholme Fjord	C	128	9175 ± 20	9980 ± 50

*Samples from Wolstenholme Fjord were collected from raised marine sediments on either side of the fjord. Samples from Harald Moltke Brae and North Ice Cap were collected from shear planes exposed at the ice surface.

**All but one of the samples were shell material and were calibrated assuming a -400 yr marine reservoir correction using the MARINE13 calibration curve. The single plant sample (the 4760 yr age from Goldthwait) was calibrated without a marine correction using the INTCAL13 calibration curve.

Table 2. Sample collection and ^{10}Be information for 28 boulder samples from Thule.

Sample Name	Location Description	Elevation (m a.s.l.)	Latitude (°N)	Longitude (°E)	Boulder Lithology	Thickness (cm)	Shielding	^{10}Be Conc. (atoms g^{-1})	^{10}Be Unc. (atoms g^{-1})	^{10}Be Age (ka)*	^{10}Be Age Unc. (ka)*
GT014	Landscape	350	76.54578	-68.15783	Gneiss	3	1.00	1.35×10^5	4.27×10^3	22.6	1.3
GT015	Landscape	276	76.55843	-68.64975	Quartzite	4.3	1.00	1.62×10^5	4.06×10^3	29.7	1.6
GT016	Landscape	252	76.55745	-68.71192	Granite gneiss	2	1.00	1.50×10^5	3.91×10^3	27.6	1.5
GT018	Landscape	251	76.54552	-68.61322	Granite gneiss	3	1.00	1.56×10^5	4.72×10^3	29.0	1.7
GT019	Landscape	178	76.55382	-68.54360	Granite	4.3	1.00	1.12×10^5	2.47×10^3	22.6	1.2
GT021	Landscape	314	76.54702	-68.07298	Granite gneiss	5	1.00	4.38×10^5	8.30×10^3	78.4	4.1
GT022	Landscape	358	76.55833	-68.19445	Gneiss	3	1.00	6.53×10^4	2.01×10^3	10.8	0.6
GT023	Landscape	346	76.56945	-68.24887	Granite	3	1.00	6.38×10^4	2.18×10^3	10.7	0.6
GT027	Moraine	175	76.55336	-68.39177	Granite	5	0.99	1.39×10^5	3.49×10^3	28.6	1.6
GT030	Moraine	171	76.55168	-68.39473	Granite gneiss	3	0.98	1.15×10^5	2.82×10^3	23.6	1.3
GT035	Moraine	71	76.55843	-68.45382	Gneiss	2.5	0.98	1.04×10^5	2.39×10^3	23.9	1.3
GT036	Moraine	77	76.55791	-68.44873	Quartzite	2	0.98	1.08×10^5	3.13×10^3	24.4	1.4
GT038	Moraine	67	76.55983	-68.42910	Gneiss	2	0.98	5.41×10^4	1.67×10^3	12.4	0.7
GT039	Moraine	74	76.56069	-68.42268	Gneiss	4	0.98	5.28×10^4	1.68×10^3	12.2	0.7
GT040	Moraine	62	76.56132	-68.42116	Gneiss	3	0.98	9.04×10^4	4.29×10^3	21.0	1.4
GT042	Moraine	138	76.55457	-68.38605	Gneiss	5.5	0.99	1.22×10^5	2.81×10^3	26.4	1.4
GT043	Moraine	175	76.55338	-68.39169	Gneiss	3.5	0.99	1.35×10^5	3.59×10^3	27.5	1.5
GT044	Moraine	185	76.55151	-68.39625	Quartzite	2.5	0.99	8.41×10^4	2.10×10^3	16.8	0.9
GT049	Moraine	198	76.57150	-68.52433	Gneiss	3	0.98	1.30×10^5	3.23×10^3	26.0	1.4
GT050	Moraine	198	76.57030	-68.51962	Gneiss	5	0.99	9.19×10^4	2.43×10^3	18.5	1.0
GT051	Moraine	195	76.56734	-68.51293	Gneiss	3	0.99	1.09×10^5	2.59×10^3	21.7	1.2
GT052	Moraine	187	76.56478	-68.50867	Granite	2	0.99	1.19×10^5	2.95×10^3	23.6	1.3
GT053	Moraine	180	76.56400	-68.50716	Gneiss	3	0.99	9.63×10^4	2.18×10^3	19.4	1.0
GT054	Landscape	183	76.55590	-68.57046	Granite	3	0.99	9.38×10^4	3.14×10^3	18.9	1.1
GT055	Landscape	201	76.56046	-68.54910	Granite	3	0.99	5.55×10^4	2.07×10^3	10.9	0.7
GT056	Landscape	324	76.58178	-68.58881	Granite	3	0.99	1.31×10^5	3.54×10^3	22.7	1.3
GT057	Landscape	143	76.53712	-68.41935	Granite	4	0.99	1.31×10^5	4.21×10^3	27.7	1.6
GT058	Landscape	158	76.53816	-68.39758	Granite	4	0.99	1.16×10^5	3.83×10^3	24.2	1.4

*Age calculations were done in CRONUS with the Northeastern North American production rate (Balco et al, 2008) assuming zero erosion, no inheritance, and a density of 2.7 g cm^{-3}. Reported uncertainties reflect external uncertainties as described in the text. Ratios are reported in the Data Repository.

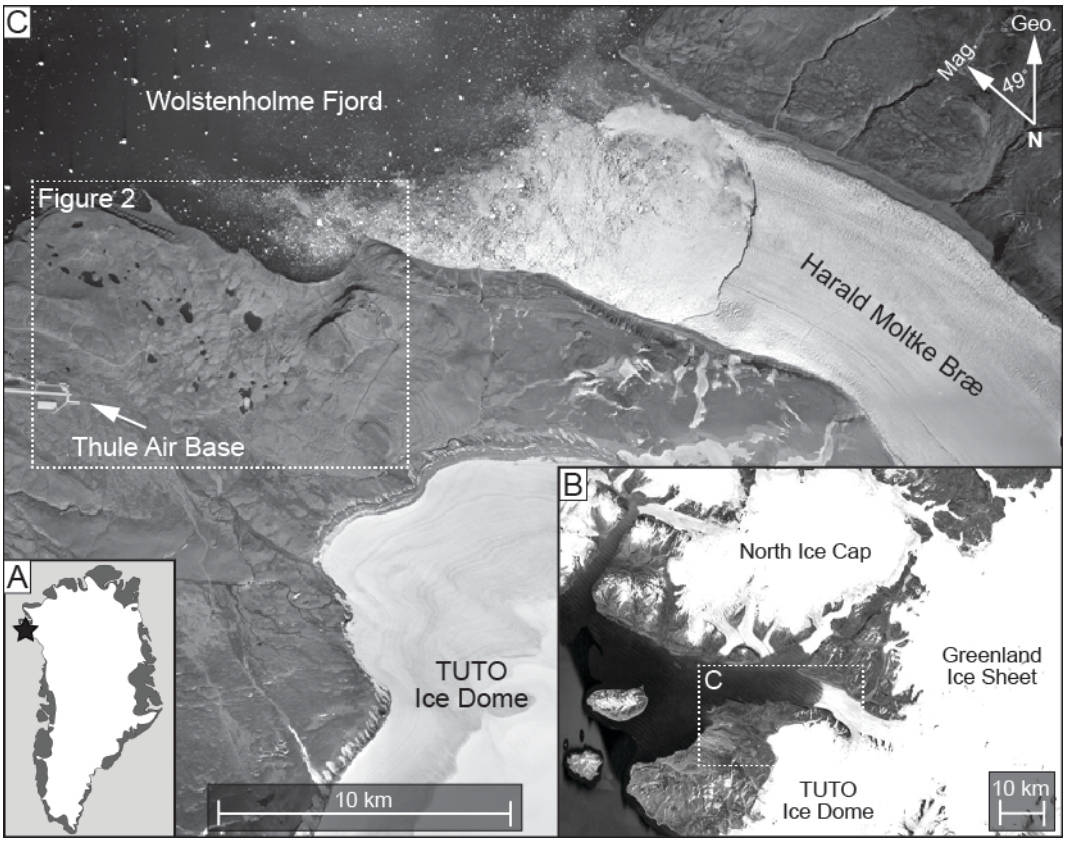

Figure 1. Location of the study area. Panel A shows the location of Thule in northwestern Greenland. Panel B shows the regional glaciological conditions and the ice bodies discussed in the text; white dashed box shows the location of Panel C (satellite imagery from Google Earth). Panel C is a 1950 air photograph of the Thule region showing the location of landscape features mentioned in the text; white dashed box shows the extent of detailed surficial mapping shown in Figure 2.

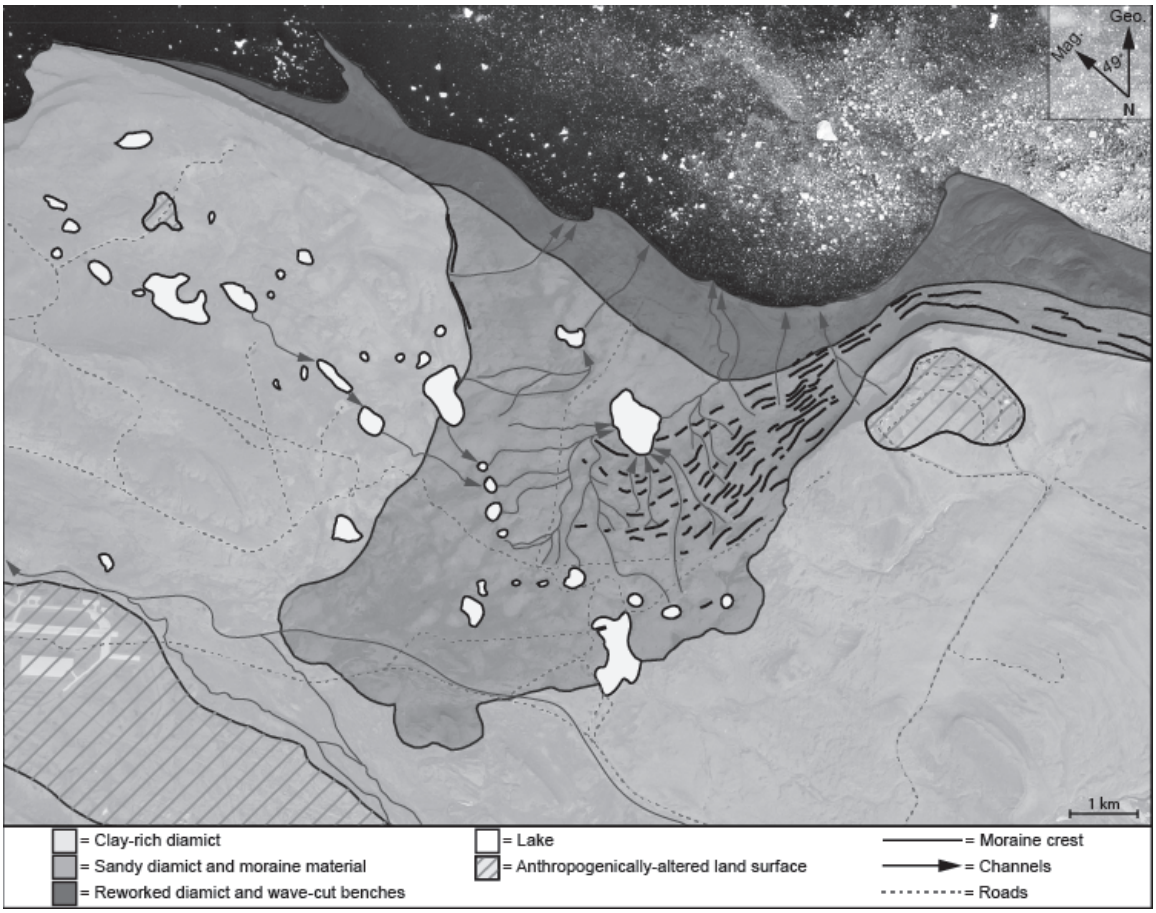

Figure 2. Surficial geologic map of the study area based on analysis of air photographs, satellite imagery, and fieldwork.

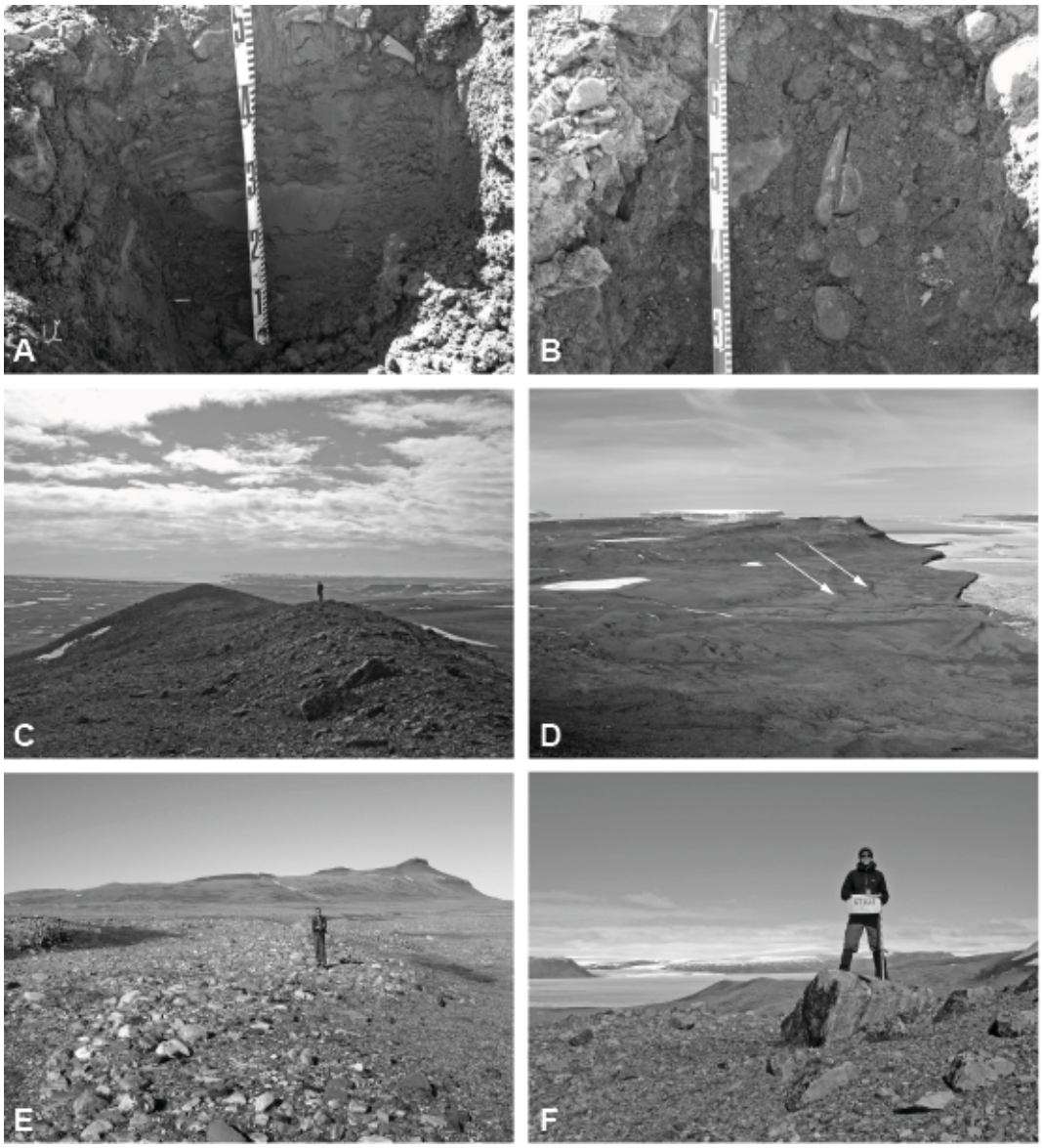

Figure 3. Photographs of field area. (A) Soil pit excavated in the clay-rich diamict covering the majority of the landscape. (B) Soil pit excavated in the sandy diamict near Wolstenholme Fjord. (C) Southeasterly view of one of the moraine ridges in the sandy diamict. (D) Westerly view of the wave-cut benches between the moraines and the fjord. (E) Ground view of the flat-topped, steep-fronted wave cut benches with abundant boulders. (F) Example of a moraine crest boulder sampled for cosmogenic nuclide analysis.

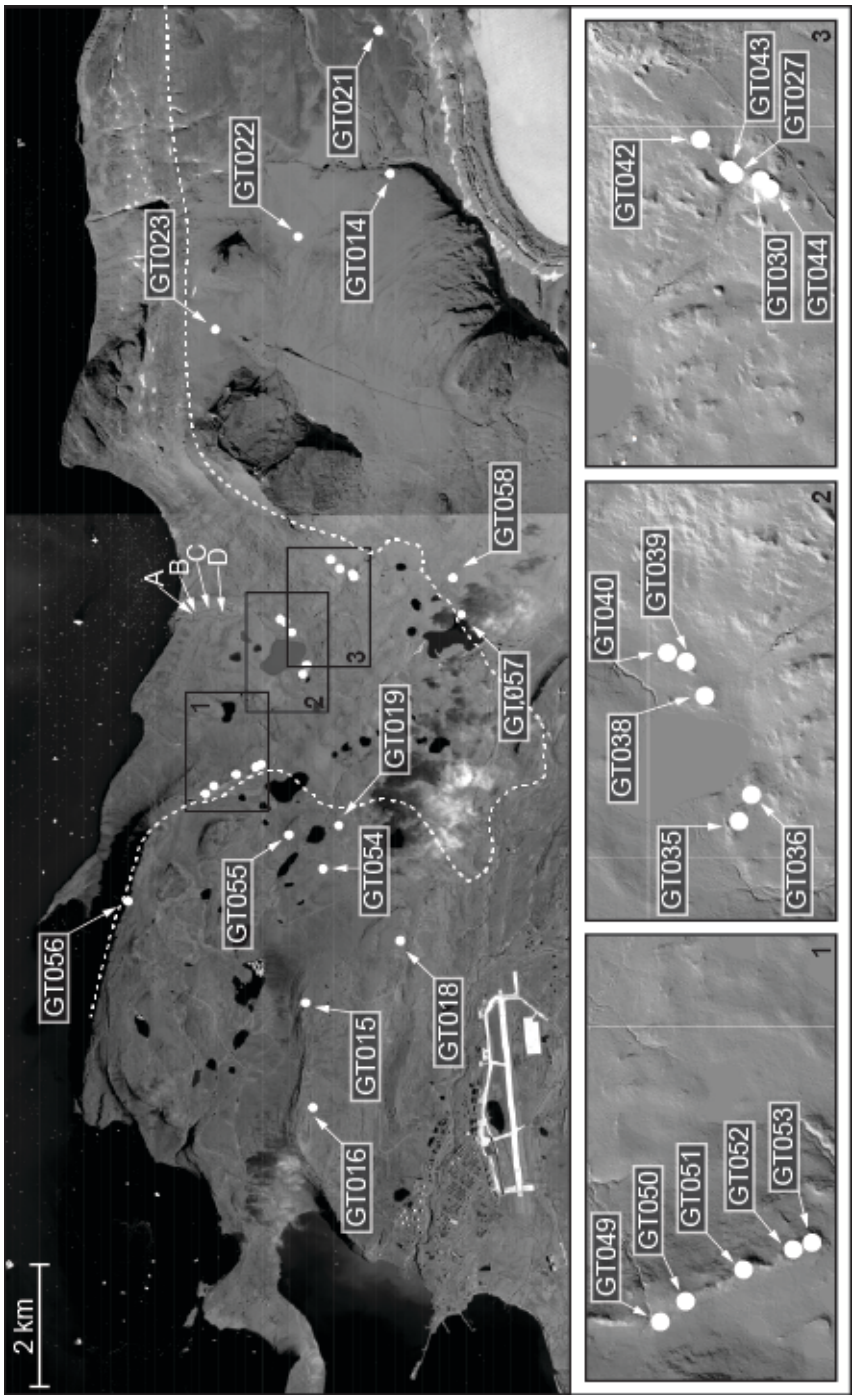

Figure 4. Map of glacially-deposited boulders (white dots) sampled for cosmogenic nuclide analysis in Thule. Main panel shows all 28 boulders. White letters A, B, C, and D show the locations of the four stratigraphic sections detailed in Figure 5. Subpanels 1, 2, and 3 (black letters) show detail of the moraines with 2011 LiDAR imagery and boulder sample sites. Dashed white line shows the approximate location of the contact between the clay-rich diamict and the sandy diamict, as detailed in Figure 2.

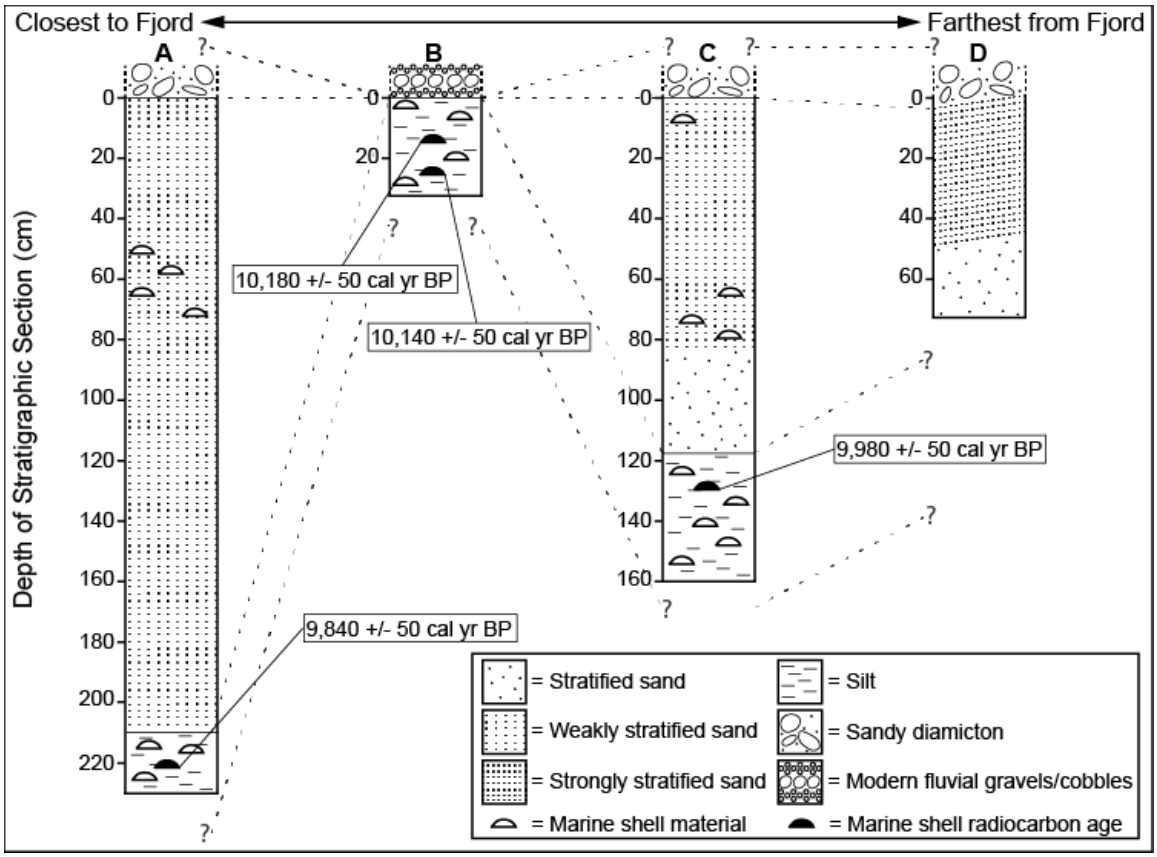

Figure 5. Illustrations of sediment stratigraphy observed in four stratigraphic sections excavated into stream banks incised into the reworked sandy diamict (see Figure 4 for section locations). Four marine shells were radiocarbon dated; ages shown here have been reservoir-corrected and calibrated.

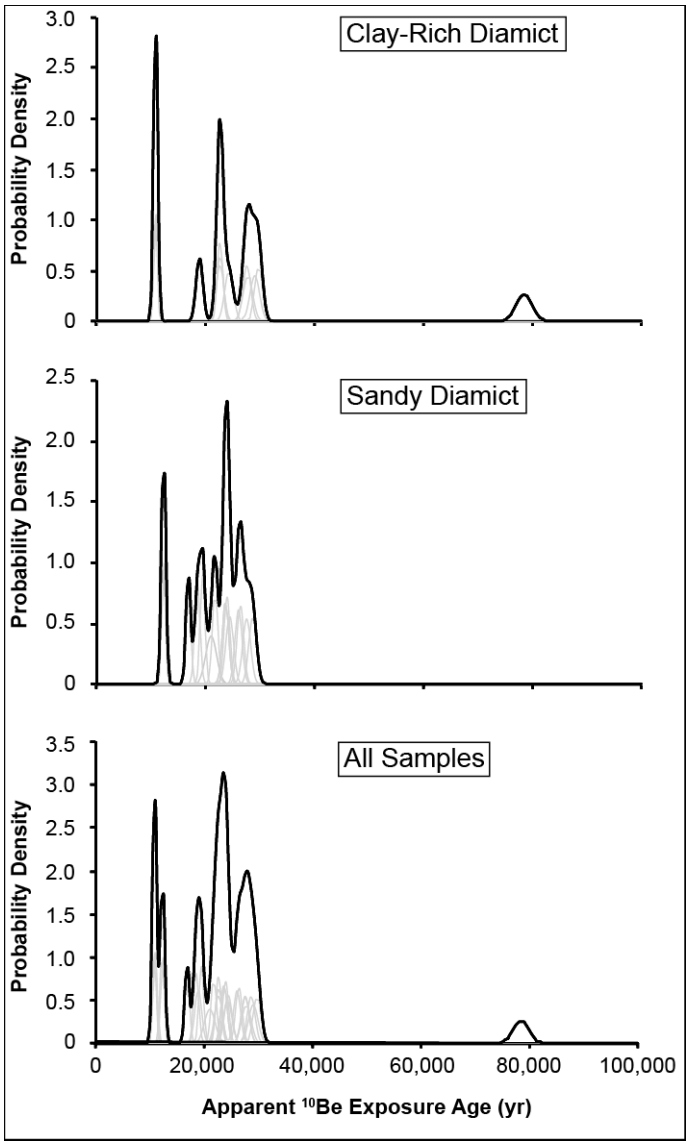

Figure 6. Probability density functions of minimum limiting ^{10}Be ages for boulders in the clay-rich diamict (n = 13, top), sandy diamict (n = 15, middle), and the entire data set (n = 28, bottom). Thin gray lines show each individual sample and its external uncertainty; thick black lines depict the sum of all sample probabilities together.

CHAPTER 3. LANDSCAPE DEVELOPMENT BENEATH NON-EROSIVE GLACIAL ICE IN THULE, GREENLAND, PART II OF II

(IN PRESS WITH EARTH AND PLANETARY SCIENCE LETTERS)

CONSTRAINING MULTI-STAGE EXPOSURE-BURIAL SCENARIOS FOR BOULDERS PRESERVED BENEATH COLD-BASED GLACIAL ICE IN THULE, NORTHWEST GREENLAND

Lee B. Corbett*[a], Paul R. Bierman[a], and Dylan H. Rood[b]

*Corresponding Author: Ashley.Corbett@uvm.edu, (802) 380-2344
[a]Department of Geology and Rubenstein School of Environment and Natural Resources, University of Vermont, Burlington, VT 05405
[b]Department of Earth Science and Engineering, Imperial College London, South Kensington Campus, London SW7 2AZ, UK & Scottish Universities Environmental Research Centre (SUERC), East Kilbride G75 0QF, UK

Abstract

Boulders and landscapes preserved beneath cold-based, non-erosive glacial ice violate assumptions associated with simple cosmogenic exposure dating. In such a setting, simple single isotope exposure ages over-estimate the latest period of surface exposure; hence, alternate approaches are required to constrain the multi-stage exposure/burial histories of such samples. Here, we report 28 paired analyses of ^{10}Be and ^{26}Al in boulder samples from Thule, northwest Greenland. We use numerical models of exposure and burial as well as Monte Carlo simulations to constrain glacial chronology and infer process in this Arctic region dominated by cold-based ice. We investigate three specific cases that can arise with paired nuclide data: (1) exposure ages that are coeval with deglaciation and ^{26}Al/^{10}Be ratios consistent with constant exposure; (2) exposure ages that pre-date deglaciation and ^{26}Al/^{10}Be ratios consistent with burial following initial exposure; and (3) exposure ages that pre-date deglaciation and ^{26}Al/^{10}Be ratios consistent with constant exposure. Most glacially-transported boulders in Thule have complex histories; some were exposed for tens of thousands of years and buried for at least hundreds of thousands of years, while others underwent only limited burial. These boulders were recycled through different generations of till over multiple glacial/interglacial cycles, likely experiencing partial or complete shielding during interglacial periods due to rotation or shallow burial by sediments. Our work demonstrates that the landscape in Thule, like many high-latitude landscapes, was shaped over long time durations and multiple glacial and interglacial periods throughout the Quaternary.

1. Introduction

In situ produced cosmogenic nuclides, such as ^{10}Be and ^{26}Al, are widely used to reconstruct glacial histories (Balco, 2011; Fabel and Harbor, 1999). These nuclides, produced predominately by nuclear spallation reactions caused by the bombardment of cosmic rays, build up in rock surfaces at predictable rates over time (Lal, 1988) and can be used to make inferences about surface exposure history (Granger et al., 2013). However, measurement of cosmogenic nuclides in cold, high-latitude areas can yield results that are complex and challenging to interpret (Briner et al., 2005). Both bedrock surfaces and boulders can yield exposure ages that are older than expected, sometimes by hundreds of thousands of years (Bierman et al., 1999). Rather than forming a single, normally distributed population, exposure ages from boulders in polar regions often form multi-modal distributions (Marsella et al., 2000), consistent with exposure during different numbers of interglacial periods as till was repeatedly reworked (Briner et al., 2005; Corbett et al., 2015). When multiple nuclides with different half lives are analyzed in the same sample, they can (but do not always) yield discordant exposure ages and isotopic ratios indicative of at least one period of burial following initial exposure (Bierman et al., 1999). Pre-deglaciation exposure ages, multi-modal age distributions, and discordant ages from different isotopes are all consistent with landscapes preserved for multiple glacial/interglacial cycles beneath cold-based, non-erosive ice.

Non-erosive glacial ice existed widely in high latitude regions in the past, including areas of Greenland (Bierman et al., 2014; Håkansson et al., 2008), Antarctica (Nishiizumi et al., 1991), Arctic Canada (Bierman et al., 1999; Briner et al., 2003), and Scandinavia (Stroeven et al., 2002). Cold-based ice also existed in mid-latitude regions,

especially at high elevations (Bierman et al., 2015) and along thin ice sheet margins (Colgan et al., 2002). Since cosmic rays attenuate as they pass through Earth materials at a rate controlled by density, burial by ~10 m of ice causes production of nuclides by spallation to become negligible (Lal, 1988). But because bedrock and boulders buried by cold-based ice are not deeply eroded, they can contain cosmogenic nuclides inherited from previous periods of exposure and thus violate the primary assumption of simple cosmogenic exposure dating: that the sample surface began the exposure period of interest containing no cosmogenic nuclides. Constraining the history of once-glaciated bedrock surfaces and boulders that have been alternately exposed and buried with little erosion requires the use of multiple isotopes including a stable nuclide (^{3}He or ^{21}Ne) and/or radioactive nuclides (e.g. ^{10}Be, ^{26}Al, ^{36}Cl, and ^{14}C) in order to quantify the durations of exposure and burial (Bierman et al., 1999; Briner et al., 2003; Briner et al., 2006; Corbett et al., 2013; Håkansson et al., 2008; Kaplan et al., 2001; Marquette et al., 2004; Stroeven et al., 2002; Sugden et al., 2005).

Measuring at least two radioactive cosmogenic nuclides in a single sample sheds light on multi-stage exposure/burial histories because the nuclides decay at different rates when the sampled surface is shielded from cosmic-ray exposure (but not eroded) and nuclide production ceases (Granger, 2006). Such data are typically plotted on a two-isotope diagram, where samples can either overlap or fall below a pathway consistent with constant surface exposure (Klein et al., 1986). Using two nuclides, a minimum total history (one period of exposure followed by one period of burial) can be calculated (Fabel and Harbor, 1999), providing minimum limits of exposure and burial durations

(Bierman et al., 1999). However, limitations still persist even with the multiple-nuclide approach since modeled histories represent non-unique inverse solutions.

Here, we present and analyze measurements of ^{10}Be and ^{26}Al in samples from 28 glacially-deposited boulders collected near Thule, northwest Greenland (Fig. 1), a long-lived landscape preserved beneath non-erosive glacial ice (Corbett et al., 2015). These boulders were sourced from two distinct diamict units that were deposited at different times and by different bodies of ice. Our goal is to make inferences about land surface development, boulder source/transport, and the history of ice cover in this cold-based ice landscape. We seek to provide additional constraints on the non-unique solutions that can arise when using cosmogenic nuclides at high latitude where ice is cold-based and exposure histories are often complex and multi-stage. Utilizing paired cosmogenic nuclides, numerical models, and Monte Carlo simulations, we provide a generalizable approach to understanding the history of cold-based ice landscapes and the sediments that mantle them.

2. Study Site, Previous Work, and Data Set

Thule, northwest Greenland (~69°W, 77°N) is located on the coast at the margin of the Greenland Ice Sheet, bordered on the east by TUTO Ice Dome and on the north by the Harald Moltke Bræ outlet glacier (Fig. 1). Little bedrock is exposed in the study area, although Late Proterozoic basin sediments of the Thule Supergroup (including shale and redbeds) crop out in the areas of high topography lying to the north and northeast of Thule Air Base, close to Wolstenholme Fjord (Dawes, 2006). Archaean basement orthogneisses and paragneisses are exposed to the east of the study area between TUTO

Ice Dome and Harald Moltke Bræ, as well as across the fjord on the north side of Harald Moltke Bræ (Dawes, 2006). Previous work constrained the timing of the last deglaciation to a minimum of ~10-9 cal ka BP with radiocarbon ages of mollusk shells in raised marine material (Goldthwait, 1960; Morner and Funder, 1990). Mollusk ages and stratigraphic analysis also suggest that Harald Moltke Bræ readvanced more recently than ~10 cal ka BP, possibly in concert with the 8.2 ka cold reversal (Corbett et al., 2015). Ice margins later receded inland of their current position during the mid-Holocene, as constrained by radiocarbon ages of marine shells embedded in glacial shear planes (Goldthwait, 1960; Morner and Funder, 1990).

Additional work investigated the glacial history of Thule with mapping and cosmogenic exposure dating. Corbett et al. (2015) documented two different surface sedimentary units: a clay-rich diamict deposited by the main Greenland Ice Sheet during the last glaciation and a sandy diamict deposited by a subsequent re-advance of the Harald Moltke Bræ outlet glacier immediately north of Thule (Fig. 1). Although simple exposure dating with ^{10}Be was complicated by the presence of nuclides inherited from past periods of exposure, Corbett et al. (2015) inferred the timing of the last deglaciation to be ~11 ka based on the youngest ^{10}Be ages from boulders in the clay-rich diamict, an age estimate supported by previous radiocarbon dating of marine bivalves. The findings of Corbett et al. (2015) strongly suggest that at least some boulders in the Thule area, which preserve tens of thousands of years worth of exposure history and form multi-modal age distributions, contain cosmogenic nuclides inherited from previous exposure due to subglacial landscape preservation beneath cold-based, non-erosive ice. Based on the old simple ^{10}Be exposure ages and small 1σ analytic uncertainties (average of 2.8 ±

0.6 %), the original dataset described in Corbett et al. (2015) is an ideal candidate for analysis of an additional nuclide (^{26}Al), the results of which we present here and assess with numerical modeling approaches.

3. Methods

3.1. Sample Collection, Laboratory Preparation, and Single-Isotope Exposure Ages

Samples were collected in 2011-2013 from 28 glacially deposited boulders, all of which were above the post-glacial marine limit of ~40-50 m (Morner and Funder, 1990). Details of sample collection and processing are presented in Corbett et al. (2015). Boulder lithologies are dominantly granite gneiss, likely derived from outcrops of the Archaean orthogneisses described by Dawes (2006) that are exposed to the north and east of the study area. Thirteen boulders were located in the clay-rich diamict unit and 15 were located in the sandy diamict unit (Table 1, Fig. 1).

We added ~250 μg of ^{9}Be to each sample using in-house-made beryl carrier. If needed, we added ^{27}Al using 1000 μg mL^{-1} SPEX Al standard. Additions of ^{27}Al carrier were optimized to reach a total of ~2500 μg Al in each sample based upon quantification of native ^{27}Al in purified quartz. We then quantified total ^{27}Al in the samples via inductively-coupled plasma optical emission spectrometry (ICP-OES) analysis of replicate aliquots removed from the samples immediately following digestion (see supplemental data); these aliquots represent ~2% and 4% of the sample mass, respectively. We used two emission lines for each element (Be, 234.861 and 249.473 nm; and Al, 308.215 and 309.271 nm) and two internal standards (Ga and Y) for all analyses. The agreement between Al estimates for the replicate analyses of process blanks is 0.4 ±

0.4 % (average, 1SD, n = 4 sets of replicates) while the agreement between Al estimates for the replicate analyses of samples is 1.1 ± 2.9 % (average, 1SD, n = 28 sets of replicates). We use the ICP-quantified total ^{27}Al (1824-4028 μg; see supplemental data) of all samples and blanks for further calculations. Since the uncertainty of our ^{27}Al quantification is less than the analytic uncertainty of the AMS measurements, we did not propagate the ^{27}Al quantification uncertainty into our calculation of sample ^{26}Al concentrations.

Isotopic ratios were measured by Accelerator Mass Spectrometry (AMS) at the Scottish Universities Environmental Research Centre (Xu et al., 2015). Measured sample ratios for ^{10}Be/^{9}Be (see supplemental data) are $6.6 \cdot 10^{-14}$ to $5.6 \cdot 10^{-13}$ (average analytic uncertainty 2.8 ± 0.5%, 1SD, n = 28). Ratios were normalized to the NIST standard, with an assumed ^{10}Be/^{9}Be ratio of $2.79 \cdot 10^{-11}$. We used a ^{10}Be/^{9}Be background ratio of 2.7 ± $0.2 \cdot 10^{-15}$ (average, 1SD, n = 3), which equates to 4.1 ± $0.4 \cdot 10^{4}$ atoms of ^{10}Be, representing a 2.0 ± 0.8 % blank correction for the samples (average, 1SD, n = 28). Measured sample ratios for ^{26}Al/^{27}Al (see supplemental data) are $1.1 \cdot 10^{-13}$ to $8.8 \cdot 10^{-13}$ (average analytic uncertainty 3.5 ± 0.8%, 1SD, n = 28). Ratios were normalized to standard Z92-0222 with an assumed ^{26}Al/^{27}Al ratio of $4.11 \cdot 10^{-11}$, which is closely inter-calibrated with standard KNSTD (Xu et al., 2015). We used a ^{26}Al/^{27}Al background ratio of 8.7 ± $3.9 \cdot 10^{-16}$ (average, 1SD, n = 4), which equates to 4.8 ± $2.2 \cdot 10^{4}$ atoms of ^{26}Al, representing a 0.3 ± 0.1 % blank correction for the samples (average, 1SD, n = 28). We subtracted background ratios from sample ratios and propagated uncertainties in quadrature.

We calculated simple exposure ages using the CRONUS Earth calculator (Balco et al., 2008) with calculator version 2.2 and constants version 2.2.1. We employed the

northeastern North American sea-level production rates of 3.93 ± 0.19 atoms g^{-1} yr^{-1} for ^{10}Be and 26.54 ± 1.35 atoms g^{-1} yr^{-1} for ^{26}Al (Balco et al., 2009) and the Lal/Stone constant production rate model and scaling scheme (Lal, 1991; Stone, 2000).

3.2. Two-Isotope Exposure and Burial Durations

To perform two-isotope exposure/burial calculations, we normalized nuclide concentrations to sea level using the CRONUS-determined production rates (Table 1). We assume a $^{26}Al/^{10}Be$ production ratio of 6.75 (Balco et al., 2009), a ^{10}Be half-life of $1.36 \cdot 10^6$ yr (Nishiizumi et al., 2007), and a ^{26}Al half-life of $7.05 \cdot 10^5$ yr (Nishiizumi, 2004). We assume no nuclide production during burial by ice. Before two-isotope calculations were performed, sample nuclide concentrations were corrected for the most recent period of continuous exposure (Table 1) based on the average ^{10}Be exposure age of the three youngest samples from this data set (10.7 ka; GT022, GT023, and GT055; Table 1). To perform this correction, we subtracted 10.7 ky worth of surface nuclide production from each sample's ^{10}Be and ^{26}Al concentrations; this correction shifts sample points downward and leftward on the two-isotope diagram, yielding shorter minimum limiting exposure durations and longer minimum burial durations than if the data had not been corrected. Using the corrected $^{26}Al/^{10}Be$ ratio as a filter, we modeled two-isotope histories only for samples that had corrected $^{26}Al/^{10}Be$ ratios indicative of burial beyond 1σ analytic uncertainties (n = 8) and report isotopic concentrations corrected for the most recent period of exposure only for these eight samples.

We conducted Monte Carlo simulations (10,000 models, varying ^{26}Al and ^{10}Be independently and assuming a normal uncertainty distribution for each isotope

concentration) for the eight samples (GT014, GT015, GT016, GT019, GT021, GT036, GT054, and GT058) that had $^{26}Al/^{10}Be$ ratios indicative of burial after initial exposure. For each randomly selected pair of independent $^{26}Al/^{10}Be$ concentrations, we calculated minimum limiting exposure and burial durations as described in Bierman et al. (1999), solving iteratively to determine the simplest numerical solution (one period of exposure followed by one period of burial, Fig. 2). We then used these 10,000 simulations to create probability density functions for the exposure and burial duration populations (Fig. 3) and calculated a mean and a standard deviation in order to assign a central tendency and an uncertainty for each sample's modeled exposure and burial durations. For these eight samples, we report (Table 2) the mean exposure and burial durations, their 1σ uncertainties, and the minimum total history (the sum of the initial exposure duration, the burial duration, and the assumed most recent exposure duration of 10.7 ky).

3.3. Forward Exposure/Burial Scenario Models

We utilize multi-stage forward exposure/burial models to constrain possible boulder histories, assuming the same production rates and half-lives described above. In these models, we assume that boulders may have been exposed during one or multiple interglacial periods with the low global ice volume: marine isotope stages (MIS) 15, 11, 9, and 5e (Lisiecki and Raymo, 2005). In scenarios involving numerous periods of exposure, we utilize incrementally increasing exposure durations (2 ky increments up to 10 ky for the last period of exposure) to simulate the boulder slowly making its way toward the coast via glacial transport and experiencing longer ice-free periods. We use burial durations of 200 ky during MIS 14-12, 75 ky during MIS 10, 225 ky during MIS 8-

6, and 100 ky during MIS 4-2, based on the timing described in Lisiecki and Raymo (2005). We do not include the most recent period of exposure (~10.7 ky) in these models so that the modeled isotopic concentrations (at the end of MIS 2) are comparable to the corrected isotopic concentrations in Thule samples for which minimum limiting exposure and burial durations were calculated.

We also use forward models to simulate cases in which boulders experience partial shielding during interglacial periods due to cover by overlying material, either because the boulder was rotated (thus placing the sample surface on the bottom during prior exposure) or was covered by till. For these models, we use 10 ky exposure periods alternating with 100 ky burial periods. During exposure, we utilize varying nuclide production scenarios that are based on portions of surface production, where 100% corresponds to no burial and full surface production. Our first modeled case (60% of surface production rates) equates to burial by ~35 cm of overlying rock or ~55 cm of overlying till. Our second modeled case (30% of surface production rates) equates to burial by ~70 cm of rock or ~110 cm of till. The above assume a cosmic ray attenuation length of 160 g cm^{-2}, a rock density of 2.7 g cm^{-3}, and a till density of 1.8 g cm^{-3}.

4. Results

For the 28 glacially-deposited boulders we sampled in the Thule area, ^{10}Be concentrations are $5.2 \cdot 10^4$ to $4.3 \cdot 10^5$ atoms g^{-1}, yielding simple exposure ages of 10.6 to 77.5 ka; ^{26}Al concentrations are $3.7 \cdot 10^5$ to $2.2 \cdot 10^6$ atoms g^{-1}, yielding simple exposure ages of 10.7 to 59.0 ka (Tables 1 and 2). Exposure ages calculated with ^{10}Be and ^{26}Al are well correlated ($R^2 = 0.95$, $p<0.01$), although ^{10}Be ages are systematically greater than

^{26}Al ages (regression slope = 0.72). Exposure ages from both isotopes form multi-modal age distributions with a distinct young peak ~11 ka, numerous overlapping peaks ~15-30 ka, and a single older outlier (Fig. 4). Measured ^{26}Al/^{10}Be ratios are 5.13 ± 0.14 to 8.50 ± 0.49 (average 6.85 ± 0.65, n = 28, 1SD), and ^{26}Al/^{10}Be ratios corrected for the most recent period of exposure (reported only for the eight samples with ^{26}Al/^{10}Be ratios indicative of complex histories) are as low as 4.88 (Table 1, Fig. 5).

There is no relationship between simple exposure age and the sedimentary unit from which the boulder was sourced (Table 2). Simple ^{10}Be boulder exposure ages from the clay-rich diamict are 25.5 ± 17.0 ka (average, 1SD, n = 13) while those from the sandy diamict are 21.2 ± 5.0 ka (average, 1SD, n = 15), representing two populations that are not statistically distinguishable (p = 0.40 for an unequal variance two-tailed Student's T-test). There is, however, a relationship between boulder history (as reflected by the ^{26}Al/^{10}Be ratio) and sedimentary unit (Table 1). Uncorrected boulder ^{26}Al/^{10}Be ratios from the clay-rich diamict are 6.55 ± 0.66 (average, 1SD, n = 13) while those from the sandy diamict are 7.11 ± 0.54 (average, 1SD, n = 15), representing two distinguishable populations (p = 0.02 for an unequal variance two-tailed Student's T-test).

For the eight samples with corrected ^{26}Al/^{10}Be ratios indicative of burial following initial exposure, we modeled exposure/burial durations and the associated uncertainties (Table 2). Modeled minimum limiting exposure durations prior to burial are 11 to 96 ky (not including the most recent period of exposure) and modeled minimum limiting burial durations are 88 to 627 ky. Minimum total histories (the sum of initial exposure duration, burial duration, and the most recent exposure duration) are 111 to 734 ky. Exposure duration uncertainties as constrained by Monte Carlo simulations are 1 to 4 ky, or 4 to

8% (average of 7%, 1SD) while burial duration uncertainties are 55 to 112 ky, or 9 to 105% (average of 37%, 1SD). Uncertainties scale inversely with modeled duration (see supplemental data).

5. Discussion

Cosmogenic data from boulders in cold-based ice regions generally fall into three different categories. 1.) Samples have simple exposure ages coincident with independent estimates of local deglaciation and $^{26}Al/^{10}Be$ ratios indistinguishable from continuous exposure within 1σ analytic uncertainties; these samples are likely free of cosmogenic nuclides from previous periods of exposure and record the timing of deglaciation. 2.) Samples have pre-deglaciation simple exposure ages and $^{26}Al/^{10}Be$ ratios that fall below the constant exposure pathway beyond 1σ analytic uncertainties; these samples likely experienced long durations of burial (hundreds of ky) by non-erosive or weakly-erosive ice and short durations of interglacial exposure. 3.) Samples have pre-deglaciation simple exposure ages but $^{26}Al/^{10}Be$ ratios that are consistent with constant exposure within 1σ analytic uncertainties; these samples may have experienced limited burial, but burial durations were not long enough to cause a detectable change in the $^{26}Al/^{10}Be$ ratio and/or the samples were re-exposed after burial long enough to increase the $^{26}Al/^{10}Be$ ratio so that it is not distinguishable from the production ratio (Bierman et al., 2015). We investigate these three different cases here, all of which are represented by the boulders from Thule.

5.1. Young Exposure Ages and $^{26}Al/^{10}Be$ Ratios Indicative of Constant Exposure

Deep subglacial erosion (at least several meters) can occur even in cold, high-latitude areas, especially in fjord bottoms where the ice is thick and the flow is channelized (Briner et al., 2009; Corbett et al., 2011; Davis et al., 1999; Hughes et al., 2012; Kaplan et al., 2001; Young et al., 2011). In these areas, boulders freshly quarried from eroded bedrock surfaces yield simple exposure ages that record the timing of deglaciation and $^{26}Al/^{10}Be$ ratios that overlap the constant exposure pathway within 1σ analytic uncertainties.

In Thule, only three of the 28 samples (GT022, GT023, and GT055, all from the clay-rich diamict) appear to have simple exposure ages that record the timing of deglaciation (Table 2). We make this inference because these samples form their own distinct population of ages (Fig. 4) and their ages agree closely with independent minimum deglaciation limits of ~10-9 cal ka BP developed using radiocarbon dating of marine bivalves in the same location (Corbett et al., 2015; Goldthwait, 1960; Morner and Funder, 1990). This implies that although deep glacial erosion can occur on this landscape, it is spatially restricted. These three boulders suggest deglaciation at 10.7 ± 0.1 ka (average, 1SD, taking into account only the ^{10}Be ages) or 11.0 ± 0.5 ka (average, 1SD, taking into account both ^{10}Be and ^{26}Al ages).

5.2. Old Exposure Ages and $^{26}Al/^{10}Be$ Ratios Indicative of Burial

Long durations of burial by cold-based, non-erosive glacial ice cause samples to have pre-deglaciation simple exposure ages and $^{26}Al/^{10}Be$ ratios inconsistent with constant exposure beyond 1σ analytic uncertainties. In cold-based environments,

subglacial erosion is minimal, thereby preserving nuclides from previous periods of exposure and leading to surfaces that reflect at least hundreds of thousands of years worth of history (Bierman et al., 1999; Corbett et al., 2013). In these areas, modern landscapes are a product of development over numerous glacial/interglacial cycles (Kleman and Borgstrom, 1994; Sugden and Watts, 1977).

In Thule, eight of the 28 samples (GT014, GT015, GT016, GT019, GT021, GT036, GT054, and GT058) have old ages and $^{26}Al/^{10}Be$ ratios lower than production (assuming a production ratio of 6.75; Table 2). Seven of these eight are from the clay-rich diamict, while only one (GT036) is from the sandy diamict. Modeled minimum limiting exposure durations are tens of ky while modeled minimum limiting burial durations are hundreds of ky (Table 2). Exposure durations (including the most recent period of exposure) represent on average only ~11% (range of 4-21%) of the total history of these samples; the small proportion of exposure is suggestive of boulders that spend most of their history buried beneath non-erosive glacial ice and possibly also by till during interglacial periods, experiencing only relatively brief periods of subaerial exposure.

Results from forward models (not including the most recent period of exposure) demonstrate that these eight samples preserve a range of histories. Samples GT014 and GT058, which have $^{26}Al/^{10}Be$ ratios of 6.45 and 6.29, respectively, are well explained by initial exposure during MIS 9 and re-exposure during MIS5e (Fig. 6). Samples GT015 and GT016 have lower $^{26}Al/^{10}Be$ ratios, necessitating more burial and hence a scenario including more glacial/interglacial cycles: possibly exposure during MIS 15, 11, 9, and 5e, with burial between (Fig. 6). Samples GT019, GT036, and GT054 have low $^{26}Al/^{10}Be$ ratios but also low concentrations of both isotopes, measurements not well explained by

scenarios involving cyclic exposure and burial. Rather, these samples may be explained by a scenario in which the boulders were initially exposed during an early interglacial period (e.g., MIS 11) and then remained completely buried (by ice during glacial periods and till during interglacial periods) until the Holocene (Fig. 6). Significantly longer-duration scenarios (at least a total of 734 ky, but likely much greater) are needed to explain the data from sample GT021, which has a low $^{26}Al/^{10}Be$ ratio and high isotopic concentrations; this boulder could have been repeatedly exposed and buried many times over much of the Quaternary period. Because there is less constraint on the behavior of the Greenland Ice Sheet during the earlier part of the Quaternary, and because so many possible scenarios could explain the location of sample GT021 on the two-isotope diagram, we do not attempt to fit this data point with a specific forward model. Rather, we suggest that this boulder likely preserves inherited nuclides from before the mid-Pleistocene transition, when the tempo of glacial cycles changed from 41 ka to 100 ka (Raymo et al., 1997).

5.3. Old Exposure Ages and $^{26}Al/^{10}Be$ Ratios Indicative of Constant Exposure

Different scenarios can lead to samples that have pre-deglaciation simple exposure ages and $^{26}Al/^{10}Be$ ratios consistent with constant exposure within 1σ analytic uncertainties. One possibility is that the land surface on which the boulder resides has been constantly exposed as a nunatak and never buried (Roberts et al., 2009; Stone et al., 1998). A second possibility is that the landscape was buried by ice in the past following initial exposure, but burial was short enough to not cause a detectable decrease in the $^{26}Al/^{10}Be$ ratio (Bierman et al., 2015).

Numerical models demonstrate that relatively short durations of burial, especially when followed by re-exposure, are insufficient to result in a $^{26}Al/^{10}Be$ ratio distinguishable from the constant exposure case at 1σ. Assuming a 10 ky period of exposure is followed by a 100 ky period of burial and subsequent Holocene exposure, a history consistent with exposure during MIS 5e and 1 and burial between, the resulting $^{26}Al/^{10}Be$ ratio is 6.59. Applying an uncertainty of 4.5% to the $^{26}Al/^{10}Be$ ratio (the average ratio uncertainty of the Thule data set), the resulting ratio of 6.59 is indistinguishable from 6.75 even though the surface spent over 80% of its history buried. In this case, the $^{26}Al/^{10}Be$ system is unable to distinguish boulders that experienced exposure during both MIS 5e and 1 from those that only experienced exposure during MIS 1. The inability to detect relatively short periods of burial is partly because the $^{26}Al/^{10}Be$ ratio uncertainty is greater than either of the single-isotope uncertainties (Gillespie and Bierman, 1995) and partly because isotopic concentrations (and hence the $^{26}Al/^{10}Be$ ratio) are more sensitive to exposure than burial due to the long half lives of these nuclides in comparison to the burial times. The relatively low concentrations of nuclides investigated in this study may represent an additional challenge for discerning short burial durations since the analytic uncertainty is more likely to overshadow small changes in nuclide concentrations caused by limited burial duration.

In Thule, 17 of the 28 samples have simple exposure ages older than expected, but $^{26}Al/^{10}Be$ ratios consistent with constant surface exposure. Only three of these 17 are from the clay-rich diamict; the remaining 14 are from the sandy diamict. Based on several lines of evidence, we conclude that these boulders are not indicative of constant exposure despite what their $^{26}Al/^{10}Be$ ratios suggest. Because the sandy diamict stratigraphically

overlies both the clay-rich diamict (deposited ~10.7 ka based on the three youngest boulders) and marine sediments (dated to ~10 cal ka BP with radiocarbon, Corbett et al. (2015)), it cannot have been deposited prior to the earliest Holocene. Rather, the boulders that record pre-deglaciation exposure ages, but have $^{26}Al/^{10}Be$ ratios indicative of constant exposure, were likely exposed during MIS 5e, when global ice volume was low (Lisiecki and Raymo, 2005) and Greenland's coastal areas were ice-free (Otto-Bliesner et al., 2006), then buried and minimally eroded until the onset of MIS 1 when they were re-exposed.

5.4. Till Recycling

Because our data indicate that most of the Thule boulders have been preserved subglacially, it is likely that the boulders we sampled are part of till units that have been repeatedly reworked and recycled. These boulders (primarily gneiss), which do not match the local bedrock (weakly metamorphosed basin sediments), were likely sourced to the east of the study area where Archaean basement orthogneisses are exposed (Dawes, 2006), although we are unable to constrain the transport distance since the subglacial extent of these basement rocks is unknown. These boulders may have been incorporated into till during one or numerous previous interglacial periods, slowly progressing coastward in flowing ice over time.

If the boulders in Thule have indeed been assimilated into different generations of till, it is likely that the surfaces we sampled were partially shielded during previous interglacial periods, either because they were buried beneath other sediments or because the boulders rotated and the surfaces we sampled were on the side or bottom during the

past. In the case of partial shielding during periods of exposure, the path taken through the two-isotope diagram compresses leftward since cosmogenic nuclides form at lesser rates than in the absence of shielding (Fig. 7). This overall leftward compression allows a larger number of exposure/burial cycles to occur before a given ^{10}Be concentration is reached than in the absence of shielding. Hence, if multiple samples have similar ^{10}Be concentrations, those that experienced partial shielding during periods of exposure have also experienced a larger total number of exposure/burial cycles, leading to longer burial durations and lower ^{26}Al/^{10}Be ratios than those that experienced no shielding (Fig. 7). Therefore, variable levels of shielding reflecting rotated or partially buried boulders in reworked till may at least partially explain the range of observed ^{26}Al/^{10}Be ratios.

The extent and patterns of till recycling (as recorded by ^{26}Al/^{10}Be ratio) appear to be related to the sedimentary unit from which the boulders were sourced, with the clay-rich diamict having been deposited by the main Greenland Ice Sheet during the last glaciation and the sandy diamict having been deposited by an early Holocene re-advance of Harald Moltke Bræ (Corbett et al., 2015). The population of 13 boulders from the clay-rich diamict includes three boulders with young ages and continuous exposure, seven boulders with old ages and complex history, and only one boulder with an old age but a ^{26}Al/^{10}Be ratio indistinguishable from constant exposure. Therefore, this unit appears to contain boulders recording heterogeneous processes, representing either no or significant recycling with little middle ground, possibly reflecting a wider source area and less erosive ice. Conversely, the population of 15 boulders from the sandy diamict includes one boulder with an old age and complex history and 14 boulders with old ages but ^{26}Al/^{10}Be ratios indistinguishable from constant exposure. Therefore, this unit appears

more homogeneous and the boulders record shorter total near-surface histories and less burial, possibly reflecting more erosive ice in the outlet glacier.

5.5. $^{26}Al/^{10}Be$ Production Ratio

A significant limitation in the ability to understand complex exposure histories with a multi-isotope approach lies in the uncertainty of how the $^{26}Al/^{10}Be$ production ratio varies over space. Although a production ratio of 6.75 is used in most calculations (Balco et al., 2008), recent work suggests that the production ratio is itself dependent on latitude and elevation. Actual $^{26}Al/^{10}Be$ production ratios may be greater than 6.75, with hypothesized values ranging as high as ~7.3, because each isotope's production rate scales differently with altitude and latitude (Argento et al., 2013; Argento et al., 2015; Borchers et al., 2015).

The $^{26}Al/^{10}Be$ ratios we report from Thule could be consistent with a higher than currently accepted production ratio. Eleven of the 28 measured $^{26}Al/^{10}Be$ ratios exceed 6.75 by more than 1σ (Table 1), compared to the four samples (16% of the population) we would expect based on measurement uncertainty. If we instead assume a production ratio of 7.16 (the median value of high latitude, low elevation CRONUS calibration samples reported in Argento et al. (2013)), only three of our 28 samples exceed the production ratio by more than 1σ and one (GT039) exceeds it by more than 2σ (Table 1), similar to what would be expected given the analytic precision of our data. Although systematic measurement error could also contribute to high $^{26}Al/^{10}Be$ ratios, with ICP-OES quantification of total Al being the most likely source (Bierman and Caffee, 2002;

Fujioka et al., 2015), we think this is unlikely since we do not see this trend for lower-latitude samples processed in our laboratory.

The assumed $^{26}Al/^{10}Be$ production ratio has important implications for determining which samples experienced a multi-stage history and for modeling those histories. Assuming a higher $^{26}Al/^{10}Be$ production ratio results in fewer samples with simple exposure histories and a greater number of samples with histories indicative of burial (Fig. 8). Although the $^{26}Al/^{10}Be$ production ratio has little impact on modeled minimum limiting exposure duration, it has a pronounced impact on modeled minimum limiting burial duration (Fig. 8). Sensitivity analysis for a representative sample in our dataset (GT016) demonstrates that modeled minimum limiting burial duration increases linearly with $^{26}Al/^{10}Be$ production ratio, with an additional 29 ky of burial added for each 0.1 increment of $^{26}Al/^{10}Be$ production ratio. More closely constraining the variability of the $^{26}Al/^{10}Be$ production ratio over space is an important direction for future work since it has significant implications for detecting and quantifying burial with the two-isotope approach.

6. Conclusions

The landscape in Thule, northwest Greenland, preserves a long record of heterogeneous subglacial processes. A small number of the boulders we sampled (three of 28) were sourced from areas deeply eroded during the last glacial period and their simple exposure ages suggest deglaciation of the landscape ~10.7 ka, consistent with radiocarbon age control. Other boulders (eight of 28) are indicative of ineffective subglacial erosion, yielding old simple exposure ages, $^{26}Al/^{10}Be$ ratios indicative of burial

following initial exposure, and modeled total histories of hundreds of ky. These boulders likely experienced initial exposure during MIS9 or an earlier interglacial period and record an exposure/burial history spanning at least several interglacial/glacial cycles. Finally, most boulders (17 of 28) have old simple exposure ages that pre-date deglaciation and $^{26}Al/^{10}Be$ ratios indistinguishable from constant exposure. These boulders have only experienced limited burial, suggesting that they were initially exposed during MIS 5e and re-exposed during MIS 1. Boulders from the clay-rich diamict unit deposited by the main Greenland Ice Sheet have nuclide concentrations indicative of either no or significant burial, whereas boulders from the sandy diamict unit deposited by a subsequent outlet glacier re-advance have nuclide concentrations largely suggestive of limited burial durations. The boulders we sampled come from till units that have likely been recycled but not deeply eroded several or many times over the Quaternary, with boulders sometimes experiencing partial or complete shielding during interglacial periods, leading to the range in exposure/burial scenarios we infer. Together these data reinforce the heterogeneity of subglacial processes and support the use of multi-nuclide approaches for studying glacial history in cold-based ice environments.

Acknowledgements

Support for this research was provided by a National Science Foundation Doctoral Dissertation Research Improvement Grant (BCS-1433878), the Geological Society of America Quaternary Geology and Geomorphology Division J. Hoover Mackin Award, an International Association of Geochemistry Student Research Grant, the Rubenstein School of Environment and Natural Resources at University of Vermont, a Dartmouth College Graduate Alumni Research Award, and NSF ARC-102319. Field support was provided by CH2MHILL, particularly J. Hurley and K. Derry. We thank G.E. Lasher and E. Osterberg for assistance during fieldwork, as well as J. Schaefer and two anonymous reviewers for improving the manuscript.

References

Argento, D., Reedy, R., Stone, J., 2013. Modeling the earth's cosmic radiation. Nuclear Instruments and Methods in Physics Research B 294, 464-469.

Argento, D., Stone, J., Reedy, R., O'Brien, K., 2015. Physics-based modeling of cosmogenic nuclides part II- Key aspects of in-situ cosmogenic nuclide production. Quaternary Geochronology 26, 44-55.

Balco, G., 2011. Contributions and unrealized potential contributions of cosmogenic-nuclide exposure dating to glacier chronology, 1990-2010. Quaternary Science Reviews 30, 3-27.

Balco, G., Briner, J., Finkel, R., Rayburn, J., Ridge, J., Schaefer, J., 2009. Regional beryllium-10 production rate calibration for late-glacial northeastern North America. Quaternary Geochronology 4, 93-107.

Balco, G., Stone, J., Lifton, N., Dunai, T., 2008. A complete and easily accessible means of calculating surface exposure ages or erosion rates from ^{10}Be and ^{26}Al measurements. Quaternary Geochronology 3, 174-195.

Bierman, P., Caffee, M., 2002. Cosmogenic exposure and erosion history of Australian bedrock landforms. Bulletin of the Geological Society of America 114, 787-803.

Bierman, P., Corbett, L., Graly, J., Neumann, T., Lini, A., Crosby, B., Rood, D., 2014. Preservation of a preglacial landscape under the center of the Greenland Ice Sheet. Science 344, 402-405.

Bierman, P., Davis, P., Corbett, L., Lifton, N., 2015. Cold-based, Laurentide ice covered New England's highest summits during the Last Glacial Maximum. Geology DOI:10.1130/G37225.1.

Bierman, P., Marsella, K., Patterson, C., Davis, P., Caffee, M., 1999. Mid-Pleistocene cosmogenic minimum-age limits for pre-Wisconsinan glacial surfaces in southwestern Minnesota and southern Baffin Island: a multiple nuclide approach. Geomorphology 27, 25-39.

Borchers, B., Marrero, S., Balco, G., Caffee, M., Goehring, B., Lifton, N., Nishiizumi, K., Phillips, F., Schaefer, J., Stone, J., 2015. Geological calibration of spallation production rates in the CRONUS-Earth project. Quaternary Geochronology http://dx.doi.org/10.1016/j.quageo.2015.01.009.

Briner, J., Bini, A., Anderson, R., 2009. Rapid early Holocene retreat of a Laurentide outlet glacier through an Arctic fjord. Nature Geoscience 2, 496-499.

Briner, J., Miller, G., Davis, P., Bierman, P., Caffee, M., 2003. Last Glacial Maximum ice sheet dynamics in Arctic Canada inferred from young erratics perched on ancient tors. Quaternary Science Reviews 22, 437-444.

Briner, J., Miller, G., Davis, P., Finkel, R., 2005. Cosmogenic exposure dating in arctic glacial landscapes: implications for the glacial history of northeastern Baffin Island, Arctic Canada. Canadian Journal of Earth Sciences 42, 67-84.

Briner, J., Miller, G., Davis, P., Finkel, R., 2006. Cosmogenic radionuclides from fjord landscapes support differential erosion by overriding ice sheets. Geological Society of America Bulletin 118, 406-420.

Colgan, P., Bierman, P., Mickelson, D., Caffee, M., 2002. Variation in glacial erosion near the southern margin of the Laurentide Ice Sheet, south-central Wisconsin, USA: Implications for cosmogenic dating of glacial terrains. Geological Society of America Bulletin 114, 1581-1591.

Corbett, L., Bierman, P., Graly, J., Neumann, T., Rood, D., 2013. Constraining landscape history and glacial erosivity using paired cosmogenic nuclides in Upernavik, northwest Greenland. Geological Society of America Bulletin 125, 1539-1553.

Corbett, L., Bierman, P., Lasher, G., Rood, D., 2015. Landscape chronology and glacial history in Thule, northwest Greenland. Quaternary Science Reviews 109, 57-67.

Corbett, L., Young, N., Bierman, P., Briner, J., Neumann, T., Graly, J., Rood, D., 2011. Paired bedrock and boulder 10Be concentrations resulting from early Holocene ice retreat near Jakobshavn Isfjord, western Greenland. Quaternary Science Reviews 30, 1739-1749.

Davis, P., Bierman, P., Marsella, K., Caffee, M., Southon, J., 1999. Cosmogenic analysis of glacial terrains in the eastern Canadian Arctic: a test for inherited nuclides and the effectiveness of glacial erosion. Annals of Glaciology 28.

Dawes, P., 2006. Geological map of Greenland, 1:500,000, Thule, Sheet 5, Geological Survey of Denmark and Greenland Map Series 2. Geological Survey of Denmark and Greenland, Danish Ministry of the Environment.

Fabel, D., Harbor, J., 1999. The use of in-situ produced cosmogenic radionuclides in glaciology and glacial geomorphology. Annals of Glaciology 28, 103-110.

Fujioka, T., Fink, D., Mifsud, C., 2015. Towards improvement of aluminium assay in quartz for in situ cosmogenic 26Al analysis at ANSTO. Nuclear Instruments and Methods in Physics Research Section B: Beam Interactions with Materials and Atoms 361, 346-353.

Gillespie, A., Bierman, P., 1995. Precision of terrestrial exposure ages and erosion rates estimated from analysis of cosmogenic isotopes produced *in situ*. Journal of Geophysical Research 100, 24,637-624,649.

Goldthwait, R., 1960. Study of ice cliff in Nunatarssuaq, Greenland. U.S. Army Snow, Ice, and Permafrost Research Establishment Technical Report 39, 106 p.

Granger, D., 2006. A review of burial dating methods using 26Al and 10Be. Geological Society of America Special Papers 415, 1-16.

Granger, D., Lifton, N., Willenbring, J., 2013. A cosmic trip: 25 years of cosmogenic nuclides in geology. Geological Society of America Bulletin 125, 1379-1402.

Håkansson, L., Alexanderson, H., Hjort, C., Moller, P., Briner, J., Aldahan, A., Possnert, G., 2008. Late Pleistocene glacial history of Jameson Land, central East Greenland, derived from cosmogenic ^{10}Be and ^{26}Al exposure dating. Boreas 38, 244-260.

Hughes, A., Rainsley, E., Murray, T., Fogwill, C., Schnabel, C., Xu, S., 2012. Rapid response of Helheim Glacier, southeast Greenland, to early Holocene climate warming. Geology 40, 427-430.

Kaplan, M., Miller, G., Steig, E., 2001. Low-gradient outlet glaciers (ice streams?) drained the Laurentide ice sheet. Geology 29, 343-346.

Klein, J., Giegengack, R., Middleton, R., Sharma, P., Underwood, J., Weeks, R., 1986. Revealing histories of exposure using *in situ* produced 26Al and 10Be in Libyan desert glass. Radiocarbon 28, 547-555.

Kleman, J., Borgstrom, I., 1994. Glacial land forms indicative of a partly frozen bed. Journal of Glaciology 40, 255-264.

Lal, D., 1988. In situ-produced cosmogenic isotopes in terrestrial rocks. Annual Review of Earth and Planetary Sciences 16, 355-388.

Lal, D., 1991. Cosmic ray labeling of erosion surfaces: in situ nuclide production rates and erosion models. Earth and Planetary Science Letters 104, 424-439.

Lisiecki, L., Raymo, M., 2005. A Plio-Pleistocene stack of 57 globally distributed benthic ^{18}O records. Paleoceanography 20, 522–533.

Marquette, G., Gray, J., Gosse, J., Courchesne, F., Stockli, L., Macpherson, G., Finkel, R., 2004. Felsenmeer persistence under non-erosive ice in the Torngat and Kaumajet mountains, Quebec and Labrador, as determined by soil weathering and cosmogenic nuclide exposure dating. Canadian Journal of Earth Sciences 41, 19-38.

Marsella, K., Bierman, P., Davis, P., Caffee, M., 2000. Cosmogenic ^{10}Be and ^{26}Al ages for the last glacial maximum, eastern Baffin Island, Arctic Canada. Geological Society of America Bulletin 112, 1296-1312.

Morner, N., Funder, S., 1990. C-14 dating of samples collected during the NORDQUA 86 expedition, and notes on the marine reservour effect. Meddelelser om Gronland 22, 57-63.

Nishiizumi, K., 2004. Preparation of ^{26}Al AMS standards. Nuclear Instruments and Methods in Physics Research Section B: Beam Interactions with Materials and Atoms 223, 388-392.

Nishiizumi, K., Imamura, M., Caffee, M., Southon, J., Finkel, R., McAninch, J., 2007. Absolute calibration of ^{10}Be AMS standards. Nuclear Instruments and Methods in Physics Research Section B: Beam Interactions with Materials and Atoms 258, 403-413.

Nishiizumi, K., Kohl, C., Arnold, J., Klein, J., Fink, D., Middleton, R., 1991. Cosmic ray produced ^{10}Be and ^{26}Al in Antarctic rocks: exposure and erosion history. Earth and Planetary Science Letters 104, 440-454.

Otto-Bliesner, B., Marshall, S., Overpeck, J., Miller, G., Hu, A., 2006. Simulating Arctic climate warmth and icefield retreat in the last interglaciation. Science 311, 1751-1753.

Raymo, M., Oppo, D., Curry, W., 1997. The mid-Pleistocene climate transition: A deep sea carbon isotopic perspective. Paleoceanography 12, 546-559.

Roberts, D., Long, A., Schnabel, C., Davies, B., Xu, S., Simpson, M., Huybrechts, P., 2009. Ice sheet extent and early deglacial history of the southwestern sector of the Greenland Ice Sheet. Quaternary Science Reviews 28, 2760-2773.

Stone, J., 2000. Air pressure and cosmogenic isotope production. Journal of Geophysical Research 105, 23753-23759.

Stone, J., Ballantyne, C., Fifield, L., 1998. Exposure dating and validation of periglacial weathering limits, northwest Scotland. Geology 26, 587-590.

Stroeven, A., Fabel, D., Hattestrand, C., Harbor, J., 2002. A relict landscape in the centre of Fennoscandian glaciation: cosmogenic radionuclide evidence of tors preserved through multiple glacial cycles. Geomorphology 44, 145-154.

Sugden, D., Balco, G., Cowdery, S., Stone, J., Sass III, L., 2005. Selective glacial erosion and weathering zones in the coastal mountains of Marie Byrd Land, Antarctica. Geomorphology 67, 317-334.

Sugden, D., Watts, S., 1977. Tors, felsenmeer, and glaciation in northern Cumberland Peninsula, Baffin Island. Canadian Journal of Earth Sciences 14, 2817-2823.

Xu, S., Freeman, S., Rood, D., Shanks, R., 2015. Decadal 10Be, 26Al and 36Cl QA measurements on the SUERC 5 MV accelerator mass spectrometer. Nuclear Instruments and Methods Section B: Beam Interactions with Materials and Atoms 361, 39-42.

Young, N., Briner, J., Stewart, H., Axford, Y., Csatho, B., Rood, D., Finkel, R., 2011. Response of Jakobshavn Isbrae, Greenland, to Holocene climate change. Geology 39, 131-134.

Table 1. Sample collection and isotopic data from 28 glacially-deposited boulders.

Sample Name[a]	Sed. Unit[b]	Latitude (°N)	Longitude (°E)	Elevation (m a.s.l.)	Measured Values[c]						Elevation-Normalized & Corrected for the Most Recent Period of Exposure[d]					
					^{10}Be (atoms g^{-1})	1σ ^{10}Be Unc. (atoms g^{-1})	^{26}Al (atoms g^{-1})	1σ ^{26}Al Unc. (atoms g^{-1})	^{26}Al/^{10}Be Ratio (1σ)		^{10}Be (atoms g^{-1})	1σ ^{10}Be Unc. (atoms g^{-1})	^{26}Al (atoms g^{-1})	1σ ^{26}Al Unc. (atoms g^{-1})	^{26}Al/^{10}Be Ratio (1σ)	
GT014	C	76.54578	-68.15783	350	1.33×10^5	4.22×10^3	8.78×10^5	2.84×10^4	6.58 ± 0.30		4.84×10^4	1.53×10^3	3.12×10^5	1.01×10^4	6.45 ± 0.29	
GT015	C	76.55843	-68.64975	276	1.60×10^5	4.01×10^3	9.95×10^5	4.81×10^4	6.20 ± 0.34		7.67×10^4	1.92×10^3	4.53×10^5	2.19×10^4	5.91 ± 0.32	
GT016	C	76.55745	-68.71192	252	1.48×10^5	3.87×10^3	8.94×10^5	2.53×10^4	6.04 ± 0.23		6.84×10^4	1.79×10^3	3.83×10^5	1.08×10^4	5.60 ± 0.21	
GT018	C	76.54552	-68.61322	251	1.54×10^5	4.67×10^3	1.03×10^6	2.74×10^4	6.64 ± 0.27		---	---	---	---	---	
GT019	C	76.55382	-68.54360	178	1.12×10^5	2.44×10^3	6.72×10^5	1.99×10^4	6.01 ± 0.22		5.00×10^4	1.09×10^3	2.70×10^5	8.00×10^3	5.40 ± 0.20	
GT021	C	76.54702	-68.07298	314	4.33×10^5	8.20×10^3	2.22×10^6	4.38×10^4	5.13 ± 0.14		2.68×10^5	5.07×10^3	1.31×10^6	2.58×10^4	4.88 ± 0.13	
GT022[(R)]	C	76.55833	-68.19445	358	6.45×10^4	1.99×10^3	4.39×10^5	1.75×10^4	6.79 ± 0.34		---	---	---	---	---	
GT023[(R)]	C	76.56945	-68.24887	346	6.30×10^4	2.15×10^3	4.71×10^5	1.94×10^4	7.47 ± 0.40		---	---	---	---	---	
GT027	S	76.55336	-68.39177	175	1.37×10^5	3.45×10^3	9.80×10^5	2.80×10^4	7.16 ± 0.27		---	---	---	---	---	
GT030	S	76.55168	-68.39473	171	1.13×10^5	2.79×10^3	7.81×10^5	2.24×10^4	6.89 ± 0.26		---	---	---	---	---	
GT035	S	76.55843	-68.45382	71	1.03×10^5	2.36×10^3	7.30×10^5	2.19×10^4	7.08 ± 0.27		---	---	---	---	---	
GT036	S	76.55791	-68.44873	77	1.06×10^5	3.10×10^3	6.32×10^5	1.93×10^4	5.94 ± 0.25		5.45×10^4	1.59×10^3	2.89×10^5	8.84×10^3	5.31 ± 0.22	
GT038	S	76.55983	-68.42910	67	5.35×10^4	1.65×10^3	3.72×10^5	1.66×10^4	6.95 ± 0.38		---	---	---	---	---	
GT039	S	76.56069	-68.42268	74	5.22×10^4	1.66×10^3	4.44×10^5	2.14×10^4	8.50 ± 0.49		---	---	---	---	---	
GT040	S	76.56132	-68.42116	62	8.93×10^4	4.24×10^3	6.85×10^5	2.32×10^4	7.67 ± 0.45		---	---	---	---	---	
GT042	S	76.55457	-68.38605	138	1.21×10^5	2.78×10^3	8.47×10^5	2.46×10^4	7.02 ± 0.26		---	---	---	---	---	
GT043	S	76.55338	-68.39169	175	1.33×10^5	3.55×10^3	9.25×10^5	4.36×10^4	6.95 ± 0.38		---	---	---	---	---	
GT044	S	76.55151	-68.39625	185	8.31×10^4	2.08×10^3	5.91×10^5	2.17×10^4	7.11 ± 0.32		---	---	---	---	---	
GT049	S	76.57150	-68.52433	198	1.28×10^5	3.19×10^3	9.16×10^5	3.72×10^4	7.13 ± 0.34		---	---	---	---	---	
GT050	S	76.57030	-68.51962	198	9.08×10^4	2.40×10^3	6.27×10^5	2.60×10^4	6.90 ± 0.34		---	---	---	---	---	
GT051	S	76.56734	-68.51293	195	1.08×10^5	2.56×10^3	8.09×10^5	2.30×10^4	7.49 ± 0.28		---	---	---	---	---	
GT052	S	76.56478	-68.50867	187	1.17×10^5	2.92×10^3	8.34×10^5	3.77×10^4	7.10 ± 0.37		---	---	---	---	---	
GT053	S	76.56400	-68.50716	180	9.51×10^4	2.15×10^3	6.37×10^5	1.95×10^4	6.70 ± 0.26		---	---	---	---	---	
GT054	C	76.55590	-68.57046	183	9.27×10^4	3.10×10^3	5.66×10^5	2.11×10^4	6.11 ± 0.31		3.30×10^4	1.11×10^3	1.75×10^5	6.55×10^3	5.31 ± 0.27	
GT055[(R)]	C	76.56046	-68.54910	201	5.49×10^4	2.05×10^3	4.09×10^5	1.74×10^4	7.46 ± 0.42		---	---	---	---	---	
GT056	C	76.58178	-68.58881	324	1.29×10^5	3.50×10^3	9.09×10^5	2.95×10^4	7.05 ± 0.30		---	---	---	---	---	
GT057	C	76.53712	-68.41935	143	1.29×10^5	4.16×10^3	9.22×10^5	2.64×10^4	7.14 ± 0.31		---	---	---	---	---	
GT058	C	76.53816	-68.39758	158	1.15×10^5	3.78×10^3	7.45×10^5	2.13×10^4	6.48 ± 0.28		5.45×10^4	1.79×10^3	3.43×10^5	9.78×10^3	6.29 ± 0.27	

[a]Sample names followed by (R) are those interpreted to have only experienced the most recent period of exposure; these ages were used to correct the remaining samples.

[b]Describes the sedimentary unit from which the boulder was collected (C = clay-rich diamict, S = sandy diamict, see Fig. 1)

[c]Ratios and ratio uncertainties for ^{10}Be/^{9}Be and ^{26}Al/^{27}Al are included in the data repository.

[d]The correction for the most recent period of exposure is the average ^{10}Be apparent exposure age of the three youngest samples (10.7 ka). Corrected data is only shown for samples whose corrected ratios are consistent with burial; these are the samples for which exposure/burial modelling was conducted.

Table 2. Age data from 28 glacially-deposited boulders.

		Single-Nuclide Apparent Exposure Ages[c]		Paired-Nuclide Minimum Limiting Durations and Uncertainties[d]						
Sample Name[a]	Sed. Unit[b]	^{10}Be Age (ka)	^{26}Al Age (ka)	Exposure Duration (ky)	1σ Exposure Unc. (ky)	1σ Exposure Unc. (%)	Burial Duration (ky)	1σ Burial Unc. (ky)	1σ Burial Unc. (%)	Total History (ky)[e]
GT014	C	22.3	21.7	13	1	7	88	92	105	111
GT015	C	29.4	26.9	22	2	7	267	112	42	300
GT016	C	27.3	24.3	21	1	6	378	80	21	410
GT018	C	28.7	28.2	---	---	---	---	---	---	---
GT019	C	22.7	20.1	16	1	5	458	75	16	484
GT021	C	77.5	59.0	96	4	4	627	55	9	734
GT022(R)	C	10.7	10.7	---	---	---	---	---	---	---
GT023(R)	C	10.6	11.6	---	---	---	---	---	---	---
GT027	S	28.0	29.7	---	---	---	---	---	---	---
GT030	S	22.9	23.3	---	---	---	---	---	---	---
GT035	S	23.2	24.2	---	---	---	---	---	---	---
GT036	S	23.7	20.7	18	1	7	491	88	18	520
GT038	S	12.0	12.3	---	---	---	---	---	---	---
GT039	S	11.8	14.8	---	---	---	---	---	---	---
GT040	S	20.4	23.1	---	---	---	---	---	---	---
GT042	S	25.8	26.8	---	---	---	---	---	---	---
GT043	S	26.9	27.7	---	---	---	---	---	---	---
GT044	S	16.5	17.3	---	---	---	---	---	---	---
GT049	S	25.2	26.6	---	---	---	---	---	---	---
GT050	S	18.1	18.4	---	---	---	---	---	---	---
GT051	S	21.3	23.5	---	---	---	---	---	---	---
GT052	S	23.1	24.3	---	---	---	---	---	---	---
GT053	S	19.0	18.8	---	---	---	---	---	---	---
GT054	C	18.5	16.6	11	1	8	493	105	21	515
GT055(R)	C	10.7	11.8	---	---	---	---	---	---	---
GT056	C	22.2	23.1	---	---	---	---	---	---	---
GT057	C	27.2	28.7	---	---	---	---	---	---	---
GT058	C	23.8	22.7	15	1	7	142	91	64	168

[a]Sample names followed by (R) are those interpreted to have only experienced the most recent period of exposure; these ages were used to correct the remaining samples.

[b]Describes the sedimentary unit from which the boulder was collected (C = clay-rich diamict, S = sandy diamict, see Fig. 1)

[c]Ages were calculated using the northeastern North American production rates of 3.93 ± 0.19 atoms g^{-1} yr^{-1} for ^{10}Be and 26.5 ± 1.3 atoms g^{-1} yr^{-1} for ^{26}Al (Balco et al., 2009) and the Lal (1991)/Stone (2001) scaling scheme in CRONUS. Ages have been scaled for elevation, sample density, sample thickness, latitude, and longitude.

[d]Calculated only for samples whose corrected ratios are indicative of burial using the corrected and elevation-normalized ^{10}Be and ^{26}Al concentrations and 10,000 Monte Carlo simulations as described in the text, assuming a ^{26}Al/^{10}Be production ratio of 6.75.

[e]Total history is the sum of the initial exposure duration, burial duration, and most recent exposure duration (10.7 ky).

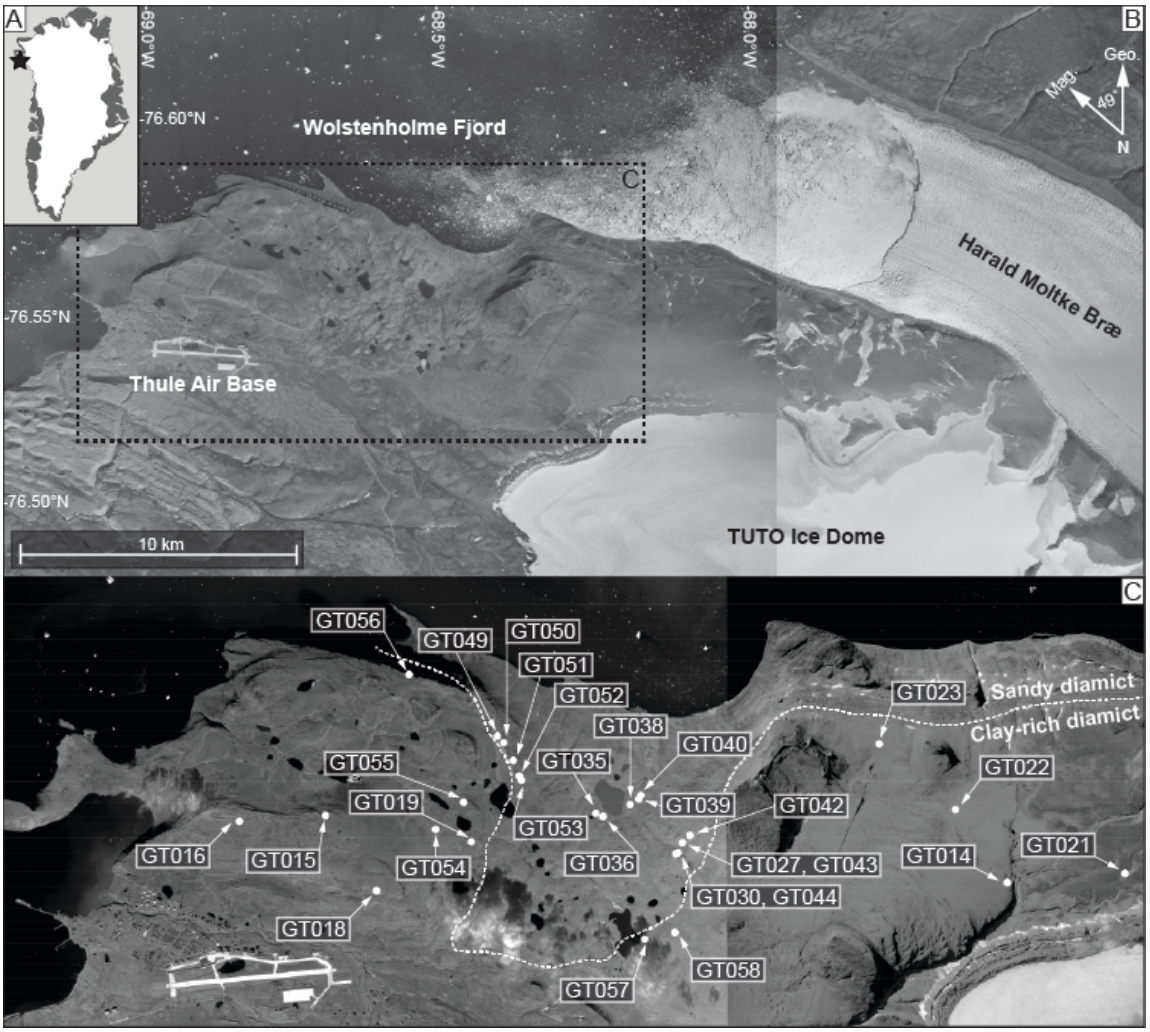

Figure 1. Location of the study site. Panel A shows the location of Thule in northwest Greenland. Panel B shows the Thule region with places described in the text. Panel C shows the location of the 28 boulder samples collected for analysis of cosmogenic $^{26}Al/^{10}Be$, with the white dashed line denoting the contact between the two diamict units described in the text.

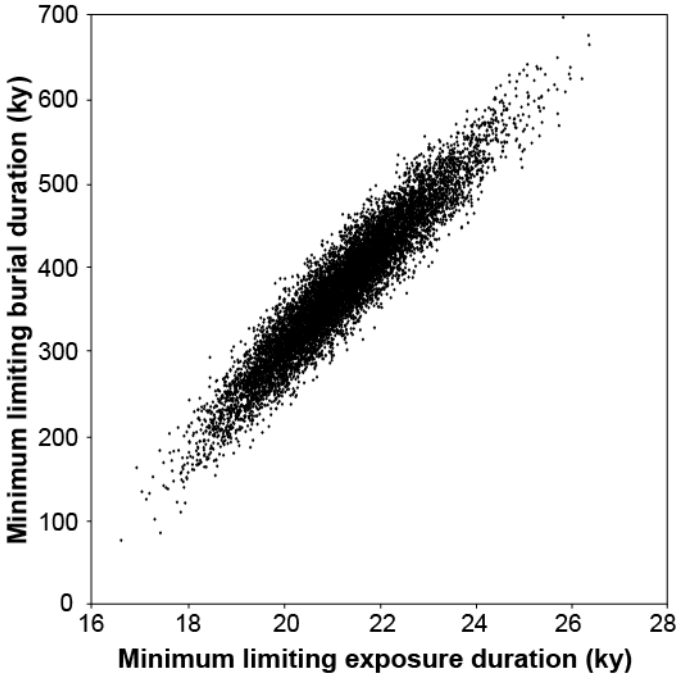

Figure 2. Example of Monte Carlo simulations for sample GT016. Each of the 10,000 simulations (black dots) indicates an iterative numerical solution of one period of exposure followed by one period of burial that explains the observed isotopic concentrations.

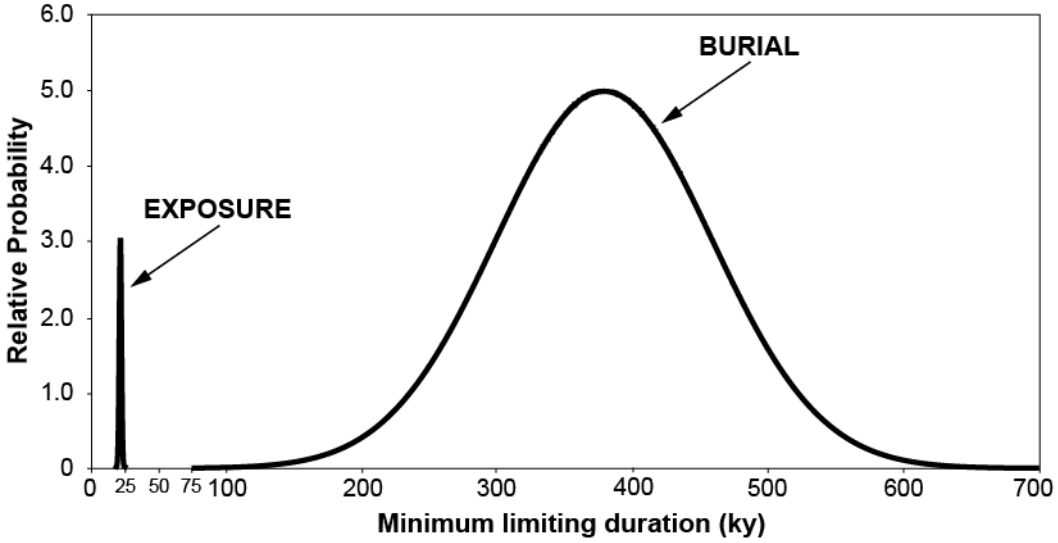

Figure 3. Example probability density functions of 10,000 exposure durations and 10,000 burial durations for sample GT016. We used these populations to calculate the mean and standard deviation of simulated exposure and burial durations for each sample.

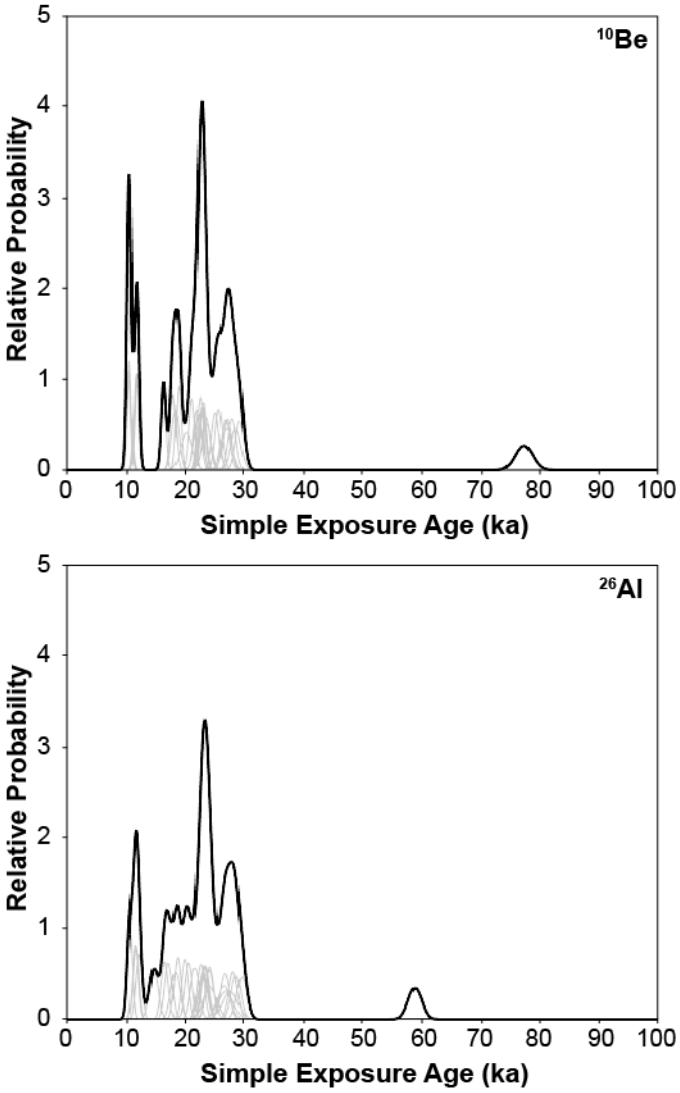

Figure 4. Probability density functions for ^{10}Be (top panel) and ^{26}Al (bottom panel) simple exposure ages of 28 boulder samples. Thin gray lines indicate the probability of each individual sample; thick black line indicates the summed probability for all samples.

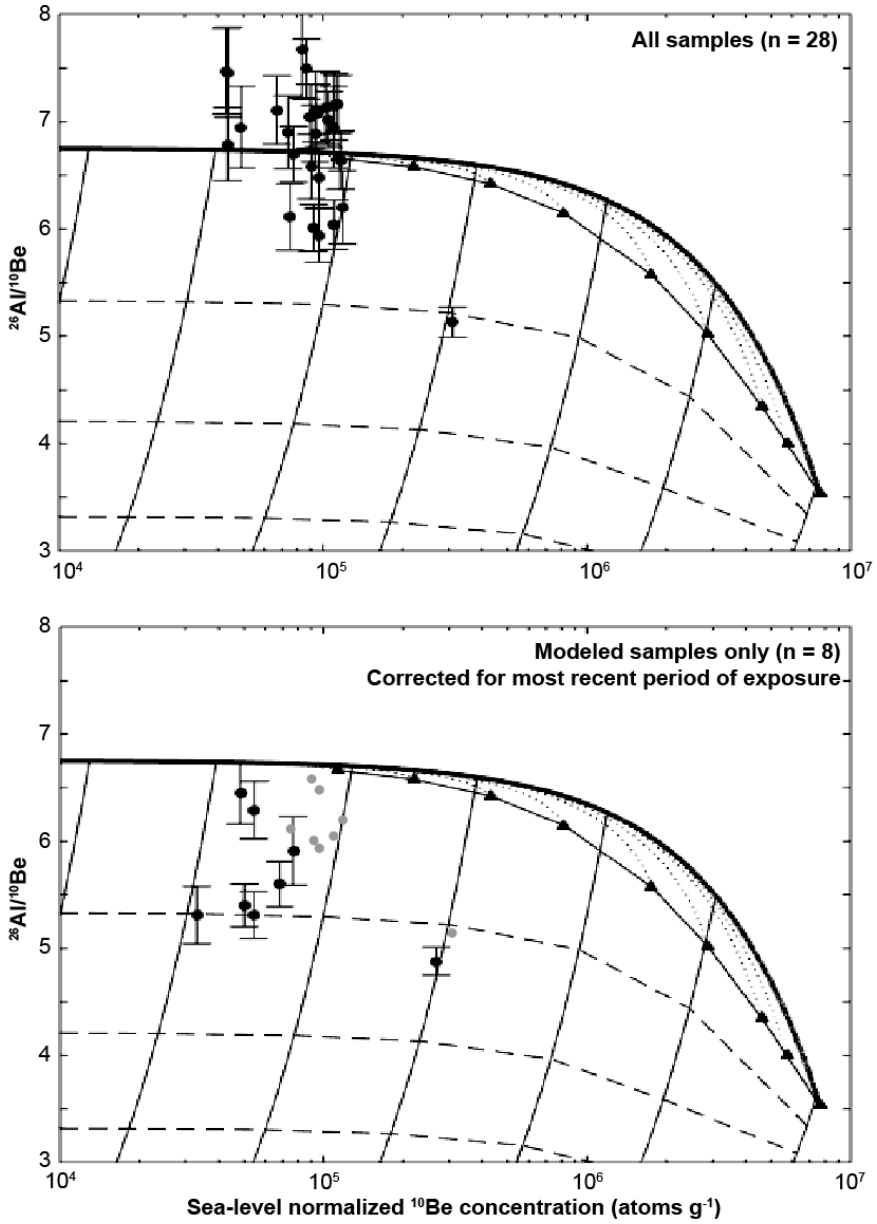

Figure 5. Measured ^{26}Al/^{10}Be ratios plotted against ^{10}Be concentrations for sea level normalized values. Top panel shows all samples, with one sample (GT039) omitted for visibility because of its high ratio (n = 27, 1σ error bars). Bottom panel shows only the samples that have been numerically modeled for exposure/burial (n = 8), with concentrations and ratios that have been corrected for the most recent period of exposure (black dots, 1σ error bars) and original uncorrected values (gray dots); see Figures 6 and 7 for sample names. Thick black line shows the constant exposure pathway. Dotted lines show erosion pathways of 25, 10, 5, 2, 1, 0.5, 0.2, and 0.1 m Ma^{-1}, from left to right. Black triangles show secular equilibrium endpoints for erosion scenarios as well as the constant exposure scenario. Burial paths are shown with thin lines, and burial isochrones (0.5, 1.0, and 1.5 Ma, from top to bottom) are shown with thin dashed lines.

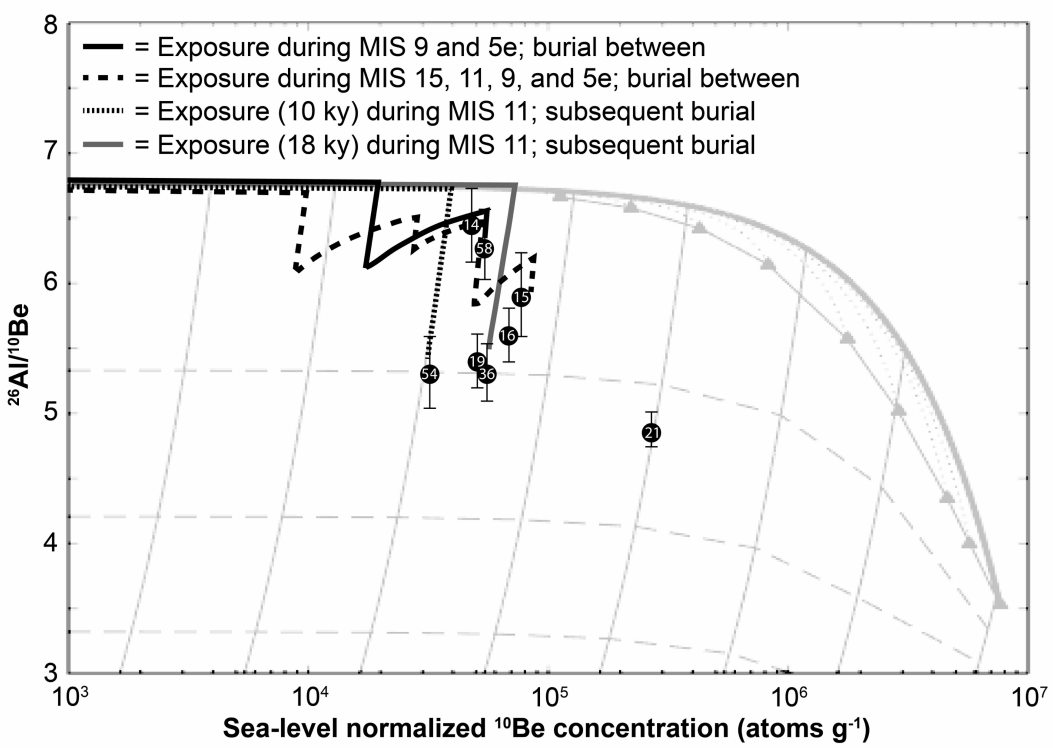

Figure 6. Two-isotope diagram as described in Fig. 5. Thick colored lines show isotopic evolution resulting from various exposure/burial scenarios. We assume that exposure durations increase incrementally with each subsequent period of exposure and we utilize burial durations that reflect the chronology described in Lisiecki and Raymo (2005). Black dots show the Thule samples that have been corrected for the most recent period of exposure; numbers indicate the sample number, error bars are 1σ.

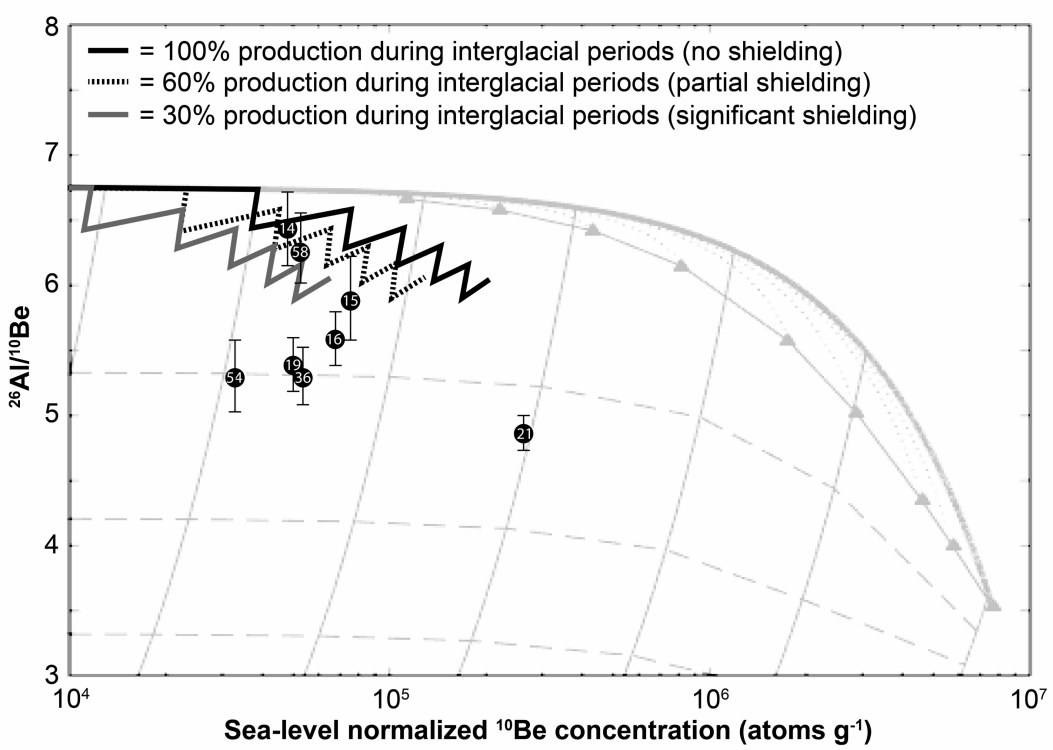

Figure 7. Two-isotope diagram as described in Fig. 5. Thick colored lines show isotopic evolution over alternate periods of exposure (10 ky) and burial (100 ky), with various levels of shielding during periods of exposure to simulate till cover or boulder rotation. Black dots show the Thule samples that have been corrected for the most recent period of exposure; numbers indicate the sample number, error bars are 1σ.

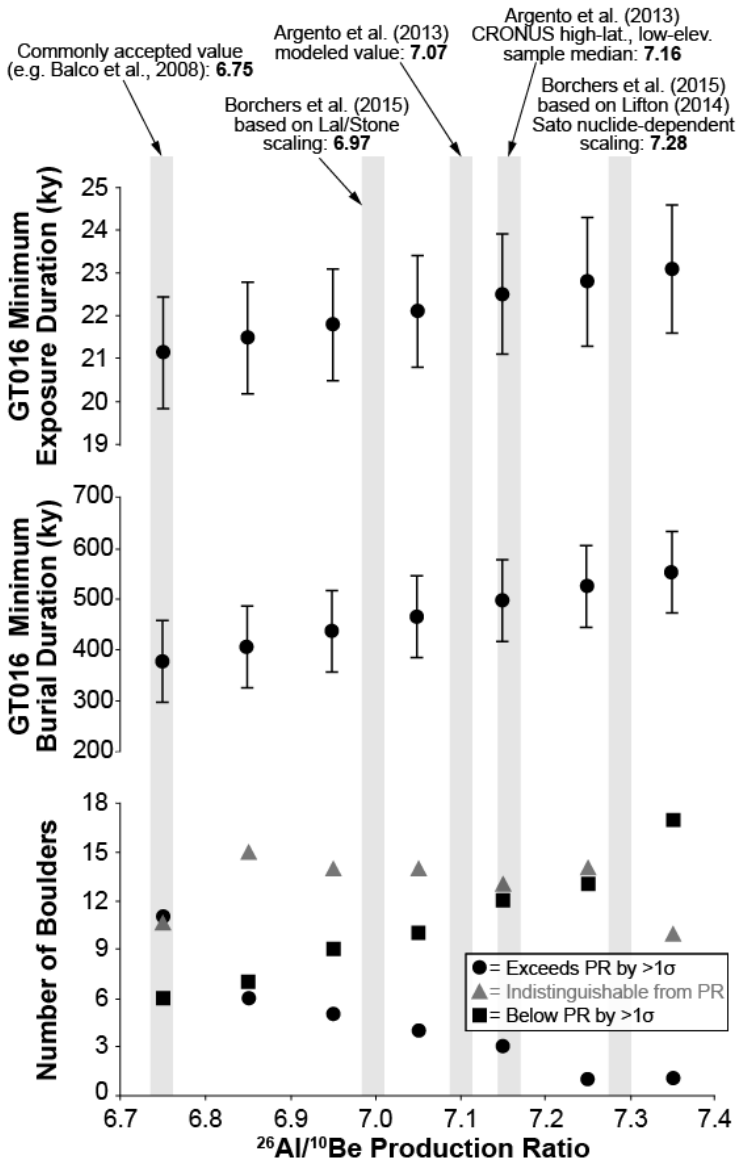

Figure 8. Sensitivity analysis investigating the effect of $^{26}Al/^{10}Be$ production ratio on inferred boulder histories using seven different production ratios: 6.75, 6.85, 6.95, 7.05, 7.15, 7.25, and 7.35. Top two panels show modeled minimum limiting exposure and burial durations for a representative sample in the dataset (GT016), with error bars showing +/- 1σ as derived by Monte Carlo analysis. Bottom panel shows the dataset as a whole and inferences regarding how many samples are above, indistinguishable from, or below the production ratio based on 1σ $^{26}Al/^{10}Be$ analytic uncertainties. Gray bars show possible $^{26}Al/^{10}Be$ production ratios from recent studies.

CHAPTER 4. LANDSCAPE DEVELOPMENT BENEATH NON-EROSIVE GLACIAL ICE ON BAFFIN ISLAND, CANADA

(IN PRESS WITH GEOLOGICAL SOCIETY OF AMERICA BULLETIN)

GLACIAL HISTORY AND LANDSCAPE EVOLUTION OF SOUTHERN CUMBERLAND PENINSULA, BAFFIN ISLAND, CANADA, CONSTRAINED BY COSMOGENIC 10BE AND 26AL

Lee B. Corbett*[a], Paul R. Bierman[a], and P. Thompson Davis[b]

*Contact Author: Ashley.Corbett@uvm.edu
[a]Department of Geology and School of Natural Resources, University of Vermont, Burlington VT 05405
[b]Department of Natural and Applied Sciences, Bentley University, Waltham MA 02452

Abstract

Since the first application of cosmogenic nuclides to the study of glacial history and processes in 1990, an increasing number of studies have used a variety of cosmogenic isotopes to quantify the exposure age and erosion rate of glaciated landscapes. However, obtaining chronological data from glaciated landscapes once covered by cold-based, non-erosive ice is challenging because these surfaces violate assumptions associated with simple cosmogenic exposure dating. Non-erosive glacial ice fails to completely remove nuclides produced during previous periods of exposure, leaving behind rock surfaces with complex, multi-genetic nuclide inventories.

Here, we constrain glacial history, landscape evolution, and the efficiency of subglacial erosion in the Pangnirtung Fiord region of southern Baffin Island using over 300 paired analyses of *in situ* cosmogenic ^{10}Be and ^{26}Al. Simple exposure ages are 6.3 to 160 ka for ^{10}Be (n = 152) and 4.3 to 124 ka for ^{26}Al (n = 153). Paired bedrock/boulder samples have discordant ages, simple exposure ages generally increase with elevation, ^{10}Be and ^{26}Al ages for the same sample disagree, and both boulders and bedrock yield multi-modal age distributions, all patterns suggestive of limited subglacial erosion. Measured ^{26}Al/^{10}Be ratios indicate that about one third of the samples in the dataset experienced at least one period of pre-Holocene exposure followed by burial with limited erosion. Modeled two-isotope minimum-limiting exposure durations are as high as hundreds of thousands of years and minimum-limiting burial durations range up to millions of years, implying that parts of southern Baffin Island have been preserved beneath non-erosive glacial ice for much if not all of the Quaternary. A subset of the samples contains few nuclides inherited from prior periods of exposure and is thus useful

for constraining the chronology of the most recent deglaciation. Using these samples, we infer that deglaciation of most of the landscape occurred ~11.7 ka and that the Duval moraines, a prominent feature of the last deglaciation, formed ~11.2 ka.

1. Introduction

Earth's high latitudes hold most of the planet's glacial ice, and thus have the potential to be significant contributors to sea level rise; these same areas are also forecasted to experience the greatest warming in the future (IPCC, 2013). For these reasons, it is particularly important to understand the response of the high-latitude cryosphere to past episodes of climate change in order to provide insight about possible future change (Long, 2009). However, the high latitudes are also some of the most difficult areas for studying glacial history because the presence of cold-based, non-erosive glacial ice violates key assumptions of "simple" cosmogenic exposure dating (one nuclide, assuming no erosion since exposure and no inheritance of nuclides from prior periods of exposure), a technique widely used to reconstruct past glacial extent and chronology (Balco, 2011).

Cosmogenic nuclides have been used to date glacial features for several decades (Balco, 2011; Fabel and Harbor, 1999; Nishiizumi et al., 1989; Phillips et al., 1990). These isotopes, including ^{10}Be and ^{26}Al, form at known rates in rock surfaces bombarded by high-energy cosmic rays (Lal, 1988). Thus, determining the nuclide concentration in a rock surface has the potential to provide insight about when the sample site was exposed from beneath retreating glacial ice (Gosse and Phillips, 2001; Phillips et al., 1990). Interpretation of a cosmogenic measurement in glacial terrain as a "simple" exposure age relies upon a critical assumption: that the surface contained no nuclides inherited from previous periods of exposure before being uncovered from beneath retreating glacial ice. Since cosmogenic nuclide production decreases exponentially with depth, erosion (e.g.

by subglacial abrasion or plucking) of at least several meters of rock is required to strip most pre-existing nuclides from a surface and make this assumption valid (Balco, 2011).

Landscapes that have been preserved beneath non-erosive glacial ice (Kleman and Borgstrom, 1994) violate the assumption of no inherited nuclides because they have experienced alternating periods of exposure and burial without sufficient erosion during periods of glaciation to remove nuclides produced during earlier periods of exposure. Cold-based, non-erosive "ghost glaciers," therefore, can preserve ancient subglacial surfaces for hundreds of thousands (Corbett et al., 2013) or even millions of years (Bierman et al., 2014). Such landscapes are therefore a product of numerous glacial-interglacial cycles (Sugden, 1977, 1978; Sugden and Watts, 1977), resulting in the juxtaposition of features with different ages and histories (Briner et al., 2003).

Landscapes that have been preserved through multiple glacial/interglacial cycles yield multi-modal simple exposure age distributions (Briner et al., 2005; Corbett et al., 2015b) and paired-isotope cosmogenic isotope data that can be interpreted in numerous, non-unique ways (Bierman et al., 1999). However, it is important to refine the methods required to constrain the timing of glacial events in areas where exposure histories are complex because these old, multi-genetic surfaces are archives of valuable long-term climatic and glacial information. Since cold, polar landscapes preserve such long histories, they compliment the study of temperate landscapes by providing insight into long-term glacial history and process rather than just the extent of ice during and since the Last Glacial Maximum (LGM).

Here, we attempt to understand better the glacial history and subglacial erosion patterns on southern Baffin Island (Fig. 1), an area known to have been buried at least in

part beneath cold-based ice numerous times throughout the Quaternary (Bierman et al., 2001; Bierman et al., 1999; Briner et al., 2003; Briner et al., 2005, 2006; Miller et al., 2006; Wolfe et al., 2001). We utilize paired analysis of cosmogenic ^{10}Be and ^{26}Al, a technique that detects burial after initial exposure and can constrain the minimum total history of surfaces subjected to periods of both exposure and burial (Bierman et al., 1999; Klein et al., 1986; Nishiizumi et al., 1991). We document the heterogeneity of the Baffin Island landscape by reporting over 300 analyses of 155 bedrock and boulder samples (including 150 paired ^{26}Al/^{10}Be measurements). We use the dataset as a whole to make inferences about patterns of subglacial erosion and to assess which samples most likely record simple surface exposure; then, we use subsets of the data to address specific questions about the spatial variability of exposure history, data reproducibility, and glacial history.

2. Study Site and Previous Work

Baffin Island, Canada (Fig. 1), is a NW-SE elongate island almost 1500 km in length, extending north to above 73°N. The island parallels the western coast of Greenland, which is ~500 km to the east across Baffin Bay. This study focuses on the southern side of Cumberland Peninsula, southern Baffin Island, an area that extends from ~65°N to ~67.5°N and borders Cumberland Sound. The study area is primarily underlain by Paleoproterozoic crystalline rocks of the Canadian Shield (Hamilton et al., 2012; Jackson and Taylor, 1972). One of the most prominent landscape features bordering Cumberland Sound is Pangnirtung Fiord, which is 43 km long, averages 2.5 km wide, and has a maximum water depth of 160 m (Gilbert, 1978). Pangnirtung Fiord is flanked

by highlands with elevations up to ~400 m a.s.l. on both its northwest and southeast sides, with the Penny Ice Cap located on the highlands directly to northwest of the fjord. The post-LGM marine limit is about 50 m asl at the hamlet of Pangnirtung, drops to about 16 m at the head of Kingnait Fiord, and rises to about 110 m at Kekerten Island and 65 m on the mainland south of the mouth of Kingnait Fiord, as mapped by Dyke (1979) and Kaplan and Miller (2003). Chronology of the marine limit is constrained by ^{14}C ages that have been recalibrated using CALIB 7.1 (Stuiver et al., 2015) and the IntCal13 calibration curve (Table 1).

Early work on Cumberland Peninsula noted the existence of distinct elevation-dependent weathering zones, which led to a prolonged debate about the extent and particularly the thickness of past glacial ice (for a review, see Marsella et al. (2000)). Many low-elevation regions (below ~100 m a.s.l.) near Pangnirtung Fiord are glacially-sculpted and bedrock outcrops appear unweathered. In contrast, outcrops in the highlands (several hundred m in elevation) are more heavily weathered and exhibit features indicative of long-lived subaerial exposure, including tors and felsenmeer (Dyke, 1977, 1979). To explain this weathering discrepancy, some argued that the Laurentide Ice Sheet during the LGM was not sufficiently thick to inundate the highlands with ice, and hence the high-elevation surfaces had been continually exposed and modified for hundreds of thousands of years (Ives, 1978). Others argued that the highlands had been glaciated during the LGM, but that the glacial ice was cold-based and incapable of performing erosion; therefore, these surfaces experienced alternating subaerial erosion and preservation beneath non-erosive ice (Sugden and Watts, 1977).

More recently, analysis of cosmogenic nuclides demonstrated that these weathering zones are related to subglacial erosion efficiency. Warm-based ice at low elevations scoured rock surfaces, leaving them fresh; in contrast, cold-based ice at higher elevations performed little erosion, leaving behind relict surfaces that had experienced repeated periods of subaerial exposure and weathering (Bierman et al., 1999; Briner et al., 2003; Briner et al., 2005, 2006; Kaplan et al., 2001; Margreth et al., 2011; Marsella et al., 2000). Modeling efforts suggest that highland ice was likely thin and cold-based during the late Wisconsinan, and that flow was concentrated in a low-gradient outlet glacier or ice stream in Cumberland Sound (Kaplan et al., 2001; Kaplan et al., 1999).

A system of moraines near the hamlet of Pangnirtung (Fig. 2) separates the upper and lower weathering zones and was thought by some to represent the most significant ice advance position recorded on the Cumberland Peninsula (Dyke, 1977, 1979). The type locality of the Duval moraines is the crest directly to the south of Mt. Duval, while the other crests are considered to be temporal equivalents to the Duval moraines. These moraines were originally interpreted to be early Wisconsinan (~60-100 ka) in age based on rock weathering, soil development, and amino acid ratios from a shell fragment in a 99 m a.s.l. glaciomarine delta on the northern side of Kingnait Fiord deposited contemporaneously with the moraines (Dyke, 1977, 1979).

However, this early Wisconsinan age is at odds with work documenting that the coastal areas of Baffin Island were inundated with ice that extended into Cumberland Sound during the LGM (Davis, 1988; Jennings, 1993; Lemmen et al., 1988). Kaplan and Miller (2003) interpreted three ^{14}C ages of 10.1-12.3 cal ka BP (Table 1) from glaciomarine sediments in Cumberland Sound (Jennings, 1993) as providing a minimum-

limiting age constraint for the moraines. Other ^{14}C ages on shells from glaciomarine sediments at the hamlet of Pangnirtung provide minimum-limiting ages of 8.6-9.6 cal ka BP (Table 1) for the type Duval moraines and the timing of marine submergence (Andrews and Miller, 1972; Dyke, 1979; Dyke et al., 1982). A 52,450 ± 1430 ^{14}C age (Table 1) on shell fragments excavated from a lower till unit at the hamlet of Pangnirtung (Hyatt, 1992) may provide a maximum-limiting age for the moraines. Later work utilized cosmogenic isotopes to constrain the age of the moraines. Marsella et al. (2000) found that the boulders on the type Duval moraines and equivalents had a bimodal age distribution, potentially recording a continuous or repeated ice margin position from ~24 to 9 ka.

3. Utilizing Cosmogenic Nuclides to Constrain Glacial History

3.1. Overview: Approach and Assumptions

Cosmogenic nuclides have been used to provide insight about glacial history and process for almost three decades (Nishiizumi et al., 1989; Phillips et al., 1990). These nuclides, including ^{10}Be and ^{26}Al, form through spallation of ^{16}O and ^{28}Si nuclei in quartz (Lal, 1988) at rates of ~3.93 and 26.54 atoms g^{-1} yr^{-1}, respectively (Balco et al., 2009). Since cosmic rays attenuate as they pass through matter, the highest rate of production occurs at Earth's surface and production decreases exponentially with depth. Interpretation of a measured cosmogenic isotope concentration in a rock surface as a simple exposure age relies upon two assumptions: first, that the surface has not been eroded or covered (e.g., by till or snow) during exposure, which would shield it and lower rates of nuclide production; and second, that the surface contained no nuclides inherited

from previous periods of exposure before being uncovered from beneath retreating glacial ice.

There are geologic settings in which the assumptions of no erosion, no cover, and no inheritance are not met; this is especially true in glaciated polar regions (Briner et al., 2005). Because cold climates can allow snow cover to persist year-round in the form of multi-year snowfields or ice caps, sampled surfaces may have been partially shielded for some or much of their near-surface history (Schildgen et al., 2005). In high-latitude environments with cold climates, glacial ice is often cold-based and non-erosive, thereby failing to scour surfaces and remove nuclides formed during previous periods of exposure (Håkansson et al., 2008; Harbor et al., 2006; Lilly et al., 2010; Marquette et al., 2004; Staiger et al., 2005; Stroeven et al., 2002b; Sugden et al., 2005). Cold-based ice is present where the temperature at the bed remains below the pressure melting point, no liquid water is generated, and processes such as abrasion or plucking cannot occur (Sugden, 1978), or can only occur in a limited fashion (Atkins et al., 2002; Fitzsimons et al., 2008). The presence of cosmogenic nuclides inherited from prior periods of exposure due to ineffective erosion under cold-based ice has been well-documented on Baffin Island (Bierman et al., 1999; Briner et al., 2003; Briner et al., 2005, 2006; Kaplan et al., 2001; Marsella et al., 2000).

Several approaches can be used to identify surfaces with inherited nuclides that have been preserved beneath non-erosive ice. In areas of cold-based ice, bedrock surfaces often have greater simple exposure ages than boulder surfaces (Bierman et al., 2001) because boulders can be plucked from areas of warm-based ice, transported glacially, and deposited in areas of cold-based ice (see Fig. 5 in Corbett et al. (2013)). Because erosivity

is controlled by the subglacial thermal regime that is at least partly related to overlying ice thickness (Jamieson et al., 2010) in addition to the temperature at the ice surface and geothermal heat flux, low-elevation surfaces tend to be more eroded than high-elevation surfaces due to pressure-induced melting point depression (Briner et al., 2003; Goehring et al., 2008), especially if the low-elevation areas have fast, channelized ice flow (Kaplan et al., 2001; Kessler et al., 2008; Steer et al., 2012). Additionally, since cold-based glacial ice can assemble boulders that may have experienced surface exposure during varying numbers of interglacial periods, boulder ages sometimes form multi-modal age distributions (Briner et al., 2005). Finally, different cosmogenic nuclides have different half-lives; hence, for surfaces that have been subjected to burial, the shorter-lived nuclide (e.g., ^{26}Al) decays more rapidly than the longer-lived nuclide (e.g., ^{10}Be), causing a disagreement in simple exposure ages from different nuclides (Bierman et al., 1999; Kaplan et al., 2001).

Utilizing multiple nuclides in tandem can constrain the relative proportions of exposure and burial durations in a surface covered by non-erosive ice (Bierman et al., 1999). When exposure begins on a fresh surface, the ^{26}Al/^{10}Be ratio matches the production ratio of the two nuclides. If a previously exposed surface is buried and shielded from further nuclide production, the ^{26}Al/^{10}Be ratio drops because the 0.71 Ma half-life of ^{26}Al (Nishiizumi, 2004) is less than that the 1.39 Ma half-life of ^{10}Be (Chmeleff et al., 2010; Korschinek et al., 2010; Nishiizumi et al., 2007). If a sample is exposed again following burial, production resumes and the ^{26}Al/^{10}Be ratio increases because the production rate of ^{26}Al is greater than that of ^{10}Be. Such two-isotope data are usually shown on a diagram in which continuously exposed samples plot along a constant

exposure pathway and samples that have experienced at least one episode of burial plot below the constant exposure pathway, with longer burial durations placing the samples further down the burial isochrones (see Fig. 4 in Corbett et al. (2013)). However, it is important to note that relatively short burial durations (<~100 ky) and/or re-exposure following burial can result in sample points that are indistinguishable from the constant exposure pathway (Bierman et al., 2015; Corbett et al., 2015b) even though they have experienced periods of burial lasting tens of thousands of years.

Using data from paired cosmogenic isotopes, a minimum-limiting history can be calculated for the simplest possible scenario: one period of exposure followed by one period of burial (Fabel and Harbor, 1999). However, because points on the two-isotope diagram represent non-unique solutions, a variety of possible exposure/burial scenarios can be used to explain the isotopic concentration and ratio of any one sample (see Fig. 2 in Granger (2006)). Thus the minimum-limiting exposure/burial durations calculated with paired isotopes can significantly underestimate the sample's true history, especially if the sample has experienced numerous exposure/burial cycles.

3.2. $^{26}Al/^{10}Be$ Production Ratio

Any inferences stemming from $^{26}Al/^{10}Be$ ratios (e.g. the minimum-limiting exposure and burial durations described above) are in part dependent upon the assumed $^{26}Al/^{10}Be$ production ratio, which is a direct function of the production rates of the two nuclides. Although nuclide production rates have long been known to vary across latitude and elevation (Lal, 1991; Stone, 2000), it has generally been assumed that ^{26}Al and ^{10}Be production rates scale similarly, resulting in a production ratio of 6.75 for all sites (Balco

et al., 2008). However, recent work has suggested that the production ratio is itself dependent on latitude and elevation because each isotope's production rate scales differently across space (Argento et al., 2013; Argento et al., 2015; Borchers et al., 2015). These studies argue that the production ratio can be greater than 6.75, with values ranging as high as ~7.3 (Borchers et al., 2015). High latitude regions appear most likely to have higher production ratios (Argento et al., 2013). For the analyses in this manuscript, we assume a $^{26}Al/^{10}Be$ production ratio of 6.75 consistent with current convention (Balco et al., 2008). However, because we recognize that the actual $^{26}Al/^{10}Be$ production ratio may be higher, especially because of Baffin Island's high latitude, we include a sensitivity analysis at the end of the Discussion that assesses the impacts of assumed production ratio on our findings.

3.3. Previous Work: Application of Cosmogenic Nuclides on Baffin Island

The application of cosmogenic nuclides has provided insight about both subglacial erosion and glacial history on Baffin Island. Uplands on Baffin Island are often characterized by glacial erratics with young simple cosmogenic exposure ages sitting directly on top of tors with old simple exposure ages (Bierman et al., 2001; Briner et al., 2003; Briner et al., 2006). Many high-elevation bedrock surfaces on Baffin Island have $^{26}Al/^{10}Be$ ratios indicative of at least one period of exposure followed by burial with limited erosion, suggesting that these surfaces have been preserved beneath cold-based ice (Bierman et al., 1999; Briner et al., 2006; Kaplan et al., 2001; Margreth et al., 2011, 2012, 2014; Marsella et al., 2000; Miller et al., 2006). Models of $^{26}Al/^{10}Be$ data assuming one period of exposure followed by one period of burial (the simplest scenario)

demonstrate that high-elevation bedrock surfaces record total histories of hundreds of thousands to millions of years, and that about three quarters of that total history is composed of periods of burial (Bierman et al., 1999; Margreth et al., 2014). Further modeling assuming multiple periods of exposure and burial found that the $^{26}Al/^{10}Be$ ratios in some high-elevation samples are consistent with initial exposure during Marine Isotope Stage 11 (~420 ka), followed by subsequent re-exposure during stages 9 (~ 330 ka), 7 (~240 ka), 5e (~120 ka), and the Holocene (Miller et al., 2006). These previous studies suggest that the high-elevation surfaces on Baffin Island have likely experienced little erosion over at least the latter half of the Quaternary and are characterized by periglacial weathering during interglacial periods and burial beneath non-erosive ice during glacial periods.

In contrast, low-elevation areas on southern Baffin Island can be free of inherited cosmogenic nuclides (Davis et al., 1999), likely because these areas were scoured at least in part by outlet glaciers (Kaplan et al., 2001; Kaplan et al., 1999); hence, some samples from such areas may provide estimates of deglaciation age. Analysis of cosmogenic nuclides has constrained the age of the prominent Duval moraines on Cumberland peninsula to ~9-24 ka (Marsella et al., 2000), showing that they are not as old as originally thought (>60 ka) based on analyses of rock weathering and soil development (Dyke, 1977, 1979). Cosmogenic nuclides have also been the basis for the chronology of deglaciation of the Pangnirtung Fiord area, which likely became ice-free in the latest Pleistocene or earliest Holocene (Marsella et al., 2000). Further north, in central-eastern Baffin, analysis of ^{10}Be in bedrock samples collected along the length of a 100-km fjord provides evidence for a period of rapid ice retreat at ~9.5 ka, likely in response to early

Holocene warming (Briner et al., 2009). Even some high-elevation erratics yielded relatively young ages (~10-17 ka), providing an estimate for the timing of deglaciation of the uplands and proving that the uplands were indeed glaciated at the LGM (Bierman et al., 2001; Briner et al., 2003; Briner et al., 2006). However, ambiguous (perhaps too old as a result of inheritance) cosmogenic exposure ages are found at the lower elevations. Even in areas that appear glacially scoured, ages of erratics may yield multi-modal distributions (Briner et al., 2005; Marsella et al., 2000) indicative of boulder recycling and inheritance of nuclides over numerous glacial/interglacial cycles.

4. Methods

4.1. Study Design and Field Sampling

In order to study landscape chronology and subglacial erosion efficiency, we sampled bedrock (n = 65) and glacially-deposited boulders (n = 84) on southern Baffin Island (Figs. 1 and 3), 149 total samples. Samples were dominantly crystalline rocks, including the gneisses and granitic gneisses that underlie most of the Cumberland Sound area (Jackson and Taylor, 1972). Twelve of the boulders came from the crest of the type Duval moraine and equivalent moraines (Figs. 2 and 3A), providing constraint on the timing of moraine deposition. An additional 19 bedrock and 14 boulder samples came from the low-elevation areas that flank Pangnirtung Fiord, representing a transect stretching ~75 km NE-SW from the valley head to where Pangnirtung Fiord intersects Cumberland Sound (Figs. 3B and 4); these samples provide constraint on the timing of deglaciation through Pangnirtung Fiord and Pangnirtung Pass.

In addition to the 149 glacially-deposited samples described above, we also sampled four boulders and two glacially molded bedrock surfaces from and adjacent to a ~99 m a.s.l. glaciomarine delta on the north side of Kingnait Fiord, ~20 km south of the Duval moraines (Fig. 1). The delta is composed of sediments that were delivered via a large meltwater channel that grades to the type Duval moraines along Pangnirtung Fiord (see Fig. 14 in Marsella et al. (2000)), hence ages from the delta represent minimum limits for the Duval moraines because of the geologic setting. We do not include these samples in our analysis of subglacial processes since they were not directly deposited by glacial ice, but do include them in our analysis of the age of the Duval moraines.

In the field, top surfaces of bedrock and boulders away from edges were sampled using a hammer and chisel. Latitude and longitude were recorded using GPS, and elevation was recorded by differential barometry, which included a Paulin surveying altimeter in the field and a barometric pressure data logger installed at a fixed location in the hamlet of Pangnirtung during the 1995 sampling campaign. Further information about sample locations is included in the Data Repository (Table R1). In this manuscript, we present data from samples collected during three field seasons: 1992 (the "PTD92" sample series), 1994 (the "PTD94" sample series), and 1995 (the "KM95" sample series). Of the 155 samples included in this paper, data from 53 were previously published in Bierman et al. (1999) and Marsella et al. (2000). In this paper, we reanalyze those data using currently accepted production rates and scaling schemes (Balco et al., 2009; Balco et al., 2008) and correct for changes in the standard used for $^{10}Be/^{9}Be$ normalization (Nishiizumi et al., 2007).

4.2. Laboratory Methods

All samples were processed in the University of Vermont cosmogenic nuclide laboratory between 1995 and 2001 using standard procedures described in Bierman and Caffee (2002). Samples were processed in batches of eight, with each batch containing either one or two fully processed blanks. Between ~200 and 300 μg of ^{9}Be were added to each sample and blank as a spike in the form of 1000 ppm SPEX Be standard. Because most of the quartz contained sufficient native Al for isotopic analysis (~2000 μg), a ^{27}Al spike was not routinely added. However, ~2000-3000 μg of ^{27}Al were added to each blank (and to the few samples containing little native Al) in the form of 1000 ppm SPEX Al standard. Immediately following quartz dissolution, two small aliquots were removed from each sample for inductively coupled plasma optical emission spectrometry (ICP-OES) quantification of total Al content as described in Bierman and Caffee (2002). Further information about sample preparation and blanks is included in the Data Repository (Tables R2 and R3).

4.3. Isotopic Analysis

Isotopic ratios were measured by Accelerator Mass Spectrometry (AMS) at Lawrence Livermore National Laboratory (Perren et al., 2012; Rood et al., 2010) between 1996 and 2001. All samples were analyzed for both ^{10}Be/^{9}Be and ^{26}Al/^{27}Al. However, several cathodes did not yield usable data; for these samples, only one isotope is reported (hence there are 152 ^{10}Be analysis and 153 ^{26}Al analyses). Depending on the timing of analysis, ^{10}Be samples were normalized to standards from the KNSTD series, LLNL1000, LLNL3000, or LLNL10000 and ^{26}Al samples were normalized to standards KNSTD5000

or KNSTD9919. Measured $^{10}Be/^{9}Be$ sample ratios ranged from $9.3 \cdot 10^{-14}$ to $3.6 \cdot 10^{-12}$ and 1σ AMS measurement precisions for ^{10}Be were 5.8 ± 3.8 % (n = 152, average, 1SD). Measured sample $^{26}Al/^{27}Al$ ratios ranged from $6.5 \cdot 10^{-14}$ to $4.1 \cdot 10^{-12}$ with 1σ AMS measurement precisions of 6.2 ± 2.4 % (n = 153, average, 1SD). Isotope ratio and standardization data are included in the Data Repository (Table R2).

To correct for laboratory and machine backgrounds (Table R3), we used the median ratio of all blanks processed in the 29 batches containing the Baffin Island samples. Omitting one outlier for Be and one outlier for Al (which were from different batches) yielded 32 total blanks for Be and 31 for Al. To account for the uncertainty of the median blank value, we used one standard deviation around the mean. The background values utilized for all samples were $2.74 \pm 0.95 \cdot 10^{-14}$ for ^{10}Be and $3.25 \pm 5.60 \cdot 10^{-15}$ for ^{26}Al.

Because of changes in the nominal $^{10}Be/^{9}Be$ ratio of standards used to normalize isotopic measurements made in 2007 (Nishiizumi et al., 2007), original analyses of these samples (which occurred in 1996-2001) were normalized to different standard values than are accepted today. To make these data comparable to modern datasets, we scaled all ^{10}Be data to the newer standard value (07KNSTD, Nishiizumi et al. (2007)). Here were report only the ^{10}Be concentrations and $^{26}Al/^{10}Be$ ratios scaled to the modern standards (Table 3); unscaled values (those dependent on the standard values accepted at the time of analysis) are in the Data Repository (Table R2).

4.4. Single-Isotope Simple Exposure Age Calculations

We calculated ^{10}Be and ^{26}Al simple exposure ages (Table 2) with the CRONUS Earth online exposure age calculator (Balco et al., 2008) using version 2.2 and constants version 2.2.1. Because both the assumed standard values and production rate estimates have changed over time, the calculated ages reported here are different from the values reported in the original publications containing some of the data (Bierman et al., 2001; Bierman et al., 1999; Marsella et al., 2000). For this study, we used the regionally-calibrated northeastern North American sea-level production rates of 3.93 ± 0.19 atoms g^{-1} yr^{-1} for ^{10}Be and 26.5 ± 1.3 atoms g^{-1} yr^{-1} for ^{26}Al (Balco et al., 2009) and the Lal/Stone constant production rate model and scaling scheme (Lal, 1991; Stone, 2000). We made corrections for latitude, elevation, sample density (assumed to be 2.7 g cm^{-3}, which is representative of the crystalline rock we sampled), and sample thickness (ranged from 1 to 11 cm; Table R1). We made no corrections for snow or till cover, both of which would lead to ^{10}Be or ^{26}Al age underestimates, and no corrections for topographic shielding because sample sites are not significantly shielded. Because many of the samples contain nuclides inherited from prior periods of exposure, we refer to the single isotope ages as simple exposure ages.

When comparing between samples within the dataset, we cite the internal/analytic uncertainties that reflect AMS measurement precision only (Table R2). We use internal uncertainties in this context because the samples come from the same area and therefore any errors in production rate calibration will affect all samples similarly. When comparing our age data to other geochronometers, we use the external uncertainties that

take into account AMS precision as well as additional uncertainty introduced through the chosen production rate and altitude/latitude scaling scheme.

4.5. Two-Isotope Exposure and Burial Duration Calculations

Before conducting two-isotope modeling, we corrected sample nuclide concentrations and $^{26}Al/^{10}Be$ ratios for the period of most recent exposure (Table 3); we performed this correction in order to remove the post-deglaciation history and enable calculation of pre-LGM exposure and burial. We used 11.7 ky for the duration of most recent exposure based on the age of the youngest large population of boulder samples from the dataset as a whole (see discussion); this age is consistent with the idea that the landscape around Pangnirtung Fiord was deglaciated rapidly following the Younger Dryas (Kaplan et al., 2001; Marsella et al., 2000). We subtracted the number of atoms of ^{10}Be and ^{26}Al produced in each sample during 11.7 ky of exposure, considering its elevation, before proceeding with numerical models.

We conducted two-isotope modeling of minimum-limiting exposure durations and burial durations on only a subset of the data. First, we did not model samples that had a simple ^{10}Be exposure age of <14.3 ka because these samples are within 2σ (based on the average ^{10}Be analytic uncertainty across the dataset, n = 152) of the time the Baffin Island landscape was deglaciated (11.7 ka). Second, we did not model samples for which Holocene-corrected $^{26}Al/^{10}Be$ ratios did not indicate a burial history beyond 1σ analytic uncertainties (i.e., the samples that overlapped or fell above the constant exposure pathway on the two-isotope diagram assuming a production ratio of 6.75). After applying

these filters, a total of 29 samples with paired $^{26}Al/^{10}Be$ data were modeled for exposure and burial history (Table 3).

Modeling of minimum-limiting exposure durations and burial durations using both ^{26}Al and ^{10}Be data was conducted in MatLab. We assumed a ^{10}Be half-life of 1.39 Ma corresponding to a decay constant of $5.00 \cdot 10^{-7}$ yr^{-1} (Chmeleff et al., 2010; Korschinek et al., 2010; Nishiizumi et al., 2007) and a ^{26}Al half-life of 0.705 Ma corresponding to a decay constant of $9.83 \cdot 10^{-7}$ yr^{-1} (Nishiizumi, 2004). We used isotopic data corrected for the most recent period of exposure and normalized to sea level using the production rates generated for each sample in CRONUS (Table 3). We then used the paired equations detailed in Bierman et al. (1999) to calculate iteratively the simplest scenario to explain the observed sample position on the two-isotope plot: one period of exposure followed by one period of burial before the current period of exposure. To quantify the uncertainties associated with our exposure/burial models, we used Monte Carlo simulations (n = 10,000 for each sample, normal uncertainty distributions for each isotope) as described in Corbett et al. (2015b). For each sample we modeled (n = 29), we report the minimum-limiting exposure duration, minimum-limiting burial duration, minimum-limiting total history (sum of exposure duration, burial duration, and the duration of most recent exposure), and their uncertainties.

5. Results

5.1. Single-Isotope Results

For glacial surfaces (n = 149, Fig. 1), 07KNSTD-scaled ^{10}Be concentrations in samples range from $3.1 \cdot 10^4$ to $1.6 \cdot 10^6$ atoms g^{-1} (Table R2), yielding simple exposure ages

of 6.3 to 160 ka (n = 146, Table 2, Fig. 5). Measured ^{26}Al concentrations in samples range from $1.2 \cdot 10^5$ to $8.3 \cdot 10^6$ atoms g^{-1} (Table R2), with simple exposure ages of 4.3 to 124 ka (n = 147, Table 2, Fig. 5).

The large number of samples in this dataset provides opportunities to study patterns and trends in the data. For paired bedrock and boulder samples, bedrock simple exposure ages tend to match or exceed boulder simple exposure ages (Figs. 3C and 6). There are 25 pairs (50 total analyses) of adjacent bedrock and boulder samples in the dataset. Of these 25 pairs, 14 have bedrock and boulder ages that are indistinguishable within their 1σ analytic uncertainties. Of the remaining 11 for which the ages are statistically distinguishable within 1σ analytic uncertainties, only three have boulder ages that exceed the bedrock ages, and these represent three of the youngest ages in the paired dataset. The remaining eight pairs consist of bedrock ages that exceed boulder ages, sometimes by as much as 3-4X.

Simple exposure ages tend to increase with elevation. This trend is significant for both bedrock samples (^{10}Be; $R^2 = 0.35$, $p = <0.01$, n = 64; Fig. 7) and boulder samples (^{10}Be; $R^2 = 0.22$, $p = <0.01$, n = 82; Fig. 7). There is, however, no trend with ^{26}Al/^{10}Be ratio and elevation (for bedrock, $R^2 < 0.01$, $p = 0.82$, n = 64; for boulders, $R^2 < 0.01$, $p = 0.76$, n = 82).

For the samples with both ^{10}Be and ^{26}Al data, simple exposure ages calculated with each isotope are significantly related ($R^2 = 0.97$, $p < 0.01$, n = 144; Fig. 8). This relationship is close to 1:1 for young samples, but falls below the 1:1 line for samples with greater simple exposure ages, indicating that ^{10}Be ages are systematically greater than ^{26}Al ages for these samples (regression slope = 0.77, Fig. 3D).

Probability density functions demonstrate that the samples from this dataset have complex age distributions. When all boulder samples are considered together, their ^{10}Be simple exposure ages yield a multi-modal age distribution with a prominent peak ~11.7 ka and several smaller, older peaks (n = 82, Fig. 9). Similarly, ^{10}Be simple exposure ages of bedrock samples also yield a multi-modal distribution with a prominent peak ~12.1 ka and several smaller, older peaks (n = 64, Fig. 9).

For the Kingnait Fiord delta (n = 6, KM95-138 through KM95-143), ^{10}Be simple exposure ages are 13.1 to 18.1 ka and ^{26}Al simple exposure ages are 11.9 to 16.2 ka (Table 2). These six samples are not included in the previous analyses because they do not represent primary glacial deposition.

5.2. Paired-Isotope Results

The 07KNSTD-scaled (not corrected for the most recent period of exposure) ^{26}Al/^{10}Be ratios of glacial surfaces are 2.6 ± 0.5 to 10.2 ± 1.4 (n = 144, Table 2, Fig. 10). Of the 144 glacial samples with ^{26}Al/^{10}Be data, 79 (or 55%) have ratios indistinguishable from an assumed production ratio of 6.75 within 1σ analytic uncertainties, meaning that their location on the two-isotope diagram is consistent with a single period of exposure. Twenty-two (or 15%) have ratios exceeding 6.75 beyond the 1σ analytic uncertainties. The remaining 43 samples (or 30%) have ratios that fall below 6.75 beyond the 1σ analytic uncertainties and can be explained by complex histories involving at least one period of exposure followed by at least one period of burial, along with a final period of most recent exposure.

For the samples for which we conducted exposure/burial simulations (29 total, filtered as described in the Methods section), modeled minimum-limiting exposure durations are 5.9 x 10^3 to 4.8 x 10^5 yr and modeled minimum-limiting burial durations are 1.4 x 10^5 to 7.5 x 10^6 yr; summed total histories range up to 8.0 x 10^6 yr (n = 29, Table 3, Fig. 11). As constrained by Monte Carlo simulations, modeled exposure durations have uncertainties of 16 ± 12 % (average, 1SD), while modeled burial durations have uncertainties of 23 ± 16 % (average, 1SD, Table 3). The uncertainty of the modeled total history is dominated by the uncertainty of the burial duration when the uncertainties are propagated in quadrature; modeled total history uncertainties are 20 ± 14 % (average, 1SD, Table 3).

5.3. Data Reproducibility

Five of the samples reported here (see Data Repository for more detail) were collected from the same bedrock outcrop of glacially molded, polished, and striated gneiss near the hamlet of Pangnirtung at an elevation of 204 m a.s.l. (KM95-044 through KM95-048, Table R2, Fig. R1). The five ^{10}Be concentrations form a single distribution with slight right skew whereas the five ^{26}Al ages form a double-humped distribution (Fig. R2). Analytic uncertainties for ^{10}Be analyses are 6%, 7%, 7%, 18%, and 5%, with the 18% uncertainty corresponding to the sample with the highest concentration (KM95-047); ^{26}Al analytic uncertainties are 7%, 6%, 8%, 8%, and 9%. Relative standard deviations of the five measurements are 14.8% for ^{10}Be and 16.8% for ^{26}Al, implying that the geologic variance exceeds the analytic variance for both isotopes. The ^{26}Al/^{10}Be ratios for the four samples with low ^{10}Be uncertainties are 6.0 ± 0.8 (average, 1SD).

Conversely, the $^{26}Al/^{10}Be$ ratio for the sample with the high ^{10}Be uncertainty (KM95-047) is 3.3 ± 0.8 (1σ), suggesting that this one sample is likely not only imprecisely but also inaccurately measured.

6. Discussion

6.1. Constraining the Subglacial Erosional Regime

Data in this paper support previous work documenting that glacial ice covering some areas of Baffin Island had limited erosive capability during numerous past glacial periods (Bierman et al., 1999; Briner et al., 2006; Kaplan et al., 2001; Miller et al., 2006). The simple exposure ages we infer here are older than those presented in Marsella et al. (2000) due to new AMS standard values (Nishiizumi et al., 2007) and a new production rate (Balco et al., 2009) that were developed since the original publication of a subset of the data. As shown above, bedrock simple exposure ages tend to exceed boulder simple exposure ages in paired bedrock/boulder samples (Figs. 3C and 6), simple exposure ages generally increase with elevation (Fig. 7), and ^{10}Be simple exposure ages are greater than ^{26}Al simple exposure ages especially for samples in the dataset with higher simple exposure ages (Figs. 3D and 8). Both boulder and bedrock sample populations form multi-modal age distributions (Fig. 9). Additionally, about one third of the $^{26}Al/^{10}Be$ ratios are indicative of burial (Fig. 10) and modeled two-isotope minimum-limiting burial durations are hundreds of thousands to millions of years (Fig. 11). All of these trends are indicative of limited subglacial erosion in parts of the field area.

Several other factors in addition to the subglacial erosional regime may exert control on the concentration of cosmogenic nuclides in the bedrock and boulder surfaces

we studied. Lithology is not likely to have a large effect on this dataset because the bedrock in the Cumberland Sound area is relatively homogeneous and primarily consists of Paleoproterozoic crystalline rocks (Hamilton et al., 2012; Jackson and Taylor, 1972) that would all be relatively resistant to subglacial abrasion. Changing ice thickness over time may also impact nuclide concentrations, especially if the marginal areas of the ice sheet thinned following the most recent (or any) glacial period, thereby exposing the uplands to nuclide production for longer than the lowlands. Although this pattern has been inferred using cosmogenic nuclides in numerous glaciated settings (Lilly et al., 2010; Rinterknecht et al., 2009), we are unable to resolve any ice thinning signal in our data (should it exist) due to the presence of inherited nuclides. Finally, interglacial shielding of sample surfaces by sediment and/or perennial snowfields could have resulted in decreased production rates during the present and/or past interglacial periods, but again we are unable to identify these samples definitively. The observation that simple exposure ages are greater at higher elevations (Fig. 7), where snowpacks are likely to be thick and linger longer, suggest snow cover does not play a large role in decreasing simple exposure ages.

Although Baffin Island was one of the first glacial landscapes where the presence of old, preserved surfaces was suggested (Sugden and Watts, 1977), evidence for minimally erosive glacial ice (indicated by failure to remove nuclides inherited from previous periods of exposure) has been found throughout the high latitudes. The incidence of young erratics sitting on ancient surfaces has been documented not only on Baffin Island (Bierman et al., 2001; Briner et al., 2003), but also in Greenland (Corbett et al., 2013) and Scandinavia (Goehring et al., 2008; Stroeven et al., 2002a). Positive

relationships between sample age and elevation have been previously noted in Baffin Island (Briner et al., 2006; Kaplan et al., 2001), Greenland (Corbett et al., 2013), and Scandinavia (Goehring et al., 2008). Mismatches between ^{10}Be and ^{26}Al ages exist widely on Baffin Island (Bierman et al., 1999; Briner et al., 2003; Briner et al., 2006; Kaplan et al., 2001; Miller et al., 2006), mainland northern Canada (Marquette et al., 2004), Greenland (Corbett et al., 2013; Håkansson et al., 2008), Scandinavia (Harbor et al., 2006; Stroeven et al., 2002b), Scotland (Phillips et al., 2006), and Antarctica (Lilly et al., 2010; Nicola et al., 2009; Sugden et al., 2005). Together, these data suggest that non-erosive ice is widespread in the high latitudes, particularly in the highlands that separate deeply-carved fjords.

In areas of cold-based, non-erosive glacial ice, the assumption that simple cosmogenic exposure ages reflect the timing of post-glacial ice retreat is often violated. We show here that bedrock surfaces generally carry greater concentrations of cosmogenic nuclides inherited from previous periods of exposure than do nearby boulders (Fig. 6), supporting the findings of numerous other high-latitude cosmogenic studies (Briner et al., 2003; Corbett et al., 2013; Goehring et al., 2008; Stroeven et al., 2002a). However, even boulder samples can contain significant concentrations of inherited nuclides and may not yield simple exposure ages that accurately reflect deglaciation timing (e.g., KM95-003, 78.7 ka; KM95-024, 49.5 ka; KM95-068, 54.9 ka; ^{10}Be ages, Table 2). Similarly, although high-elevation surfaces tend to contain greater concentrations of inherited nuclides (Fig. 7), both lower-elevation bedrock samples (e.g., KM95-049, 30.1 ka, Table 2) and boulder samples (e.g., KM95-030, 21.0 ka, Table 2) can still contain significant inherited nuclides and may not yield accurate estimates of deglaciation timing.

6.2. Subglacial Erosion: Spatial Distribution, Depths, and Rates

The preservation of nuclides from previous periods of exposure in sampled surfaces, an indication of subglacial erosion efficiency, has a spatial pattern in which the fjords have been more deeply eroded than the highlands (Fig. 12). Bedrock samples from the lowlands of Pangnirtung Fiord preserve no or little ^{10}Be inherited from previous periods of exposure, suggesting that channelized ice flow through the fjord was erosive and at least partially scoured bedrock surfaces during the last glaciation. This pattern is consistent with observations in other high-latitude areas (Briner et al., 2005, 2006; Kessler et al., 2008; Steer et al., 2012), where erosion was focused in the fjords. In contrast, bedrock samples from the highlands to the north and south of Pangnirtung Fiord contain the equivalent of tens of ky up to almost 150 ky of inherited ^{10}Be (Fig. 12). Fast-flowing, erosive ice flow through Pangnirtung Fiord would have coalesced with the ice stream inferred to have occupied Cumberland Sound (Kaplan et al., 2001; Kaplan et al., 1999), presumably flowing around rather than over the highlands, thereby limiting erosion of upland surfaces.

The prevalence of (47 of 63) bedrock outcrops with simple ^{10}Be exposure ages great than the age of deglaciation (~11.7 ka, as described below in more detail) can be used, if several assumptions are made, to estimate a range of erosion depths during the last glaciation of our field area. Such calculations assume no inherited nuclides at the onset of the previous interglacial period and an estimate of the exposure duration prior to the last glaciation, a duration that is not well constrained for this part of Baffin Island. Because of this uncertainty, we tested a range of prior exposure times (22.5, 55, and 110 ky). The minimum exposure duration (22.5 ky) is supported by radiocarbon ages from

lake sediment cores (Wolfe et al., 2001), while the maximum exposure duration (110 ky) assumes that the study area was exposed from MIS 5e until the LGM, an unlikely end-member assumption. The analysis (described in the Data Repository) yields erosion depths that average between 160 cm (22.5 ky exposure) and 220 cm (110 ky exposure) during the time that the area was ice-covered (Fig. R3). In all three cases, median erosion depths are less than mean erosion depths because the distributions are skewed. Calculation of erosion rates is not reasonable with this dataset because such rates are much more highly dependent than erosion depths on the duration of intervening ice cover.

6.3. Landscape Longevity

Many of the samples discussed here have likely been buried beneath cold-based, non-erosive glacial ice. Therefore, parts of the landscapes we sampled were not deeply eroded (removal of at least several meters of rock and thus most nuclides from prior exposure) during the late Wisconsinan; instead, they have been preserved for numerous glacial/interglacial cycles with little erosion. Modeled minimum-limiting total histories (the sum of exposure and burial) are at least hundreds of thousands of years, with 10 of the 29 modeled samples recording over a million years of total history and seven samples (KM95-013, KM95-023, KM95-030, KM95-042, KM95-098, KM95-100, and KM95-113, Fig. 3D) possibly pre-dating inception of the Laurentide Ice Sheet ~2.5 My (Table 3, Fig. 11).

Although our Monte Carlo analysis of exposure/burial uncertainties assumes that the isotopic concentrations are accurate and does not account for sources of laboratory

error (e.g., ICP-OES quantification of total Al), the long burial durations we infer are relatively well-constrained statistically and are consistent with millions of years of subglacial preservation. These burial durations are longer than those recorded in multiple locations in northwestern Greenland (~0.5 My, Corbett et al. (2013)), in northeastern mainland Canada (several hundred ky, Marquette et al. (2004), Staiger et al. (2005)), and Marie Byrd Land in Antarctica (several hundred ky, with one sample at several My, Sugden et al. (2005)), suggesting very limited erosive capacity of the cold, thin ice caps covering southern Baffin Island throughout much of the Quaternary. In Central Baffin Island, Miller et al. (2006) documented high-elevation bedrock surfaces that preserved histories reflecting numerous glacial/interglacial cycles, possibly having experienced the first period of exposure during Marine Isotope Stage 11. At least some of the high-elevation areas we studied on the Cumberland Peninsula appear to have been preserved for appreciably longer durations, maybe because ice flow was effectively channelized through Cumberland Sound (Kaplan et al., 2001; Kaplan et al., 1999), leaving the upland ice consistently frozen to the bed.

6.4. Boulder History and Recycling

Even boulders, which here and elsewhere tend to carry fewer inherited nuclides than bedrock (Bierman et al., 2001; Briner et al., 2003; Corbett et al., 2013; Goehring et al., 2008; Stroeven et al., 2002a), do not yield straightforward age distributions on Cumberland Peninsula in southern Baffin Island. This observation indicates that at least certain parts of the landscape in the study area were covered by cold-based ice at one or numerous times in the past, that boulders were reworked in till over numerous

glacial/interglacial cycles (Corbett et al., 2015b), or both. Assessment of the cumulative probability of ages and analytic uncertainties of the 82 boulder samples with ^{10}Be analyses in this dataset results in a multi-modal distribution with distinct peaks at 7.0, 11.7, 27.3, and 38.9 ka (Fig. 9).

We infer that the prominent peaks at 7.0 and 11.7 ka (Fig. 9) represent samples largely free of inherited nuclides, and hence that these peaks record surface exposure ages. The 7.0 ka peak encompasses eight samples from 6.3 to 7.5 ka, six of which (PTD94- 11a, 15a, 15b, 15c, 18a, and 18c, Table 2) come from the sampling areas between Meta Incognita and Hall Peninsulas and between Hall and Cumberland Peninsulas, rather than from the primary sampling area around Pangnirtung Fiord (Fig. 1). Only one of these eight youngest samples (KM95-094, 7.5 ka, Table 2) was collected from below the marine limit and is discussed later; the remainder are from well above the marine limit. The coincidence of numerous young exposure ages from above the marine limit suggests that the regions lying to the west and southwest of Cumberland Sound were eroded deeply (more than several meters of rock removed) during Marine Isotope Stage 2 and remained covered by ice for longer than the high topography surrounding Pangnirtung Fiord. This relationship is consistent with the idea of a large ice stream occupying Cumberland Sound (Kaplan et al., 2001; Kaplan et al., 1999) and persisting into the Holocene.

The slightly right-skewed 11.7 ka peak (Fig. 9) encompasses 60 samples from 8.7 to 21 ka, although 90% of the samples fall between 10.1 and 17.6 ka. The older of these samples likely contain inherited nuclides and may have experienced histories involving multiple periods of exposure. However, at least a portion of the boulders comprising the

11.7 ka peak probably record accurate, simple surface exposure ages. Of the 60 boulders encompassed in this peak, 43 are indistinguishable from or above an assumed $^{26}Al/^{10}Be$ production ratio of 6.75 at 1σ; only 16 boulders are below 6.75 by more than 1σ, and one boulder lacks ^{26}Al data and is not included here. Although the presence of inherited nuclides in this dataset hinders our ability to determine the timing of the most recent deglaciation, we infer that the landscape around Pangnirtung Fiord became ice-free in the latest Pleistocene or earliest Holocene based on the large number of samples around this 11.7 ka peak. We interpret a similarly large peak at 12.1 ka in the summed probability density function of bedrock samples (Fig. 11) as also representing the latest Pleistocene deglaciation of southern Baffin Island.

The peaks at 27.3 and 38.9 ka (Fig. 9) in the boulder distribution are appreciably older and are likely composed of boulders containing significant concentrations of inherited nuclides. These boulders may have been deposited on the landscape during glacial periods preceding Marine Isotope Stage 2, and were then preserved with minimal erosion during numerous glacial/interglacial cycles or they may have been quarried from outcrops with large concentrations of inherited nuclides. The complex, multi-modal distribution seen here is similar to that described by Briner et al. (2005) on the Clyde Foreland of central-eastern Baffin Island and by Corbett et al. (2015a) in northwestern Greenland. Such distinct multi-modal distributions seem unlikely to arise from random amounts of inherited nuclides that could be derived from heterogeneous subglacial erosion. Rather, each peak may represent a distinct exposure/burial history, with older peaks being indicative of a larger number of glacial/interglacial cycles that the boulder

(or the bedrock from which the boulder was sourced) spent at or near the surface (Briner et al., 2005; Corbett et al., 2015a; Corbett et al., 2015b).

6.5. Age of the Duval Moraines

A portion of this dataset provides information for revising the age of the Duval moraines on southern Cumberland Peninsula (Figs. 2 and 3A). Within the dataset presented here, there are 12 boulders from crests of the type Duval moraine or equivalent moraines. Eleven of these 12 boulders were presented in Marsella et al. (2000); however, because of recent changes in AMS standard values (Nishiizumi et al., 2007) and the development of the northeastern North American production rate (Balco et al., 2009), recalculated ages are at least several ka older than the ages that were originally presented. Of these 12 boulders, six (KM95-06, KM95-07, and KM95-33 through KM95-36, Fig. 3A) are from the type Duval moraine upslope of the hamlet of Pangnirtung, whereas the other six (KM95-08, KM95-09, KM95-24, KM95-25, KM95-28, and KM95-29) are from Duval equivalent moraines along Pangnirtung Fiord (Fig. 2). Of the 12 type Duval and equivalent moraine boulders, all but one have $^{26}Al/^{10}Be$ ratios that are either indistinguishable from or slightly exceed the production ratio of 6.75 (average ratio 7.32 ± 0.73, 1SD, n = 11). Only one moraine sample (KM95-035, 5.92 ± 0.39) has a $^{26}Al/^{10}Be$ ratio that falls below 6.75 by more than 1σ.

Recalculated ^{10}Be simple exposure ages (Table 2) are similar between samples from the type Duval and equivalent moraines, ranging from 11.2 to 49.5 ka, with uncertainties of 8.4 ± 2.7 % (average, 1SD; we utilize external uncertainties here so that the moraine ages are comparable chronologies developed with other methods). The

boulder ages form a multi-modal distribution (Fig. 13), with a first distinct mode at ~11.2 ka (n = 4), a broad mode at ~16.3 ka (n = 3), a distinct mode at ~27.9 ka (n = 3), and two older ages of 38.5 and 39.5 ka. Since relatively short durations of burial (tens of ky) are not detectable within the resolution of the $^{26}Al/^{10}Be$ system, the older Duval boulders may contain nuclides inherited from previous periods of exposure, even though their $^{26}Al/^{10}Be$ ratios are indistinguishable from the constant exposure case (Bierman et al., 2015). However, the samples comprising the youngest age peak may record a true deglaciation age; these four boulders (KM95-007, KM95-025, KM95-028, and KM95-034, Table 2) have ages that are indistinguishable within uncertainties and form an overlapping age distribution centered at 11.2 ± 0.2 ka (^{10}Be, average, 1SD).

An additional minimum-limiting constraint on the age of the moraines comes from the ~99 m a.s.l. glaciomarine delta on the north side near the mouth of Kingnait Fiord (Fig. 1). Samples from the delta (KM95-138 through KM95-142, Table 2, Fig. 14) yield ^{10}Be simple exposure ages of 13.1-18.1 ka, representing a minimum-limiting age in a geologic context, even though the ages themselves are maximum limits because of the likely presence of inherited nuclides. The three radiocarbon ages of 10.1-12.3 cal ka BP (Table 1, Fig. 14) on shells in glaciomarine sediments from Cumberland Sound (Jennings, 1993; Jennings et al., 1996) may provide a more accurate minimum limit (Kaplan and Miller, 2003) than direct dates of moraine boulders because of the presence of inherited nuclides in many of our samples.

Our ability to determine the age of the Duval moraines (Fig. 14) is inhibited by the relatively small number of samples from the moraine crests and the presence of inherited nuclides in many samples. However, using the current accepted values for

isotopic standards and production rates, the average ^{10}Be age is 11.2 ± 0.2 ka (n = 4, 1SD) for the youngest population of Duval moraine boulders. This age estimate for the Duval moraines is coincident with the Younger Dryas cold reversal (Broecker et al., 1988), which lasted from approximately 12.7 to 11.5 ka (Johnsen et al., 2001), terminated abruptly (Dansgaard et al., 1989; Taylor et al., 1993; Taylor et al., 1997), and is recorded across the North Atlantic region (Alley, 2000). Arctic land-based evidence of the Younger Dryas is rare because much of the northeastern Laurentide and Greenland Ice Sheet margins were still offshore at the time of the cold interval (Cofaigh et al., 2012).

6.6. Deglaciation Chronology of Pangnirtung Fiord and Cumberland Sound

A portion of the dataset (19 bedrock and 14 boulder samples) from the low-elevation areas of Pangnirtung Pass and the flanks of Pangnirtung Fiord were collected to provide insight about the timing and dynamics of deglaciation. Two polished bedrock (KM95-060 and KM95-061, Table 2) and four boulder (KM95-062 through KM95-064 and KM95-066, Table 2) samples were collected from Summit Lake at the head of Pangnirtung Pass (Fig. 4). Additionally, both boulders and glacially molded or polished bedrock were sampled from the four major stoss-lee forms that occur along both sides of Pangnirtung Fiord between the hamlet of Pangnirtung and the head of the fjord (Figs. 3B and 4). When all of the Pangnirtung Pass and Fiord samples are examined together, they show no trend in ^{10}Be simple exposure age with down-fjord distance ($R^2 = 0.01$, $p = 0.51$, $n = 33$). Nor is any trend of age with distance noted if only samples whose ^{26}Al/^{10}Be ratios are indistinguishable from constant exposure are included ($R^2 = 0.00$, $p = 0.94$, $n = 24$), if only boulder samples are included ($R^2 = 0.17$, $p = 0.14$, $n = 14$), and if only

boulders with ratios consistent with constant exposure are included ($R^2 = 0.19$, $p = 0.20$, $n = 10$). We find a similar lack of trends in exposure ages over ice retreat distance after recalibrating (for changed standard values and production rates) ^{10}Be and ^{26}Al ages reported for the eastern edge of Cumberland Sound by Kaplan et al. (2001) and Kaplan and Miller (2003) (Table 4, Fig. 4).

Like Kaplan et al. (2001) and Kaplan and Miller (2003) found for Cumberland Sound, we are unable to infer a unique solution to explain the lack of progressively younger ages with distance from the coast up Pangnirtung Fiord and Pass. The lack of relationship may be because the fjord deglaciated more rapidly than can be captured with the ^{10}Be chronometer as described in Briner et al. (2009), Hughes et al. (2012), and Corbett et al. (2013). In this case, the 75-km of Pangnirtung Pass and Pangnirtung Fiord spanned by our samples would have deglaciated likely within several hundred to at most a thousand years (Corbett et al., 2013), and supports the inference of Kaplan et al. (2001) and Kaplan and Miller (2003) that the margin of a low-profile ice lobe retreated rapidly up the sound during deglaciation. However, this lack of a trend in simple exposure ages may also result from the presence of small amounts of inherited ^{10}Be in some or many of the samples, obscuring the subtle differences in age that we might expect to observe along the length of Pangnirtung Pass and Pangnirtung Fiord.

We also have limited ability to discern a signal of post-glacial isostatic emergence in our cosmogenic ages. On Kekerten Island at the mouth of Kingnait Fiord, we collected six samples from both above (KM95-130 through KM95-133, Table 2, Fig. 4) and below (KM95-098 and KM95-099, Table 2, Fig. 4) the marine limit, which all have ages overlapping within 1σ uncertainties (excluding one older outlier, KM95-133). Our six

samples from Kekerten Island are also indistinguishable from or younger than those of Kaplan et al. (2001) that were collected from above the marine limit at the same location (CM46 and CM61, Table 4, Fig. 4). The ages from Kekerten Island are similar to those from above the marine limit on nearby Kekertukdjuak Island (PTD94-03 and PTD94-04, Table 2, Fig. 4). The only younger ages come from Beacon Island at the mouth of Pangnirtung Fiord (Fig. 4). Here, we collected two bedrock/boulder pairs from below the marine limit in which the bedrock samples (KM95-095, 12.5 ± 1.8 ka; and KM95-097, 12.0 ± 1.8 ka, Table 2) are both older than the corresponding boulders (KM95-094, 7.5 ± 1.4 ka; and KM95-096, 8.7 ± 2.1 ka, Table 2). In this case, the young boulders may be free of inherited nuclides and record the timing of post-glacial marine emergence. Our limited ability to distinguish between samples above and below the marine limit along Cumberland Sound is likely due to both the magnitude of the 1σ analytic uncertainties and the presence of inherited nuclides in some or many of the samples.

6.7. $^{26}Al/^{10}Be$ Production Ratio

Any inferences we draw from $^{26}Al/^{10}Be$ ratios depend on the assumed $^{26}Al/^{10}Be$ production ratio. In particular, the assumed $^{26}Al/^{10}Be$ production ratio has significant implications for identifying and quantifying complex exposure histories. For the 144 paired-isotope measurements we present here, the majority of the $^{26}Al/^{10}Be$ ratios (~80, regardless of the assumed production ratio) are indistinguishable from the production ratio because of the relatively large analytic uncertainties associated with the late-1990's AMS measurements. However, as greater production ratios are assumed, sensitivity analysis demonstrates that the number of samples exceeding the production ratio by more

than 1σ decreases whereas the number of samples falling below the production ratio by more than 1σ increases (Fig. 15). For example, based on an assumed $^{26}Al/^{10}Be$ production ratio of 6.75 (Balco et al., 2008), 43 of 144 samples appear to have a complex history (>1σ below the production ratio); conversely, with an assumed $^{26}Al/^{10}Be$ production ratio of 7.3 (Borchers et al., 2015), 71 of 144 samples appear to have a complex history.

We cannot use our data to assess which $^{26}Al/^{10}Be$ production ratio is most suitable for Baffin Island. Based on the distribution of analytic uncertainties, we would expect 15.9% of the 144 samples (23 total) to have $^{26}Al/^{10}Be$ ratios more than 1σ above the assumed ratio. The fact that our dataset has 22 samples more than 1σ above 6.75 appears to suggest that 6.75 may be an accurate production ratio. However, as documented above, many of the samples in the dataset have experienced burial and should thus have $^{26}Al/^{10}Be$ ratios below production. The statistical distribution around the sample's actual $^{26}Al/^{10}Be$ ratio is therefore likely to be shifted downward on the two-isotope plot, with values more than 1σ above the central tendency not necessarily being more than 1σ above the production ratio.

The incidence of high $^{26}Al/^{10}Be$ production ratios appears to be biased toward the high latitudes (Argento et al., 2013; Argento et al., 2015; Borchers et al., 2015). However, high latitudes are also the locations more likely to have non-erosive glacial ice, leading to the preservation of surfaces with complex exposure/burial histories (Briner et al., 2003; Briner et al., 2005, 2006; Corbett et al., 2013; Håkansson et al., 2008; Harbor et al., 2006; Lilly et al., 2010; Marquette et al., 2004; Staiger et al., 2005; Stroeven et al., 2002b; Sugden et al., 2005). Therefore, the glacial landscapes for which multi-isotope approaches are most useful are also the landscapes for which production ratios are most

uncertain. Future work assessing how the $^{26}Al/^{10}Be$ production ratio scales across spatial area, particularly at high latitude, will allow for more reliable identification of samples that have been buried beneath non-erosive ice and thus accurate quantification of burial durations from those samples.

7. Conclusions

Consideration of over 300 paired cosmogenic analyses of 155 bedrock and boulder samples from the Pangnirtung Fiord region of southern Baffin Island constrains glacial history and landscape development. Many lines of evidence (mismatched paired bedrock/boulder ages, increasing age with elevation, discordant ^{10}Be and ^{26}Al ages, multi-model age distributions, low $^{26}Al/^{10}Be$ ratios, and long modeled burial durations) indicate that some areas of the landscape, particularly the highlands, have been preserved beneath cold-based, non-erosive glacial ice for numerous glacial/interglacial cycles. The oldest of these surfaces have minimum-limiting burial durations of hundreds of thousands to millions of years, representing an archive of long-term information about Quaternary glaciation, with some surfaces pre-dating inception of the Laurentide Ice Sheet. A subset of the samples, especially those from lower elevations, were deeply eroded during Marine Isotope Stage 2 and allow us to learn about more recent glacial events. We infer that most of the landscape was deglaciated ~11.7 ka, except for the low-elevation areas that were occupied by the Cumberland Sound ice stream. The type Duval moraines and equivalents were deposited ~11.2 ka, possibly contemporaneous with the Younger Dryas cold interval.

Acknowledgements

We thank P. Hackett, C. Killian, J. Leonard, K. Marsella, C. Massey, S. Nichipor, B. O'Reilly, M. Reasoner, G. Rigby, S. Rigby, J. Steir, J. Turner, S. Ziff, and the staff of Parks Canada for assistance in the field; K. Marsella for processing samples; R. Finkel, M. Caffee, and J. Southon at Lawrence Livermore Laboratory (LLNL) Center for Accelerator Mass Spectrometry for AMS analysis; and M. Kaplan for assistance with recalculating data from Kaplan et al. (2001). LLNL work was supported by U.S. Department of Energy contract W-7405-ENG-48. This project was funded by the National Science Foundation grant OPP-93-21733, data analysis was in part supported by OPP-1023191, with additional support from the American Association of Petroleum Geologists and Bentley University. Reviews from M. Duhnforth and J. Heyman helped to improve the manuscript.

References

Alley, R., 2000, The Younger Dryas cold interval as viewed from central Greenland: Quaternary Science Reviews, v. 19, p. 213-226.

Andrews, J., 1975, Radiocarbon date list II from Cumberland Peninsula, Baffin Island, N.W.T., Canada: Arctic and Alpine Research, v. 7, p. 77-92.

Andrews, J., and Miller, G., 1972, The Quaternary history of northern Cumberland Peninsula, eastern Baffin Island, N.W.T. Part X: Radiocarbon date list: Arctic and Alpine Research, v. 4, p. 261-277.

Argento, D., Reedy, R., and Stone, J., 2013, Modeling the earth's cosmic radiation: Nuclear Instruments and Methods in Physics Research B, v. 294, p. 464-469.

Argento, D., Stone, J., Reedy, R., and O'Brien, K., 2015, Physics-based modeling of cosmogenic nuclides part II- Key aspects of in-situ cosmogenic nuclide production: Quaternary Geochronology, v. 26, p. 44-55.

Atkins, C., Barrett, P., and Hicock, S., 2002, Cold glaciers erode and deposit: evidence from Allan Hills, Antarctica: Geology, v. 30, no. 7, p. 659-662.

Balco, G., 2011, Contributions and unrealized potential contributions of cosmogenic-nuclide exposure dating to glacier chronology, 1990-2010: Quaternary Science Reviews, v. 30, no. 1-2, p. 3-27.

Balco, G., Briner, J., Finkel, R., Rayburn, J., Ridge, J., and Schaefer, J., 2009, Regional beryllium-10 production rate calibration for late-glacial northeastern North America: Quaternary Geochronology, v. 4, no. 2, p. 93-107.

Balco, G., Stone, J., Lifton, N., and Dunai, T., 2008, A complete and easily accessible means of calculating surface exposure ages or erosion rates from ^{10}Be and ^{26}Al measurements: Quaternary Geochronology, v. 3, no. 3, p. 174-195.

Bierman, P., and Caffee, M., 2002, Cosmogenic exposure and erosion history of Australian bedrock landforms: Bulletin of the Geological Society of America, v. 114, no. 7, p. 787-803.

Bierman, P., Corbett, L., Graly, J., Neumann, T., Lini, A., Crosby, B., and Rood, D., 2014, Preservation of a preglacial landscape under the center of the Greenland Ice Sheet: Science, v. 344, p. 402-405.

Bierman, P., Davis, P., Corbett, L., and Lifton, N., 2015, Cold-based, Laurentide ice covered New England's highest summits during the Last Glacial Maximum: Geology, v. 43, no. 12, p. 1059-1062.

Bierman, P., Marsella, K., Davis, P., and Caffee, M., 2001, Response to Discussion by Wolfe et al. on Bierman et al. (Geomorphology 25 (1999) 25–39): Geomorphology, v. 39, p. 255-260.

Bierman, P., Marsella, K., Patterson, C., Davis, P., and Caffee, M., 1999, Mid-Pleistocene cosmogenic minimum-age limits for pre-Wisconsinan glacial surfaces in southwestern Minnesota and southern Baffin Island: a multiple nuclide approach: Geomorphology, v. 27, no. 1, p. 25-39.

Borchers, B., Marrero, S., Balco, G., Caffee, M., Goehring, B., Lifton, N., Nishiizumi, K., Phillips, F., Schaefer, J., and Stone, J., 2015, Geological calibration of spallation production rates in the CRONUS-Earth project: Quaternary Geochronology, v. doi:10.1016/j.quageo.2015.01.009.

Briner, J., Bini, A., and Anderson, R., 2009, Rapid early Holocene retreat of a Laurentide outlet glacier through an Arctic fjord: Nature Geoscience, v. 2, p. 496-499.
Briner, J., Miller, G., Davis, P., Bierman, P., and Caffee, M., 2003, Last Glacial Maximum ice sheet dynamics in Arctic Canada inferred from young erratics perched on ancient tors: Quaternary Science Reviews, v. 22, no. 5-7, p. 437-444.
Briner, J., Miller, G., Davis, P., and Finkel, R., 2005, Cosmogenic exposure dating in arctic glacial landscapes: implications for the glacial history of northeastern Baffin Island, Arctic Canada: Canadian Journal of Earth Sciences, v. 42, p. 67-84.
Briner, J., Miller, G., Davis, P., and Finkel, R., 2006, Cosmogenic radionuclides from fjord landscapes support differential erosion by overriding ice sheets: Geological Society of America Bulletin, v. 118, no. 3/4, p. 406-420.
Broecker, W., Andree, M., Wolfi, W., Oeschger, H., Bonani, G., Kennett, J., and Peteet, D., 1988, The chronology of the last deglaciation: Implications to the cause of the Younger Dryas event.: Paleoceanography, v. 3, p. 1-19.
Chmeleff, J., Von Blanckenburg, F., Kossert, K., and Jakob, D., 2010, Determination of the ^{10}Be half-life by multicollector ICP-MS and liquid scintillation counting: Nuclear Instruments and Methods in Physics Research Section B: Beam Interactions with Materials and Atoms, v. 268, no. 2, p. 192-199.
Cofaigh, C., Dowdeswell, J., Jennings, A., Hogan, K., Kilfeather, A., Hiemstra, J., Noormets, R., Evans, J., McCarthy, D., Andrews, J., Lloyd, J., and Moros, M., 2012, An extensive and dynamic ice sheet on the West Greenland shelf during the last glacial cycle: Geology, v. 41, p. 219-222.
Corbett, L., Bierman, P., Graly, J., Neumann, T., and Rood, D., 2013, Constraining landscape history and glacial erosivity using paired cosmogenic nuclides in Upernavik, northwest Greenland: Geological Society of America Bulletin, v. 125, no. 9/10, p. 1539-1553.
Corbett, L., Bierman, P., Lasher, G., and Rood, D., 2015a, Landscape chronology and glacial history in Thule, northwest Greenland: Quaternary Science Reviews, v. 109, p. 57-67.
Corbett, L., Bierman, P., and Rood, D., 2015b, Constraining multi-stage exposure-burial scenarios for boulders preserved beneath cold-based ice in Thule, Northwest Greenland: Geological Society of America Abstracts with Programs, v. 47, no. 7, p. 712.
Dansgaard, W., White, J., and Johnsen, S., 1989, The abrupt termination of the Younger Dryas climate event: Nature, v. 339, p. 532-534.
Davis, P., 1988, Possible evidence for extensive late Wisconsin (late Foxe) glaciation in Pangnirtung Pass area, southern Cumberland Peninsula, Baffin Island: Geological Society of America Abstracts with Programs, v. 20, no. 7, p. 208.
Davis, P., Bierman, P., Marsella, K., Caffee, M., and Southon, J., 1999, Cosmogenic analysis of glacial terrains in the eastern Canadian Arctic: a test for inherited nuclides and the effectiveness of glacial erosion: Annals of Glaciology, v. 28, no. 181-188.
Dyke, A., 1977, Quaternary geomorphology, glacial chronology, and climatic and sea-level history of southwestern Cumberland Peninsula, Baffin Island, Northwest Territories, Canada [PhD dissertation: University of Colorado, 184 p.

Dyke, A, 1979, Quaternary geomorphology, glacial chronology, and climatic and sea-level history of southwestern Cumberland Peninsula, Baffin Island, Northwest Territories, Canada: Arctic and Alpine Research, v. 11, no. 2, p. 179-202.
Dyke, A., Andrews, J., and Miller, G., 1982, Quaternary geology of Cumberland Peninsula, Baffin Island, District of Franklin: Geological Survey of Canada Memoir 403, p. 1-32.
Fabel, D., and Harbor, J., 1999, The use of in-situ produced cosmogenic radionuclides in glaciology and glacial geomorphology: Annals of Glaciology, v. 28, no. 1, p. 103-110.
Fitzsimons, S., Webb, N., Mager, S., MacDonell, S., Lorrain, R., and Samyn, D., 2008, Mechanisms of basal ice formation in polar glaciers: An evaluation of the apron entrainment model: Journal of Geophysical Research, v. 113, p. F02010.
Gilbert, R., 1978, Observations on oceanography and sedimentation at Pangnirtung Fiord, Baffin Island: Maritime Sediments, v. 14, no. 1, p. 1-9.
Goehring, B., Brook, E., Linge, H., Raisbeck, G., and Yiou, F., 2008, Beryllium-10 exposure ages of erratic boulders in southern Norway and implications for the history of the Fennoscandian Ice Sheet: Quaternary Science Reviews, v. 27, p. 320-336.
Gosse, J., and Phillips, F., 2001, Terrestrial in situ cosmogenic nuclides: theory and application: Quaternary Science Reviews, v. 20, no. 14, p. 1475-1560.
Granger, D., 2006, A review of burial dating methods using 26Al and 10Be: Geological Society of America Special Papers, v. 415, p. 1-16.
Håkansson, L., Alexanderson, H., Hjort, C., Moller, P., Briner, J., Aldahan, A., and Possnert, G., 2008, Late Pleistocene glacial history of Jameson Land, central East Greenland, derived from cosmogenic ^{10}Be and ^{26}Al exposure dating: Boreas, v. 38, no. 2, p. 244-260.
Hamilton, B., Pattison, D., Sanborn-Barrie, M., and Young, M., 2012, Preliminary characterization of metamorphism on Cumberland Peninsula, Baffin Island, Nunavut: Geologic Survey of Current Research 2012-9, 17 pp.
Harbor, J., Stroeven, A., Fabel, D., Clarhäll, A., Kleman, J., Li, Y., Elmore, D., and Fink, D., 2006, Cosmogenic nuclide evidence for minimal erosion across two subglacial sliding boundaries of the late glacial Fennoscandian ice sheet: Geomorphology, v. 75, no. 1-2, p. 90-99.
Hughes, A., Rainsley, E., Murray, T., Fogwill, C., Schnabel, C., and Xu, S., 2012, Rapid response of Helheim Glacier, southeast Greenland, to early Holocene climate warming: Geology, v. 40, no. 5, p. 427-430.
Hyatt, J., 1992, Cavity development in ice-rich permafrost, Pangnirtung, Baffin Island, Northwest Territories: Permafrost and Periglacial Processes, v. 3, p. 293-313.
IPCC, 2013, Climate Change 2013: The Physical Science Basis. Working Group I Contribution to the Fifth Assessment Report of the Intergovernmental Panel on Climate Change, Cambridge University Press.
Ives, J., 1978, The maximum extent of the Laurentide Ice Sheet along the east coast of North America during the last deglaciation: Arctic, v. 32, p. 24-35.
Jackson, G., and Taylor, F., 1972, Correlation of major Aphebian rock units in the northern Canadian Shield: Canadian Journal of Earth Sciences, v. 9, p. 1650-1669.

Jamieson, S., Sugden, D., and Hulton, N., 2010, The evolution of the subglacial landscape of Antarctica: Earth and Planetary Science Letters, v. 293, p. 1-27.
Jennings, A., 1993, The Quaternary history of Cumberland Sound, southeastern Baffin Island: The marine evidence: Geographie Physique et Quaternaire, v. 47, p. 21-42.
Jennings, A., Tedesco, K., Andrews, J., and Kirby, M., 1996, Shelf erosion and glacial ice proximity in the Labrador Sea during and after Heinrich events (H-3 or 4 to H-0): Geological Society of London Special Publications, v. 111, p. 29-49.
Johnsen, S., Dahl-Jensen, D., Gundestrup, N., Steffensen, J., Clausen, H., Miller, H., Masson-Delmotte, V., Sveinbjornsdottir, A., and White, J., 2001, Oxygen isotope and palaeotemperature records from six Greenland ice-core stations: Camp Century, Dye-3, GRIP, GISP2, Renland and NorthGRIP: Journal of Quaternary Science, v. 16, p. 299-307.
Kaplan, M., and Miller, G., 2003, Early Holocene delevelling and deglaciation of the Cumberland Sound region, Baffin Island, Arctic Canada: Geological Society of America Bulletin, v. 115, no. 4, p. 445-462.
Kaplan, M., Miller, G., and Steig, E., 2001, Low-gradient outlet glaciers (ice streams?) drained the Laurentide ice sheet: Geology, v. 29, no. 4, p. 343-346.
Kaplan, M., Pfeffer, W., Sassolas, C., and Miller, G., 1999, Numerical modelling of the Laurentide Ice Sheet in the Baffin Island region: the role of a Cumberland Sound ice stream: Canadian Journal of Earth Sciences, v. 36, p. 1315-1326.
Kessler, M., Anderson, R., and Briner, J., 2008, Fjord insertion into continental margins driven by topographic steering of ice: Nature Geoscience, v. 1, p. 365-369.
Klein, J., Giegengack, R., Middleton, R., Sharma, P., Underwood, J., and Weeks, R., 1986, Revealing histories of exposure using *in situ* produced 26Al and 10Be in Libyan desert glass: Radiocarbon, v. 28, no. 2A, p. 547-555.
Kleman, J., and Borgstrom, I., 1994, Glacial land forms indicative of a partly frozen bed: Journal of Glaciology, v. 40, no. 135, p. 255-264.
Korschinek, G., Bergmaier, A., Faestermann, T., Gerstmann, U., Knie, K., Rugel, G., Wallner, A., Dillmann, I., Dollinger, G., Lierse von Gostomski, C., Kossert, K., Maiti, M., Poutivtsev, M., and Remmert, A., 2010, A new value for the half-life of ^{10}Be by Heavy-Ion Elastic Recoil Detection and liquid scintillation counting: Nuclear Instruments and Methods in Physics Research Section B: Beam Interactions with Materials and Atoms, v. 268, p. 187-191.
Lal, D., 1988, In situ-produced cosmogenic isotopes in terrestrial rocks: Annual Review of Earth and Planetary Sciences, v. 16, no. 1, p. 355-388.
Lal, D., 1991, Cosmic ray labeling of erosion surfaces: in situ nuclide production rates and erosion models: Earth and Planetary Science Letters, v. 104, no. 2-4, p. 424-439.
Lemmen, D., Glbert, R., Smol, J., and Hall, R., 1988, Holocene sedimentation in glacial Tasikutaaq Lake, Baffin Island: Canadian Journal of Earth Sciences, v. 25, p. 810-823.
Lilly, K., Fink, D., Fabel, D., and Lambeck, K., 2010, Pleistocene dynamics of the interior of the East Antarctic ice sheet: Geology, v. 38, no. 8, p. 703-706.
Long, A., 2009, Back to the future: Greenland's contribution to sea-level change: GSA Today, v. 19, no. 6, p. 4-10.

Lowdon, J., and Blake, W., 1975, Geological Survey of Canada radiocarbon dates XV: Geologic Survey of Canada Paper 75-7, p. 32 pp.
Margreth, A., Gosse, J., and Dyke, A., 2011, Testing the concept of altitudinal weathering zones on Cumberland Peninsula, Baffin Island, using terrestrial cosmogenic nuclide (TCN) exposure dating: Atlantic Geology Society Abstracts, v. 47, p. 30.
Margreth, A., Gosse, J., and Dyke, A., 2012, Ice cap evolution and polythermal ice dynamics derived from multiple terrestrial cosmogenic nuclide (TCN) dating of tors on Cumberland Peninsula, Baffin Island: Atlantic Geology Society Abstracts, v. 48, p. 37.
Margreth, A., Gosse, J., and Dyke, A., 2014, Constraining the timing of last glacial plucking of tors on Cumberland Peninsula, Baffin Island, Eastern Canadian Arctic: European Geophysical Union Geophysical Research Abstracts, v. 16, p. EGU2014-9043.
Marquette, G., Gray, J., Gosse, J., Courchesne, F., Stockli, L., Macpherson, G., and Finkel, R., 2004, Felsenmeer persistence under non-erosive ice in the Torngat and Kaumajet mountains, Quebec and Labrador, as determined by soil weathering and cosmogenic nuclide exposure dating: Canadian Journal of Earth Sciences, v. 41, no. 1, p. 19-38.
Marsella, K., Bierman, P., Davis, P., and Caffee, M., 2000, Cosmogenic ^{10}Be and ^{26}Al ages for the last glacial maximum, eastern Baffin Island, Arctic Canada: Geological Society of America Bulletin, v. 112, no. 8, p. 1296-1312.
Miller, G., Briner, J., Lifton, N., and Finkel, R., 2006, Limited ice-sheet erosion and complex exposure histories derived from in situ cosmogenic 10Be, 26Al, and 14C on Baffin Island, Arctic Canada: Quaternary Geochronology, v. 1, p. 74-85.
Nicola, L., Strasky, S., Schluchter, C., Salvatore, M., Akcar, N., Kubik, P., Christl, M., Kasper, H., Wieler, R., and Baroni, C., 2009, Multiple cosmogenic nuclides document complex Pleistocene exposure history of glacial drifts in Terra Nova Bay (northern Victoria Land, Antarctica): Quaternary Research, v. 71, p. 83-92.
Nishiizumi, K., 2004, Preparation of ^{26}Al AMS standards: Nuclear Instruments and Methods in Physics Research Section B: Beam Interactions with Materials and Atoms, v. 223, p. 388-392.
Nishiizumi, K., Imamura, M., Caffee, M., Southon, J., Finkel, R., and McAninch, J., 2007, Absolute calibration of ^{10}Be AMS standards: Nuclear Instruments and Methods in Physics Research Section B: Beam Interactions with Materials and Atoms, v. 258, no. 2, p. 403-413.
Nishiizumi, K., Kohl, C., Arnold, J., Klein, J., Fink, D., and Middleton, R., 1991, Cosmic ray produced ^{10}Be and ^{26}Al in Antarctic rocks: exposure and erosion history: Earth and Planetary Science Letters, v. 104, no. 2-4, p. 440-454.
Nishiizumi, K., Winterer, E., Kohl, C., Klein, J., Middleton, R., Lal, D., and Arnold, J., 1989, Cosmic ray production rates of ^{10}Be and ^{26}Al in quartz from glacially polished rocks: Journal of Geophysical Research, v. 94, no. B12, p. 17907.
Perren, B., Anderson, N., Douglas, M., and Fritz, S., 2012, The influence of temperature, moisture, and eolian activity on Holocene lake development in West Greenland: Journal of Paleolimnology, v. 48, p. 223-239.

Phillips, F., Zreda, M., Smith, S., Elmore, D., Kubik, P., and Sharma, P., 1990, Cosmogenic chlorine-36 chronology for glacial deposits at Bloody Canyon, eastern Sierra Nevada: Science, v. 248, no. 4962, p. 1529-1532.

Phillips, W., Hall, A., Mottram, R., Fifield, L., and Sugden, D., 2006, Cosmogenic 10Be and 26Al exposure ages of tors and erratics, Cairngorm Mountains, Scotland: Timescales for the development of a classic landscape of selective linear glacial erosion: Geomorphology, v. 73, p. 222-245.

Rinterknecht, V., Gorokhovich, Y., Schaefer, J., and Caffee, M., 2009, Preliminary ^{10}Be chronology for the last deglaciation of the western margin of the Greenland Ice Sheet: Journal of Quaternary Science, v. 24, no. 3, p. 270-278.

Rood, D., Hall, S., Guilderson, T., Finkel, R., and Brown, T., 2010, Challenges and opportunities in high-precision Be-10 measurements at CAMS: Nuclear Instruments and Methods in Physics Research Section B: Beam Interactions with Materials and Atoms, v. 268, no. 7-8, p. 730-732.

Schildgen, T., Phillips, W., and Purves, R., 2005, Simulation of snow shielding corrections for cosmogenic nuclide surface exposure studies: Geomorphology, v. 64, no. 1-2, p. 67-85.

Staiger, J., Gosse, J., Johnson, J., Fastook, J., Gray, J., Stockli, D., Stockli, L., and Finkel, R., 2005, Quaternary relief generation by polythermal glacier ice: Earth Surface Processes and Landforms, v. 30, no. 9, p. 1145-1159.

Steer, P., Huismans, R., Valla, P., Gac, S., and Herman, F., 2012, Bimodal Plio–Quaternary glacial erosion of fjords and low-relief surfaces in Scandinavia: Nature Geoscience, v. 5, no. 635-639.

Stone, J., 2000, Air pressure and cosmogenic isotope production: Journal of Geophysical Research, v. 105, no. B10, p. 23753-23759.

Stroeven, A., Fabel, D., Harbor, J., Hattestrand, C., and Kleman, J., 2002a, Quantifying the erosional impact of the Fennoscandian Ice Sheet in the Torneträsk-Narvik corridor, northern Sweden, based on cosmogenic radionuclide data: Geografiska Annaler; Series A, Physical Geography, v. 84, no. 3/4, p. 275-287.

Stroeven, A., Fabel, D., Hattestrand, C., and Harbor, J., 2002b, A relict landscape in the centre of Fennoscandian glaciation: cosmogenic radionuclide evidence of tors preserved through multiple glacial cycles: Geomorphology, v. 44, no. 1-2, p. 145-154.

Stuiver, M., Reimer, P., and Reimer, R., 2015, CALIB Radiocarbon Calibration 7.1: calib.qub.ac.uk/calib/.

Sugden, D., 1977, Reconstruction of the morphology, dynamics, and thermal characteristics of the Laurentide Ice Sheet at its maximum: Arctic and Alpine Research, v. 9, no. 1, p. 21-47.

Sugden, D., 1978, Glacial erosion by the Laurentide ice sheet: Journal of Glaciology, v. 20, no. 83, p. 367-391.

Sugden, D., Balco, G., Cowdery, S., Stone, J., and Sass III, L., 2005, Selective glacial erosion and weathering zones in the coastal mountains of Marie Byrd Land, Antarctica: Geomorphology, v. 67, no. 3-4, p. 317-334.

Sugden, D., and Watts, S., 1977, Tors, felsenmeer, and glaciation in northern Cumberland Peninsula, Baffin Island: Canadian Journal of Earth Sciences, v. 14, no. 2, p. 2817-2823.

Taylor, K., Lamorey, G., Doyle, G., Alley, R., Grootes, P., Mayewski, P., White, J., and Barlow, L., 1993, The 'flickering switch'of late Pleistocene climate change: Nature, v. 361, p. 432-436.

Taylor, K., Mayewski, P., Alley, R., Brook, E., Gow, A., Grootes, P., Meese, D., Saltzman, E., Severinghaus, J., and Twickler, M., 1997, The Holocene-Younger Dryas transition recorded at Summit, Greenland: Science, v. 278, no. 5339, p. 825-827.

Wolfe, A., Steig, E., and Kaplan, M., 2001, An alternative model for the geomorphic history of pre-Wisconsinan surfaces on eastern Baffin Island: a comment on Bierman et al (Geomorphology 25 (1999) 25-39): Geomorphology, v. 39, no. 251-254.

Table 1. Selected radiocarbon ages from the Pangnirtung Fiord area that provide age constraints for glacier retreat and marine submergence relevant to the ^{10}Be exposure ages examined in this paper.

Site Name	Latitude (°N)	Longitude (°W)	Sample Elevaton (m)	Marine Limit Elevation (m)	Uncorrected Age (^{14}C yr BP)	Laboratory Number	Material	Corrected Age (^{14}C yr BP)*	Calibrated Age (yr BP)†	Reference(s)
Pangnirtung hamlet§	66.1333	65.7167	145	50	52450 ± 1430	TO-2198	Marine shells in till	---	---	Hyatt, 1992
Pangnirtung hamlet	66.1333	65.7167	39	50	8690 ± 90	GSC-2001	Marine shells	8650 ± 45	9605 (9545-9655)	Dyke, 1979; Dyke et al., 1982
Pangnirtung hamlet	66.1333	65.7167	26	50	7870 ± 150	GaK-3093	Marine shells	7830 ± 75	8635 (8520-8760)	Andrews and Miller, 1972
Pangnirtung hamlet	66.1333	65.7167	16	50	8570 ± 80	GSC-6032	Marine shells	8120 ± 40	9060 (9005-9090)	This study
Pangnirtung hamlet	66.1333	65.7167	10	50	8480 ± 110	GSC-6019	Marine shells	8030 ± 55	8890 (8780-9010)	This study
Usualuk River	66.5417	66.2667	34	70	8670 ± 110	GSC-2183	Marine shells	8630 ± 55	9600 (9540-9660)	Dyke et al., 1982
Kingnait Fiord head	66.3583	64.3500	8	16	8480 ± 270	GSC-2083	Marine shells	8440 ± 135	9420 (9275-9550)	Dyke, 1979; Dyke et al., 1982
Kingnait Fiord head	66.3500	64.3500	8	16	7990 ± 170	GaK-4837	Marine shells	7950 ± 85	8810 (8655-8980)	Andrews, 1975; Lowdon and Blake, 1975
SE Cumberland Peninsula	65.5657	65.3143	2	65	9970 ± 50	CURL-2953	Marine shells	9520 ± 50	10,855 (10,705-11,065)	Kaplan and Miller, 2003
SE Cumberland Peninsula	65.5657	65.3143	2	65	9760 ± 50	CURL-2954	Marine shells	9310 ± 50	10,515 (10,425-10,580)	Kaplan and Miller, 2003
SE Cumberland Peninsula	65.5657	65.3143	6	65	9250 ± 50	CURL-2952	Marine shells	8800 ± 50	9835 (9700-9915)	Kaplan and Miller, 2003
SE Cumberland Peninsula	65.5557	65.1777	8	65	8310 ± 50	CURL-2951	Marine shells	7860 ± 50	8660 (8585-8750)	Kaplan and Miller, 2003
Cumberland Sound mouth	65.9072	64.9630	marine core	---	9450 ± 95	AA-2633	Marine shells	9000 ± 95	10,120 (9930-10,245)	Jennings, 1993
Cumberland Sound mouth	65.0428	64.9918	marine core	---	10010 ± 110	AA-3585&6	Benthic forams and mollusc	9560 ± 110	10,905 (10,735-11,090)	Jennings, 1993
Cumberland Sound mouth	65.3890	65.5088	marine core	---	10920 ± 250	AA-3939	Benthic forams	10470 ± 250	12,255 (12,000-12,685)	Jennings, 1993
Cumberland Sound mouth	62.5165	59.4470	marine core	---	10630 ± 180	AA-7136	Benthic forams	10180 ± 180	11,845 (11,405-12,125)	Jennings et al., 1996
Cumberland Sound mouth	62.5165	59.4470	marine core	---	10530 ± 95	AA-5032	*Neogloboquadrina pachyderma*	10080 ± 95	11,645 (11,400-11,820)	Jennings et al., 1996

*Radiocarbon ages corrected by subtraction of 450 yr for marine reservoir effect in Pangnirtung Fiord, addition of 410 yr to samples with GSC and GaK prefixes for δ^{13}C correction, and conversion of errors to 1σ for samples with GSC prefixes.
†Calibrated age estimates include the median probability and minimum and maximum ages based on 1SD from minimum and maximum intercepts using CALIB 7.1 (Stuiver et al., 2015) and the IntCal13 calibration curve.
§This sample's age exceeds the calibration threshold, hence no corrected or calibrated ages are shown here.

Table 2. Single-isotope simple exposure ages and uncertainties as well as $^{26}Al/^{10}Be$ ratios and uncertainties for the 155 samples reported in this analysis.

Sample Name	Sample Type	^{10}Be Simple Exposure Age (ka)*	^{10}Be Internal Uncertainty (ka)*	^{26}Al Simple Exposure Age (ka)*	^{26}Al Internal Uncertainty (ka)*	07KNSTD $^{26}Al/^{10}Be$ Ratio†	07KNSTD $^{26}Al/^{10}Be$ Ratio Uncertainty†
KM95-001	Bedrock	10.3	1.3	10.0	0.5	6.6	0.9
KM95-002	Boulder	26.5	1.0	26.5	1.4	6.7	0.4
KM95-003	Boulder	78.7	1.7	73.9	2.4	6.3	0.2
KM95-004	Boulder	11.7	2.7	11.5	0.9	6.7	1.6
KM95-005	Boulder	18.2	1.4	18.5	0.9	6.9	0.6
KM95-006	Boulder	14.8	0.9	14.8	0.6	6.8	0.5
KM95-007	Boulder	11.0	1.1	11.9	0.5	7.3	0.8
KM95-008	Boulder	38.5	0.9	39.4	1.9	6.9	0.4
KM95-009	Boulder	16.5	0.9	18.2	0.8	7.5	0.5
KM95-010	Boulder	15.4	0.7	15.4	0.6	6.8	0.4
KM95-011	Boulder	11.9	0.7	11.9	0.5	6.8	0.5
KM95-012	Boulder	15.1	1.1	15.6	0.8	7.0	0.6
KM95-013	Boulder	14.6	2.4	11.6	0.7	5.4	1.0
KM95-014	Bedrock	16.6	2.4	17.1	0.8	7.0	1.1
KM95-015	Bedrock	10.3	1.5	12.3	1.0	8.0	1.4
KM95-016	Bedrock	159.9	3.4	124.3	2.7	5.2	0.2
KM95-017	Cobble	39.7	1.1	35.2	1.3	6.0	0.3
KM95-018	Boulder	17.2	0.7	16.5	0.7	6.5	0.4
KM95-019	Boulder	27.6	0.9	29.5	1.1	7.2	0.4
KM95-020	Bedrock	12.9	0.8	16.0	0.7	8.4	0.6
KM95-021	Bedrock	13.1	0.9	15.5	0.9	8.0	0.7
KM95-022	Boulder	12.2	1.2	10.6	0.8	5.9	0.7
KM95-023	Bedrock	16.8	2.8	12.6	1.0	5.1	0.9
KM95-024	Boulder	49.5	1.5	50.0	1.9	6.8	0.3
KM95-025	Boulder	11.4	0.8	13.0	0.7	7.7	0.7
KM95-026	Boulder	12.1	1.0	No Data	No Data	No Data	No Data
KM95-027	Bedrock	28.9	1.2	30.1	1.2	7.0	0.4
KM95-028	Boulder	11.3	0.7	12.1	0.6	7.3	0.6
KM95-029	Boulder	17.6	1.1	18.9	1.0	7.3	0.6
KM95-030	Boulder	21.0	4.7	11.5	1.6	3.7	1.0
KM95-031	Boulder	13.2	1.0	14.9	0.7	7.6	0.7
KM95-032	Boulder	15.7	2.2	5.9	0.9	2.6	0.5
KM95-033	Boulder	28.5	1.2	39.1	3.1	9.2	0.8
KM95-034	Boulder	11.2	1.5	12.1	0.6	7.3	1.1
KM95-035	Boulder	26.3	1.3	23.0	1.1	5.9	0.4
KM95-036	Boulder	28.9	3.1	27.5	0.9	6.4	0.7
KM95-037	Bedrock	No Data	No Data	27.5	1.3	No Data	No Data
KM95-038	Boulder	13.4	2.0	10.5	1.3	5.3	1.0
KM95-039	Bedrock	27.9	1.2	31.4	1.2	7.6	0.4
KM95-040	Bedrock	31.3	1.4	32.8	1.6	7.1	0.5
KM95-041	Bedrock	11.4	1.5	14.0	0.9	8.3	1.2
KM95-042	Bedrock	15.7	1.7	11.7	1.0	5.1	0.7
KM95-043	Bedrock	9.7	1.3	12.0	0.8	8.4	1.3
KM95-044	Bedrock	13.3	1.2	11.3	0.8	5.8	0.7
KM95-045	Bedrock	14.0	1.8	14.1	0.9	6.8	1.0
KM95-046	Bedrock	11.8	1.3	13.6	1.1	7.9	1.1
KM95-047	Bedrock	16.3	3.5	8.7	0.7	3.6	0.8
KM95-048	Bedrock	13.0	1.1	12.0	1.1	6.3	0.8
KM95-049	Bedrock	30.7	1.7	30.8	1.4	6.8	0.5
KM95-059	Boulder	12.2	1.5	10.7	1.4	6.0	1.1
KM95-060	Bedrock	13.4	2.2	11.7	1.0	5.9	1.1
KM95-061	Bedrock	17.2	1.7	14.3	0.9	5.6	0.7
KM95-062	Boulder	10.7	1.7	10.9	0.8	6.9	1.2
KM95-063	Cobble	13.0	1.5	9.2	1.0	4.8	0.8
KM95-064	Boulder	12.4	1.5	10.6	0.8	5.8	0.8

Table 2, cont.

Sample Name	Sample Type	^{10}Be Simple Exposure Age (ka)*	^{10}Be Internal Uncertainty (ka)*	^{26}Al Simple Exposure Age (ka)*	^{26}Al Internal Uncertainty (ka)*	07KNSTD ^{26}Al/^{10}Be Ratio†	07KNSTD ^{26}Al/^{10}Be Ratio Uncertainty†
KM95-066	Boulder	16.7	1.9	16.5	1.1	6.7	0.9
KM95-067	Bedrock	20.0	0.9	21.0	0.8	7.1	0.4
KM95-068	Boulder	54.9	2.3	46.9	3.1	5.7	0.4
KM95-069	Cobble	9.9	0.9	9.3	0.9	6.4	0.8
KM95-070	Boulder	10.3	0.9	10.9	0.5	7.2	0.7
KM95-071	Boulder	19.9	1.0	18.4	0.9	6.3	0.4
KM95-072	Bedrock	10.7	0.6	13.8	0.6	8.7	0.6
KM95-073	Boulder	No Data	No Data	13.9	0.6	No Data	No Data
KM95-074	Boulder	11.2	1.8	9.7	0.8	5.9	1.0
KM95-075	Bedrock	12.6	1.9	9.3	1.1	5.1	0.9
KM95-076	Bedrock	11.6	1.9	12.6	1.0	7.4	1.3
KM95-077	Boulder	12.0	1.6	12.2	0.9	6.9	1.0
KM95-078	Bedrock	10.9	1.3	11.5	0.8	7.2	1.0
KM95-079	Bedrock	12.2	2.2	12.5	0.8	7.0	1.3
KM95-080	Boulder	10.7	1.1	12.1	1.1	7.7	1.1
KM95-081	Boulder	13.5	2.5	12.4	1.1	6.2	1.3
KM95-082	Bedrock	11.1	1.4	11.8	0.8	7.2	1.1
KM95-083	Boulder	13.5	1.7	11.6	0.9	5.8	0.9
KM95-084	Bedrock	11.7	2.1	11.8	0.8	6.8	1.3
KM95-086	Bedrock	11.7	1.5	12.4	0.8	7.2	1.0
KM95-087	Boulder	12.7	1.4	12.6	1.0	6.7	0.9
KM95-088	Bedrock	14.6	1.9	13.1	1.1	6.1	0.9
KM95-089	Boulder	14.3	1.6	11.5	1.0	5.5	0.8
KM95-090	Bedrock	13.6	1.5	12.1	0.8	6.1	0.8
KM95-091	Bedrock	11.0	1.7	9.4	0.8	5.8	1.0
KM95-092	Boulder	10.4	1.2	15.6	1.1	10.2	1.4
KM95-093	Bedrock	11.5	1.6	11.1	1.3	6.6	1.2
KM95-094	Boulder	7.5	1.4	6.9	0.6	6.3	1.3
KM95-095	Bedrock	12.5	1.8	6.1	0.6	3.4	0.6
KM95-096	Boulder	8.7	2.1	4.3	0.6	3.4	0.9
KM95-097	Bedrock	12.0	1.8	7.0	0.6	4.0	0.7
KM95-098	Boulder	14.3	1.9	11.8	0.9	5.6	0.9
KM95-099	Bedrock	11.8	1.9	10.1	0.9	5.8	1.1
KM95-100	Boulder	25.6	1.5	14.1	0.7	3.8	0.3
KM95-101	Boulder	29.0	1.4	26.7	1.2	6.2	0.4
KM95-102	Boulder	13.1	0.8	14.7	1.3	7.6	0.8
KM95-103	Boulder	11.4	0.8	11.1	0.6	6.6	0.6
KM95-104	Boulder	12.1	1.0	12.0	0.9	6.7	0.7
KM95-105	Boulder	11.9	0.9	12.3	0.7	7.0	0.7
KM95-106	Bedrock	109.7	2.9	86.8	3.0	5.3	0.2
KM95-107	Bedrock	140.7	3.8	112.2	2.2	5.3	0.2
KM95-108	Bedrock	99.9	3.3	80.2	3.0	5.4	0.3
KM95-109	Bedrock	88.3	2.4	69.8	3.1	5.3	0.3
KM95-110	Bedrock	153.9	7.9	109.1	3.9	4.7	0.3
KM95-112	Bedrock	136.3	3.7	104.0	3.7	5.1	0.2
KM95-113	Boulder	14.5	1.3	11.9	0.7	5.6	0.6
KM95-114	Boulder	15.0	1.7	13.6	0.9	6.1	0.8
KM95-115	Boulder	13.8	1.3	11.8	1.3	5.8	0.9
KM95-116	Boulder	12.5	1.4	12.5	0.9	6.8	0.9
KM95-117	Boulder	12.7	1.7	12.4	1.0	6.7	1.0
KM95-130	Boulder	13.0	1.5	10.7	0.8	5.6	0.8
KM95-131	Boulder	11.9	1.2	13.4	0.8	7.6	0.9
KM95-132	Boulder	13.5	1.9	13.4	1.0	6.8	1.1
KM95-133	Bedrock	18.1	1.8	19.8	1.4	7.4	0.9
KM95-134	Bedrock	14.2	1.7	11.5	0.9	5.5	0.8

Table 2, cont.

Sample Name	Sample Type	^{10}Be Simple Exposure Age (ka)*	^{10}Be Internal Uncertainty (ka)*	^{26}Al Simple Exposure Age (ka)*	^{26}Al Internal Uncertainty (ka)*	07KNSTD ^{26}Al/^{10}Be Ratio†	07KNSTD ^{26}Al/^{10}Be Ratio Uncertainty†
KM95-135	Boulder	14.4	1.3	12.9	0.9	6.1	0.7
KM95-136	Bedrock	16.2	1.8	9.2	0.9	3.9	0.6
KM95-138	Boulder	18.0	1.5	13.5	0.7	5.1	0.5
KM95-139	Boulder	13.1	1.9	12.2	1.3	6.3	1.1
KM95-140	Bedrock	13.9	3.9	12.8	0.7	6.3	1.8
KM95-141	Bedrock	13.4	1.0	13.5	0.7	6.9	0.6
KM95-142	Boulder	14.4	2.3	11.9	1.2	5.6	1.2
KM95-143	Boulder	18.1	2.7	16.2	1.3	6.1	1.2
KM95-144	Boulder	13.0	1.7	10.8	0.9	5.6	0.9
KM95-145	Bedrock	11.2	1.5	10.0	1.1	6.1	1.0
KM95-146	Boulder	11.8	0.8	12.1	0.7	6.9	0.6
KM95-147	Bedrock	35.7	1.2	36.5	1.2	6.9	0.3
KM95-149	Bedrock	17.9	1.5	21.4	1.2	8.1	0.8
PTD92-01	Boulder	7.1	0.7	7.5	0.5	7.2	0.9
PTD92-02	Bedrock	31.4	1.2	30.7	1.3	6.6	0.4
PTD92-03	Bedrock	16.1	1.0	17.0	1.5	7.2	0.8
PTD92-04	Boulder	11.7	0.7	12.7	0.9	7.4	0.7
PTD92-05	Boulder	32.4	1.2	29.6	1.5	6.2	0.4
PTD92-07	Bedrock	10.9	0.8	10.1	1.2	6.3	0.9
PTD92-08	Bedrock	12.0	0.6	12.3	0.6	7.0	0.5
PTD92-09	Boulder	23.7	1.2	23.7	0.9	6.8	0.4
PTD94-01	Bedrock	22.4	0.9	19.4	0.9	5.9	0.4
PTD94-02	Bedrock	15.3	0.9	14.6	0.8	6.5	0.5
PTD94-03	Bedrock	11.1	0.9	10.8	0.5	6.6	0.6
PTD94-04	Bedrock	12.1	1.0	13.2	0.7	7.4	0.7
PTD94-05	Bedrock	12.6	0.6	13.3	0.7	7.1	0.5
PTD94-06	Boulder	No Data	No Data	12.9	0.7	No Data	No Data
PTD94-07	Bedrock	69.1	1.8	62.6	1.5	6.1	0.2
PTD94-08	Bedrock	10.3	1.0	11.9	0.5	7.8	0.8
PTD94-09a	Cobble	11.8	0.9	15.4	0.6	8.9	0.8
PTD94-09b	Cobble	10.1	1.0	11.9	0.5	8.0	0.9
PTD94-09c	Cobble	10.6	0.9	11.7	0.5	7.5	0.7
PTD94-10	Bedrock	14.2	0.9	15.1	0.8	7.2	0.6
PTD94-11a	Cobble	7.2	0.9	8.0	0.5	7.6	1.0
PTD94-11b	Cobble	9.4	0.9	9.9	0.5	7.1	0.8
PTD94-13	Boulder	10.5	1.0	11.4	0.5	7.4	0.8
PTD94-14	Bedrock	20.2	0.9	22.5	0.8	7.5	0.4
PTD94-15a	Cobble	6.3	0.8	7.6	0.4	8.2	1.1
PTD94-15b	Cobble	6.4	0.8	7.9	0.5	8.4	1.2
PTD94-15c	Cobble	6.8	0.9	8.3	0.4	8.3	1.1
PTD94-16	Bedrock	9.4	0.9	10.3	1.1	7.4	1.1
PTD94-17	Bedrock	10.6	1.0	No Data	No Data	No Data	No Data
PTD94-18a	Cobble	7.3	1.1	7.8	0.7	7.2	1.3
PTD94-18b	Cobble	10.7	1.0	12.3	0.8	7.8	0.9
PTD94-18c	Cobble	7.5	0.9	8.5	0.4	7.7	1.0

*Ages were calculated using the northeastern North American production rates of 3.93 ± 0.19 atoms g^{-1} yr^{-1} for ^{10}Be and 26.5 ± 1.3 atoms g^{-1} yr^{-1} for ^{26}Al (Balco et al., 2009) and the Lal (1991)/Stone (2001) scaling scheme in CRONUS. Ages have been scaled for elevation, sample density, sample thickness, latitude, and longitude. Location information as well as isotopic ratios and concentrations are included in the data repository.

†Ratios have been scaled from their original, measured values to reflect the new consensus values for the ^{10}Be standards (Nishiizumi et al., 2007) that were developed after these data were collected. Unscaled concentrations and ratios are included in the data repository.

Table 3. Concentrations and modeled exposure/burial history for the 29 samples for which multi-stage scenario modeling was conducted.

Sample Name	07KNSTD Elevation-Normalized and Holocene-Corrected ^{10}Be Concentration (atoms g^{-1})*	Elevation-Normalized and Holocene-Corrected ^{26}Al Concentration (atoms g^{-1})*	Holocene-Corrected 07KNSTD ^{26}Al/^{10}Be Ratio*	Modeled Minimum-Limiting Exposure Duration (yr)†	Modeled Minimum-Limiting Burial Duration (yr)	Modeled Minimum-Limiting Total History (yr)§
KM95-003	$2.66 \pm 0.06 \times 10^5$	$1.65 \pm 0.05 \times 10^6$	6.20 ± 0.24	$7.4 \pm 0.4 \times 10^4$	$1.4 \pm 0.8 \times 10^5$	$2.1 \pm 0.8 \times 10^5$
KM95-013	$1.32 \pm 0.22 \times 10^4$	$1.02 \pm 0.06 \times 10^4$	0.77 ± 0.13	$3.3 \pm 1.1 \times 10^4$	$4.5 \pm 0.4 \times 10^6$	$4.5 \pm 0.4 \times 10^6$
KM95-016	$5.73 \pm 0.12 \times 10^5$	$2.89 \pm 0.06 \times 10^6$	5.05 ± 0.15	$2.0 \pm 0.1 \times 10^5$	$5.1 \pm 0.6 \times 10^5$	$7.1 \pm 0.6 \times 10^5$
KM95-017	$1.13 \pm 0.03 \times 10^5$	$6.38 \pm 0.23 \times 10^5$	5.66 ± 0.26	$3.4 \pm 0.2 \times 10^4$	$3.5 \pm 0.9 \times 10^5$	$3.8 \pm 0.9 \times 10^5$
KM95-018	$2.31 \pm 0.09 \times 10^4$	$1.38 \pm 0.06 \times 10^5$	5.98 ± 0.34	$6.7 \pm 0.6 \times 10^3$	$2.5 \pm 1.2 \times 10^5$	$2.6 \pm 1.2 \times 10^5$
KM95-023	$2.18 \pm 0.36 \times 10^4$	$3.59 \pm 0.29 \times 10^4$	1.65 ± 0.30	$2.4 \pm 0.9 \times 10^4$	$2.9 \pm 0.4 \times 10^6$	$2.9 \pm 0.4 \times 10^6$
KM95-030	$3.93 \pm 0.87 \times 10^4$	$6.53 \pm 0.89 \times 10^3$	0.17 ± 0.04	$4.8 \pm 2.5 \times 10^5$	$7.5 \pm 0.5 \times 10^6$	$8.0 \pm 0.5 \times 10^6$
KM95-035	$6.02 \pm 0.29 \times 10^4$	$3.18 \pm 0.15 \times 10^5$	5.29 ± 0.35	$2.0 \pm 0.2 \times 10^4$	$5.0 \pm 1.4 \times 10^5$	$5.2 \pm 1.4 \times 10^5$
KM95-042	$1.80 \pm 0.19 \times 10^4$	$1.41 \pm 0.12 \times 10^4$	0.78 ± 0.11	$4.4 \pm 1.0 \times 10^4$	$4.5 \pm 0.3 \times 10^6$	$4.5 \pm 0.3 \times 10^6$
KM95-061	$2.37 \pm 0.23 \times 10^4$	$8.14 \pm 0.54 \times 10^4$	3.44 ± 0.40	$1.2 \pm 0.3 \times 10^4$	$1.4 \pm 0.2 \times 10^6$	$1.4 \pm 0.2 \times 10^6$
KM95-068	$1.73 \pm 0.07 \times 10^5$	$9.48 \pm 0.62 \times 10^5$	5.47 ± 0.42	$5.5 \pm 0.6 \times 10^4$	$4.1 \pm 1.6 \times 10^5$	$4.6 \pm 1.6 \times 10^5$
KM95-071	$3.35 \pm 0.16 \times 10^4$	$1.88 \pm 0.09 \times 10^5$	5.61 ± 0.39	$1.0 \pm 0.1 \times 10^4$	$3.8 \pm 1.4 \times 10^5$	$3.9 \pm 1.4 \times 10^5$
KM95-088	$1.38 \pm 0.18 \times 10^4$	$5.50 \pm 0.44 \times 10^4$	3.98 ± 0.61	$6.1 \pm 1.8 \times 10^3$	$1.1 \pm 0.3 \times 10^6$	$1.1 \pm 0.3 \times 10^6$
KM95-098	$1.27 \pm 0.17 \times 10^4$	$1.73 \pm 0.14 \times 10^4$	1.37 ± 0.21	$1.7 \pm 0.5 \times 10^4$	$3.3 \pm 0.3 \times 10^6$	$3.3 \pm 0.3 \times 10^6$
KM95-100	$5.72 \pm 0.33 \times 10^4$	$7.69 \pm 0.36 \times 10^4$	1.34 ± 0.10	$7.9 \pm 1.0 \times 10^4$	$3.3 \pm 0.2 \times 10^6$	$3.4 \pm 0.2 \times 10^6$
KM95-101	$7.11 \pm 0.34 \times 10^4$	$4.17 \pm 0.18 \times 10^5$	5.86 ± 0.38	$2.1 \pm 0.2 \times 10^4$	$2.8 \pm 1.3 \times 10^5$	$3.1 \pm 1.3 \times 10^5$
KM95-106	$3.86 \pm 0.10 \times 10^5$	$1.98 \pm 0.07 \times 10^6$	5.13 ± 0.21	$1.3 \pm 0.1 \times 10^5$	$5.0 \pm 0.8 \times 10^5$	$6.4 \pm 0.8 \times 10^5$
KM95-107	$5.04 \pm 0.13 \times 10^5$	$2.61 \pm 0.05 \times 10^6$	5.19 ± 0.17	$1.7 \pm 0.1 \times 10^5$	$4.7 \pm 0.6 \times 10^5$	$6.3 \pm 0.6 \times 10^5$
KM95-108	$3.49 \pm 0.11 \times 10^5$	$1.81 \pm 0.07 \times 10^6$	5.20 ± 0.25	$1.2 \pm 0.1 \times 10^5$	$4.8 \pm 1.0 \times 10^5$	$6.0 \pm 1.0 \times 10^5$
KM95-109	$3.04 \pm 0.08 \times 10^5$	$1.55 \pm 0.07 \times 10^6$	5.09 ± 0.26	$1.0 \pm 0.1 \times 10^5$	$5.4 \pm 1.0 \times 10^5$	$6.4 \pm 1.0 \times 10^5$
KM95-110	$5.53 \pm 0.27 \times 10^5$	$2.53 \pm 0.09 \times 10^6$	4.58 ± 0.27	$2.1 \pm 0.2 \times 10^5$	$7.0 \pm 1.1 \times 10^5$	$9.2 \pm 1.2 \times 10^5$
KM95-112	$4.87 \pm 0.13 \times 10^5$	$2.41 \pm 0.08 \times 10^6$	4.95 ± 0.21	$1.7 \pm 0.1 \times 10^5$	$5.6 \pm 0.8 \times 10^5$	$7.4 \pm 0.8 \times 10^5$
KM95-113	$1.31 \pm 0.12 \times 10^4$	$1.83 \pm 0.11 \times 10^4$	1.40 ± 0.15	$1.7 \pm 0.4 \times 10^4$	$3.3 \pm 0.2 \times 10^6$	$3.3 \pm 0.2 \times 10^6$
KM95-114	$1.50 \pm 0.17 \times 10^4$	$6.37 \pm 0.42 \times 10^4$	4.24 ± 0.56	$6.2 \pm 1.5 \times 10^3$	$9.7 \pm 2.7 \times 10^5$	$9.7 \pm 2.7 \times 10^5$
KM95-135	$1.24 \pm 0.11 \times 10^4$	$4.60 \pm 0.31 \times 10^4$	3.71 ± 0.41	$5.9 \pm 1.2 \times 10^3$	$1.2 \pm 0.2 \times 10^6$	$1.2 \pm 0.2 \times 10^6$
PTD92-05	$8.08 \pm 0.29 \times 10^4$	$4.98 \pm 0.24 \times 10^5$	6.16 ± 0.36	$2.4 \pm 0.2 \times 10^4$	$1.8 \pm 1.2 \times 10^5$	$2.0 \pm 1.2 \times 10^5$
PTD94-01	$4.87 \pm 0.20 \times 10^4$	$2.23 \pm 0.10 \times 10^5$	4.58 ± 0.29	$1.9 \pm 0.2 \times 10^4$	$8.0 \pm 1.3 \times 10^5$	$8.2 \pm 1.3 \times 10^5$
PTD94-02	$1.91 \pm 0.11 \times 10^4$	$9.29 \pm 0.47 \times 10^4$	4.87 ± 0.39	$6.8 \pm 0.9 \times 10^3$	$6.8 \pm 1.6 \times 10^5$	$6.8 \pm 1.6 \times 10^5$
PTD94-07	$2.40 \pm 0.06 \times 10^5$	$1.35 \pm 0.03 \times 10^6$	5.62 ± 0.20	$7.4 \pm 0.4 \times 10^4$	$3.5 \pm 0.7 \times 10^5$	$4.2 \pm 0.7 \times 10^5$

*Values are scaled to the 07KNSTD standard (Nishiizumi et al., 2007; for Be only), normalized to sea level, and corrected for the most recent period of exposure (11.7 ky).

†Refers to the pre-LGM history; values do not include the most recent period of exposure.

§Total history includes the modeled minimum-limiting exposure duration, the modeled minimum limiting burial duration, and the most recent period of exposure (11.7 ky).

Table 4. Recalculated single-isotope simple exposure ages and uncertainties as well as $^{26}Al/^{10}Be$ ratios and uncertainties for samples in Kaplan et al. (2001) and Kaplan and Miller (2003).

Sample Name	Sample Type	^{10}Be Simple Exposure Age (ka)*	^{10}Be Internal Uncertainty (ka)*	^{26}Al Simple Exposure Age (ka)*	^{26}Al Internal Uncertainty (ka)*	07KNSTD $^{26}Al/^{10}Be$ Ratio†	07KNSTD $^{26}Al/^{10}Be$ Ratio Uncertainty†
CM1	Bedrock	20.1	1.5	No Data	No Data	No Data	No Data
CM10C	Boulder	11.9	1.0	No Data	No Data	No Data	No Data
CM13	Bedrock	68.9	4.0	59.5	3.9	5.8	0.3
CM14	Boulder	72.4	5.6	No Data	No Data	No Data	No Data
CM15	Boulder	33.3	2.9	No Data	No Data	No Data	No Data
CM17	Bedrock	14.0	1.4	13.7	1.5	6.6	0.9
CM24	Bedrock	46.6	3.0	No Data	No Data	No Data	No Data
CM3	Bedrock	22.5	3.0	22.9	2.3	6.9	1.0
CM39	Bedrock	19.6	3.1	8.9	1.3	3.1	0.6
CM40	Bedrock	48.2	3.5	45.2	2.9	6.3	0.4
CM42	Bedrock	24.5	2.5	No Data	No Data	No Data	No Data
CM44	Bedrock	15.7	2.7	No Data	No Data	No Data	No Data
CM46	Bedrock	18.8	1.3	20.0	1.3	7.2	0.5
CM58	Bedrock	18.5	1.3	24.7	3.6	9.0	1.3
CM61	Bedrock	14.3	1.2	16.5	1.5	7.8	0.8
CM62	Bedrock	15.0	1.2	11.1	2.5	5.1	1.1
CM66	Bedrock	56.6	3.4	No Data	No Data	No Data	No Data
CM67	Bedrock	92.2	5.5	No Data	No Data	No Data	No Data
CM72	Bedrock	16.3	1.2	14.6	2.0	6.1	0.9
CM75	Bedrock	72.8	4.2	No Data	No Data	No Data	No Data
CM79	Boulder	14.9	1.3	No Data	No Data	No Data	No Data
CM7C	Boulder	14.5	1.2	13.7	1.7	6.4	0.9
CM80	Bedrock	14.5	2.0	16.1	2.7	7.5	1.6
CM84	Bedrock	14.2	1.3	13.5	2.1	6.5	1.1
CM9	Boulder	20.5	2.2	No Data	No Data	No Data	No Data

*Ages were calculated using the northeastern North American production rates of 3.93 ± 0.19 atoms g^{-1} yr^{-1} for ^{10}Be and 26.5 ± 1.3 atoms g^{-1} yr^{-1} for ^{26}Al (Balco et al., 2009) and the Lal (1991)/Stone (2001) scaling scheme in CRONUS. Ages have been scaled for elevation, sample density, sample thickness, latitude, and longitude. Further details are presented in Kaplan et al. (2001) and Kaplan and Miller (2003).

†Ratios have been scaled from their original, measured values to reflect the new consensus values for the ^{10}Be standards (Nishiizumi et al., 2007) that were developed after these data were collected.

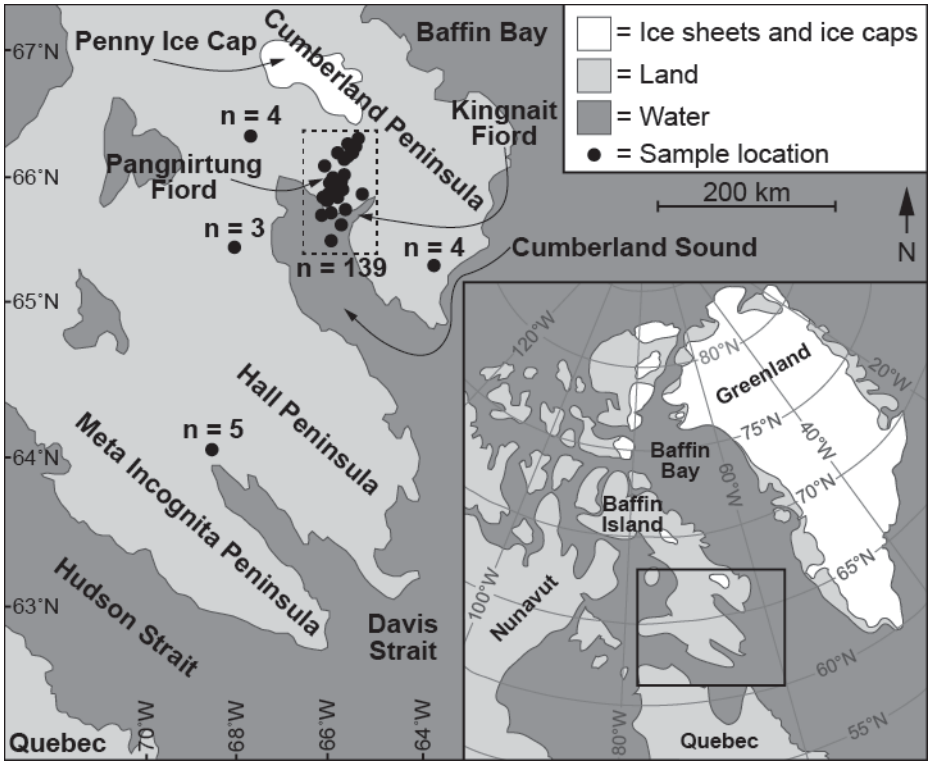

Figure 1. Map showing southern Baffin Island and the location of samples (n = 155 total). Inset shows the location of Baffin Island in the Arctic. Exact sample locations (latitude, longitude, and elevation) are included in the Data Repository (Table R1). Single isotope simple exposure ages and $^{26}Al/^{10}Be$ ratios are shown in Table 2.

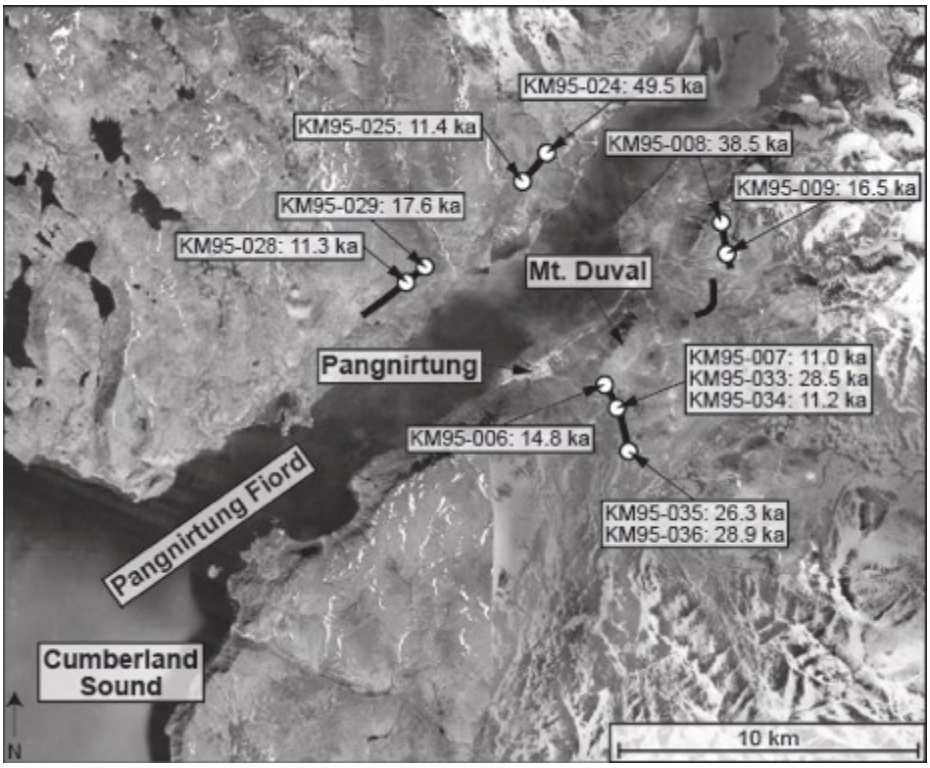

Figure 2. Map showing Pangnirtung Fiord and the Duval moraines (black lines). The type locality is the crest directly south of Mt. Duval, while other crests shown are considered to be equivalent. Sample locations (n = 12) are shown with white dots and denote ^{10}Be simple exposure ages. Additional chronological information (^{26}Al simple exposure ages and ^{26}Al/^{10}Be ratios) is included in Table 2.

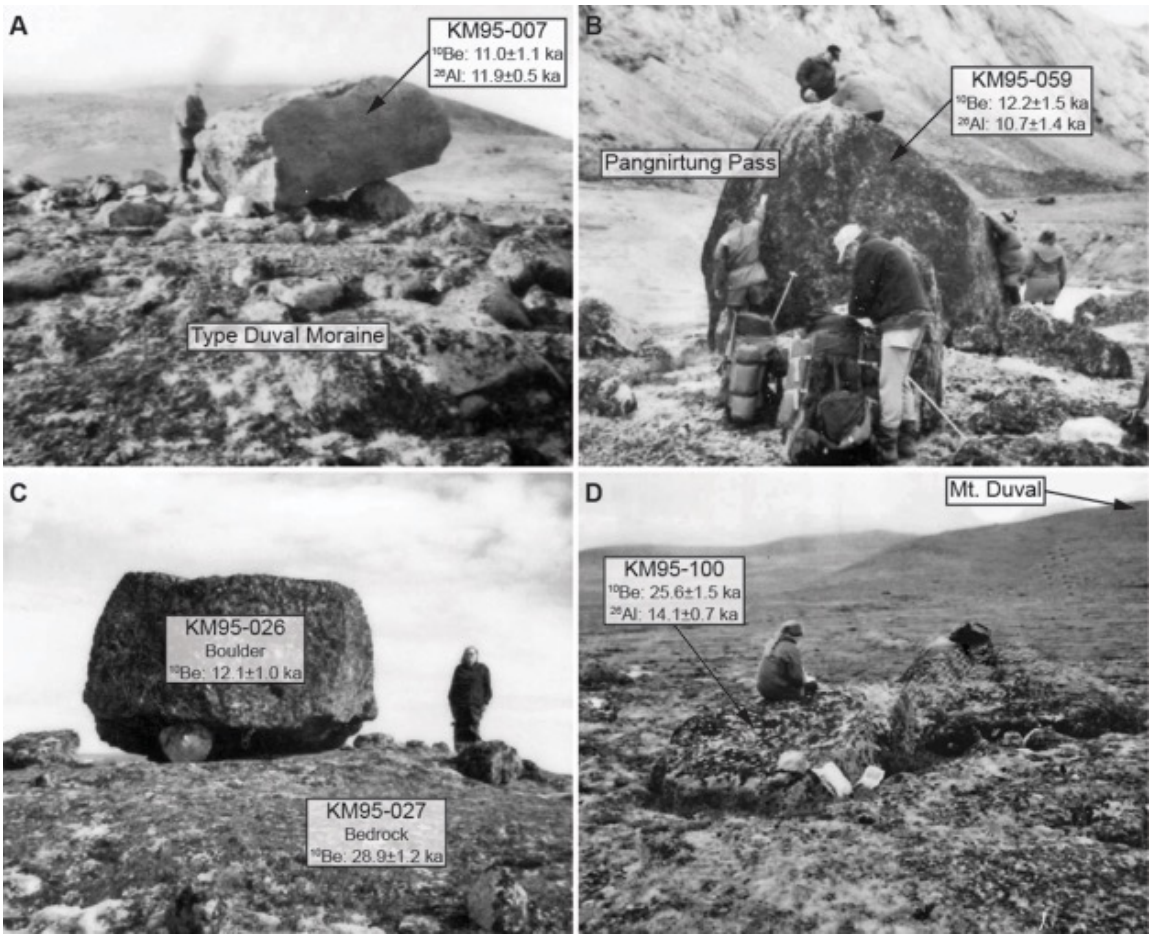

Figure 3. Photographs of selected samples discussed in the text. A: Boulder on type Duval moraine on the east side of Pangnirtung Fiord (specific location on Fig. 2). B: Boulder near the head of Pangnirtung Pass (specific location on Fig. 4). C: Bedrock/boulder pair on the west side of Pangnirtung Fiord (345 m asl). D: Boulder on the upland east of Pangnirtung (520 m asl).

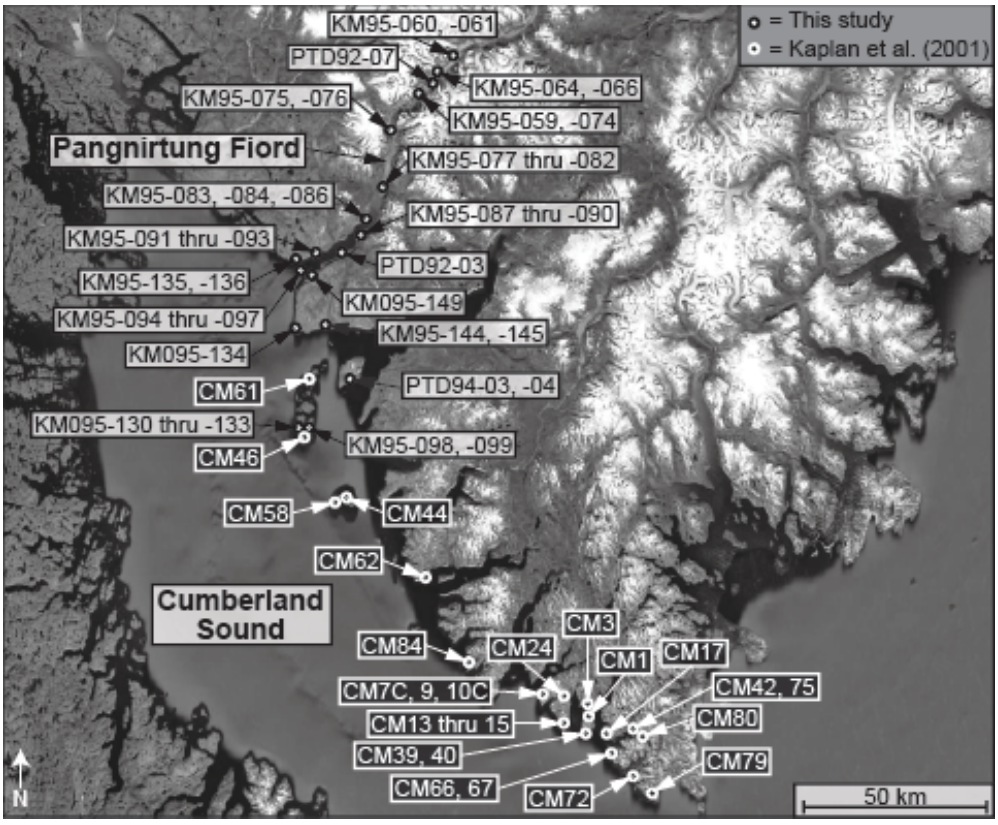

Figure 4. Map showing the location of samples from this study and from Kaplan et al. (2001) that may record the timing of deglaciation through Pangnirtung Fiord and Cumberland Sound. Exact sample locations (latitude, longitude, and elevation) are included in the Data Repository (Table R1). Chronologic information is presented in Table 2 for samples from this study and in Table 4 for samples from Kaplan et al. (2001).

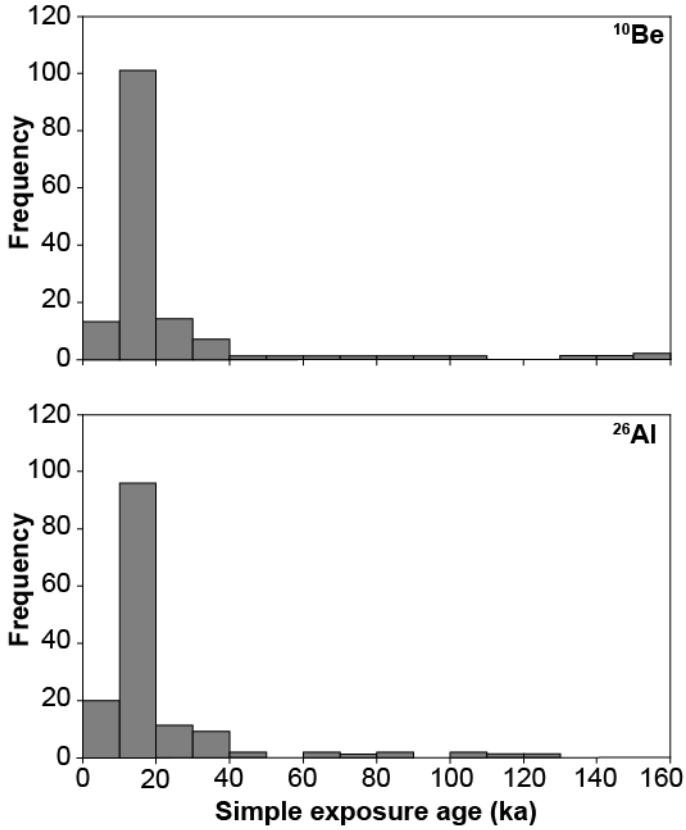

Figure 5. Histograms of ^{10}Be simple exposure ages (top, n = 152) and ^{26}Al simple exposure ages (bottom, n = 153) for all samples.

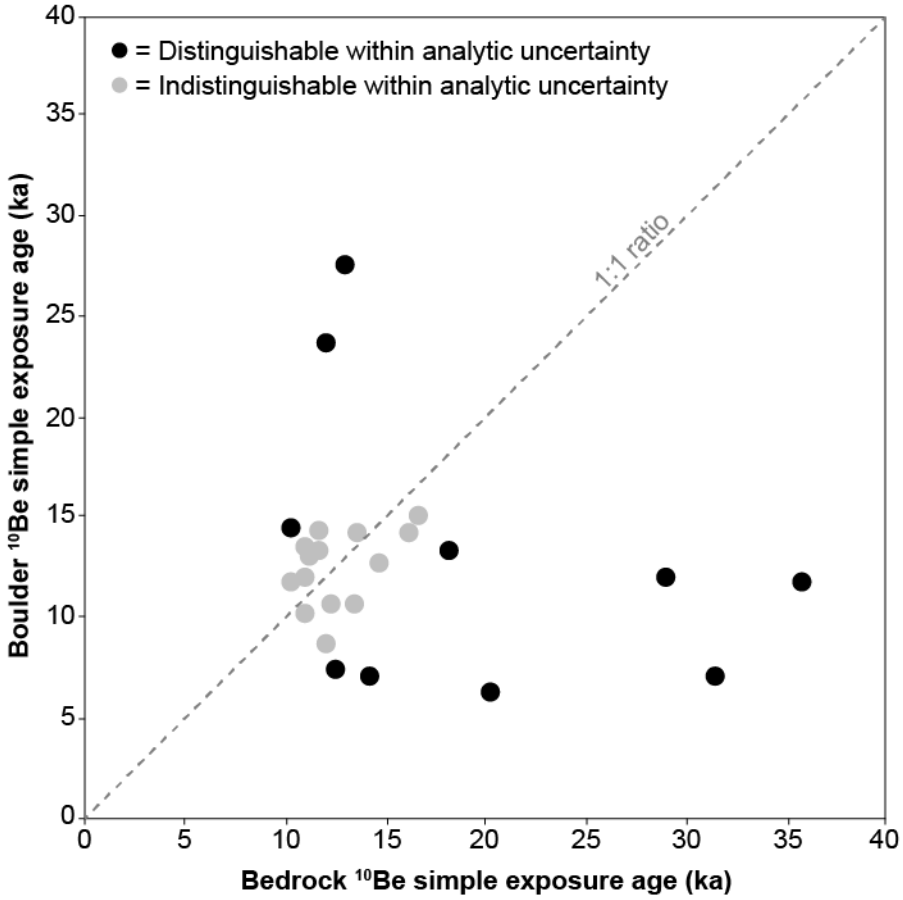

Figure 6. Regression of bedrock simple exposure ages versus boulder simple exposure ages for the 25 bedrock-boulder pairs in the dataset. Gray dots indicate pairs for which the bedrock and boulder ages are not separable within 1σ analytic uncertainties (n = 14). Black dots indicate pairs for which the bedrock and boulder ages are separable beyond 1σ analytic uncertainties (n = 11; note that one outlier, for which the bedrock age greatly exceeds the boulder age, is not shown here).

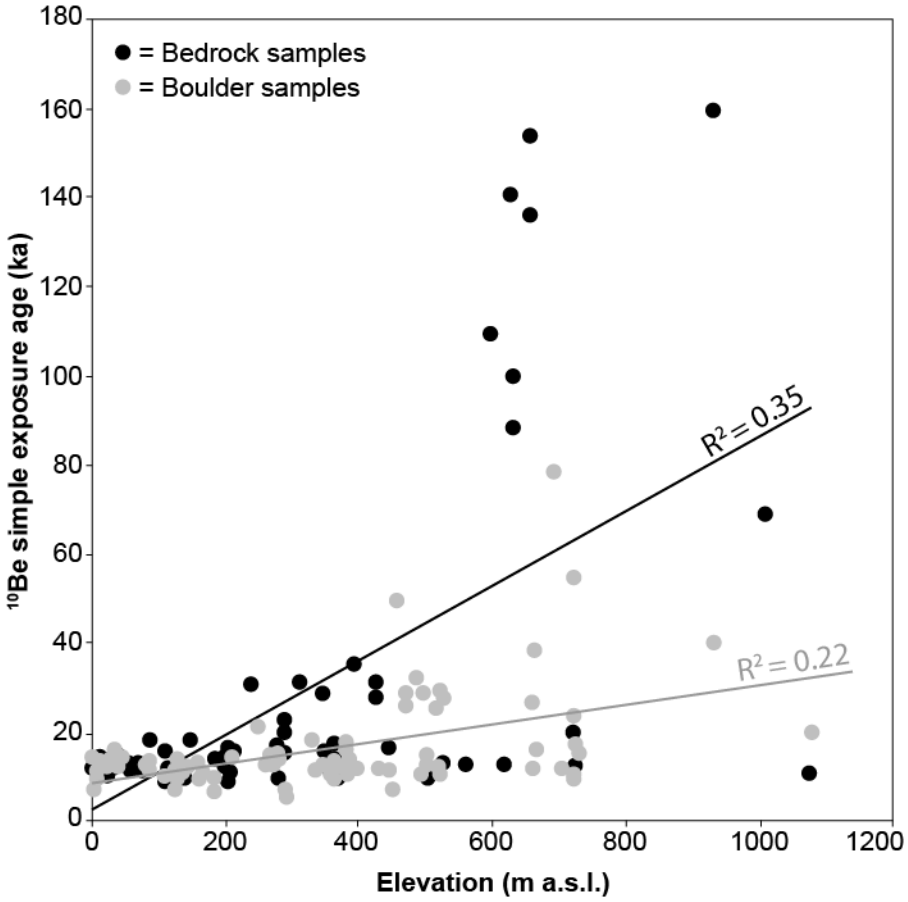

Figure 7. Regression of ^{10}Be simple exposure ages with elevation for all glacially-deposited samples with ^{10}Be data (n = 146). Black dots indicate bedrock samples (n = 64) and gray dots indicate boulder samples (n = 82).

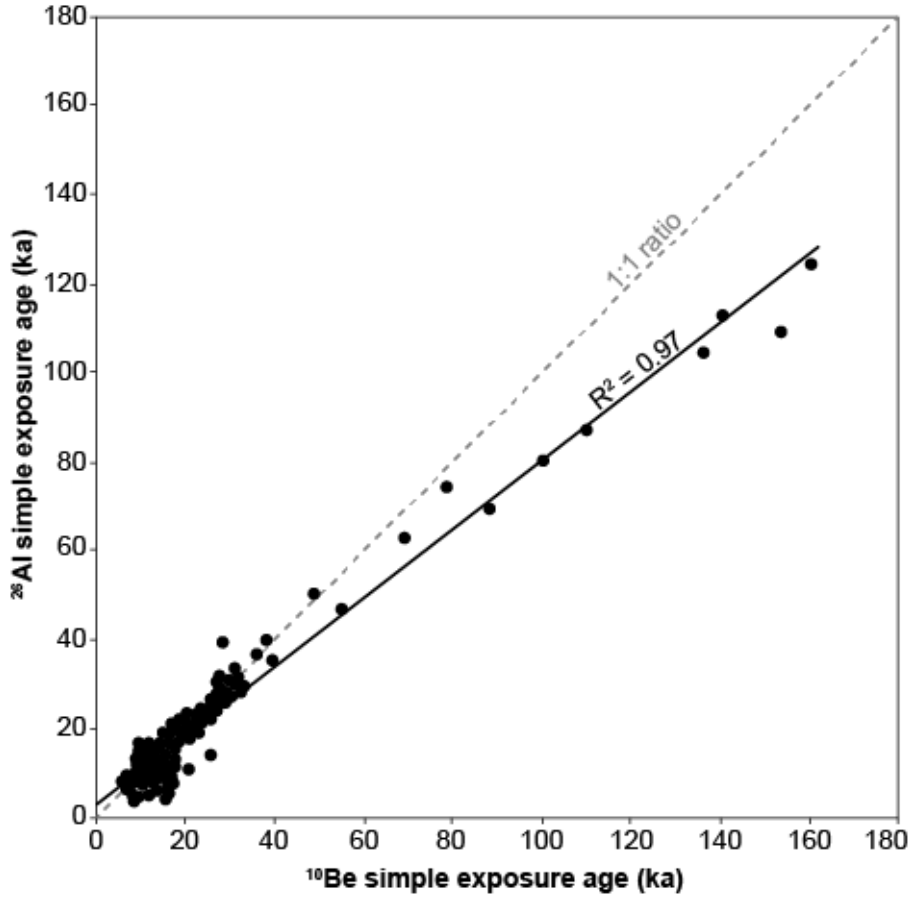

Figure 8. Regression of simple exposure ages calculated with ^{10}Be versus simple exposure ages calculated with ^{26}Al for both bedrock and glacially-deposited boulder samples (n = 144). Dashed gray line shows 1:1 relationship.

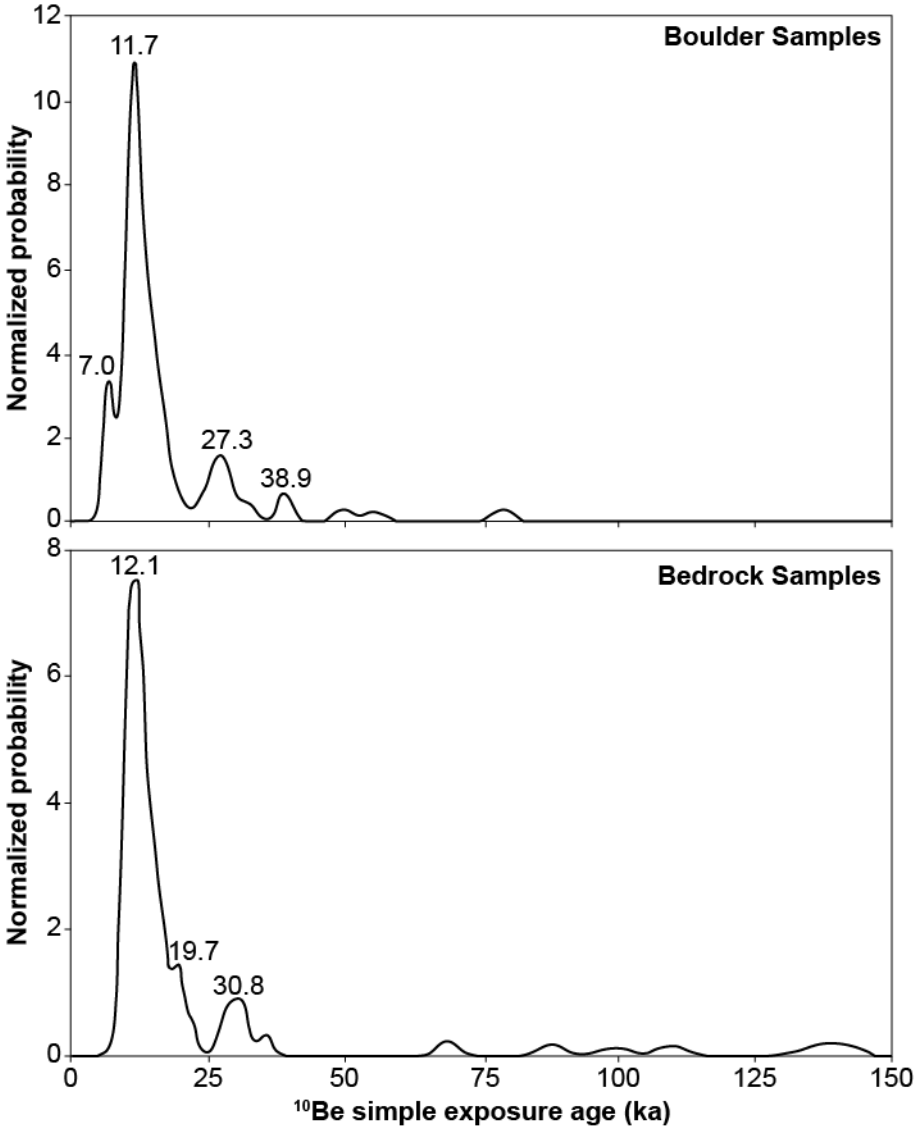

Figure 9. Probability density functions of simple ^{10}Be exposure ages of glacially deposited boulders (n = 82, top panel) and bedrock surfaces (n = 64, bottom panel) with ^{10}Be analyses. Thin gray lines represent the measured isotopic concentrations and internal uncertainties for each sample; thick black line represents the summed probability. Prominent peaks are labeled by age (in ka).

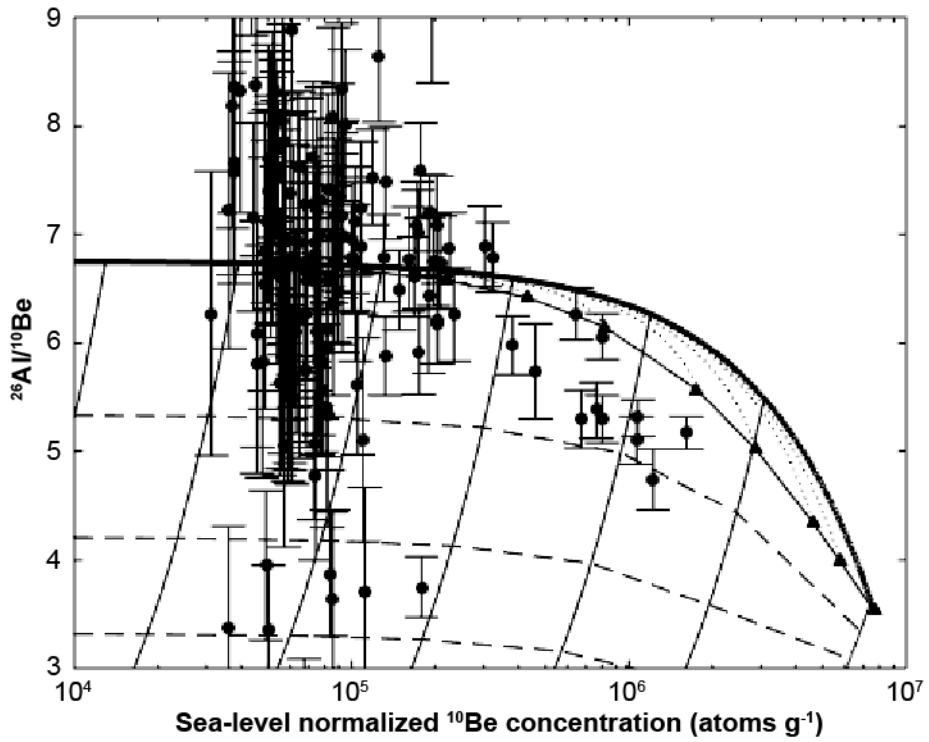

Figure 10. Measured ^{26}Al/^{10}Be ratios plotted against ^{10}Be concentrations (n = 144; normalized to 07KNSTD and sea level, not Holocene-corrected). Thick black line shows the constant exposure pathway. Dotted lines show erosion pathways of 25, 10, 5, 2, 1, 0.5, 0.2, and 0.1 m My^{-1}, from left to right. Black triangles show secular equilibrium endpoints for erosion scenarios as well as the constant exposure scenario. Burial paths are shown with thin lines, and burial isochrones (0.5, 1.0, and 1.5 My, from top to bottom) are shown with thin dashed lines. Several samples with ^{26}Al/^{10}Be ratios <3 (n = 1) or >9 (n = 2, Table 2) have been omitted for visualization.

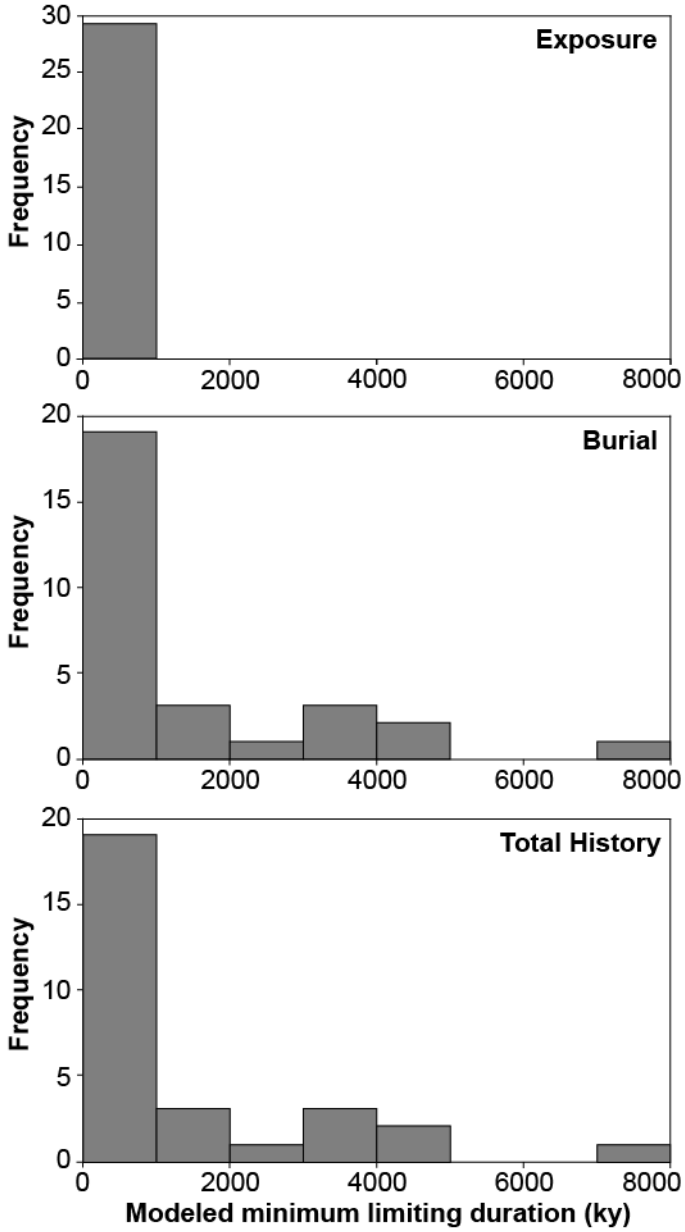

Figure 11. Histograms of minimum-limiting exposure durations (top), burial durations (middle), and total histories (bottom) calculated using 07KNSTD elevation-normalized ^{10}Be and ^{26}Al concentrations that have been corrected for the most recent period of exposure. Samples shown here (n = 29) met two criteria described further in the text: old simple exposure ages and corrected ratios indicative of burial.

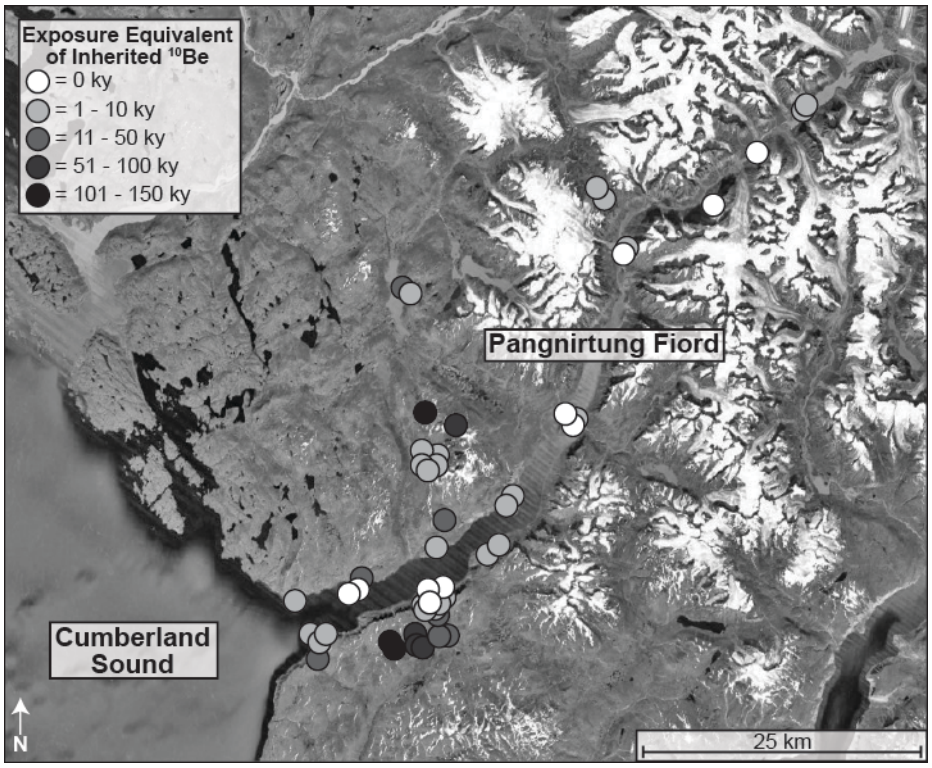

Figure 12. Spatial distribution of ^{10}Be data from bedrock samples in vicinity of Pangnirtung Fiord. Results are expressed as equivalent exposure durations, assuming a single period of exposure. We subtracted 11.7 ky of ^{10}Be (the assumed duration of most recent exposure) from all samples so that the values are indicative of nuclides inherited from previous periods of exposure.

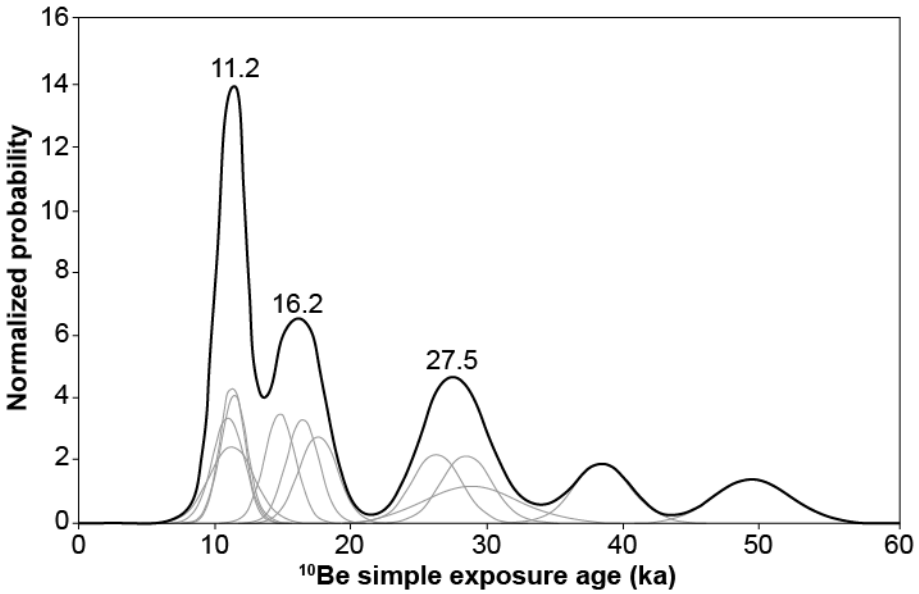

Figure 13. Probability density function showing simple ^{10}Be exposure ages of the 12 erratics from type Duval (n = 6) and equivalent (n = 6) moraines. Thin gray lines represent the measured isotopic concentrations and internal uncertainties for each sample; thick black line represents the summed probability. Prominent peaks are labeled by age (in ka).

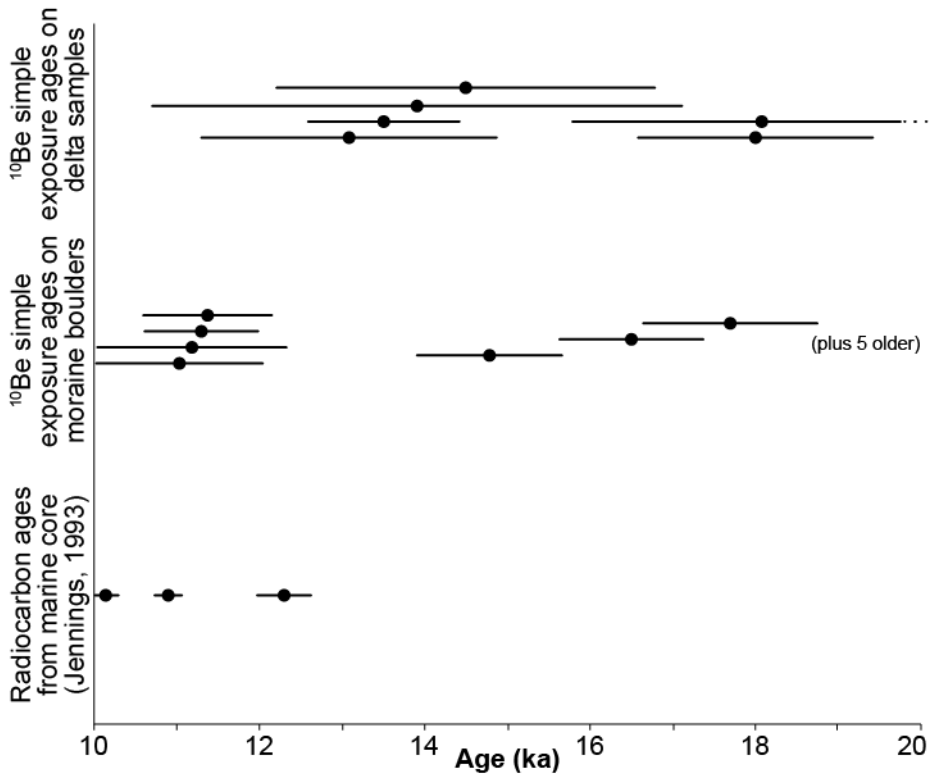

Figure 14. Existing age control for the type Duval and equivalent moraines and the 99 m a.s.l. glaciomarine delta from this study, as well as marine sediment cores from Cumberland Sound from Jennings (1993) and Jennings et al. (1996).

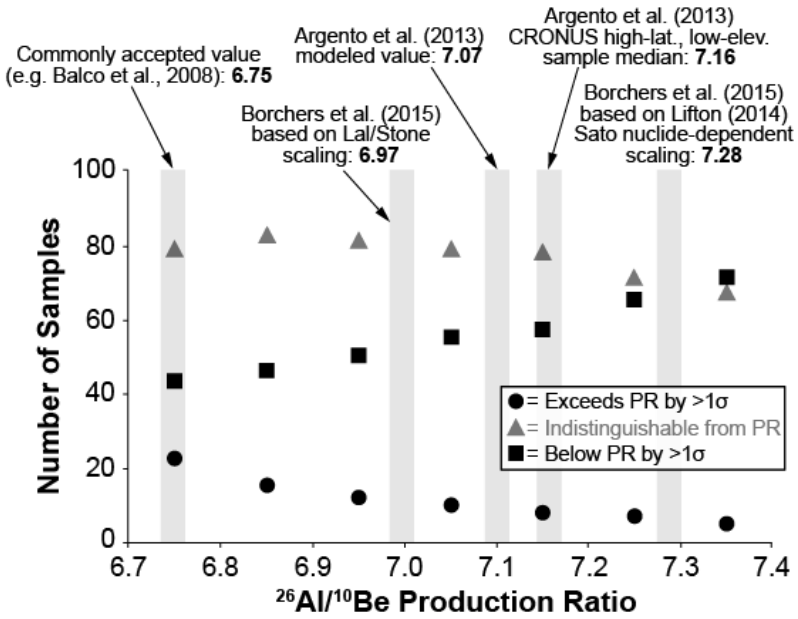

Figure 15. Sensitivity analysis investigating the effect of $^{26}Al/^{10}Be$ production ratio on inferred sample histories using seven different production ratios: 6.75, 6.85, 6.95, 7.05, 7.15, 7.25, and 7.35. Gray bars show possible $^{26}Al/^{10}Be$ production ratios from recent studies. Sample points are not corrected for the most recent period of exposure.

CHAPTER 5. METHODOLOGICAL DEVELOPMENT
(IN PRESS WITH QUATERNARY GEOCHRONOLOGY)

AN APPROACH FOR OPTIMIZING IN SITU COSMOGENIC ^{10}BE SAMPLE PREPARATION

Lee B. Corbett[a]*
Paul R. Bierman[a]
Dylan H. Rood[b,c]

*Contact author: Ashley.Corbett@uvm.edu, 802-380-2344
[a]Department of Geology and Rubenstein School of the Environment and Natural Resources, University of Vermont, Burlington VT 05405, USA
[b]Department of Earth Science and Engineering, Imperial College London, South Kensington Campus, London SW7 2AZ, UK
[c]Center for Accelerator Mass Spectrometry, Lawrence Livermore National Laboratory, Livermore CA 94550, USA

Abstract

Optimizing sample preparation for the isotopic measurement of ^{10}Be extracted from quartz mineral separates has a direct positive effect on the efficiency of sample production and the accuracy and precision of isotopic analysis. Here, we demonstrate the value of tracing Be throughout the extraction process (both after dissolution and after processing), producing pure Be (by optimizing column chromatography methods and quantifying quartz mineral separate purity), and minimizing backgrounds (through reducing both laboratory process blanks and ^{10}B isobaric interference). These optimization strategies increase the amount of ^{10}Be available for analysis during accelerator mass spectrometry (AMS), while simultaneously decreasing interference and contamination, and ensuring that sample performance matches standard performance during analysis. After optimization of our laboratory's extraction methodology, $^{9}Be^{3+}$ beam currents, a metric for sample purity and Be yield through the extraction process, matched the $^{9}Be^{3+}$ beam currents of AMS standards analyzed at the same time considering nearly 800 samples. Optimization of laboratory procedures leads to purer samples that perform better, more consistently, and more similarly to standards during AMS analysis, allowing for improved dating and quantification of Earth surface processes.

1. Introduction

Measurement of *in situ* produced cosmogenic ^{10}Be in geologic samples provides insight about a wide variety of geologic processes (Bierman and Nichols, 2004; Gosse and Phillips, 2001; Granger et al., 2013; Nishiizumi et al., 1993; von Blanckenburg and Willenbring, 2014). For example, quantifying ^{10}Be concentrations in moraine boulders (Heyman et al., 2011; Phillips et al., 1990) or previously-glaciated bedrock surfaces (Bierman et al., 1999) provides information about past glacial behavior, thus yielding valuable paleoclimatic insight (Balco, 2011; Fabel and Harbor, 1999). Cosmogenic ^{10}Be is useful for measuring displacement rates on fault systems by dating offset landforms (Bierman et al., 1995; Brown et al., 1998; Matmon et al., 2005; Rood et al., 2010). It can also be employed to study landscape erosion rates, both on outcrop scales (Nishiizumi et al., 1991; Nishiizumi et al., 1986) and basin scales (Bierman and Steig, 1996; Brown et al., 1995; Granger et al., 1996; von Blanckenburg, 2005), thereby providing insight about Earth's changing surface (Portenga and Bierman, 2011).

Cosmogenic ^{10}Be forms *in situ* when high-energy cosmic rays bombard rock in the upper-most few meters of Earth's surface (Lal, 1988). In the mineral quartz, ^{10}Be is produced primarily by spallation of oxygen at low rates, on the order of ~4 atoms g^{-1} quartz yr^{-1} at sea level and high latitude (Balco et al., 2008). Production of ^{10}Be in rock and soil is primarily dependent on latitude and elevation, and effectively ceases if the sample surface is buried to a depth of more than a few meters (for example, by glacial ice, sediment, or soil). ^{10}Be has a half-life of ~1.4 million years (Chmeleff et al., 2010; Korschinek et al., 2010; Nishiizumi et al., 2007). Therefore, while concentrations of ^{10}Be

initially increase in exposed rock over time, they eventually level off as production, erosion, and decay reach steady state.

Preparing and analyzing a sample for ^{10}Be measurement requires numerous steps. After a sample is collected, the mineral quartz is isolated from the other mineral phases through a series of physical and chemical processes (Kohl and Nishiizumi, 1992). The quartz is then dissolved in the presence of a ^{9}Be carrier solution, and Be is chemically isolated. To measure ^{10}Be, atoms of this rare isotope are counted in relation to the ion current of stable ^{9}Be via accelerator mass spectrometry, or AMS (Muzikar et al., 2003; Tuniz et al., 1998). Because isotopic fractionation can occur in the AMS, primary standards such as the 07KNSTD dilution series (Nishiizumi et al., 2007) are analyzed in association with samples. A correction factor for the measured versus the assumed ^{10}Be/^{9}Be ratio of primary standards is determined, then applied to samples analyzed at the same time.

The accuracy of sample measurement is controlled in part by the overall closeness of match between standards and samples. Developing a correction factor from standard ^{10}Be/^{9}Be ratios and using it to scale sample ^{10}Be/^{9}Be ratios relies upon the assumption that standards and samples behave similarly during measurement. Important characteristics may include matrix effects (e.g. accessory elements that could interfere with measurement; Hunt et al. (2008), Merchel et al. (2008)), cathode geometry (e.g. depth to the sputtering surface and shape of the surface; Hunt et al. (2007), Rood et al. (2010), Shanks and Freeman (2015)), total mass, and performance during measurement (the ion source yield, or "beam current", which we measure as the $^{9}Be^{3+}$ current but which can alternatively be measured as the $^{9}Be^{16}O^{-}$ current). The similarity of beam

currents between standards and samples across multiple measurement cycles is particularly important (Rood et al., 2014). Additionally, contamination of a sample with the isobar ^{10}B, above the ability of the detector to reject such interference, inhibits reliable detection of ^{10}Be and has the potential to degrade accuracy (Merchel et al., 2012).

The precision of low $^{10}Be/^{9}Be$ samples is primarily controlled by Poisson counting statistics, with greater numbers of ^{10}Be counts yielding more precise analyses. The total number of attainable counts is a product of the ^{10}Be concentration of the material being analyzed, the total mass of the sample, and the AMS total system efficiency (including ionization, transmission, transport, and detection efficiencies), all of which dictate the number of ^{10}Be counts that can be obtained before the sample material is ablated away during sputtering (Rood et al., 2013; Rood et al., 2010). For higher $^{10}Be/^{9}Be$ samples, precision is primarily controlled by the reproducibility of ratio measurements, which is often poorer than that predicted by counting statistics alone (Rood et al., 2013). For these higher $^{10}Be/^{9}Be$ samples that are limited by reproducibility rather than counting statistics, closeness of match to standards dictates precision in addition to accuracy (Rood et al., 2014). Background levels of ^{10}Be introduced during sample processing also control the precision of measured isotopic ratios, with relatively higher process blanks increasing the uncertainty of sample $^{10}Be/^{9}Be$ ratios especially in samples with little ^{10}Be, because background uncertainties are typically added in quadrature.

There are several reasons why it is advantageous to optimize the preparation of samples for ^{10}Be isotopic analysis. Ensuring that sample performance matches standard performance during AMS analysis likely increases the accuracy of sample measurements,

a prerequisite for accurate determination of dates and rates across a variety of applications. Increasing the precision of analyses enhances not only the interpretations that can be made from dates and rates, but also enables approaches involving multiple isotopic systems such as burial dating (Granger and Muzikar, 2001) and burial isochron dating (Balco and Rovey, 2008), and allows for improved calibration of cosmogenic nuclide production rates (Balco et al., 2009; Borchers et al., 2015; Briner et al., 2012; Putnam et al., 2010). Very low concentration samples, such as those from young exposures (Licciardi et al., 2009), rapidly eroding landscapes (Portenga et al., 2015), or long-buried sediments (Erlanger et al., 2012; Gibbon et al., 2014), require low detection limits to be measurable above background levels. High $^{9}Be^{3+}$ beam currents reduce the counting times required to achieve desired precisions, thereby speeding AMS throughput and better utilizing the limited beam time available for analysis.

This paper discusses optimization of the Be extraction procedure (Fig. 1) used at the University of Vermont, with the aim of increasing data accuracy and precision as well as the efficiency of sample preparation and AMS analysis. Our goal is to produce pure samples of Be that match the performance of standards, with particular focus on obtaining high Be yield, consistent $^{9}Be^{3+}$ beam currents, low $^{10}Be/^{9}Be$ background levels, and minimal isobaric interference. The optimization strategies discussed here are generalizable to other laboratories as well as to other AMS facilities.

2. Brief History of ^{10}Be Extraction and Measurement

Over time, different methods have been used to measure cosmogenic ^{10}Be. Initially, abundances of cosmogenic ^{10}Be were quantified by radioactive decay counting

after Be was isolated from silicate minerals by dissolution in acid (Fairhall, 1960). However, only samples with the highest ^{10}Be concentrations, for example those exposed at high elevations for long durations, could be measured. Later, it became possible to measure ^{10}Be/^{9}Be ratios via AMS (Lanford et al., 1980; Raisbeck et al., 1978; Southon et al., 1983; Thomas et al., 1981; Turekian et al., 1979), including on lower-energy AMS systems (Raisbeck et al., 1987). Be yields from chemical preparation were typically high (85-90%), but samples frequently retained impurities, especially Al (Lanford et al., 1980). At that time, precisions were generally 5-10%, and detection was limited to ^{10}Be/^{9}Be ratios greater than ~10^{-13} (Southon et al., 1983).

Although measurements of ^{10}Be became more common into the 1980's, average AMS beam currents remained relatively low (Klein and Middleton, 1984). By 1990, the quality of AMS measurements of ^{10}Be increased, and precisions of several percent were attainable (Suter, 1990). At around the same time, *in situ* ^{10}Be became a more widely used dating technique as AMS analysis improved and after it was confirmed that meteoric ^{10}Be produced in the atmosphere and adhered to the surface of grains could be removed from the grain coatings of a sample with repeated acid etches (Brown et al., 1991; Kohl and Nishiizumi, 1992; Nishiizumi et al., 1991; Nishiizumi et al., 1986; Nishiizumi et al., 1989). Adding column chromatography to the extraction protocol ensured that Be could be cleanly separated from other elements (Ditchburn and Whitehead, 1994; Tera et al., 1986).

Recent methodological advances have further increased the quality of AMS ^{10}Be measurements by improving beam currents. BeO had traditionally been mixed with Ag before being packing into cathodes for AMS analysis; however, using Nb instead of Ag

increased $^{9}Be^{3+}$ beam currents (Hunt et al., 2006; Merchel et al., 2008). It is uncertain whether impurities in the final Be fraction decrease AMS $^{9}Be^{3+}$ beam currents beyond dilution effects. Merchel et al. (2008) suggested that additions of Ti did not directly decrease $^{9}Be^{3+}$ beam currents, although the resulting dilution of Be did. However, Hunt et al. (2008) found that Al and Ti both depressed $^{9}Be^{3+}$ beam currents beyond the effects of dilution (although Ca, Fe, Mg, and Mn did not).

Detection limits have also improved over the past several decades. The discovery that commercial aluminum often contains non-negligible amounts of ^{10}Be occasioned the use of stainless steel and copper cathodes for sample analysis (Middleton et al., 1994), lowering backgrounds. Although commercially-available ^{9}Be carrier is commonly used, its $^{10}Be/^{9}Be$ ratio is $\sim10^{-14}$, which hinders the analysis of low-level samples. In contrast, ^{9}Be carriers made from deeply-mined phenakite (Be_2SiO_4) and beryl ($Be_3Al_2Si_6O_{18}$) often yield $^{10}Be/^{9}Be$ ratios two orders of magnitude lower (Merchel et al., 2008), which are better suited for the analysis of low-level samples. Experiments at Lawrence Livermore National Laboratory suggests that the AMS detection limit is now as low as ~1000 total ^{10}Be atoms in a sample (or ~10 ^{10}Be counts, assuming a 1% total AMS efficiency) as long as backgrounds are low, making it possible to obtain high-precision measurements on small samples or samples with little ^{10}Be (Rood et al., 2010). Samples with as few as several hundred ^{10}Be atoms g^{-1} quartz, the equivalent of less than 100 years of surface exposure at sea level and high latitude, can now be measured above background (Corbett et al., 2015).

3. Background and Study Design

In 2008, a new cosmogenic extraction laboratory was built at the University of Vermont. The laboratory was designed to maximize sample throughput, minimize isobaric ^{10}B interference, and provide a clean workspace so as to lower $^{10}Be/^{9}Be$ backgrounds. While developing the new laboratory space, we refined the sample preparation methodology that the laboratory had used for more than a decade (Hunt et al., 2008). The goal was to produce pure, high-yield samples of BeO that consistently performed similarly to standards during AMS analysis in order to maximize both accuracy and precision.

During the first half of 2009, we tested and refined sample processing procedures (Fig. 1). We focused on three parts of the procedure: tracing beryllium through the extraction process to maximize yield, improving column performance to generate high-purity Be, and reducing backgrounds to improve detection limits. From 2009-2012, five University of Vermont graduate students, three laboratory visitors, and a faculty member processed ~800 *in situ* ^{10}Be samples in the new laboratory using these modified procedures and then measured the samples by AMS at Lawrence Livermore National Laboratory. Here, we use data from these ~800 samples to make inferences about the effectiveness of methodological optimization following the guidance provided by Hunt et al. (2008).

We use $^{9}Be^{3+}$ beam currents of samples as our primary, first-order metric for quantifying sample performance during AMS analysis. For the sake of consistency between samples, which were counted between two and four separate times depending on the $^{10}Be/^{9}Be$ ratio and desired precision, we report the average $^{9}Be^{3+}$ beam current of the

first two 300-second counting cycles of each sample. We present both measured beam currents (μA) as well as normalized beam currents in order to remove run-to-run variability in AMS tuning and source performance. We normalized sample beam currents to the average beam current from the first run of all (both primary and secondary) standards on the same wheel. A normalized current of 1.0 indicates that the sample performed as well as the standards, a normalized current of less than 1.0 indicates that the sample did not perform as well as the standards, and a normalized current of greater than 1.0 indicates that the sample outperformed the standards.

Much of our analysis and discussion focuses on cation exchange column chromatography, which removes B and Ti and separates Be from Al (Clifford, 1999; Ochs and Ivy-Ochs, 1997). The rate at which Ti, Be, and Al elute through cation exchange columns depends on multiple factors including column geometry, resin type, resin mesh size, resin bed volume, and acid strength (Clifford, 1999). In our discussion of sample purity and column chromatography, we report both the total mass of the ions of interest (in μg) as well as their charge equivalents (in milli-equivalents, or meq, where one meq is equal to one milli-mol of charge). For example, for Al, which forms a +3 cation and has a molar mass of ~27 g mol^{-1}, 1000 μg Al is equivalent to 0.11 meq; for Ti, which forms a +4 cation but has a greater molar mass (~48 g mol^{-1}), 1000 μg Ti is equivalent to 0.08 meq.

4. Methods

4.1. Laboratory Design and Method Development

We optimized laboratory design to minimize background levels of ^{10}Be. Air is supplied to the laboratory by a dedicated air handler with three filtration stages (35% and 90% boron-free polypropylene filter media, followed by diffuser-mounted Ultra Low Particle (ULPA) filters made of synthetic material). Each fully exhausting laminar flow fume hoods draws ambient air from the laboratory; this air is 35% and ULPA filtered before entering the hoods and all lab air is exhausted rather than recirculated. Although the laboratory was not built to a specific cleanroom standard, particle tests run during operation indicate that laboratory air contains about 0.2 particles per cubic centimeter, consistent with a class 100 to class 1000 cleanroom. Only deionized water (17.3-17.7 Mohm) is supplied to the laboratory; before the water is used for dilution or washing, it is polished using Milli-Q deionization units equipped with boron-specific, Q-gard cartridges. We use two fully separate processing streams with dedicated labware and hood space to separate high-level samples ($^{10}Be/^{9}Be > 10^{-13}$) from low-level samples ($^{10}Be/^{9}Be < 10^{-13}$).

We also optimized laboratory design to minimize ambient boron levels. Fiberglass insulation was replaced by foam and rock wool, and prefabricated aluminum wall panels were used in place of sheetrock. We used water leaching to test all laboratory materials and, finding detectable boron in most paper and cardboard products, have minimized their use in the lab and in air filtration materials.

We designed the laboratory to have perchloric-acid compatible fume hoods with a washdown system. Post-dissolution high-temperature sample fuming with perchloric acid

breaks down insoluble fluoride compounds and evaporates residual fluorides (Ochs and Ivy-Ochs, 1997), which can negatively impact the cation column elution curve if they persist in samples.

To minimize acid consumption and speed throughput, we use 3 mL anion columns (Dowex 1X8 200-400 mesh resin, 1.2 meq mL^{-1}, total capacity = 3.6 meq) and 5 mL cation columns (Dowex 50WX8 200-400 mesh resin, 1.7 meq mL^{-1}, total capacity = 8.5 meq). We use double-fritted columns for both (Fig. 2); the second frit sits 1-2 mm above the resin bed and maintains a thin layer of solution between the top of the resin bed and the bottom of the second frit.

We repeatedly tested column performance before processing samples using quartz digests spiked with differing concentrations of additional Al and Ti. During the earlier tests, the goal was to determine the most effective way to separate the three elution peaks (Ti, Be, and Al) by experimenting with acid strength and elution volume, and collecting all of the eluted solution for Inductively-Coupled Plasma Optical Emission Spectrometry (ICP-OES) analysis (Fig. 3). To ensure that samples are Ti-free, we continue Ti elution until all Ti is removed, even if small amounts of Be (several percent of the total load) may be lost. We add hydrogen peroxide to the sample before column chromatography which stains the Ti red, providing a visual confirmation that it has been completely removed before Be elution begins (Clifford, 1999).

After optimizing the column elution procedure, later tests were targeted at determining the total cation load (charge equivalent) that the columns could handle by spiking quartz to various impurity levels and determining the threshold of column failure. Column failure occurred when elements eluted prematurely, contaminating the Be

fraction with both Ti and Al (Fig. 3). In our experiments, failure occurred at ~10% capacity, or ~0.85 meq for the cation columns. For Al (+3 charge, ~27 g mol^{-1} molar mass), this equates to 7,650 μg; for Ti (+4 charge, ~48 g mol^{-1} molar mass), this equates to 10,200 μg (however, actual quartz contains many different cations).

4.2. Quartz Purity and Sample Massing

Rock samples are crushed, ground, and sieved, while sediment samples are just sieved. To isolate quartz from other mineral phases, we use magnetic separation, repeated acid etches, and density separation if necessary (Kohl and Nishiizumi, 1992). After etching, 0.25 g aliquots of purified quartz are dissolved in concentrated HF and tested for purity with regard to major elements (Al, Ca, Fe, K, Mg, Na, and Ti) using a rapid ICP-OES method. Quartz with high impurity levels is re-etched for an additional week, then tested again.

We use quartz cation concentrations to decide how much sample can be dissolved without overloading the ion exchange columns. Because our experimentation has shown that cation column failure occurs at ~10% of the total resin capacity, we limit the amount of quartz we dissolve based on its purity such that we load only ~0.85 meq to our 5 mL cation columns. This is a conservative approach because perchloric acid treatments oxidize much of the Ti (Hunt et al., 2008), which is later removed by centrifugation. We use up to ~20 g of quartz for high-level samples ($^{10}Be/^{9}Be > 10^{-13}$) and up to ~40 g of quartz for low-level samples ($^{10}Be/^{9}Be < 10^{-13}$); these upper limits for quartz mass were chosen based on the capacity of the Teflon labware we use for dissolution and extraction.

To the quartz, we add 250 μg ^{9}Be via in-house made beryl-derived carrier solution. Additions of ^{27}Al (via SPEX Al standard) are determined based on the quantified native Al in the quartz, with the aim of having ~2000 μg Al in each sample. We digest samples in HF (~5 g HF per g quartz) over several days, increasing the digest temperature incrementally up to 135°C.

4.3. Blanks

Each batch of ten samples includes one blank and one CRONUS standard for high-level samples (^{10}Be/^{9}Be > 10^{-13}) and two blanks for low-level samples (^{10}Be/^{9}Be < 10^{-13}). We currently use ^{9}Be carrier made in-house by the flux fusion of beryl (Stone, 1998) for all samples; however, the earliest high-level samples had blanks of SPEX brand 1000 ppm ICP elemental standard. All of these process blanks as well as samples contain ~250 μg ^{9}Be.

4.4. Post-Dissolution Aliquots

Immediately following dissolution, we remove replicate aliquots directly from the HF digestion solution, quantifying the percentage of solution removed by mass. These aliquots represent ~2% and 4% of the total sample mass, respectively. To each aliquot we add a small amount of H_2SO_4 to ensure the aliquot does not reach dryness, evaporate the HF, and then add (by mass) a 1% H_2SO_4 solution spiked with Ga and Y to act as an internal standards and correct for instrument drift. We use these aliquots to quantify Be and Al at high precision (percent level) with ICP-OES, using multiple measurement lines for each element (Be, 234.861 and 249.473 nm; and Al, 308.215 and 309.271 nm).

4.5. Beryllium Isolation and Post-Processing Aliquots

Following removal of post-dissolution aliquots, we evaporate the remaining HF and fume the samples three separate times with perchloric acid at 230°C to break up and drive off fluoride compounds (Ochs and Ivy-Ochs, 1997). We then centrifuge samples to remove Ti and insoluble fluorides, convert samples to chloride form by fuming with and dissolving in HCl, and perform anion column chromatography to remove Fe. After anion column chromatography, we evaporate the HCl, convert samples to sulfate form, and perform cation column chromatography to remove B and Ti and separate Be from Al (Clifford, 1999; Ochs and Ivy-Ochs, 1997).

At the end of the extraction process and before hydroxide precipitation, we test the Be fraction for yield and purity by extracting small aliquots. Because we employ a volumetric dilution and a rapid ICP-OES method to speed the process, the precision of these data is less than that of the post-dissolution aliquots. Samples are then precipitated as Be hydroxide at pH ~8 (using methyl red, a liquid pH indicator), dried, converted to BeO using an air/wall gas flame, combined with Nb at a 1:1 molar ratio (Hunt et al., 2006), and packed into stainless steel cathodes for AMS analysis.

5. Results

5.1. Quartz Purity

Quartz purity varies appreciably between study sites. Of the 797 quartz samples tested during 2009-2012, the average total cation concentration was 333 ± 359 μg g^{-1} (1SD) in terms of mass, or 0.024 ± 0.038 meq g^{-1} (1SD) in terms of charge (Fig. 4). On average, almost half of this concentration is comprised of Al (119 ± 117 μg g^{-1}, or 0.013

± 0.013 meq g^{-1}, 1SD, Fig. 4). However, since Fe is removed during anion column chromatography, the effective total load during cation chromatography excludes Fe and averages 272 μg g^{-1} (0.021 meq g^{-1}).

5.2. Post-Dissolution Aliquots

Because samples have only been dissolved at the point we remove these aliquots and there is no mechanism for Be loss, post-dissolution aliquots should return 100% of the Be that was added to the sample through ^{9}Be carrier (plus any native ^{9}Be contained within the quartz).

Aliquot measurements of blanks yielded 100.7 ± 2.1 % (mean, n = 114, 1SD) of the expected Be based on the mass and concentration of ^{9}Be carrier added (Fig. 5a). This value suggests that our ICP-OES precision for Be measurements in this context is ~2% (1SD), which is greater than the uncertainty of individual ICP replicates (usually ≤ 1%) but similar to nominal precision of many AMS ^{10}Be analyses at present (Rood et al., 2013). Aliquot measurements of blanks are normally-distributed.

Aliquot measurements of samples are more variable than those of the blanks and have a long-tailed distribution skewed toward higher values. Quantification of Be in samples yielded an average of 100.8 ± 22.4 % (mean, n = 797, 1SD) of the expected Be based on the mass and concentration of ^{9}Be carrier added (Fig. 5b).

5.3. Post-Processing Aliquots

For the post-processing aliquots, Be yield should be 94% because 6% of the total sample is removed for the post-dissolution aliquots. For the process blanks, the measured

Be yield is 94.0 ± 3.6 % (mean, n = 114, 1SD, Fig. 6a) of the total Be based on the mass and concentration of ^{9}Be carrier added. For samples, the measured Be yield is 93.9 ± 21.6 % (mean, n = 797, 1SD, Fig. 6b) of the total. When considered in reference to the quartz that was dissolved, laboratory treatment of Be fractions decreased average total sample Al contents by 99.1%, Fe contents by 99.5%, and Ti contents by 99.9% (n = 797, Fig. 7).

5.4. Background ^{10}Be/^{9}Be Ratios

Measured isotopic ratios of process blanks reflect the type of carrier used in their preparation and the average ^{10}Be concentration of samples processed in the batches accompanying the blanks. Beryl blanks are lower ($5.6 \pm 3.2 \times 10^{-16}$, 1SD, n = 59) in the hood used to process low-level samples and higher ($9.0 \pm 8.9 \times 10^{-16}$, 1SD, n = 29) in the hood used to process high-level samples (Fig. 8). When assessed in an unequal variance Student's T-Test, beryl blank ratios between the two hoods are statistically separable (p = 0.004). SPEX carrier blanks in the high-level hood have an average ratio more than an order of magnitude higher than beryl blanks in the same hood ($1.2 \pm 0.1 \times 10^{-14}$, 1SD, n = 19, Fig. 8). When assessed in an unequal variance Student's T-Test, the ratios of the SPEX blanks and the beryl blanks processed in the same hood are statistically separable ($p < 0.001$).

For beryl blanks processed in the low-level hood, the standard deviation of the 59 different measurements (57%) is larger than the average measurement uncertainty (36%). For beryl blanks processed in the high-level hood, the discrepancy between the standard deviation of the 29 measurements (82%) and the average measurement uncertainty (29%) is greater. For SPEX blanks processed in the high-level hood, the standard deviation of

the 19 measurements (4%) is less than the average measurement uncertainty (7%), although both values are appreciably smaller than for beryl blanks because there are more ^{10}Be counts resulting in more precise data. Over time (2009-2012), there appears to be no trend in process blank $^{10}Be/^{9}Be$ ratios (Fig. 9).

5.5. Sample Beam Currents

The AMS $^{9}Be^{3+}$ beam currents of samples were consistent for samples processed during 2009-2012 (Fig. 10). The average beam current for samples was 21.4 ± 3.8 μA (1 SD, n = 797). The beam current normalized to standards run with these samples averaged 1.0 ± 0.2 (1 SD, n = 797). Quartz purity (expressed as total cation load) is not significantly related to normalized sample $^{9}Be^{3+}$ beam current ($R^2 = 0.004$, $p = 0.066$) indicating that our optimized laboratory methods are able to compensate for a wide range of initial quartz impurity concentrations.

Analysis of $^{9}Be^{3+}$ beam currents also indicates that the methods we describe here yield more predictable sample performance than those used previously in the University of Vermont cosmogenic nuclide laboratory. A previous assessment of data quality by Hunt et al. (2008) showed a greater range of beam currents, yielding a relative standard deviation of ~40% (n = 63). The beam current data we show here have a relative standard deviation of 18% (n = 797).

6. Discussion

6.1. Tracing Beryllium Through the Extraction Process

Tracing Be throughout the extraction process provides insight about the samples at two steps. Analysis of post-dissolution aliquots (Fig. 5) quantifies if any native ^{9}Be is present in the quartz (Portenga et al., 2015), while analysis of post-processing aliquots (Fig. 6) serves as a quality control metric to assess final Be yield and ensure that all samples have consistent Be mass (Hunt et al., 2008). Rare departures from the expected values for these two parameters may indicate the need for corrections, either accounting for native ^{9}Be in the data reduction or identifying and remediating sources of Be loss.

For the post-dissolution aliquots (Fig. 5), which should return 100% of the expected Be based on carrier addition, the few samples more than 2% (the 1SD precision of our analyses based on the performance of the blanks) below the central tendency likely reflect massing errors or ICP-OES interferences from rare accessory elements in quartz. Samples more than 2% (1SD, based on analysis of blanks) above the central tendency are those in which the quartz likely contained native ^{9}Be. For the post-processing aliquots (Fig 6), which should return 94% Be yield, samples considerably below 94% may be a result of laboratory error (for example, spilling a sample) and/or limitations during measurement such as interfering peaks. Samples falling considerably above 94% Be yield likely indicate the presence of ^{9}Be in quartz, which can be verified by cross-checking against the higher-precision post-dissolution aliquot measurements.

Be tracing unambiguously demonstrates the presence of native ^{9}Be in some purified quartz mineral separates (Figs. 5b and 6b) and allows the mass of native ^{9}Be to be incorporated in the calculation of ^{10}Be concentrations derived from the measured

$^{10}Be/^{9}Be$ ratio. Although our ability to detect small amounts (few μg) of native Be is limited by the overall precision of ICP-OES analysis (~2% for the post-dissolution aliquots, as described above), such small additions of native Be are less important as they do not change calculated ^{10}Be concentrations beyond the precision of the AMS measurements. Because the method we use can reliably detect larger amounts (> 10 μg) of native Be, an amount which begins to impact the resulting data at the several percent level, we can correct for its presence. Considering the dataset assessed here (Fig. 5b), 56 of the 797 samples (or ~7% of the population) exceed the expected Be measurement by 2 SD (4%) and 38 of the 797 samples (or ~5% of the population) exceed the expected Be measurement by 3 SD (6%).

Failing to identify and correct for native Be in those samples for which quartz contributes more than a few μg of Be will cause errors in the calculation of ^{10}Be concentration and thus in the inferred erosion rates, exposure ages, and dual isotope ratios. For example, in a suite of 49 samples from Bhutan prepared at University of Vermont, most samples contained detectable native ^{9}Be (Portenga et al., 2015). Approximately 240 μg of ^{9}Be carrier was added to each of the Bhutan samples as a spike; however, ICP-OES analysis of aliquots demonstrated that samples contained 244-1158 μg total ^{9}Be, indicating native ^{9}Be loads of as much as 900 μg per sample and native ^{9}Be concentrations in quartz as high as 38 μg g^{-1} (see Figure 3 in Portenga et al. (2015)). These native ^{9}Be concentrations are as much as 4-5 times greater than the amount of ^{9}Be carrier added. The source of this native Be may include beryl crystals, fluid inclusions in quartz grains, and/or structural substitution in quartz grains (Grew, 2002). Failure to

detect and correct for this native ^{9}Be would have caused erosion rate overestimates of as much as 400% (Portenga et al., 2015).

Post-processing aliquots (Fig. 6) serve as a quality check at the end of the extraction procedure to verify that samples are ready for AMS analysis and provides quality control in a laboratory where many different people each year are preparing samples. Quantifying the Be yield determines if enough Be is present for a successful AMS measurement. If sufficient Be is not present in the sample, the Ti fraction is analyzed by ICP-OES; in this case (which has happened only once when elution acid was incorrectly mixed), the missing Be eluted through the cation column early and was recovered by reprocessing the Ti fraction.

6.2. Producing Pure Beryllium

Creation of high-purity Be fractions ensures that samples will perform similarly to the standards during AMS analysis and provides a constant mass of material to load into cathodes. We demonstrate here that Be purity can be maximized by improving and calibrating/verifying column chromatography methods, tailoring the mass of quartz so as not to overload the columns, and verifying purity via quality control post-processing aliquots (Fig. 7). Constant ^{9}Be mass results in a uniform depth to the material surface and a consistent mixing ratio with Nb, which optimizes the ionization yield, the AMS sputtering efficiency, and the measurement reproducibility (Rood et al., 2010) for sputter sources using front-loaded cathodes.

Optimized column methodology improves data quality and reduces the time needed to make AMS measurements. After cation column chromatography, post-

processing aliquots show that Be fractions are consistently free of impurities (Fig. 7), contain virtually all of the original Be (Fig. 6), and that the resulting $^{9}Be^{3+}$ beam current is not related to the purity of the quartz. Even in small concentrations, Ti is thought to diminish $^{9}Be^{3+}$ beam currents beyond the dilution effects (Hunt et al., 2008). If Al, Fe, or Ti are present at greater than trace levels (>100 μg for Al, Fe, and Ti) in the post-column Be fraction, which occurs only rarely, the Be fraction can be neutralized, precipitated, re-dissolved, and cycled through anion and/or cation columns a second time to remove remaining impurities. We are unable to definitively address the impact of Ti on $^{9}Be^{3+}$ beam currents with our dataset since we have successfully removed Ti from the samples described here (Fig. 7) and hence do not have a range of Ti values over which to assess resulting beam currents.

The double-fritted column configuration (Fig. 2) has several benefits. The second frit prevents the column from drying out during the elution process, thereby avoiding channeling which can allow solution to bypass the resin. In addition, the second frit ensures that the resin bed is not disturbed while adding solutions, allowing the column steps to be performed in a more time-efficient and reproducible manner; cation column chromatography on a batch of 12 samples can be performed in 3-4 hours. These double-fritted columns have successfully been regenerated and re-used for several years (more than 50 batches of samples) by stripping them with acid, flushing them with water, and storing them fully saturated in water between uses. Over that time, there has been no change in column performance or blank values.

6.3. Reducing Backgrounds to Improve Detection Limits

Backgrounds are an important control on the accuracy and precision of ^{10}Be analyses, especially for samples with low ^{10}Be/^{9}Be ratios. Improved AMS techniques now consistently produce machine blanks with ^{10}Be/^{9}Be ratios well below 10^{-15} (Rood et al., 2010), placing greater demands on processing laboratories to both minimize sample cross-talk and lower the amount of the interfering isobar, ^{10}B.

Using beryl carrier and processing low-level samples in a separate fully-exhausting laminar flow hood with dedicated labware resulted in blanks almost two orders of magnitude lower than using commercial carrier (Figs. 8 and 9). The methodology described here routinely achieves blanks with ^{10}Be/^{9}Be ratios in the mid 10^{-16} level, allowing samples with ratios in the low 10^{-15} level to be measured. Decreasing the detection limits of ^{10}Be analysis by AMS opens new frontiers for the types of samples that can be studied. In particular, having lower detection limits enables the analysis of samples with little ^{10}Be, including those that are very young (Licciardi et al., 2009), those that have been subjected to rapid erosion (Portenga et al., 2015), or those that have been buried for long durations (Erlanger et al., 2012; Gibbon et al., 2014).

7. Conclusions

Analysis of quality control data associated with ~800 ^{10}Be samples prepared at the University of Vermont and measured at Lawrence Livermore National Laboratory shows that methodological optimization can yield samples that perform consistently and similarly to standards during AMS analysis. While data accuracy and precision are, to some extent, controlled by design, performance, and operation of the AMS, both are also

influenced by the chemistry and sample preparation performed by cosmogenic extraction laboratories. We demonstrate that methodological optimization aimed at maximizing Be yield, while minimizing contaminants and background levels of ^{10}Be and ^{10}B, can increase data accuracy and precision and lower detection limits (although replicate analyses of internal geologic standards could further assess accuracy and precision of the chemical methods we employ here). Methodological optimization also helps to identify and address problematic samples, such as those containing native Be or high concentrations of accessory cations, and improves time efficiency of laboratory methods and AMS analysis. Such enhancements in data quality and efficiency can open new frontiers for the scientific questions that can be addressed with *in situ* produced ^{10}Be.

Acknowledgements

Method development and sample analyses described here were supported by the National Science Foundation (especially ARC-1023191 and ARC-0713956 to Bierman and EAR-0948350 to Rood) and the University of Vermont. Corbett was supported by a National Science Foundation Graduate Research Fellowship and a Doctoral Dissertation Research Improvement Grant (BCS-1433878). We thank L. Reusser for assistance with method development, the staff of CAMS-LLNL for assistance in making ^{10}Be measurements, and two anonymous reviewers for improving the manuscript.

References

Balco, G., 2011. Contributions and unrealized potential contributions of cosmogenic-nuclide exposure dating to glacier chronology, 1990-2010. Quaternary Science Reviews 30, 3-27.

Balco, G., Briner, J., Finkel, R., Rayburn, J., Ridge, J., Schaefer, J., 2009. Regional beryllium-10 production rate calibration for late-glacial northeastern North America. Quaternary Geochronology 4, 93-107.

Balco, G., Rovey, C., 2008. An isochron method for cosmogenic-nuclide dating of buried soils and sediments. American Journal of Science 308, 1083-1114.

Balco, G., Stone, J., Lifton, N., Dunai, T., 2008. A complete and easily accessible means of calculating surface exposure ages or erosion rates from ^{10}Be and ^{26}Al measurements. Quaternary Geochronology 3, 174-195.

Bierman, P., Gillespie, A., Caffee, M., 1995. Cosmogenic ages for earthquake recurrence intervals and debris flow fan deposition, Owens Valley, California. Science 270, 447-450.

Bierman, P., Marsella, K., Patterson, C., Davis, P., Caffee, M., 1999. Mid-Pleistocene cosmogenic minimum-age limits for pre-Wisconsinan glacial surfaces in southwestern Minnesota and southern Baffin Island: a multiple nuclide approach. Geomorphology 27, 25-39.

Bierman, P., Nichols, K., 2004. Rock to sediment- slope to sea with ^{10}Be- rates of landscape change. Annual Review of Earth and Planetary Sciences 32, 215-255.

Bierman, P., Steig, E., 1996. Estimating rates of denudation using cosmogenic isotope abundances in sediment. Earth Surface Processes and Landforms 21, 125-139.

Borchers, B., Marrero, S., Balco, G., Caffee, M., Goehring, B., Lifton, N., Nishiizumi, K., Phillips, F., Schaefer, J., Stone, J., 2015. Geological calibration of spallation production rates in the CRONUS-Earth project. Quaternary Geochronology doi:10.1016/j.quageo.2015.01.009.

Briner, J., Young, N., Goehring, B., Schaefer, J., 2012. Constraining Holocene ^{10}Be production rates in Greenland. Journal of Quaternary Science 27, 2-6.

Brown, E., Bourles, D., Raisbeck, G., Yiou, F., Burchfiel, B., Molnar, P., Qidong, D., Jun, L., 1998. Estimation of slip rates in the southern Tien Shan using cosmic ray exposure dates of abandoned alluvial fans. Geological Society of America Bulletin 110, 377-386.

Brown, E., Edmond, J., Raisbeck, G., Yiou, F., Kurz, M., Brook, E., 1991. Examination of surface exposure ages of Antarctic moraines using in situ produced ^{10}Be and ^{26}Al. Geochimica et Cosmochimica Acta 55, 2269-2283.

Brown, E., Stallard, R., Larsen, M., Raisbeck, G., Yiou, F., 1995. Denudation rates determined from the accumulation of in situ-produced ^{10}Be in the Luquillo Experimental Forest, Puerto Rico. Earth and Planetary Science Letters 129, 193-202.

Chmeleff, J., Von Blanckenburg, F., Kossert, K., Jakob, D., 2010. Determination of the ^{10}Be half-life by multicollector ICP-MS and liquid scintillation counting. Nuclear Instruments and Methods in Physics Research Section B: Beam Interactions with Materials and Atoms 268, 192-199.

Clifford, D., 1999. Ion-exchange and inorganic adsorption, Water Quality and Treatment: A Handbook of Community Water Supplies. American Water Works Association, McGraw-Hill, New York.
Corbett, L., Bierman, P., Neumann, T., Graly, J., 2015. Inferring glacial history and subglacial process through analysis of cosmogenic nuclides in icebound cobbles. American Geophysical Union Fall Meeting Abstract ID C11A-0745.
Ditchburn, R., Whitehead, N., 1994. The separation of ^{10}Be from silicates, 3rd Workshop of the South Pacific Environmental Radioactivity Association, pp. 4-7.
Erlanger, E., Granger, D., Gibbon, R., 2012. Rock uplift rates in South Africa from isochron burial dating of fluvial and marine terraces. Geology 40, 1019-1022.
Fabel, D., Harbor, J., 1999. The use of in-situ produced cosmogenic radionuclides in glaciology and glacial geomorphology. Annals of Glaciology 28, 103-110.
Fairhall, A., 1960. The Radiochemistry of Beryllium, Nuclear Science Series. National Academy of Sciences and National Research Council, Washington, DC.
Gibbon, R., Pickering, T., Sutton, M., Heaton, J., Kuman, K., Clarke, R., Brain, C., Granger, D., 2014. Cosmogenic nuclide burial dating of hominin-bearing Pleistocene cave deposits at Swartkrans, South Africa. Quaternary Geochronology 24, 10-15.
Gosse, J., Phillips, F., 2001. Terrestrial in situ cosmogenic nuclides: theory and application. Quaternary Science Reviews 20, 1475-1560.
Granger, D., Kirchner, J., Finkel, R., 1996. Spatially averaged long-term erosion rates measured from in situ-produced cosmogenic nuclides in alluvial sediment. The Journal of Geology 104, 249-257.
Granger, D., Lifton, N., Willenbring, J., 2013. A cosmic trip: 25 years of cosmogenic nuclides in geology. Geological Society of America Bulletin 125, 1379-1402.
Granger, D., Muzikar, P., 2001. Dating sediment burial with in situ-produced cosmogenic nuclides: theory, techniques, and limitations. Earth and Planetary Science Letters 188, 269-281.
Grew, E., 2002. Beryllium in metamorphic environments (emphasis on aluminous compositions), in: Grew, E. (Ed.), Volume 50: Beryllium: Mineralogy, Petrology, and Geocheminstry. Mineralogical Society of America, Chantilly, Virginia, p. 690.
Heyman, J., Stroeven, A., Harbor, J., Caffee, M., 2011. Too young or too old: Evaluating cosmogenic exposure dating based on an analysis of compiled boulder exposure ages. Earth and Planetary Science Letters 302, 71-80.
Hunt, A., Larsen, J., Bierman, P., Petrucci, G., 2008. Investigation of factors that affect the sensitivity of accelerator mass spectrometry for cosmogenic ^{10}Be and ^{26}Al isotope analysis. Analytical Chemistry 80, 1656-1663.
Hunt, A., Petrucci, G., Bierman, P., Finkel, R., 2006. Metal matrices to optimize ion beam currents for accelerator mass spectrometry. Nuclear Instruments and Methods in Physics Research Section B: Beam Interactions with Materials and Atoms 243, 216-222.
Hunt, A., Petrucci, G., Bierman, P., Finkel, R., 2007. Investigation of metal matrix systems for cosmogenic 26Al analysis by accelerator mass spectrometry. Nuclear Instruments and Methods in Physics Research B 260, 633-636.

Klein, J., Middleton, R., 1984. Accelerator mass spectrometry at the University of Pennsylvania. Nuclear Instruments and Methods in Physics Research Section B: Beam Interactions with Materials and Atoms 5, 129-133.

Kohl, C., Nishiizumi, K., 1992. Chemical isolation of quartz for measurement of in-situ-produced cosmogenic nuclides. Geochimica et Cosmochimica Acta 56, 3583-3587.

Korschinek, G., Bergmaier, A., Faestermann, T., Gerstmann, U., Knie, K., Rugel, G., Wallner, A., Dillmann, I., Dollinger, G., Lierse von Gostomski, C., Kossert, K., Maiti, M., Poutivtsev, M., Remmert, A., 2010. A new value for the half-life of ^{10}Be by Heavy-Ion Elastic Recoil Detection and liquid scintillation counting. Nuclear Instruments and Methods in Physics Research Section B: Beam Interactions with Materials and Atoms 268, 187-191.

Lal, D., 1988. In situ-produced cosmogenic isotopes in terrestrial rocks. Annual Review of Earth and Planetary Sciences 16, 355-388.

Lanford, W., Parker, P., Bauer, K., Turekian, K., Cochran, J., Krishnaswami, S., 1980. Measurements of ^{10}Be distributions using a Tandem Van De Graaff accelerator. Nuclear Instruments and Methods 168, 505-510.

Licciardi, J., Schaefer, J., Taggart, J., Lund, D., 2009. Holocene glacier fluctuations in the Peruvian Andes indicate northern climate linkages. Science 325, 1677-1679.

Matmon, A., Schwartz, D., Finkel, R., Clemmens, S., Hanks, T., 2005. Dating offset fans along the Mojave section of the San Andreas fault using cosmogenic 26Al and 10Be Geological Society of America Bulletin 117, 795-807.

Merchel, S., Arnold, M., Aumaitre, G., Benedetti, L., Bourles, D., Braucher, R., Alfimov, V., Freeman, S., Steier, P., Wallner, A., 2008. Towards more precise ^{10}Be and ^{36}Cl data from measurements at the 10^{-14} level: Influence of sample preparation. Nuclear Instruments and Methods in Physics Research Section B: Beam Interactions with Materials and Atoms 266, 4921-4926.

Merchel, S., Bremser, W., Akhmadaliev, S., Arnold, M., Aumaitre, G., Bourles, D., Braucher, R., Caffee, M., Christl, M., Fifield, K., Finkel, R., Freeman, S., Ruiz-Gomez, A., Kubik, P., Martschini, M., Rood, D., Tims, S., Wallner, A., Wilcken, K., Xu, S., 2012. Quality assurance in accelerator mass spectrometry: Results from an international round-robin exercise for 10Be. Nuclear Instruments and Methods Section B: Beam Interactions with Materials and Atoms 289, 68-73.

Middleton, R., Klein, J., Dezfouly-Arjomandy, B., Albrecht, A., Xue, S., Herzog, G., 1994. ^{10}Be in bauxite and commercial aluminum. Nuclear Instruments and Methods in Physics Research Section B: Beam Interactions with Materials and Atoms 92, 362-366.

Muzikar, P., Elmore, D., Granger, D., 2003. Accelerator mass spectrometry in geologic research. Geological Society of America Bulletin 115, 643-654.

Nishiizumi, K., Imamura, M., Caffee, M., Southon, J., Finkel, R., McAninch, J., 2007. Absolute calibration of ^{10}Be AMS standards. Nuclear Instruments and Methods in Physics Research Section B: Beam Interactions with Materials and Atoms 258, 403-413.

Nishiizumi, K., Kohl, C., Arnold, J., Dorn, R., Klein, I., Fink, D., Middleton, R., Lal, D., 1993. Role of in situ cosmogenic nuclides ^{10}Be and ^{26}Al in the study of diverse geomorphic processes. Earth Surface Processes and Landforms 18, 407-425.

Nishiizumi, K., Kohl, C., Arnold, J., Klein, J., Fink, D., Middleton, R., 1991. Cosmic ray produced ^{10}Be and ^{26}Al in Antarctic rocks: exposure and erosion history. Earth and Planetary Science Letters 104, 440-454.

Nishiizumi, K., Lal, D., Klein, J., Middleton, R., Arnold, J., 1986. Production of ^{10}Be and ^{26}Al by cosmic rays in terrestrial quartz in situ and implications for erosion rates. Nature 319, 134-136.

Nishiizumi, K., Winterer, E., Kohl, C., Klein, J., Middleton, R., Lal, D., Arnold, J., 1989. Cosmic ray production rates of ^{10}Be and ^{26}Al in quartz from glacially polished rocks. Journal of Geophysical Research 94, 17907.

Ochs, M., Ivy-Ochs, S., 1997. The chemical behavior of Be, Al, Fe, Ca and Mg during AMS target preparation from terrestrial silicates modeled with chemical speciation calculations. Nuclear Instruments and Methods in Physics Research B 123, 235-240.

Phillips, F., Zreda, M., Smith, S., Elmore, D., Kubik, P., Sharma, P., 1990. Cosmogenic chlorine-36 chronology for glacial deposits at Bloody Canyon, eastern Sierra Nevada. Science 248, 1529-1532.

Portenga, E., Bierman, P., 2011. Understanding Earth's eroding surface with ^{10}Be. GSA Today 21, 4-10.

Portenga, E., Bierman, P., Duncan, C., Corbett, L., Kehrwald, N., Rood, D., 2015. Erosion rates of the Bhutanese Himalaya determined using in situ-produced 10Be. Geomorphology 233, 112-126.

Putnam, A., Schaefer, J., Barrell, D., Vandergoes, M., Denton, G., Kaplan, M., Finkel, R., Schwartz, R., Goehring, B., Kelley, S., 2010. In situ cosmogenic 10Be production-rate calibration from the Southern Alps, New Zealand. Quaternary Geochronology 5, 392-409.

Raisbeck, G., Yiou, F., Bourles, D., Ledtringuez, J., Deboffle, D., 1987. Measurements of 10Be and 26Al with a tandetron AMS facility. Nuclear Instruments and Methods in Physics Research Section B: Beam Interactions with Materials and Atoms 29, 22-26.

Raisbeck, G., Yiou, F., Fruneau, M., Loiseaux, J., 1978. Beryllium-10 mass spectrometry with a cyclotron. Science 202, 215-217.

Rood, D., Brown, T., Finkel, R., Guilderson, T., 2013. Poisson and non-Poisson uncertainty estimations of 10Be/9Be measurements at LLNL-CAMS. Nuclear Instruments and Methods in Physics Research B 294, 426-429.

Rood, D., Hall, S., Guilderson, T., Finkel, R., Brown, T., 2010. Challenges and opportunities in high-precision Be-10 measurements at CAMS. Nuclear Instruments and Methods in Physics Research Section B: Beam Interactions with Materials and Atoms 268, 730-732.

Rood, D., Xu, S., Shank, R., Dougans, A., Gallacher, P., Keefe, K., Miguens-Rodriguez, M., Bierman, P., Carlson, A., Freeman, S., 2014. Towards high precision and low ratio Be-10 measurements with the SUERC 5MV tandem: bigger isn't always better. The Thirteenth International Conference on Accelerator Mass Spectrometry Programme and Abstracts, 53.

Shanks, R., Freeman, S., 2015. Sputter-pits casting to measure AMS sample consumption. Nuclear Instruments and Methods Section B: Beam Interactions with Materials and Atoms 361, 168-172.

Southon, J., Vogel, J., Nowikow, I., Nelson, D., Korteling, R., Ku, T., Kusakabe, M., Huh, C., 1983. The measurement of ^{10}Be concentrations with a tandem accelerator. Nuclear Instruments and Methods in Physics Research 205, 251-257.
Stone, J., 1998. A rapid fusion method for separation of beryllium-10 from soils and silicates. Geochimica et Cosmochimica Acta 62, 555-561.
Suter, M., 1990. Accelerator mass spectrometry: state of the art in 1990. Nuclear Instruments and Methods in Physics Research Section B: Beam Interactions with Materials and Atoms 52, 211-223.
Tera, F., Brown, L., Morris, J., Sacks, S., 1986. Sediment incorporation in island-arc magmas: Inferences from ^{10}Be. Geochimica et Cosmochimica Acta 50, 535-550.
Thomas, J., Manglni, A., Parker, P., 1981. Improvements in an Accelerator Based Mass Spectrometer for Measuring 10Be. IEEE Transactions on Nuclear Science 28, 1478-1480.
Tuniz, C., Bird, J., Fink, D., Herzog, G., 1998. Accelerator Mass Spectrometry: Ultrasensitive Analysis for Global Science. CRC Press, Boston.
Turekian, K., Cochran, J., Krishnaswami, S., Lanford, W., Parker, P., Bauer, K., 1979. The measurement of 10Be in manganese nodules using a tandem Van De Graaff accelerator. Geophysical Research Letters 6, 417-420.
von Blanckenburg, F., 2005. The control mechanisms of erosion and weathering at basin scale from cosmogenic nuclides in river sediment. Earth and Planetary Science Letters 237, 462-479.
von Blanckenburg, F., Willenbring, J., 2014. Cosmogenic nuclides: dates and rates of Earth-surface change. Elements 10, 341-346.

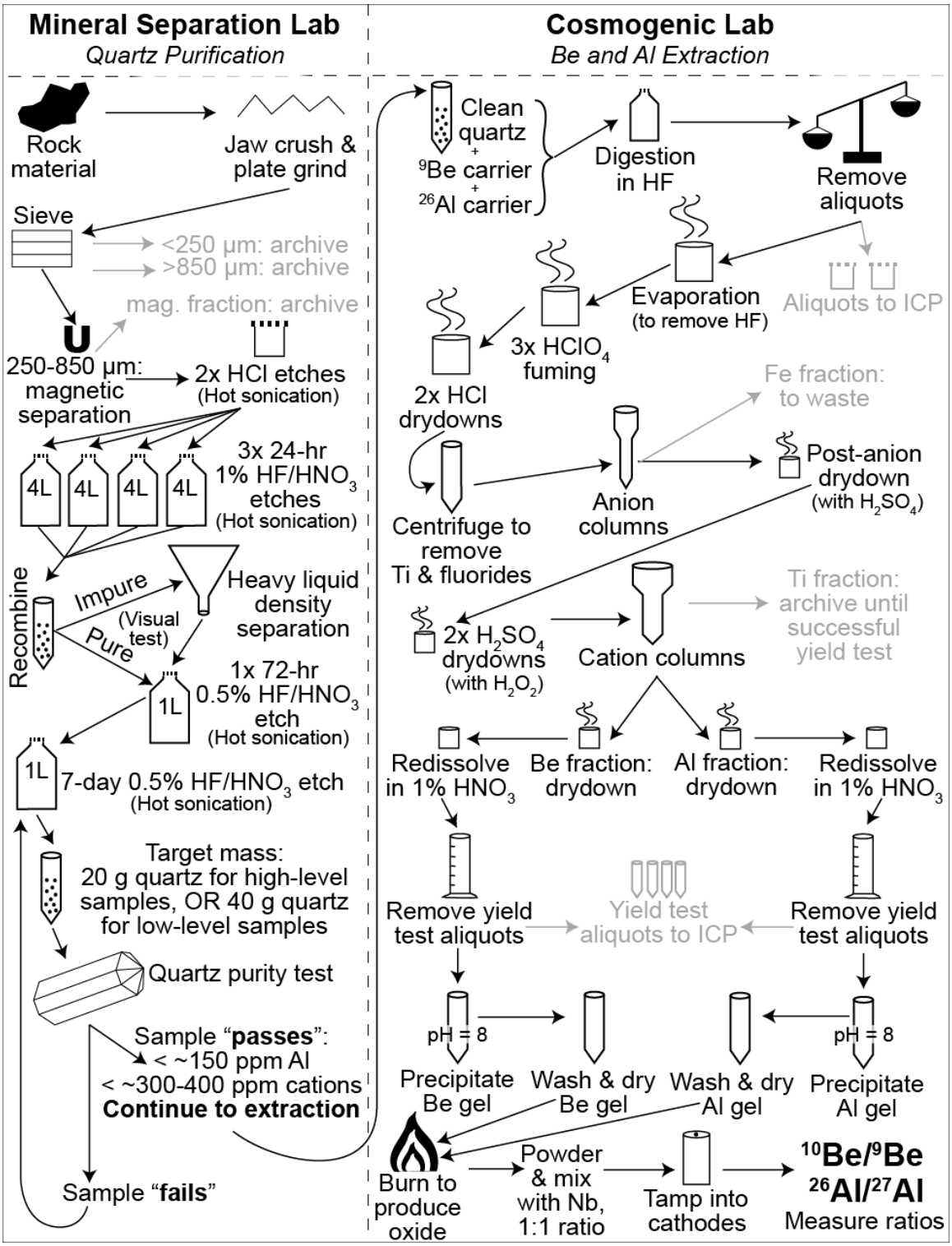

Figure 1. Flow chart of Be isotopic sample preparation. Arrows designate the direction of sample progression through the process, and gray font indicates sample fractions removed from the flow.

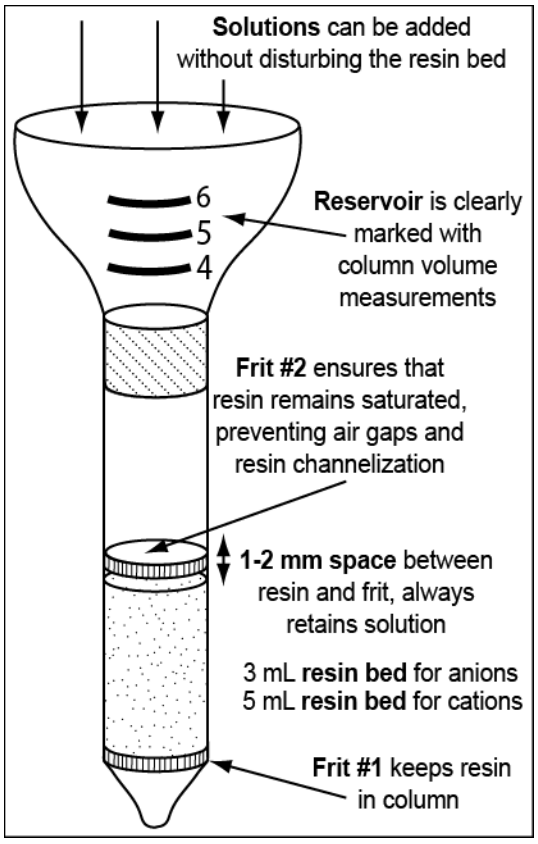

Figure 2. Diagram of a double-fritted column implemented for both anion and cation chromatography methods.

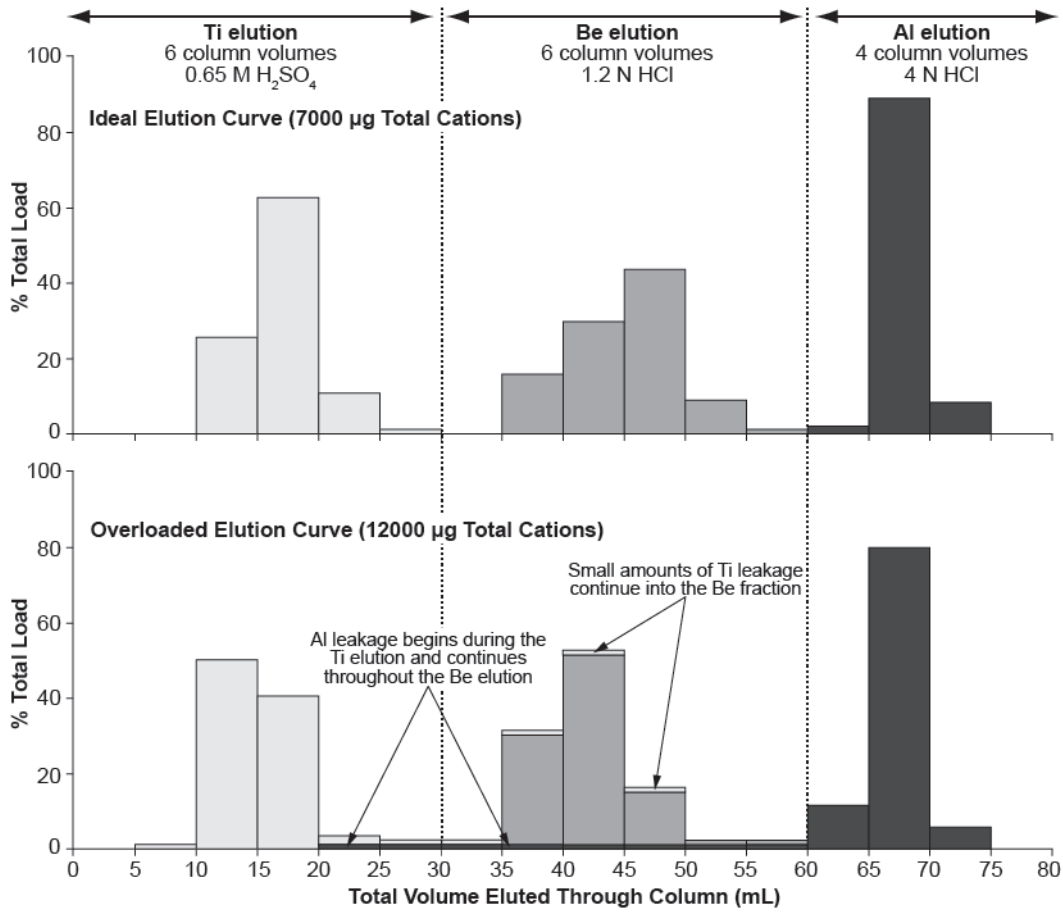

Figure 3. Cation chromatograms from tests performed during method development. Ti, Be, and Al are shown in light gray, medium gray, and dark gray, respectively. Top pannel shows an optimized elution curve that cleanly separates the three fractions (total cation load of 7000 µg). Bottom pannel shows an overloaded elution curve (total cation load of 12000 µg).

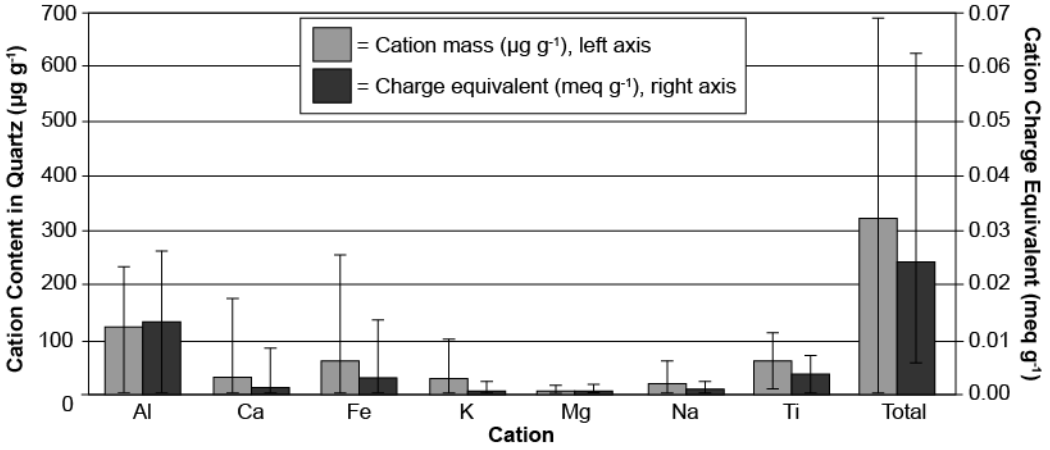

Figure 4. Average cation concentrations in quartz analyzed during 2009-2012 (n = 797), expressed both in terms of mass (µg g^{-1}, light gray bars, left axis) and charge equivalent (meq g^{-1}, dark gray bars, right axis). Error bars show ± one standard deviation. The total capacity of our 5 mL cation columns is 8.5 meq, and we determined that column failure occurred at ~10% capacity (0.85 meq). Assuming we use 20 g of average quartz shown here (0.021 meq g^{-1} excluding Fe, which is removed during anion chromatography), then our columns are on average operating half-way (0.42 meq) to their failure capacity.

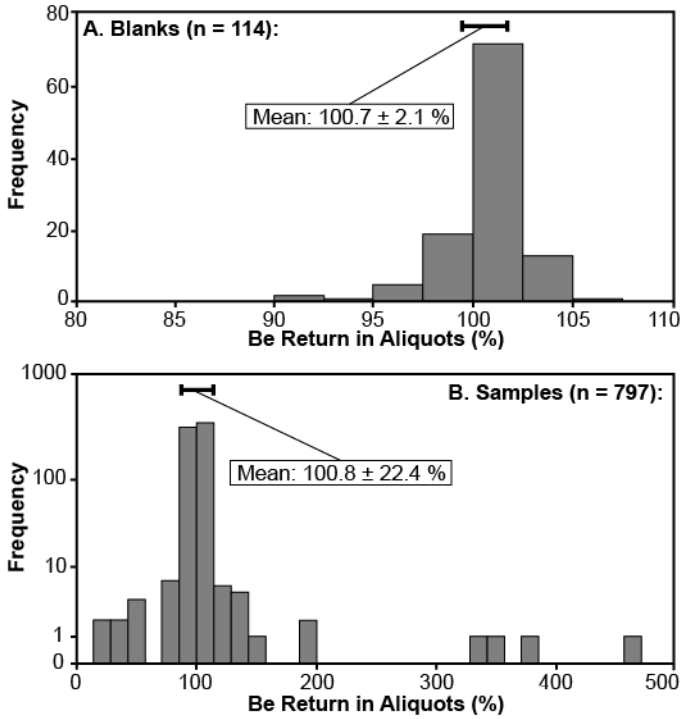

Figure 5. Histograms of Be measurements from ICP-OES aliquots taken from samples directly following dissolution. Top panel shows data for blanks (n = 114) and bottom panel shows data for samples (n = 797; note log scale on y-axis). Since no processing (except dissolution) has occurred at this point in the process, samples should return 100% of the expected Be. Samples containing more than 100% of the expected Be likely contain native ^{9}Be. Thick bar shows average ± 1SD.

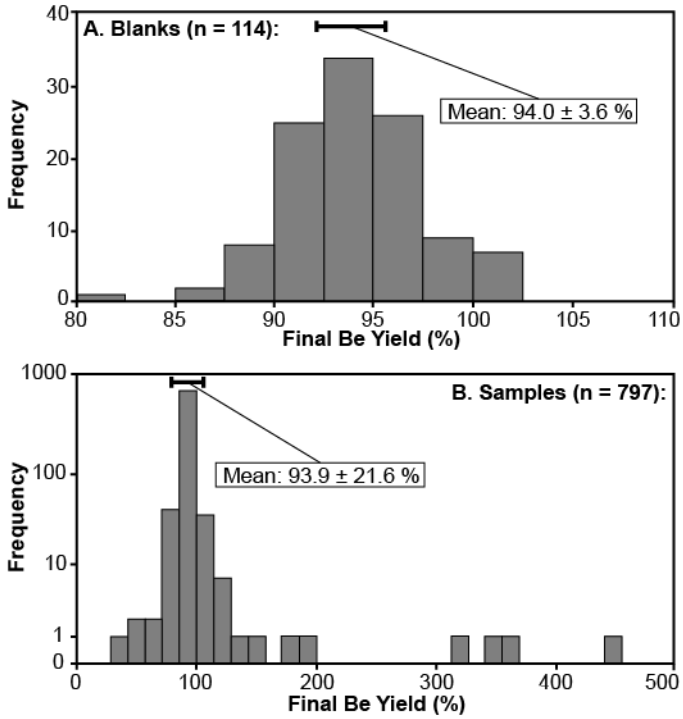

Figure 6. Histograms of Be measurements from ICP-OES aliquots taken from samples just before final precipitation. Top panel shows data for blanks (n = 114) and bottom panel shows data for samples (n = 797; note log scale on y-axis). Since 6% of the sample was removed in the first set of aliquots, final yields should be 94%. Samples containing more than 94% of the expected Be likely contain native ^{9}Be. Thick bar shows average ± 1SD.

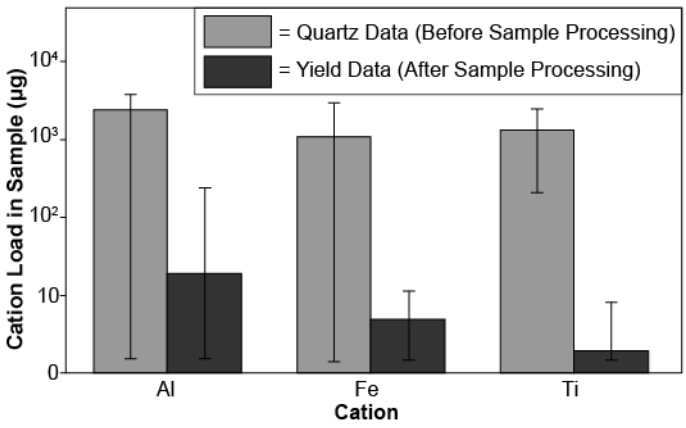

Figure 7. Final cation contents in Be fractions (from yield test data; black bars) compared to initial total cation contents in quartz (from quartz test data; gray bars; obtained by multiplying the concentration of cations in quartz by the mass of quartz used for each sample). Y-axis is in logarithmic scale.

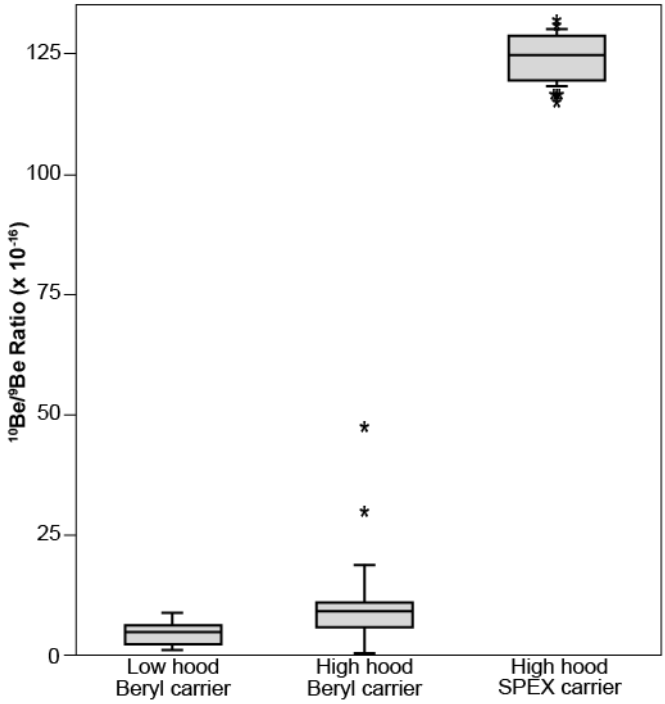

Figure 8. Box and whisker plots of process blanks from three different scenarios: beryl carrier in the low-level hood (n = 59), beryl carrier in the high-level hood (n = 29), and SPEX carrier in the high-level hood (n= 22). The box encloses the area between the first and third quartiles and the horizontal line represents the median. Whiskers show one standard deviation. Samples that lie outside one standard deviation from the mean are shown with an asterisk.

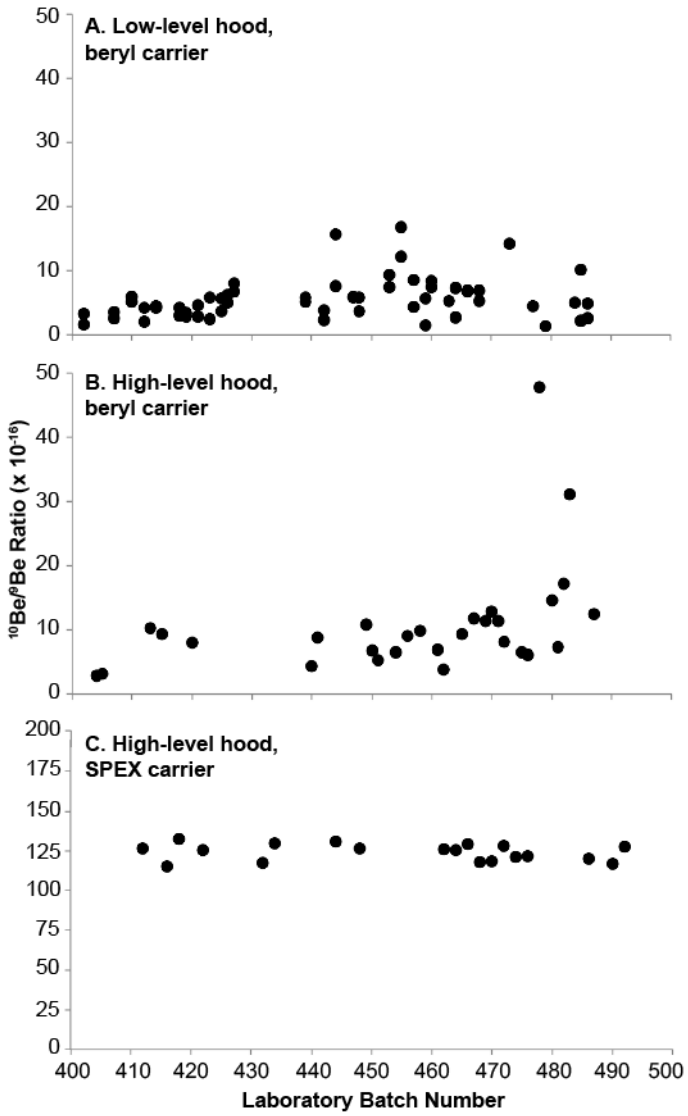

Figure 9. Blank $^{10}Be/^{9}Be$ ratios from 2009-2012 from three different scenarios: beryl carrier in the low-level hood (A; n = 59), beryl carrier in the high-level hood (B; n = 29), and SPEX carrier in the high-level hood (C; n= 22).

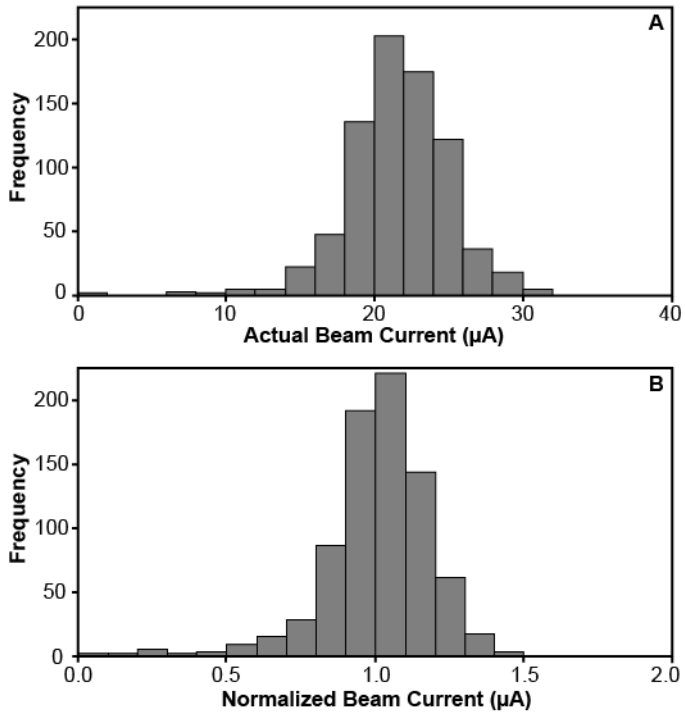

Figure 10. AMS $^{9}Be^{3+}$ beam currents (n = 797). Top pannel shows beam currents (μA) measured on the Lawrence Livermore National Laboratory AMS. Bottom pannel shows sample beam currents normalized to standard beam currents.

CHAPTER 6. CONCLUSIONS

Throughout my doctoral dissertation work, I sought to both develop and employ new approaches for constraining glacial history in areas of cold-based glacial ice. The methodological challenges presented by such landscapes lead to the growth of several new techniques. In the laboratory, I optimized methods for the preparation of cosmogenic nuclide samples, focusing on tracing beryllium through the extraction process, producing high yields of pure beryllium, and minimizing backgrounds, all of which yielded increased data accuracy and precision (Chapter 5). In the realm of data analysis, I refined numerical two-stage exposure/burial models by implementing Monte Carlo analysis to constrain uncertainties and developed multi-stage forward models to constrain possible boulder exposure/burial scenarios (Chapters 3 and 4). The methodological advances described in this dissertation will facilitate further investigation of ancient high-latitude landscapes preserved beneath non-erosive "ghost glaciers".

In Thule, northwest Greenland, I investigated a landscape mantled in sediments that have been recycled for hundreds of thousands of years and subjected to heterogeneous subglacial processes (Chapters 2 and 3). A small portion of boulders were sourced from areas deeply eroded during the last glacial period and suggest deglaciation of the landscape ~10.7 ka. Other boulders are indicative of ineffective subglacial erosion and record an exposure/burial history spanning at least several interglacial/glacial cycles. However, most boulders have experienced only limited burial, suggesting that they were initially exposed during the previous interglacial period. Boulders from different sedimentary units suggest different exposure/burial histories, underscoring the

heterogeneity of the landscape. The boulders I sampled in Thule have likely been recycled but not deeply eroded several or many times over the Quaternary, sometimes experiencing partial or complete shielding during interglacial periods, leading to a wide range in exposure/burial histories.

On Baffin Island, Canada, I investigated a complex landscape composed of deeply-carved fjords and ancient highlands using over 300 paired cosmogenic analyses of 155 bedrock and boulder samples (Chapter 4). Numerous lines of evidence (mismatched paired bedrock/boulder ages, increasing age with elevation, discordant ^{10}Be and ^{26}Al ages, multi-model age distributions, low ^{26}Al/^{10}Be ratios, and long modeled burial durations) indicate that some areas of the landscape, particularly the highlands, have been preserved beneath cold-based, non-erosive glacial ice for numerous glacial/interglacial cycles. The oldest of these surfaces have minimum-limiting burial durations of hundreds of thousands to millions of years, representing an archive of long-term information about Quaternary glaciation, with some surfaces pre-dating inception of the Laurentide Ice Sheet.

Consideration of these two Arctic landscapes (Thule, Greenland and Baffin Island, Canada) reveals the heterogeneity of subglacial processes in operation at high latitudes. Landscapes are alternately subjected to efficient subglacial erosion, inefficient subglacial erosion (and hence preservation), subaerial weathering, and periglacial processes. Certain land surfaces can be preserved for hundreds of thousands to millions of years subglacially, leading to the development of ancient, relict surfaces that have experienced many glacial/interglacial cycles. Other land surfaces are deeply eroded and only preserve a record of the time since the last deglaciation. The heterogeneity of glacial processes in Arctic regions places surfaces with drastically different histories directly

adjacent to one another at a variety of different spatial scales, leading to the complex topography, surface morphology, and ecosystems that characterize these regions today.

Although high-latitude landscapes preserved beneath non-erosive "ghost glaciers" represent methodological challenges, they also represent a scientific opportunity. Since these land surfaces have been preserved over long timescales, they hold a record of many Quaternary climate and glacial cycles, rather than just the most recent interglacial period. These ancient landscapes, therefore, contain information about long-term climate changes, glacial response to the most extreme Quaternary warm periods, and the regrowth of glacial ice following periods of ice retreat. Such information, which is critical to understanding modern climate change, cannot be found in rock surfaces that were deeply eroded during the last glacial period, but only in ancient surfaces preserved beneath cold-based glacial ice.

COMPREHENSIVE BIBLIOGRAPHY

Alley, R., 2000. The Younger Dryas cold interval as viewed from central Greenland. Quaternary Science Reviews 19, 213-226.

Alley, R., Ágústsdóttir, A., 2005. The 8k event: cause and consequences of a major Holocene abrupt climate change. Quaternary Science Reviews 24, 1123-1149.

Alley, R., Andrews, J., Brigham-Grette, J., Clarke, G., Cuffey, K., Fitzpatrick, J., Funder, S., Marshall, S., Miller, G., Mitrovica, J., 2010. History of the Greenland Ice Sheet: paleoclimatic insights. Quaternary Science Reviews 29, 1728-1756.

Alley, R., Clark, P., Huybrechts, P., Joughin, I., 2005. Ice-sheet and sea-level changes. Science 310, 456-460.

Alley, R., Mayewski, P., Sowers, T., Stuiver, M., Taylor, K., Clark, P., 1997. Holocene climatic instability: a prominent, widespread event 8200 yr ago. Geology 25, 483-486.

Andrews, J., 1975. Radiocarbon date list II from Cumberland Peninsula, Baffin Island, N.W.T., Canada. Arctic and Alpine Research 7, 77-92.

Andrews, J., Barry, R., Bradley, R., Miller, G., Williams, L., 1972. Past and present glaciological responses to climate in eastern Baffin Island. Quaternary Research 2, 303-314.

Andrews, J., Miller, G., 1972. The Quaternary history of northern Cumberland Peninsula, eastern Baffin Island, N.W.T. Part X: Radiocarbon date list. Arctic and Alpine Research 4, 261-277.

Argento, D., Reedy, R., Stone, J., 2013. Modeling the earth's cosmic radiation. Nuclear Instruments and Methods in Physics Research B 294, 464-469.

Argento, D., Stone, J., Reedy, R., O'Brien, K., 2015. Physics-based modeling of cosmogenic nuclides part II- Key aspects of in-situ cosmogenic nuclide production. Quaternary Geochronology 26, 44-55.

Atkins, C., Barrett, P., Hicock, S., 2002. Cold glaciers erode and deposit: evidence from Allan Hills, Antarctica. Geology 30, 659-662.

Balco, G., 2011. Contributions and unrealized potential contributions of cosmogenic-nuclide exposure dating to glacier chronology, 1990-2010. Quaternary Science Reviews 30, 3-27.

Balco, G., Briner, J., Finkel, R., Rayburn, J., Ridge, J., Schaefer, J., 2009. Regional beryllium-10 production rate calibration for late-glacial northeastern North America. Quaternary Geochronology 4, 93-107.

Balco, G., Rovey, C., 2008. An isochron method for cosmogenic-nuclide dating of buried soils and sediments. American Journal of Science 308, 1083-1114.

Balco, G., Stone, J., Lifton, N., Dunai, T., 2008. A complete and easily accessible means of calculating surface exposure ages or erosion rates from ^{10}Be and ^{26}Al measurements. Quaternary Geochronology 3, 174-195.

Balco, G., Stone, J., Porter, S., Caffee, M., 2002. Cosmogenic-nuclide ages for New England coastal moraines, Martha's Vineyard and Cape Cod, Massachusetts, USA. Quaternary Science Reviews 21, 2127-2135.

Balkwill, H., Bustin, R., 1975. Stratigraphic and structural studies; central Ellesmere Island and eastern Axel Heiberg Island, District of Franklin. Geological Survey of Canada Paper 75-1A, 513-517.

Bennike, O., 2008. An early Holocene Greenland whale from Melville Bugt, Greenland. Quaternary Research 69, 72-76.

Bennike, O., Abrahamsen, N., Bak, M., Israelson, C., Konradi, P., Matthiessen, J., Witkowski, A., 2002. A multi-proxy study of Pliocene sediments from Ile de France, North-East Greenland. Palaeogeography, Palaeoclimatology, Palaeoecology 186, 1-23.

Bennike, O., Björck, S., 2002. Chronology of the last recession of the Greenland Ice Sheet. Journal of Quaternary Science 17, 211-219.

Bennike, O., Knudsen, K., Abrahamsen, N., Bocher, J., Cremer, H., Wagner, B., 2010. Early Pleistocene sediments on Store Koldewey, northeast Greenland. Boreas 39, 603-619.

Bierman, P., Caffee, M., 2002. Cosmogenic exposure and erosion history of Australian bedrock landforms. Bulletin of the Geological Society of America 114, 787-803.

Bierman, P., Corbett, L., Graly, J., Neumann, T., Lini, A., Crosby, B., Rood, D., 2014. Preservation of a preglacial landscape under the center of the Greenland Ice Sheet. Science 344, 402-405.

Bierman, P., Davis, P., Corbett, L., Lifton, N., 2015. Cold-based, Laurentide ice covered New England's highest summits during the Last Glacial Maximum. Geology 43, 1059-1062.

Bierman, P., Gillespie, A., Caffee, M., 1995. Cosmogenic ages for earthquake recurrence intervals and debris flow fan deposition, Owens Valley, California. Science 270, 447-450.

Bierman, P., Marsella, K., Davis, P., Caffee, M., 2001. Response to Discussion by Wolfe et al. on Bierman et al. (Geomorphology 25 (1999) 25–39). Geomorphology 39, 255-260.

Bierman, P., Marsella, K., Patterson, C., Davis, P., Caffee, M., 1999. Mid-Pleistocene cosmogenic minimum-age limits for pre-Wisconsinan glacial surfaces in southwestern Minnesota and southern Baffin Island: a multiple nuclide approach. Geomorphology 27, 25-39.

Bierman, P., Nichols, K., 2004. Rock to sediment- slope to sea with ^{10}Be- rates of landscape change. Annual Review of Earth and Planetary Sciences 32, 215-255.

Bierman, P., Steig, E., 1996. Estimating rates of denudation using cosmogenic isotope abundances in sediment. Earth Surface Processes and Landforms 21, 125-139.

Bishop, B., 1957. Shear moraines in the Thule area, Northwest Greenland. U.S. Army Snow, Ice, and Permafrost Research Establishment Research Report 17, 47 p.

Blake, W., 1970. Studies of glacial history in Arctic Canada: Pumice, radiocarbon dates, and differential postglacial uplift in the eastern Queen Elizabeth Islands. Canadian Journal of Earth Sciences 7, 634-664.

Borchers, B., Marrero, S., Balco, G., Caffee, M., Goehring, B., Lifton, N., Nishiizumi, K., Phillips, F., Schaefer, J., Stone, J., 2016. Geological calibration of spallation production rates in the CRONUS-Earth project. Quaternary Geochronology 31, 188-198.

Briner, J., Bini, A., Anderson, R., 2009. Rapid early Holocene retreat of a Laurentide outlet glacier through an Arctic fjord. Nature Geoscience 2, 496-499.

Briner, J., Gosse, J., Bierman, P., 2006a. Applications of cosmogenic nuclides to Laurentide Ice Sheet history and dynamics. Geological Society of America Special Papers 415, 29-41.

Briner, J., Miller, G., Davis, P., Bierman, P., Caffee, M., 2003. Last Glacial Maximum ice sheet dynamics in Arctic Canada inferred from young erratics perched on ancient tors. Quaternary Science Reviews 22, 437-444.

Briner, J., Miller, G., Davis, P., Finkel, R., 2005. Cosmogenic exposure dating in arctic glacial landscapes: implications for the glacial history of northeastern Baffin Island, Arctic Canada. Canadian Journal of Earth Sciences 42, 67-84.

Briner, J., Miller, G., Davis, P., Finkel, R., 2006. Cosmogenic radionuclides from fjord landscapes support differential erosion by overriding ice sheets. Geological Society of America Bulletin 118, 406-420.

Briner, J., Stewart, H., Young, N., Phillips, W., Losee, S., 2010. Using proglacial-threshold lakes to constrain fluctuations of the Jakobshavn Isbrae ice margin, western Greenland, during the Holocene. Quaternary Science Reviews 29, 3861-3874.

Briner, J., Young, N., Goehring, B., Schaefer, J., 2012. Constraining Holocene ^{10}Be production rates in Greenland. Journal of Quaternary Science 27, 2-6.

Broecker, W., Andree, M., Wolfi, W., Oeschger, H., Bonani, G., Kennett, J., Peteet, D., 1988. The chronology of the last deglaciation: Implications to the cause of the Younger Dryas event. Paleoceanography 3, 1-19.

Brown, E., Bourles, D., Raisbeck, G., Yiou, F., Burchfiel, B., Molnar, P., Qidong, D., Jun, L., 1998. Estimation of slip rates in the southern Tien Shan using cosmic ray exposure dates of abandoned alluvial fans. Geological Society of America Bulletin 110, 377-386.

Brown, E., Edmond, J., Raisbeck, G., Yiou, F., Kurz, M., Brook, E., 1991. Examination of surface exposure ages of Antarctic moraines using in situ produced ^{10}Be and ^{26}Al. Geochimica et Cosmochimica Acta 55, 2269-2283.

Brown, E., Stallard, R., Larsen, M., Raisbeck, G., Yiou, F., 1995. Denudation rates determined from the accumulation of in situ-produced ^{10}Be in the Luquillo Experimental Forest, Puerto Rico. Earth and Planetary Science Letters 129, 193-202.

Buizert, C., Gkinis, V., Severinghaus, J., He, F., Lecavalier, B., Kindler, P., Leuenberger, M., Carlson, A., Vinther, B., Masson-Delmotte, V., White, J., Liu, Z., Otto-Bliesner, B., Brook, E., 2014. Greenland temperature response to climate forcing during the last deglaciation. Science 345, 1177-1180.

Butt, F., Elverhoi, A., Forsberg, C., Solheim, A., 2001. Evolution of the Scoresby Sund Fan, central East Green land - evidence from ODP Site 987. Norweigan Journal of Geology 81, 3-15.

Carlson, A., Winsor, K., 2012. Northern Hemisphere ice-sheet responses to past climate warming. Nature Geoscience 5, 607-613.

Chmeleff, J., Von Blanckenburg, F., Kossert, K., Jakob, D., 2010. Determination of the ^{10}Be half-life by multicollector ICP-MS and liquid scintillation counting. Nuclear Instruments and Methods in Physics Research Section B: Beam Interactions with Materials and Atoms 268, 192-199.

Clifford, D., 1999. Ion-exchange and inorganic adsorption, Water Quality and Treatment: A Handbook of Community Water Supplies. American Water Works Association, McGraw-Hill, New York.

Cofaigh, C., Dowdeswell, J., Jennings, A., Hogan, K., Kilfeather, A., Hiemstra, J., Noormets, R., Evans, J., McCarthy, D., Andrews, J., Lloyd, J., Moros, M., 2012. An extensive and dynamic ice sheet on the West Greenland shelf during the last glacial cycle. Geology 41, 219-222.

Colgan, P., Bierman, P., Mickelson, D., Caffee, M., 2002. Variation in glacial erosion near the southern margin of the Laurentide Ice Sheet, south-central Wisconsin, USA: Implications for cosmogenic dating of glacial terrains. Geological Society of America Bulletin 114, 1581-1591.

Corbett, L., Bierman, P., Graly, J., Neumann, T., Rood, D., 2013. Constraining landscape history and glacial erosivity using paired cosmogenic nuclides in Upernavik, northwest Greenland. Geological Society of America Bulletin 125, 1539-1553.

Corbett, L., Bierman, P., Lasher, G., Rood, D., 2015. Landscape chronology and glacial history in Thule, northwest Greenland. Quaternary Science Reviews 109, 57-67.

Corbett, L., Bierman, P., Neumann, T., Graly, J., 2015. Inferring glacial history and subglacial process through analysis of cosmogenic nuclides in icebound cobbles. American Geophysical Union Fall Meeting Abstract ID C11A-0745.

Corbett, L., Bierman, P., Rood, D., 2015. Constraining multi-stage exposure-burial scenarios for boulders preserved beneath cold-based ice in Thule, Northwest Greenland. Geological Society of America Abstracts with Programs 47, 712.

Corbett, L., Young, N., Bierman, P., Briner, J., Neumann, T., Graly, J., Rood, D., 2011. Paired bedrock and boulder 10Be concentrations resulting from early Holocene ice retreat near Jakobshavn Isfjord, western Greenland. Quaternary Science Reviews 30, 1739-1749.

Csatho, B., Schenk, T., Van der Veen, C., Krabill, W., 2008. Intermittent thinning of Jakobshavn Isbræ, West Greenland, since the Little Ice Age. Journal of Glaciology 54, 131-144.

Cuffey, K., Conway, H., Gades, A., Hallet, B., Lorrain, R., Severinghaus, J., Steig, E., Vaughn, B., White, J., 2000. Entrainment at cold glacier beds. Geology 28, 351-354.

Cuffey, K., Marshall, S., 2000. Substantial contribution to sea-level rise during the last interglacial from the Greenland ice sheet. Nature 404, 591-594.

Dansgaard, W., Johnsen, S.J., Moller, J., Langway, C., 1969. One thousand centuries of climate record from Camp Century on the Greenland Ice Sheet. Science 166, 377-381.

Dansgaard, W., White, J., Johnsen, S., 1989. The abrupt termination of the Younger Dryas climate event. Nature 339, 532-534.

Davies, N., Gosse, J., Rybczynski, N., 2014. Cross-bedded woody debris from a Pliocene forested river system in the high Arctic: Beaufort Formation, Meighen Island, Canada. Journal of Sedimentary Research 84, 19-25.

Davis, P., 1988. Possible evidence for extensive late Wisconsin (late Foxe) glaciation in Pangnirtung Pass area, southern Cumberland Peninsula, Baffin Island. Geological Society of America Abstracts with Programs 20, 208.

Davis, P., Bierman, P., Marsella, K., Caffee, M., Southon, J., 1999. Cosmogenic analysis of glacial terrains in the eastern Canadian Arctic: a test for inherited nuclides and the effectiveness of glacial erosion. Annals of Glaciology 28.

Davis, R., 1967. Ice surface movemebt on the Tuto Ramp in North Greenland. Cold Regions Research and Engineering Laboratory Technical Report 164, 16 p.

Dawes, P., 2006. Geological map of Greenland, 1:500,000, Thule, Sheet 5, Geological Survey of Denmark and Greenland Map Series 2. Geological Survey of Denmark and Greenland, Danish Ministry of the Environment.

De Vernal, A., Hillaire-Marcel, C., 2008. Natural variability of Greenland climate, vegetation, and ice volume during the past million years. Science 320, 1622-1625.

Ditchburn, R., Whitehead, N., 1994. The separation of ^{10}Be from silicates, 3rd Workshop of the South Pacific Environmental Radioactivity Association, pp. 4-7.

Dyke, A., 1977. Quaternary geomorphology, glacial chronology, and climatic and sea-level history of southwestern Cumberland Peninsula, Baffin Island, Northwest Territories, Canada. University of Colorado, Boulder, p. 184.

Dyke, A., 1979. Quaternary geomorphology, glacial chronology, and climatic and sea-level history of southwestern Cumberland Peninsula, Baffin Island, Northwest Territories, Canada. Arctic and Alpine Research 11, 179-202.

Dyke, A., Andrews, J., Miller, G., 1982. Quaternary geology of Cumberland Peninsula, Baffin Island, District of Franklin. Geological Survey of Canada Memoir 403, 1-32.

Eldrett, J., Harding, I., Wilson, P., Butler, E., Roberts, A., 2007. Continental ice in Greenland during the Eocene and Oligocene. Nature 466, 176-179.

England, J., 1976. Postglacial isobases and uplift curves from the Canadian and Greenland high Arctic. Arctic and Alpine Research 8, 61-78.

England, J., 1998. Suport for the Innutian Ice Sheet in the Canadian High Arctic during the Last Glacial Maximum. Journal of Quaternary Science 13, 275-280.

England, J., 1999. Coalescent Greenland and Innuitian ice during the Last Glacial Maximum: revising the Quaternary of the Canadian High Arctic. Quaternary Science Reviews 18, 421-456.

England, J., Atkinson, N., Bednarski, J., Dyke, A., Hodgson, D., Cofaigh, C., 2006. The Innutian Ice Sheet: configuration, dynamics, and chronology. Quaternary Science Reviews 25, 689-703.

England, J., Bednarski, J., 1986. Postglacial isobases from northern Ellesmere Island and Greenland: new data. Geographie physique and Quaternaire 40, 299-305.

Erlanger, E., Granger, D., Gibbon, R., 2012. Rock uplift rates in South Africa from isochron burial dating of fluvial and marine terraces. Geology 40, 1019-1022.

Fabel, D., Harbor, J., 1999. The use of in-situ produced cosmogenic radionuclides in glaciology and glacial geomorphology. Annals of Glaciology 28, 103-110.

Fairhall, A., 1960. The Radiochemistry of Beryllium, Nuclear Science Series. National Academy of Sciences and National Research Council, Washington, DC.

Feyling-Hanssen, R., 1990. Foraminiferal stratigraphy in the Plio-Pleistocene Kap Kobenhavn Formation, North Greenland. Meddelelser om Gronland 24, 1-32.

Feyling-Hanssen, R., Funder, S., Petersen, K., 1983. The Lodin Elv Formation; a Plio-Pleistocene occurrence in Greenland. Bulletin of the Geological Society of Denmark 31, 81-106.

Fitzsimons, S., Webb, N., Mager, S., MacDonell, S., Lorrain, R., Samyn, D., 2008. Mechanisms of basal ice formation in polar glaciers: An evaluation of the apron entrainment model. Journal of Geophysical Research 113, F02010.

Fleitmann, D., Mudelsee, M., Burns, S., Bradley, R., Kramers, J., Matter, A., 2008. Evidence for a widespread climatic anomaly at around 9.2 ka before present. Paleoceanography 23, PA1102.

Flesche-Kleiven, H., Jansen, E., Fronval, T., Smith, T., 2002. Intensification of Northern Hemisphere glaciations in the circum Atlantic region (3.5–2.4 Ma) – ice-rafted detritus evidence. Palaeogeography, Palaeoclimatology, Palaeoecology 184, 213-223.

Fujioka, T., Fink, D., Mifsud, C., 2015. Towards improvement of aluminium assay in quartz for in situ cosmogenic 26Al analysis at ANSTO. Nuclear Instruments and Methods in Physics Research Section B: Beam Interactions with Materials and Atoms 361, 346-353.

Funder, S., Abrahamsen, N., Bennike, O., Feyling-Hanssen, R., 1985. Forested arctic: evidence from north Greenland. Geology 13, 542-546.

Funder, S., Bennike, O., Bocher, J., Israelson, C., Petersen, K., Simonarson, L., 2001. Late Pliocene Greenland- The Kap Kobenhavn Formation in North Greenland. Bulletin of the Geological Society of Denmark 48, 117-134.

Funder, S., Hansen, L., 1996. The Greenland ice sheet-a model for its culmination and decay during and after the last glacial maximum. Bulletin of the Geological Society of Denmark 42, 137-152.

Funder, S., Simonarson, L., 1984. Bio- and aminostratigraphy of some Quaternary marine deposits in West Greenland. Canadian Journal of Earth Sciences 21, 843-852.

Gibbon, R., Pickering, T., Sutton, M., Heaton, J., Kuman, K., Clarke, R., Brain, C., Granger, D., 2014. Cosmogenic nuclide burial dating of hominin-bearing Pleistocene cave deposits at Swartkrans, South Africa. Quaternary Geochronology 24, 10-15.

Gilbert, R., 1978. Observations on oceanography and sedimentation at Pangnirtung Fiord, Baffin Island. Maritime Sediments 14, 1-9.

Gillespie, A., Bierman, P., 1995. Precision of terrestrial exposure ages and erosion rates estimated from analysis of cosmogenic isotopes produced *in situ*. Journal of Geophysical Research 100, 24,637-624,649.

Goehring, B., Brook, E., Linge, H., Raisbeck, G., Yiou, F., 2008. Beryllium-10 exposure ages of erratic boulders in southern Norway and implications for the history of the Fennoscandian Ice Sheet. Quaternary Science Reviews 27, 320-336.

Goldthwait, R., 1960. Study of ice cliff in Nunatarssuaq, Greenland. U.S. Army Snow, Ice, and Permafrost Research Establishment Technical Report 39, 106 p.

Goldthwait, R., 1971. Restudy of red rock ice cliff, Nunatarssuaq, Greenland. Cold Regions Research and Engineering Laboratory Report, 29 p.

Gosse, J., Grant, D., Klein, J., Klassen, R., Evenson, E., Lawn, B., Middleton, R., 1993. Significance of altitudinal weathering zones in Atlantic Canada, inferred from in situ produced cosmogenic radionuclides. Geological Society of America Abstracts with Programs 25, A394.

Gosse, J., Grant, D., Klein, J., Lawn, B., 1995. Cosmogenic ^{10}Be and ^{26}Al constraints on weathering zone genesis, ice cap basal conditions, and Long Range Mountain (Newfoundland) glacial history. CANQUA-CGRG conference abstracts CA19.

Gosse, J., Phillips, F., 2001. Terrestrial in situ cosmogenic nuclides: theory and application. Quaternary Science Reviews 20, 1475-1560.

Granger, D., 2006. A review of burial dating methods using 26Al and 10Be. Geological Society of America Special Papers 415, 1-16.

Granger, D., Kirchner, J., Finkel, R., 1996. Spatially averaged long-term erosion rates measured from in situ-produced cosmogenic nuclides in alluvial sediment. The Journal of Geology 104, 249-257.

Granger, D., Lifton, N., Willenbring, J., 2013. A cosmic trip: 25 years of cosmogenic nuclides in geology. Geological Society of America Bulletin 125, 1379-1402.

Granger, D., Muzikar, P., 2001. Dating sediment burial with in situ-produced cosmogenic nuclides: theory, techniques, and limitations. Earth and Planetary Science Letters 188, 269-281.

Greve, R., 2005. Relation of measured basal temperatures and the spatial distribution of the geothermal heat flux for the Greenland ice sheet. Annals of Glaciology 42, 424-432.

Grew, E., 2002. Beryllium in metamorphic environments (emphasis on aluminous compositions), in: Grew, E. (Ed.), Volume 50: Beryllium: Mineralogy, Petrology, and Geocheminstry. Mineralogical Society of America, Chantilly, Virginia, p. 690.

Griffiths, T., 1960. Glaciological investigations in the TUTO area of Greenland. U.S. Army Snow, Ice, and Permafrost Research Establishment Report 47, 63 p.

Håkansson, L., Alexanderson, H., Hjort, C., Moller, P., Briner, J., Aldahan, A., Possnert, G., 2008. Late Pleistocene glacial history of Jameson Land, central East Greenland, derived from cosmogenic ^{10}Be and ^{26}Al exposure dating. Boreas 38, 244-260.

Håkansson, L., Briner, J., Aldahan, A., Possnert, G., 2011. ^{10}Be data from meltwater channels suggest that Jameson Land, east Greenland, was ice-covered during the last glacial maximum. Quaternary Research 76, 452-459.

Håkansson, L., Briner, J., Alexanderson, H., Aldahan, A., Possnert, G., 2007. ^{10}Be ages from central east Greenland constrain the extent of the Greenland ice sheet during the Last Glacial Maximum. Quaternary Science Reviews 26, 2316-2321.

Hakansson, L., Graf, A., Strasky, S., Ivy-Ochs, S., Kubik, P., Hjort, C., Schluchter, C., 2007. Cosmogenic 10Be ages from the Store Koldewey Island, NE Greenland.

Hamilton, B., Pattison, D., Sanborn-Barrie, M., Young, M., 2012. Preliminary characterization of metamorphism on Cumberland Peninsula, Baffin Island, Nunavut. Geologic Survey of Current Research 2012-9, 17 pp.

Harbor, J., Stroeven, A., Fabel, D., Clarhäll, A., Kleman, J., Li, Y., Elmore, D., Fink, D., 2006. Cosmogenic nuclide evidence for minimal erosion across two subglacial sliding boundaries of the late glacial Fennoscandian ice sheet. Geomorphology 75, 90-99.

Helland, P., Holmes, M., 1997. Surface Textural Analysis of Quartz Sand Grains from ODP Site 918 Off the Southeast Coast of Greenland Suggests Glaciation of Southern Greenland at 11 Ma. Palaeogeography, Palaeoclimatology, Palaeoecology 135, 109-121.

Herman, F., Beaud, F., Champagnac, J., Lemieux, J., Sternai, P., 2011. Glacial hydrology and erosion patterns: A mechanism for carving glacial valleys. Earth and Planetary Science Letters 310, 498-508.

Heyman, J., Stroeven, A., Harbor, J., Caffee, M., 2011. Too young or too old: Evaluating cosmogenic exposure dating based on an analysis of compiled boulder exposure ages. Earth and Planetary Science Letters 302, 71-80.

Hills, L., Bustin, R., 1976. Picea banksii from Axel Heiberg Island, District of Franklin. Geological Survey of Canada Paper 76-1B, 61-63.

Hills, L., Matthews, J., 1974. A preliminary list of fossil plants from the Beaufort Formation, Meighen Island, District of Franklin. Geological Survey of Canada Paper 74-1B, 224-226.

Houmark-Nielsen, M., Kelly, M., Landvik, J., Sorby, L., 1990. The pre-Holocene Quaternary: Lithostratigraphic and geomorphic evidence. Meddelelser om Gronland 22, 8-18.

Hughes, A., Rainsley, E., Murray, T., Fogwill, C., Schnabel, C., Xu, S., 2012. Rapid response of Helheim Glacier, southeast Greenland, to early Holocene climate warming. Geology 40, 427-430.

Hunt, A., Larsen, J., Bierman, P., Petrucci, G., 2008. Investigation of factors that affect the sensitivity of accelerator mass spectrometry for cosmogenic ^{10}Be and ^{26}Al isotope analysis. Analytical Chemistry 80, 1656-1663.

Hunt, A., Petrucci, G., Bierman, P., Finkel, R., 2006. Metal matrices to optimize ion beam currents for accelerator mass spectrometry. Nuclear Instruments and Methods in Physics Research Section B: Beam Interactions with Materials and Atoms 243, 216-222.

Hunt, A., Petrucci, G., Bierman, P., Finkel, R., 2007. Investigation of metal matrix systems for cosmogenic 26Al analysis by accelerator mass spectrometry. Nuclear Instruments and Methods in Physics Research B 260, 633-636.

Huybrechts, P., 1996. Basal temperature conditions of the Greenland ice sheet during the glacial cycles. Annals of Glaciology 23, 226-236.

Huybrechts, P., Letreguilly, A., Reeh, N., 1991. The Greenland ice sheet and greenhouse warming. Global and Planetary Change 3, 399-412.

Hyatt, J., 1992. Cavity development in ice-rich permafrost, Pangnirtung, Baffin Island, Northwest Territories. Permafrost and Periglacial Processes 3, 293-313.

IPCC, 2013. Climate Change 2013: The Physical Science Basis. Working Group I Contribution to the Fifth Assessment Report of the Intergovernmental Panel on Climate Change. Cambridge University Press.

Ives, J., 1978. The maximum extent of the Laurentide Ice Sheet along the east coast of North America during the last deglaciation. Arctic 32, 24-35.

Jackson, G., Taylor, F., 1972. Correlation of major Aphebian rock units in the northern Canadian Shield. Canadian Journal of Earth Sciences 9, 1650-1669.

Jamieson, S., Sugden, D., Hulton, N., 2010. The evolution of the subglacial landscape of Antarctica. Earth and Planetary Science Letters 293, 1-27.

Jennings, A., 1993. The Quaternary history of Cumberland Sound, southeastern Baffin Island: The marine evidence. Geographie Physique et Quaternaire 47, 21-42.

Jennings, A., Tedesco, K., Andrews, J., Kirby, M., 1996. Shelf erosion and glacial ice proximity in the Labrador Sea during and after Heinrich events (H-3 or 4 to H-0). Geological Society of London Special Publications 111, 29-49.

Johnsen, S., Dahl-Jensen, D., Gundestrup, N., Steffensen, J., Clausen, H., Miller, H., Masson-Delmotte, V., Sveinbjornsdottir, A., White, J., 2001. Oxygen isotope and palaeotemperature records from six Greenland ice-core stations: Camp Century, Dye-3, GRIP, GISP2, Renland and NorthGRIP. Journal of Quaternary Science 16, 299-307.

Joughin, I., Das, S., King, M., Smith, B., Howat, I., Moon, T., 2008. Seasonal speedup along the western flank of the Greenland Ice Sheet. Science 320, 781-783.

Kaplan, M., Miller, G., 2003. Early Holocene delevelling and deglaciation of the Cumberland Sound region, Baffin Island, Arctic Canada. Geological Society of America Bulletin 115, 445-462.

Kaplan, M., Miller, G., Steig, E., 2001. Low-gradient outlet glaciers (ice streams?) drained the Laurentide ice sheet. Geology 29, 343-346.

Kaplan, M., Pfeffer, W., Sassolas, C., Miller, G., 1999. Numerical modelling of the Laurentide Ice Sheet in the Baffin Island region: the role of a Cumberland Sound ice stream. Canadian Journal of Earth Sciences 36, 1315-1326.

Kelley, S., Briner, J., Young, N., 2013. Rapid ice retreat in Disko Bugt supported by 10Be dating of the last recession of the western Greenland Ice Sheet. Quaternary Science Reviews 82, 13-22.

Kelley, S., Briner, J., Young, N., Babonis, G., Csatho, B., 2012. Maximum late Holocene extent of the western Greenland Ice Sheet during the late 20th century. Quaternary Science Reviews 56, 89-98.

Kelly, M., 1985. A review of the Quaternary geology of western Greenland, In: Andrews, J. (Ed.), Quaternary Environments; Eastern Canadian Arctic, Baffin Bay and Western Greenland. Allen and Unwin, Boston, pp. 461-501.

Kelly, M., Funder, S., Houmark-Nielsen, M., Knudsen, K., Kronborg, C., Landvik, J., Sorby, L., 1999. Quaternary glacial and marine environmental history of northwest Greenland: a review and reappraisal. Quaternary Science Reviews 18, 373-392.

Kelly, M., Lowell, T., Hall, B., Schaefer, J., Finkel, R., Goehring, B., Alley, R., Denton, G., 2008. A ^{10}Be chronology of lateglacial and Holocene mountain glaciation in the Scoresby Sund region, east Greenland: implications for seasonality during lateglacial time. Quaternary Science Reviews 27, 2273-2282.

Kessler, M., Anderson, R., Briner, J., 2008. Fjord insertion into continental margins driven by topographic steering of ice. Nature Geoscience 1, 365-369.

Klein, J., Giegengack, R., Middleton, R., Sharma, P., Underwood, J., Weeks, R., 1986. Revealing histories of exposure using *in situ* produced 26Al and 10Be in Libyan desert glass. Radiocarbon 28, 547-555.

Klein, J., Middleton, R., 1984. Accelerator mass spectrometry at the University of Pennsylvania. Nuclear Instruments and Methods in Physics Research Section B: Beam Interactions with Materials and Atoms 5, 129-133.

Kleman, J., Borgstrom, I., 1994. Glacial land forms indicative of a partly frozen bed. Journal of Glaciology 40, 255-264.

Koerner, R., 1989. Ice core evidence for extensive melting of the Greenland ice sheet in the last interglacial. Science 244, 964-968.

Kohl, C., Nishiizumi, K., 1992. Chemical isolation of quartz for measurement of in-situ-produced cosmogenic nuclides. Geochimica et Cosmochimica Acta 56, 3583-3587.

Korschinek, G., Bergmaier, A., Faestermann, T., Gerstmann, U., Knie, K., Rugel, G., Wallner, A., Dillmann, I., Dollinger, G., Lierse von Gostomski, C., Kossert, K., Maiti, M., Poutivtsev, M., Remmert, A., 2010. A new value for the half-life of ^{10}Be by Heavy-Ion Elastic Recoil Detection and liquid scintillation counting. Nuclear Instruments and Methods in Physics Research Section B: Beam Interactions with Materials and Atoms 268, 187-191.

Kronborg, C., Mejdahl, V., Sejrup, H., 1990. Thermoluminescence dating and amino acid analysis. Meddelelser om Gronland 22, 33-39.

Kuc, M., 1973. Fossil flora of the Beaufort Formation, Meighen Island, NWT, Canada. Canadian-Polish Research Institute Biology and Earth Sciences Series A No. 1, 1-41.

Kuc, M., 1974. The interglacial flora of Worth Point, western Banks Island. Geological Survey of Canada Paper 74-1B 227-231.

Lal, D., 1988. In situ-produced cosmogenic isotopes in terrestrial rocks. Annual Review of Earth and Planetary Sciences 16, 355-388.

Lal, D., 1991. Cosmic ray labeling of erosion surfaces: in situ nuclide production rates and erosion models. Earth and Planetary Science Letters 104, 424-439.

Lanford, W., Parker, P., Bauer, K., Turekian, K., Cochran, J., Krishnaswami, S., 1980. Measurements of ^{10}Be distributions using a Tandem Van De Graaff accelerator. Nuclear Instruments and Methods 168, 505-510.

Larsen, H., Saunders, A., Clift, P., Beget, J., Wei, W., Spezzaferri, S., 1994. Seven million years of glaciation in Greenland. Science 264, 952-955.

Larsen, N., Funder, S., Kjaer, K., Kjeldsen, K., Knudsen, M., Linge, H., 2014. Rapid early Holocene ice retreat in West Greenland. Quaternary Science Reviews 92, 310-323.

Larsen, N., Hjaer, K., Lecavalier, B., Bjork, A., Colding, S., Huybrechts, P., Jakobsen, K., Kjeldsen, K., Knudsen, K., Odgaard, B., Olsen, J., 2015. The response of the southern Greenland ice sheet to the Holocene thermal maximum. Geology 43, 291-294.

Lecavalier, B., Milne, G., Simpson, M., Wake, L., Huybrechts, P., Tarasov, L., Kjeldsen, K., Funder, S., Long, A., Woodroffe, S., Dyke, A., Larsen, N., 2014. A model of Greenland ice sheet deglaciation constrained by observations of relative sea level and ice extent. Quaternary Science Reviews 102, 54-84.

Lemmen, D., Glbert, R., Smol, J., Hall, R., 1988. Holocene sedimentation in glacial Tasikutaaq Lake, Baffin Island. Canadian Journal of Earth Sciences 25, 810-823.

Letréguilly, A., Reeh, N., Huybrechts, P., 1991. The Greenland ice sheet through the last glacial-interglacial cycle. Global and Planetary Change 4, 385-394.

Levy, L., Kelly, M., Howley, J., Virginia, R., 2012. Age of the Ørkendalen moraines, Kangerlussuaq, Greenland: constraints on the extent of the southwestern margin of the Greenland Ice Sheet during the Holocene. Quaternary Science Reviews 52, 1-5.

Licciardi, J., Schaefer, J., Taggart, J., Lund, D., 2009. Holocene glacier fluctuations in the Peruvian Andes indicate northern climate linkages. Science 325, 1677-1679.

Lilly, K., Fink, D., Fabel, D., Lambeck, K., 2010. Pleistocene dynamics of the interior of the East Antarctic ice sheet. Geology 38, 703-706.

Lisiecki, L., Raymo, M., 2005. A Plio-Pleistocene stack of 57 globally distributed benthic ^{18}O records. Paleoceanography 20, 522–533.

Long, A., 2009. Back to the future: Greenland's contribution to sea-level change. GSA Today 19, 4-10.

Long, A., Roberts, D., 2002. A revised chronology for the 'Fjord Stade' moraine in Disko Bugt, West Greenland. Journal of Quaternary Science 17, 561-579.

Long, A., Roberts, D., Dawson, S., 2006. Early Holocene history of the West Greenland Ice Sheet and the GH-8.2 event. Quaternary Science Reviews 25, 904-922.

Lowdon, J., Blake, W., 1975. Geological Survey of Canada radiocarbon dates XV. Geologic Survey of Canada Paper 75-7, 32 pp.

Margreth, A., Gosse, J., Dyke, A., 2011. Testing the concept of altitudinal weathering zones on Cumberland Peninsula, Baffin Island, using terrestrial cosmogenic nuclide (TCN) exposure dating. Atlantic Geology Society Abstracts 47, 30.

Margreth, A., Gosse, J., Dyke, A., 2012. Ice cap evolution and polythermal ice dynamics derived from multiple terrestrial cosmogenic nuclide (TCN) dating of tors on Cumberland Peninsula, Baffin Island. Atlantic Geology Society Abstracts 48, 37.

Margreth, A., Gosse, J., Dyke, A., 2014. Constraining the timing of last glacial plucking of tors on Cumberland Peninsula, Baffin Island, Eastern Canadian Arctic. European Geophysical Union Geophysical Research Abstracts 16, EGU2014-9043.

Marquette, G., Gray, J., Gosse, J., Courchesne, F., Stockli, L., Macpherson, G., Finkel, R., 2004. Felsenmeer persistence under non-erosive ice in the Torngat and Kaumajet mountains, Quebec and Labrador, as determined by soil weathering and cosmogenic nuclide exposure dating. Canadian Journal of Earth Sciences 41, 19-38.

Marsella, K., Bierman, P., Davis, P., Caffee, M., 2000. Cosmogenic ^{10}Be and ^{26}Al ages for the last glacial maximum, eastern Baffin Island, Arctic Canada. Geological Society of America Bulletin 112, 1296-1312.

Matmon, A., Schwartz, D., Finkel, R., Clemmens, S., Hanks, T., 2005. Dating offset fans along the Mojave section of the San Andreas fault using cosmogenic 26Al and 10Be Geological Society of America Bulletin 117, 795-807.

Matthews, J., 1977. Coleoptera fossils: their potential value for dating and correlation of late Cenozoic sediments. Canadian Journal of Earth Sciences 14, 2339-2347.

Matthews, J., Ovenden, L., 1990. Late Tertiary plant macrofossils from localities in Arctic/Subarctic North America: A review of the data. Arctic 43, 384-392.

Merchel, S., Arnold, M., Aumaitre, G., Benedetti, L., Bourles, D., Braucher, R., Alfimov, V., Freeman, S., Steier, P., Wallner, A., 2008. Towards more precise ^{10}Be and ^{36}Cl data from measurements at the 10^{-14} level: Influence of sample preparation. Nuclear Instruments and Methods in Physics Research Section B: Beam Interactions with Materials and Atoms 266, 4921-4926.

Merchel, S., Bremser, W., Akhmadaliev, S., Arnold, M., Aumaitre, G., Bourles, D., Braucher, R., Caffee, M., Christl, M., Fifield, K., Finkel, R., Freeman, S., Ruiz-Gomez, A., Kubik, P., Martschini, M., Rood, D., Tims, S., Wallner, A., Wilcken, K., Xu, S., 2012. Quality assurance in accelerator mass spectrometry: Results from an international round-robin exercise for 10Be. Nuclear Instruments and Methods Section B: Beam Interactions with Materials and Atoms 289, 68-73.

Middleton, R., Klein, J., Dezfouly-Arjomandy, B., Albrecht, A., Xue, S., Herzog, G., 1994. ^{10}Be in bauxite and commercial aluminum. Nuclear Instruments and Methods in Physics Research Section B: Beam Interactions with Materials and Atoms 92, 362-366.

Miller, G., Briner, J., Lifton, N., Finkel, R., 2006. Limited ice-sheet erosion and complex exposure histories derived from in situ cosmogenic 10Be, 26Al, and 14C on Baffin Island, Arctic Canada. Quaternary Geochronology 1, 74-85.

Morner, N., Funder, S., 1990. C-14 dating of samples collected during the NORDQUA 86 expedition, and notes on the marine reservour effect. Meddelelser om Gronland 22, 57-63.

Muzikar, P., Elmore, D., Granger, D., 2003. Accelerator mass spectrometry in geologic research. Geological Society of America Bulletin 115, 643-654.

Nghiem, S., Hall, D., Mote, T., Tedesco, M., Albert, M., Keegan, K., Shuman, C., DiGirolamo, N., Neumann, G., 2012. The extreme melt across the Greenland Ice Sheet in 2012. Geophysical Research Letters 39, L20502.

Nichols, R., 1953. Geomorphologic observations at Thule, Greenland and Resolute Bay, Cornwallis Island, N.W.T. American Journal of Science 251, 268-275.

Nichols, R., 1969. Geomorphology of Inglefield Land, North Greenland. Meddelelser om Gronland 188, 3-105.

Nicola, L., Strasky, S., Schluchter, C., Salvatore, M., Akcar, N., Kubik, P., Christl, M., Kasper, H., Wieler, R., Baroni, C., 2009. Multiple cosmogenic nuclides document complex Pleistocene exposure history of glacial drifts in Terra Nova Bay (northern Victoria Land, Antarctica). Quaternary Research 71, 83-92.

Nielsen, T., Kuijpers, A., 2013. Only 5 southern Greenland shelf edge glaciations since the early Pliocene. Scientific Reports 3, 1-5.

Nishiizumi, K., 2004. Preparation of ^{26}Al AMS standards. Nuclear Instruments and Methods in Physics Research Section B: Beam Interactions with Materials and Atoms 223, 388-392.

Nishiizumi, K., Finkel, R., Ponganis, K., Graf, T., Kohl, C., Marti, K., 1996. *In situ* produced cosmogenic nuclides in GISP2 rock core from Greenland summit. EOS Transactions of the American Geophysical Union 77, Abstract 06945142.

Nishiizumi, K., Imamura, M., Caffee, M., Southon, J., Finkel, R., McAninch, J., 2007. Absolute calibration of ^{10}Be AMS standards. Nuclear Instruments and Methods in Physics Research Section B: Beam Interactions with Materials and Atoms 258, 403-413.

Nishiizumi, K., Kohl, C., Arnold, J., Dorn, R., Klein, I., Fink, D., Middleton, R., Lal, D., 1993. Role of in situ cosmogenic nuclides ^{10}Be and ^{26}Al in the study of diverse geomorphic processes. Earth Surface Processes and Landforms 18, 407-425.

Nishiizumi, K., Kohl, C., Arnold, J., Klein, J., Fink, D., Middleton, R., 1991. Cosmic ray produced ^{10}Be and ^{26}Al in Antarctic rocks: exposure and erosion history. Earth and Planetary Science Letters 104, 440-454.

Nishiizumi, K., Lal, D., Klein, J., Middleton, R., Arnold, J., 1986. Production of ^{10}Be and ^{26}Al by cosmic rays in terrestrial quartz in situ and implications for erosion rates. Nature 319, 134-136.

Nishiizumi, K., Winterer, E., Kohl, C., Klein, J., Middleton, R., Lal, D., Arnold, J., 1989. Cosmic ray production rates of ^{10}Be and ^{26}Al in quartz from glacially polished rocks. Journal of Geophysical Research 94, 17907.

Nobles, L., 1960. Glaciological investigations, Nunatarssuaq ice ramp, northwestern Greenland. U.S. Army Snow, Ice, and Permafrost Research Establishment Technical Report 66, 57 p.

Ochs, M., Ivy-Ochs, S., 1997. The chemical behavior of Be, Al, Fe, Ca and Mg during AMS target preparation from terrestrial silicates modeled with chemical speciation calculations. Nuclear Instruments and Methods in Physics Research B 123, 235-240.

Otto-Bliesner, B., Marshall, S., Overpeck, J., Miller, G., Hu, A., 2006. Simulating Arctic climate warmth and icefield retreat in the last interglaciation. Science 311, 1751-1753.

Overpeck, J., Otto-Bliesner, B., Miller, G., Muhs, D., Alley, R., Kiehl, J., 2006. Paleoclimatic evidence for future ice-sheet instability and rapid sea-level rise. Science 311, 1747-1750.

Perren, B., Anderson, N., Douglas, M., Fritz, S., 2012. The influence of temperature, moisture, and eolian activity on Holocene lake development in West Greenland. Journal of Paleolimnology 48, 223-239.

Phillips, F., Zreda, M., Smith, S., Elmore, D., Kubik, P., Sharma, P., 1990. Cosmogenic chlorine-36 chronology for glacial deposits at Bloody Canyon, eastern Sierra Nevada. Science 248, 1529-1532.

Phillips, W., Hall, A., Mottram, R., Fifield, L., Sugden, D., 2006. Cosmogenic 10Be and 26Al exposure ages of tors and erratics, Cairngorm Mountains, Scotland: Timescales for the development of a classic landscape of selective linear glacial erosion. Geomorphology 73, 222-245.

Portenga, E., Bierman, P., 2011. Understanding Earth's eroding surface with ^{10}Be. GSA Today 21, 4-10.

Portenga, E., Bierman, P., Duncan, C., Corbett, L., Kehrwald, N., Rood, D., 2015. Erosion rates of the Bhutanese Himalaya determined using in situ-produced 10Be. Geomorphology 233, 112-126.

Putnam, A., Schaefer, J., Barrell, D., Vandergoes, M., Denton, G., Kaplan, M., Finkel, R., Schwartz, R., Goehring, B., Kelley, S., 2010. In situ cosmogenic 10Be production-rate calibration from the Southern Alps, New Zealand. Quaternary Geochronology 5, 392-409.

Raisbeck, G., Yiou, F., Bourles, D., Ledtringuez, J., Deboffle, D., 1987. Measurements of 10Be and 26Al with a tandetron AMS facility. Nuclear Instruments and Methods in Physics Research Section B: Beam Interactions with Materials and Atoms 29, 22-26.

Raisbeck, G., Yiou, F., Fruneau, M., Loiseaux, J., 1978. Beryllium-10 mass spectrometry with a cyclotron. Science 202, 215-217.

Rasmussen, S., Vinther, B., Clausen, H., Andersen, K., 2007. Early Holocene climate oscillations recorded in three Greenland ice cores. Quaternary Science Reviews 26, 1907-1914.

Raymo, M., Oppo, D., Curry, W., 1997. The mid-Pleistocene climate transition: A deep sea carbon isotopic perspective. Paleoceanography 12, 546-559.

Reeh, N., Thomsen, H., Frich, P., Clausen, H., 1990. Stable isotope studies on ice margins in the Thule area, In: Funder, S. (Ed.), Meddelelser om Gronland, Geoscience, pp. 47-63.

Reimer, P., Bard, E., Bayliss, A., Beck, J., Blackwell, P., Ramsey, C., Buck, C., Cheng, H., Edwards, R., Friedrich, M., Grootes, P., Guilderson, T., Haflidason, H., Hajdas, I., Hatte, C., Heaton, T., Hoffman, D., Hogg, A., Hughen, K., Kaiser, K., Kromer, B., Manning, S., Niu, M., Reimer, R., Richards, D., Scott, E., Southon, J., Staff, R., Turney, C., van der Plicht, J., 2013. IntCal13 and Marine13 radiocarbon age calibration curves 0–50,000 years cal BP. Radiocarbon 55, 1869-1887.

Reyes, A., Carlson, A., Beard, B., Hatfield, R., Stoner, J., Winsor, K., Welke, B., Ullman, D., 2014. South Greenland ice-sheet collapse during Marine Isotope Stage 11. Nature 510, 525-528.

Ridge, J., Balco, G., Bayless, R., Beck, C., Carter, L., Cean, J., Voytek, E., Wei, J., 2012. The new North American varve chronology: A precise record of southeastern Laurentide Ice Sheet deglaciation and climate 18.2-12.5 kyr BP, and correlations with Greenland Ice Core records. American Journal of Science 312, 685-722.

Rinterknecht, V., Gorokhovich, Y., Schaefer, J., Caffee, M., 2009. Preliminary ^{10}Be chronology for the last deglaciation of the western margin of the Greenland Ice Sheet. Journal of Quaternary Science 24, 270-278.

Roberts, D., Long, A., Schnabel, C., Davies, B., Xu, S., Simpson, M., Huybrechts, P., 2009. Ice sheet extent and early deglacial history of the southwestern sector of the Greenland Ice Sheet. Quaternary Science Reviews 28, 2760-2773.

Roberts, D., Long, A., Schnabel, C., Freeman, S., Simpson, M., 2008. The deglacial history of southeast sector of the Greenland Ice Sheet during the Last Glacial Maximum. Quaternary Science Reviews 27, 1505-1516.

Rood, D., Brown, T., Finkel, R., Guilderson, T., 2013. Poisson and non-Poisson uncertainty estimations of 10Be/9Be measurements at LLNL-CAMS. Nuclear Instruments and Methods in Physics Research B 294, 426-429.

Rood, D., Hall, S., Guilderson, T., Finkel, R., Brown, T., 2010. Challenges and opportunities in high-precision Be-10 measurements at CAMS. Nuclear Instruments and Methods in Physics Research Section B: Beam Interactions with Materials and Atoms 268, 730-732.

Rood, D., Xu, S., Shank, R., Dougans, A., Gallacher, P., Keefe, K., Miguens-Rodriguez, M., Bierman, P., Carlson, A., Freeman, S., 2014. Towards high precision and low ratio Be-10 measurements with the SUERC 5MV tandem: bigger isn't always better. The Thirteenth International Conference on Accelerator Mass Spectrometry Programme and Abstracts, 53.

Schildgen, T., Phillips, W., Purves, R., 2005. Simulation of snow shielding corrections for cosmogenic nuclide surface exposure studies. Geomorphology 64, 67-85.

Shanks, R., Freeman, S., 2015. Sputter-pits casting to measure AMS sample consumption. Nuclear Instruments and Methods Section B: Beam Interactions with Materials and Atoms 361, 168-172.

Simonarson, L., Petersen, K., Funder, S., 1998. Molluscan palaeontology of the Pliocene-Pleistocene Kap Kobenhavn Formation, North Greenland. Meddelelser om Gronland, Geoscience 36, 1-104.

Simpson, M., Milne, G., Huybrechts, P., Long, A., 2009. Calibrating a glaciological model of the Greenland Ice Sheet from the last glacial maximum to present-day using field observations of relative sea level and ice extent. Quaternary Science Reviews 28, 1631-1657.

Southon, J., Santos, G., 2004. Ion source development at KCCAMS, University of California, Irvine. Radiocarbon 46, 33-39.

Southon, J., Santos, G., 2007. Life with MC-SNICS part II: Further ion source development at the Keck carbon cycle AMS facility. Nuclear Instruments and Methods in Physics Research B 259, 88-93.

Southon, J., Santos, G., Druffel-Rodriguez, K., Druffel, E., Trumbore, S., Xu, X., Griffin, S., Ali, S., Mazon, M., 2004. The Keck carbon cycle AMS Laboratory, University of California, Irvine: Initial operation and a background surprise. 46 1.

Southon, J., Vogel, J., Nowikow, I., Nelson, D., Korteling, R., Ku, T., Kusakabe, M., Huh, C., 1983. The measurement of ^{10}Be concentrations with a tandem accelerator. Nuclear Instruments and Methods in Physics Research 205, 251-257.

St John, K., Krissek, L., 2002. The late Miocene to Pleistocene ice-rafting history of southeast Greenland. Boreas 31, 28-35.

Staiger, J., Gosse, J., Johnson, J., Fastook, J., Gray, J., Stockli, D., Stockli, L., Finkel, R., 2005. Quaternary relief generation by polythermal glacier ice. Earth Surface Processes and Landforms 30, 1145-1159.

Steer, P., Huismans, R., Valla, P., Gac, S., Herman, F., 2012. Bimodal Plio–Quaternary glacial erosion of fjords and low-relief surfaces in Scandinavia. Nature Geoscience 5.

Steig, E., Wolfe, A., 2008. Sprucing Up Greenland. Science 320, 1595-1596.

Stone, J., 1998. A rapid fusion method for separation of beryllium-10 from soils and silicates. Geochimica et Cosmochimica Acta 62, 555-561.

Stone, J., 2000. Air pressure and cosmogenic isotope production. Journal of Geophysical Research 105, 23753-23759.

Stone, J., Ballantyne, C., Fifield, L., 1998. Exposure dating and validation of periglacial weathering limits, northwest Scotland. Geology 26, 587-590.

Stroeven, A., Fabel, D., Harbor, J., Hattestrand, C., Kleman, J., 2002. Quantifying the erosional impact of the Fennoscandian Ice Sheet in the Torneträsk-Narvik corridor, northern Sweden, based on cosmogenic radionuclide data. Geografiska Annaler; Series A, Physical Geography 84, 275-287.

Stroeven, A., Fabel, D., Hattestrand, C., Harbor, J., 2002. A relict landscape in the centre of Fennoscandian glaciation: cosmogenic radionuclide evidence of tors preserved through multiple glacial cycles. Geomorphology 44, 145-154.

Stuiver, M., Reimer, P., Reimer, R., 2015. CALIB Radiocarbon Calibration 7.1. calib.qub.ac.uk/calib/.

Sugden, D., 1977. Reconstruction of the morphology, dynamics, and thermal characteristics of the Laurentide Ice Sheet at its maximum. Arctic and Alpine Research 9, 21-47.

Sugden, D., 1978. Glacial erosion by the Laurentide ice sheet. Journal of Glaciology 20, 367-391.

Sugden, D., Balco, G., Cowdery, S., Stone, J., Sass III, L., 2005. Selective glacial erosion and weathering zones in the coastal mountains of Marie Byrd Land, Antarctica. Geomorphology 67, 317-334.

Sugden, D., Watts, S., 1977. Tors, felsenmeer, and glaciation in northern Cumberland Peninsula, Baffin Island. Canadian Journal of Earth Sciences 14, 2817-2823.

Suter, M., 1990. Accelerator mass spectrometry: state of the art in 1990. Nuclear Instruments and Methods in Physics Research Section B: Beam Interactions with Materials and Atoms 52, 211-223.

Taylor, K., Lamorey, G., Doyle, G., Alley, R., Grootes, P., Mayewski, P., White, J., Barlow, L., 1993. The 'flickering switch'of late Pleistocene climate change. Nature 361, 432-436.

Taylor, K., Mayewski, P., Alley, R., Brook, E., Gow, A., Grootes, P., Meese, D., Saltzman, E., Severinghaus, J., Twickler, M., 1997. The Holocene-Younger Dryas transition recorded at Summit, Greenland. Science 278, 825-827.

Tera, F., Brown, L., Morris, J., Sacks, S., 1986. Sediment incorporation in island-arc magmas: Inferences from ^{10}Be. Geochimica et Cosmochimica Acta 50, 535-550.

Terasmae, J., Webber, P., Andrews, J., 1966. A study of late Quaternary plant-bearing beds in north-central Baffin Island, Canada. Arctic 19, 296-318.

Thomas, J., Manglni, A., Parker, P., 1981. Improvements in an Accelerator Based Mass Spectrometer for Measuring 10Be. IEEE Transactions on Nuclear Science 28, 1478-1480.

Thorsteinsson, R., 1961. History and geology of Meighen Island. Geological Survey of Canada Bulletin 75, 1-19.

Tripati, A., Eagle, R., Morton, A., Dowdeswell, J., Atkinson, N., Bahe, Y., Dawber, C., Khadun, E., Shaw, R., Shorttle, O., Thanabalasundaram, L., 2008. Evidence for glaciation in the Northern Hemisphere back to 44 Ma from ice-rafted debris in the Greenland Sea. Earth and Planetary Science Letters 265, 112-122.

Tuniz, C., Bird, J., Fink, D., Herzog, G., 1998. Accelerator Mass Spectrometry: Ultrasensitive Analysis for Global Science. CRC Press, Boston.

Turekian, K., Cochran, J., Krishnaswami, S., Lanford, W., Parker, P., Bauer, K., 1979. The measurement of 10Be in manganese nodules using a tandem Van De Graaff accelerator. Geophysical Research Letters 6, 417-420.

Vasskog, K., Langebroek, P., Andrews, J., Nilsen, J., Nesje, A., 2015. The Greenland Ice Sheet during the last glacial cycle: Current ice loss and contribution to sea-level rise from a palaeoclimatic perspective. Earth-Science Reviews 150, 45-67.

Vaughan, J., England, J., Evans, D., 2014. Glaciotectonic deformation and reinterpretation of the Worth Point stratigraphic sequence: Banks Island, NT, Canada. Quaternary Science Reviews 91, 124-145.

Vincent, J., Morris, W., Ochietti, S., 1984. Glacial and nonglacial sedimens of Matuyama paleomagnetic age on Banks Island, Canadian Arctic Archipelago. Geology 12, 139-142.

Vinther, B., Buchardt, S., Clausen, H., Dahl-Jensen, D., Johnsen, S., Fisher, D., Koerner, R., Raynaud, D., Lipenkov, V., Andersen, K., 2009. Holocene thinning of the Greenland ice sheet. Nature 461, 385-388.

von Blanckenburg, F., 2005. The control mechanisms of erosion and weathering at basin scale from cosmogenic nuclides in river sediment. Earth and Planetary Science Letters 237, 462-479.

von Blanckenburg, F., Willenbring, J., 2014. Cosmogenic nuclides: dates and rates of Earth-surface change. Elements 10, 341-346.

Waller, R., Murton, J., Kristensen, L., 2012. Glacier–permafrost interactions: processes, products and glaciological implications. Sedimentary Geology 255-256, 1-28.

Waterhouse, R., Tobiasson, W., Scott, B., 1963. Camp Century movement record, Cold Regions Research and Engineering Laboratory Technical Report, p. 79 p.

Weidick, A., 1968. Observations on some Holocene glacier fluctuations in West Greenland, Meddelelser om Gronland, p. 194 pp.

Weidick, A., 1976. Glaciations of Northern Greenland- New evidence. Polarforschung 46, 26-33.

Weidick, A., Bennike, O., 2007. Quaternary glaciation history and glaciology of Jakobshavn Isbrae and the Disko Bugt region, west Greenland: a review. Geologic Survey of Denmark and Greenland Bulletin 14, 1-13.

Weidick, A., Oerter, H., Reeh, N., Thomsen, H., Thorning, L., 1990. The recession of the Inland Ice margin during the Holocene climatic optimum in the Jakobshavn Isfjord area of West Greenland. Global and Planetary Change 2, 389-399.

Willerslev, E., Cappellini, E., Boomsma, W., Nielsen, R., Hebsgaard, M., Brand, T., Hofreiter, M., Bunce, M., Poinar, H., Dahl-Jensen, D., 2007. Ancient biomolecules from deep ice cores reveal a forested southern Greenland. Science 317, 111-114.

Winsor, K., Carlson, A., Rood, D., 2014. 10Be dating of the Narsarsuaq moraine in southernmost Greenland: evidence for a late-Holocene ice advance exceeding the Little Ice Age maximum. Quaternary Science Reviews 98, 135-143.

Wolfe, A., Steig, E., Kaplan, M., 2001. An alternative model for the geomorphic history of pre-Wisconsinan surfaces on eastern Baffin Island: a comment on Bierman et al (Geomorphology 25 (1999) 25-39). Geomorphology 39.

Wouters, B., Chambers, D., Schrama, E., 2008. GRACE observes small-scale mass loss in Greenland. Geophysical Research Letters 35, L20501.

Xu, S., Dougans, A., Freeman, S., Schanbel, C., Wilcken, K., 2010. Improved 10Be and 26Al - AMS with a 5 MV spectrometer. Nuclear Instruments and Methods in Physics Research B 268.

Xu, S., Freeman, S., Rood, D., Shanks, R., 2015. Decadal 10Be, 26Al and 36Cl QA measurements on the SUERC 5 MV accelerator mass spectrometer. Nuclear Instruments and Methods Section B: Beam Interactions with Materials and Atoms 361, 39-42.

Young, N., Briner, J., Rood, D., Finkel, R., Corbett, L., Bierman, P., 2013. Age of the Fjord Stade moraines in the Disko Bugt region, western Greenland, and the 9.3 and 8.2 ka cooling events. Quaternary Science Reviews 60, 76-90.

Young, N., Briner, J., Stewart, H., Axford, Y., Csatho, B., Rood, D., Finkel, R., 2011. Response of Jakobshavn Isbrae, Greenland, to Holocene climate change. Geology 39, 131-134.

Young, N., Schweinsberg, A., Briner, J., Schaefer, J., 2015. Glacier maxima in Baffin Bay during the Medieval Warm Period coeval with Norse settlement. Science Advances 1, e1500806.

APPENDIX A: SUPPLEMENTARY DATA FOR CHAPTER 2
(ASSOCIATED WITH QUATERNARY SCIENCE REVIEWS MANUSCRIPT)

Data Repository:
LANDSCAPE CHRONOLOGY AND GLACIAL HISTORY IN THULE, NORTHWEST GREENLAND

Lee B. Corbett*[a], Paul R. Bierman[a], G. Everett Lasher[b], and Dylan H. Rood[c,d]

*Contact Author: Ashley.Corbett@uvm.edu, (802) 380-2344
[a]Department of Geology and Rubenstein School of Environment and Natural Resources, University of Vermont, Burlington, VT 05405
[b]Department of Earth and Planetary Sciences, Northwestern University, Evanston IL 60208
[c]Department of Earth Science and Engineering, Imperial College London, South Kensington Campus, London SW7 2AZ, UK
[d]Scottish Universities Environmental Research Centre (SUERC), East Kilbride G75 0QF, UK

Table R1. Additional information for boulder samples from Thule, northwest Greenland

Sample Name	Boulder Dimensions (L x W x H, meters)	SUERC ID Number	Quartz Mass (g)	Be Carrier Added (g)	Be Carrier Concentration (ug/g)	$^{10}Be/^{9}Be$ Ratio*	$^{10}Be/^{9}Be$ Ratio Uncertainty*
GT014	3 x 2.5 x 3	b8141	14.1265	0.7602	322	1.191E-13	3.655E-15
GT015	3 x 1.5 x 1.5	b8142	22.3421	0.7603	322	2.243E-13	5.524E-15
GT016	3 x 2 x 2	b8143	20.1238	0.7588	322	1.872E-13	4.799E-15
GT018	2 x 1 x 1	b8144	21.9277	0.7578	322	2.126E-13	6.333E-15
GT019	2 x 2 x 3	b8145	22.1865	0.7582	322	1.152E-13	3.320E-15
GT021	3 x 2 x 2.5	b8148	20.7360	0.7612	322	5.569E-13	1.049E-14
GT022	3 x 2 x 1	b8150	21.7348	0.7559	322	8.984E-14	2.648E-15
GT023	5 x 5 x 3	b8151	16.1837	0.7580	322	6.584E-14	2.112E-15
GT027	1.8 x 1.9 x 0.7	b8444	21.9419	0.8377	274	2.009E-13	4.966E-15
GT030	1.3 x 1.6 x 1.7	b8445	22.5609	0.8357	274	1.719E-13	4.129E-15
GT035	0.6 x 0.6 x 0.5	b8449	23.1413	0.8369	274	1.601E-13	3.571E-15
GT036	0.6 x 0.5 x 0.3	b8450	23.7032	0.8360	274	1.694E-13	4.827E-15
GT038	1.1 x 1.1 x 0.5	b8451	21.2182	0.8407	274	7.728E-14	2.252E-15
GT039	1.4 x 1 x 0.5	b8422	22.7264	0.8411	274	8.063E-14	2.422E-15
GT040	2.3 x 2 x 0.9	b8423	22.0682	0.8389	274	1.325E-13	6.138E-15
GT042	2 x 1.9 x 0.8	b8425	22.9631	0.8363	274	1.858E-13	4.185E-15
GT043	0.9 x 0.7 x 0.7	b8426	11.8996	0.8386	274	1.071E-13	2.740E-15
GT044	0.9 x 0.8 x 0.6	b8428	21.9156	0.8388	274	1.228E-13	2.957E-15
GT049	1.9 x 1.1 x 1.3	b8429	22.0100	0.8380	274	1.892E-13	4.604E-15
GT050	1.8 x 0.8 x 0.5	b8430	22.7959	0.8377	274	1.392E-13	3.571E-15
GT051	1.4 x 1.2 x 0.4	b8431	22.1779	0.8370	274	1.610E-13	3.711E-15
GT052	1.5 x 1 x 0.5	b8435	17.5370	0.8354	274	1.389E-13	3.348E-15
GT053	1.3 x 1.4 x 0.5	b8436	23.3843	0.8418	274	1.487E-13	3.264E-15
GT054	2.8 x 2.9 x 1.2	b8152	20.6268	0.7601	322	1.208E-13	3.934E-15
GT055	1.7 x 1.2 x 0.6	b1854	21.0599	0.7584	322	7.421E-14	2.631E-15
GT056	1.9 x 1.1 x 0.7	b8156	22.6858	0.7610	322	1.833E-13	4.883E-15
GT057	2.4 x 2.7 x 1.2	b8157	19.4918	0.7595	322	1.585E-13	4.994E-15
GT058	2.2 x 2 x 0.8	b8158	21.4217	0.7593	322	1.551E-13	4.994E-15

*Reported ratios have been normalized to the NIST standard (with an assumed ratio of 2.79×10^{-11}) and blank-corrected to the average of the four blanks ($2.7 +/- 1.1 \times 10^{-15}$) as described in the text.

APPENDIX B: SUPPLEMENTARY DATA FOR CHAPTER 3
(ASSOCIATED WITH EARTH AND PLANETARY SCIENCE LETTERS MANUSCRIPT)

Data Repository:
CONSTRAINING MULTI-STAGE EXPOSURE-BURIAL SCENARIOS FOR BOULDERS PRESERVED BENEATH COLD-BASED ICE IN THULE, NORTHWEST GREENLAND

Lee B. Corbett*[a], Paul R. Bierman[a], and Dylan H. Rood[b]

*Corresponding Author: Ashley.Corbett@uvm.edu, (802) 380-2344
[a]Department of Geology and Rubenstein School of Environment and Natural Resources, University of Vermont, Burlington, VT 05405
[b]Department of Earth Science and Engineering, Imperial College London, South Kensington Campus, London SW7 2AZ, UK & Scottish Universities Environmental Research Centre (SUERC), East Kilbride G75 0QF, UK

Table R1. Sample collection, preparation, and ratio information

Sample Name	Boulder Dimensions (L x W x H, meters)	Quartz Mass (g)	Be Carrier Added (g)	Be Carrier Concentration (µg g^{-1})	ICP-Quantified Total Al Based on Small Aliquot (µg)[a]	ICP-Quantified Total Al Based on Large Aliquot (µg)[a]	Average ICP-Quantified Total Al (µg)[a]	Measured ^{10}Be/^{9}Be Ratio[b]	^{10}Be/^{9}Be Ratio Uncertainty[b]	Measured ^{26}Al/^{27}Al Ratio[b]	^{26}Al/^{27}Al Ratio Uncertainty[b]
GT014	3 x 2.5 x 3	14.1265	0.7602	322	1873	1855	1864	1.191E-13	3.655E-15	3.027E-13	9.720E-15
GT015	3 x 1.5 x 1.5	22.3421	0.7603	322	2412	2406	2409	2.243E-13	5.524E-15	4.191E-13	2.020E-14
GT016	3 x 2 x 2	20.1238	0.7588	322	2348	2340	2344	1.872E-13	4.799E-15	3.488E-13	9.817E-15
GT018	2 x 1 x 1	21.9277	0.7578	322	2131	2120	2126	2.126E-13	6.333E-15	4.806E-13	1.281E-14
GT019	2 x 2 x 3	22.1865	0.7582	322	2523	2158	2340	1.152E-13	3.320E-15	2.896E-13	8.536E-15
GT021	3 x 2 x 2.5	20.7360	0.7612	322	2385	2346	2365	5.569E-13	1.049E-14	8.827E-13	1.741E-14
GT022	3 x 2 x 1	21.7348	0.7559	322	1833	1816	1824	8.984E-14	2.648E-15	2.381E-13	9.447E-15
GT023	5 x 5 x 3	16.1837	0.7580	322	2176	2135	2155	6.584E-14	2.112E-15	1.612E-13	6.571E-15
GT027	1.8 x 1.9 x 0.7	21.9419	0.8377	274	2225	2229	2227	2.009E-13	4.966E-15	4.386E-13	1.249E-14
GT030	1.3 x 1.6 x 1.7	22.5609	0.8357	274	2201	2203	2202	1.719E-13	4.129E-15	3.638E-13	1.037E-14
GT035	0.6 x 0.6 x 0.5	23.1413	0.8369	274	2429	2413	2421	1.601E-13	3.571E-15	3.171E-13	9.466E-15
GT036	0.6 x 0.5 x 0.3	23.7032	0.8360	274	2445	2428	2436	1.694E-13	4.827E-15	2.795E-13	8.492E-15
GT038	1.1 x 1.1 x 0.5	21.2182	0.8407	274	2453	2423	2438	7.728E-14	2.252E-15	1.476E-13	6.521E-15
GT039	1.4 x 1 x 0.5	22.7264	0.8411	274	4030	4025	4028	8.063E-14	2.422E-15	1.140E-13	5.474E-15
GT040	2.3 x 2 x 0.9	22.0682	0.8389	274	2555	2535	2545	1.325E-13	6.138E-15	2.701E-13	9.120E-15
GT042	2 x 1.9 x 0.8	22.9631	0.8363	274	2572	2573	2572	1.858E-13	4.185E-15	3.437E-13	9.954E-15
GT043	0.9 x 0.7 x 0.7	11.8996	0.8386	274	2535	2535	2535	1.071E-13	2.740E-15	1.978E-13	9.261E-15
GT044	0.9 x 0.8 x 0.6	21.9156	0.8388	274	2584	2568	2576	1.228E-13	2.957E-15	2.288E-13	8.369E-15
GT049	1.9 x 1.1 x 1.3	22.0100	0.8380	274	1921	1937	1929	1.892E-13	4.604E-15	4.750E-13	1.925E-14
GT050	1.8 x 0.8 x 0.5	22.7959	0.8377	274	2154	2145	2149	1.392E-13	3.571E-15	3.023E-13	1.247E-14
GT051	1.4 x 1.2 x 0.4	22.1779	0.8370	274	2442	2442	2442	1.610E-13	3.711E-15	3.340E-13	9.474E-15
GT052	1.5 x 1 x 0.5	17.5370	0.8354	274	2181	2150	2165	1.389E-13	3.348E-15	3.072E-13	1.382E-14
GT053	1.3 x 1.4 x 0.5	23.3843	0.8418	274	2360	2369	2364	1.487E-13	3.264E-15	2.867E-13	8.744E-15
GT054	2.8 x 2.9 x 1.2	20.6268	0.7601	322	2371	2363	2367	1.208E-13	3.934E-15	2.246E-13	8.337E-15
GT055	1.7 x 1.2 x 0.6	21.0599	0.7584	322	2330	2324	2327	7.421E-14	2.631E-15	1.688E-13	7.126E-15
GT056	1.9 x 1.1 x 0.7	22.6858	0.7610	322	2274	2283	2279	1.833E-13	4.883E-15	4.112E-13	1.331E-14
GT057	2.4 x 2.7 x 1.2	19.4918	0.7595	322	2436	2433	2434	1.585E-13	4.994E-15	3.355E-13	9.565E-15
GT058	2.2 x 2 x 0.8	21.4217	0.7593	322	2227	2214	2221	1.551E-13	4.994E-15	3.268E-13	9.279E-15

[a]Replicate aliquots were withdrawn from samples immediately following digestion. The small aliquot is 2 mL (~2% of the sample) and the large aliquot is 4 mL (~4% of the sample). Total Al was quantified by ICP-OES using two emission lines and internal standardization.

[b]Reported Be ratios have been normalized to the NIST standard with an assumed ^{10}Be/^{9}Be ratio of 2.79×10^{-11}; Al ratios have been normalized to standard Z92-0222 with an assumed ^{26}Al/^{27}Al ratio of $4.11 \cdot 10^{-11}$.

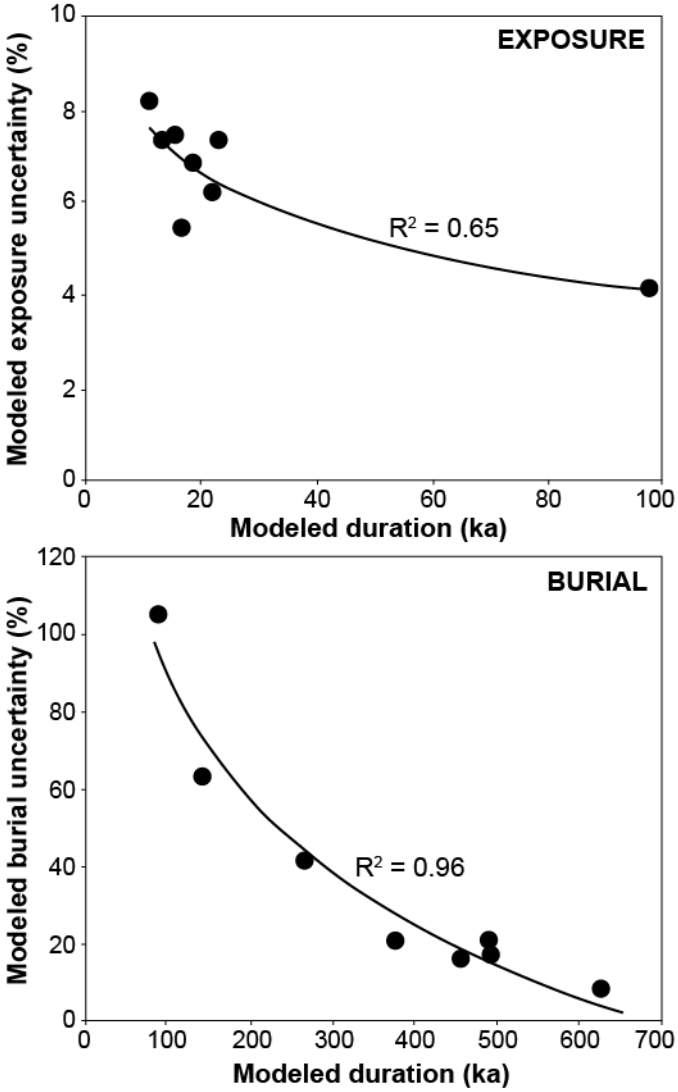

Figure R1. Plots of uncertainty versus modeled minimum limiting duration for exposure (top panel) and burial (bottom panel) for the eight boulders used for exposure/burial modeling.

APPENDIX C: SUPPLEMENTARY DATA FOR CHAPTER 4
(ASSOCIATED WITH GEOLOGICAL SOCIETY OF AMERICA BULLETIN MANUSCRIPT)

Data Repository:
GLACIAL HISTORY AND LANDSCAPE EVOLUTION OF SOUTHERN CUBMERLAND PENINSULA, BAFFIN ISLAND, CANADA, CONSTRAINED BY COSMOGENIC 10BE AND 26AL

Lee B. Corbett*[a], Paul R. Bierman[a], and P. Thompson Davis[b]

* Contact Author: Ashley.Corbett@uvm.edu
[a]Department of Geology and School of Natural Resources, University of Vermont, Burlington VT 05405
[b]Department of Natural and Applied Sciences, Bentley University, Waltham MA 02452

Erosion Rate Model Description

We modeled erosion depth for bedrock samples (n = 64 with ^{10}Be data) using the following approach:

1. We assumed a deglacial age of 11.7 ka as presented in the main body of the manuscript.
2. We subtracted that age from the age of every bedrock sample. 16 bedrock samples have simple exposure ages < 11.7 ka and are not considered further in our analysis.
3. We then used site-specific, CRONUS calculated spallation only production rates to calculate the concentration of ^{10}Be (atoms g^{-1}) present at deglaciation (11.7 ka) for each remaining bedrock sample.
4. Using those same site specific spallation production rates, we calculated the concentration of ^{10}Be (atoms g^{-1}) that would be produced during different, snow and ice-free, interglacial exposure times of 27.5, 55, and 110 ky.

Using a spallation only depth-production rate model, and assuming an attenuation length of 165 g cm^{-2}, we calculated the erosion depth needed to provide the calculated concentration of ^{10}Be present at deglaciation (11.7 ka).

Table R1. Sample collection and preparation information.

Sample Name	Latitude (°N)	Longitude (°E)	Elevation (m asl)	Sample Thickness (cm)	Quartz Mass (g)	Be Carrier (g)*	ICP-OES Quantified Total Al (mg)
KM95-001	63.74340	-68.46762	500	8	29.420	0.251	1.916
KM95-002	66.15067	-65.64622	657	5	30.620	0.248	2.815
KM95-003	66.15503	-65.64033	689	3	39.282	0.188	3.608
KM95-004	66.13717	-65.56039	335	4	26.570	0.253	2.525
KM95-005	66.13722	-65.65939	329	1	32.520	0.253	4.631
KM95-006	66.14300	-65.64608	500	5	38.043	0.251	3.226
KM95-007	66.13789	-65.64236	493	4	26.940	0.250	2.845
KM95-008	66.18372	-65.56358	661	6	39.315	0.210	2.807
KM95-009	66.18394	-65.56097	665	4	28.290	0.252	2.310
KM95-010	66.18392	-65.54100	728	5	40.648	0.246	3.898
KM95-011	66.18422	-65.54575	703	3	36.150	0.252	2.166
KM95-012	66.26550	-65.81642	278	2	34.550	0.250	4.327
KM95-013	66.26550	-65.81642	278	2	22.440	0.253	2.335
KM95-014	66.26550	-65.81642	278	2	42.630	0.253	5.350
KM95-015	66.26550	-65.81642	278	5	25.050	0.252	2.568
KM95-016	66.29597	-65.81053	928	2	33.000	0.250	3.045
KM95-017	66.29600	-65.81031	928	11	37.130	0.247	1.764
KM95-018	66.28872	-65.80200	723	2	40.910	0.248	4.380
KM95-019	66.26714	-65.77319	524	5	42.425	0.261	3.434
KM95-020	66.26714	-65.77319	524	3	39.034	0.247	3.985
KM95-021	66.26519	-65.78353	559	5	31.553	0.242	2.783
KM95-022	66.26606	-65.79989	393	3	40.316	0.301	2.547
KM95-023	66.18717	-65.70953	444	3	13.030	0.303	1.073
KM95-024	66.20911	-65.69406	455	4	32.700	0.252	3.216
KM95-025	66.20517	-65.70008	445	7	39.510	0.252	3.886
KM95-026	66.14547	-65.85556	345	2	36.751	0.250	3.805
KM95-027	66.14547	-65.85556	345	2	38.845	0.248	3.466
KM95-028	66.16689	-65.80914	375	4	47.790	0.253	4.450
KM95-029	66.16911	-65.80183	380	3	29.840	0.250	2.949
KM95-030	66.21656	-65.80122	250	5	41.719	0.300	4.123
KM95-031	66.18411	-65.76011	158	4	41.810	0.250	2.996
KM95-032	66.17797	-65.75211	36	2	21.000	0.251	1.111
KM95-033	66.13800	-65.64108	495	3	32.597	0.213	2.901
KM95-034	66.13733	-65.64139	495	3	33.040	0.254	3.340
KM95-035	66.12936	-65.63828	470	4	27.447	0.252	2.760
KM95-036	66.12831	-65.63761	470	5	31.550	0.250	3.050
KM95-037	66.11756	-65.64536	385	4	25.340	0.252	3.013
KM95-038	66.11756	-65.64536	385	4	18.300	0.302	2.023
KM95-039	66.11556	-65.64053	425	4	32.598	0.252	2.845
KM95-040	66.11556	-65.64053	425	1	25.070	0.250	1.655
KM95-041	66.13972	-65.71583	119	4	34.225	0.302	2.868
KM95-042	66.13992	-65.71539	109	2	30.996	0.302	2.526
KM95-043	66.13764	-65.71767	109	2	41.617	0.302	3.249
KM95-044	66.13764	-65.71767	204	3	40.641	0.251	5.189

Table R1, cont.

KM95-045	66.13764	-65.71767	204	1	25.115	0.303	3.043
KM95-046	66.13764	-65.71767	204	11	42.139	0.300	4.086
KM95-047	66.13764	-65.71767	204	1	36.443	0.300	2.111
KM95-048	66.13764	-65.71767	204	1	39.433	0.300	3.207
KM95-049	66.13519	-65.71736	238	5	39.861	0.301	2.747
KM95-059	66.55767	-65.33164	156	2	32.630	0.301	2.775
KM95-060	66.62917	-65.20689	361	1	41.660	0.301	4.257
KM95-061	66.62917	-65.20689	361	1	35.170	0.302	3.188
KM95-062	66.62917	-65.20689	361	2	40.720	0.297	5.553
KM95-063	66.62917	-65.20689	361	10	31.840	0.300	2.347
KM95-064	66.60986	-65.24383	381	1	39.830	0.299	5.634
KM95-066	66.60986	-65.24383	381	2	38.410	0.304	3.476
KM95-067	66.50677	-65.56497	721	2	39.702	0.248	3.702
KM95-068	66.50677	-65.56497	721	4	20.720	0.302	1.525
KM95-069	66.50677	-65.56497	721	2	27.630	0.251	0.649
KM95-070	66.50677	-65.56497	721	4	33.790	0.251	3.088
KM95-071	66.52538	-65.32219	1076	3	39.408	0.252	5.352
KM95-072	66.52483	-65.32867	1071	4	37.684	0.253	4.366
KM95-073	66.52483	-65.32867	1071	1	26.272	0.252	3.446
KM95-074	66.55644	-65.32758	166	1	28.191	0.301	3.071
KM95-075	66.47398	-65.49466	76	1	31.013	0.300	3.295
KM95-076	66.47118	-65.49338	61	3	34.050	0.304	3.665
KM95-077	66.31861	-65.51289	139	3	33.160	0.301	2.200
KM95-078	66.31861	-65.51289	139	4	41.770	0.300	3.575
KM95-079	66.31936	-65.51267	129	2	36.440	0.299	3.470
KM95-080	66.31936	-65.51267	129	4	39.521	0.216	3.683
KM95-081	66.31936	-65.51303	129	2	23.160	0.302	2.180
KM95-082	66.31936	-65.51303	129	6	39.540	0.298	3.470
KM95-083	66.24506	-65.58242	19	1	32.695	0.301	2.120
KM95-084	66.24506	-65.58242	19	4	30.864	0.300	2.210
KM95-086	66.23636	-65.57911	64	4	42.933	0.301	2.937
KM95-087	66.20125	-65.59817	39	4	36.248	0.300	3.219
KM95-088	66.20125	-65.59817	39	2	26.827	0.300	1.677
KM95-089	66.20125	-65.59817	39	3	36.830	0.302	4.054
KM95-090	66.20125	-65.59817	39	1	41.701	0.301	2.761
KM95-091	66.13283	-65.86686	24	5	33.680	0.301	2.746
KM95-092	66.13231	-65.86678	9	1	38.497	0.211	3.612
KM95-093	66.13150	-65.86533	24	2	37.540	0.299	2.426
KM95-094	66.08794	-65.93311	5	1	40.820	0.300	3.415
KM95-095	66.08794	-65.93311	5	6	39.440	0.300	2.931
KM95-096	66.08714	-65.93061	5	3	40.730	0.302	3.542
KM95-097	66.08714	-65.93061	5	4	38.240	0.301	2.982
KM95-098	65.71308	-65.78339	5	3	39.250	0.302	1.758
KM95-099	65.71308	-65.78339	5	5	40.000	0.301	1.752
KM95-100	66.13861	-65.62325	516	4	35.315	0.253	3.776
KM95-101	66.13969	-65.62147	521	4	32.255	0.253	2.091
KM95-102	66.14042	-65.63172	501	5	40.197	0.249	2.875
KM95-103	66.14742	-65.62425	521	2	37.390	0.264	4.068
KM95-104	66.14775	-65.62494	521	2	27.760	0.254	1.920

Table R1, cont.

KM95-105	66.13083	-65.69603	431	5	33.330	0.253	3.611
KM95-106	66.12233	-65.70281	596	5	34.830	0.252	3.341
KM95-107	66.12019	-65.70550	626	2	41.490	0.259	3.524
KM95-108	66.11992	-65.70875	631	4	26.940	0.252	2.580
KM95-109	66.11936	-65.71011	631	5	28.000	0.248	2.650
KM95-110	66.11294	-65.73378	656	1	27.870	0.250	2.375
KM95-112	66.11275	-65.71917	656	3	36.050	0.254	3.603
KM95-113	66.13747	-65.65928	271	5	41.896	0.299	3.032
KM95-114	66.13747	-65.66031	271	4	36.199	0.300	4.011
KM95-115	66.13814	-65.66150	266	3	42.845	0.298	3.878
KM95-116	66.13781	-65.66172	266	3	37.265	0.301	1.943
KM95-117	66.13781	-65.66172	271	7	31.085	0.296	2.264
KM95-130	65.70833	-65.83542	83	1	34.880	0.302	2.633
KM95-131	65.70833	-65.83542	83	2	38.280	0.252	2.510
KM95-132	65.70833	-65.83542	88	2	28.310	0.300	1.737
KM95-133	65.70833	-65.83542	88	3	30.870	0.301	1.097
KM95-134	65.94267	-65.92506	38	3	31.850	0.301	4.524
KM95-135	66.11411	-65.97164	210	2	41.360	0.301	3.928
KM95-136	66.11411	-65.97164	210	2	29.450	0.342	2.469
KM95-138	65.98044	-65.75608	93	1	37.250	0.251	2.468
KM95-139	65.98103	-65.74944	103	2	26.120	0.298	2.679
KM95-140	65.98186	-65.74919	103	2	42.601	0.210	2.708
KM95-141	65.98186	-65.74919	103	1	42.190	0.263	3.263
KM95-142	65.97617	-65.74653	63	3	19.500	0.301	1.565
KM95-143	65.97264	-65.75333	63	1	31.140	0.302	2.895
KM95-144	65.96356	-65.77553	10	1	39.300	0.303	3.536
KM95-145	65.96356	-65.77553	10	5	44.920	0.302	3.619
KM95-146	66.07522	-65.89767	393	3	39.580	0.256	3.019
KM95-147	66.07522	-65.89767	393	1	41.840	0.254	3.943
KM95-149	66.08439	-65.90694	148	4	38.660	0.300	4.288
PTD92-01	66.21000	-65.70667	450	7	39.971	0.259	1.935
PTD92-02	66.21000	-65.70667	310	8	40.640	0.253	2.162
PTD92-03	66.14315	-65.71465	350	5	39.060	0.254	2.813
PTD92-04	66.18367	-65.56217	660	4	39.510	0.253	2.783
PTD92-05	66.10917	-65.63883	485	8	38.870	0.253	2.663
PTD92-07	66.58100	-65.27267	366	8	39.800	0.253	2.363
PTD92-08	66.51133	-65.57300	720	6	39.580	0.302	3.456
PTD92-09	66.51133	-65.57300	720	6	41.848	0.303	2.849
PTD94-01	66.39283	-65.92750	290	2	39.570	0.253	4.740
PTD94-02	66.39283	-65.92750	290	4	39.640	0.252	4.427
PTD94-03	65.84500	-65.56417	128	2	41.770	0.252	2.799
PTD94-04	65.84500	-65.56417	128	3	39.460	0.254	2.759
PTD94-05	66.26650	-65.76633	616	3	38.270	0.253	3.197
PTD94-06	66.26650	-65.76633	616	3	39.530	0.253	2.353
PTD94-07	66.29233	-65.72333	1006	2	39.640	0.253	3.048
PTD94-08	65.44364	-63.45487	160	3	39.710	0.252	1.996
PTD94-09a	65.44364	-63.45487	160	2	39.130	0.253	2.229
PTD94-09b	65.44364	-63.45487	160	2	35.620	0.252	2.021
PTD94-09c	65.44364	-63.45487	160	3	39.740	0.252	2.038

Table R1, cont.

PTD94-10	65.64153	-68.05429	183	2	40.080	0.252	4.511
PTD94-11a	65.64153	-68.05429	183	3	39.740	0.253	4.086
PTD94-11b	65.64153	-68.05429	183	3	39.500	0.254	2.607
PTD94-13	66.13717	-65.08400	110	5	39.710	0.253	6.765
PTD94-14	66.69100	-67.75017	290	3	39.260	0.252	5.472
PTD94-15a	66.69100	-67.75017	290	3	39.370	0.252	4.134
PTD94-15b	66.69100	-67.75017	290	3	39.320	0.253	4.390
PTD94-15c	66.69100	-67.75017	290	3	39.310	0.253	3.956
PTD94-16	66.13750	-65.71750	204	3	37.620	0.252	3.047
PTD94-17	63.74340	-68.46762	125	3	42.310	0.253	2.749
PTD94-18a	63.74340	-68.46762	125	3	31.930	0.252	2.854
PTD94-18b	63.74340	-68.46762	125	4	39.100	0.252	2.796
PTD94-18c	63.74340	-68.46762	125	3	38.590	0.253	3.389

*Be carrier (SPEX) concentration is 1000 μg mL^{-1} for all samples.

Table R2. AMS and isotopic information.

Sample Name	AMS Be Standard	Measured $^{10}Be/^{9}Be$ Ratio*	$^{10}Be/^{9}Be$ Ratio Unc.*	Analytic Unc. (%)	^{10}Be Conc. (atoms g^{-1})	07KNSTD ^{10}Be Conc. (atoms g^{-1})†	07KNSTD ^{10}Be Unc. (atoms g^{-1})†	AMS Al Standard	Measured $^{26}Al/^{27}Al$ Ratio*	$^{26}Al/^{27}Al$ Ratio Unc.*	Analytic Unc. (%)	^{26}Al Conc. (atoms g^{-1})	^{26}Al Unc. (atoms g^{-1})	Measured $^{26}Al/^{10}Be$ Ratio	07KNSTD $^{26}Al/^{10}Be$ Ratio†	07KNSTD $^{26}Al/^{10}Be$ Ratio Unc.†
KM95-001	LLNL10000	1.63E-13	1.30E-14	8.0	7.64E+04	6.91E+04	8.89E-03	KNSTD9919	3.16E-13	1.40E-14	4.4	4.54E+05	2.19E-04	5.9	6.6	0.9
KM95-002	LLNL10000	4.57E-13	1.10E-14	2.4	2.31E+05	2.09E+05	7.78E-03	KNSTD9919	6.90E-13	3.60E-14	5.2	1.41E+06	7.43E-04	6.1	6.7	0.4
KM95-003	LLNL10000	2.27E-12	4.50E-14	2.0	7.13E+05	6.45E+05	1.37E-04	KNSTD9919	1.98E-12	6.10E-14	3.1	4.05E+06	1.25E-05	5.7	6.3	0.2
KM95-004	LLNL10000	1.48E-13	2.50E-14	16.8	7.59E+04	6.87E+04	1.58E-04	KNSTD9919	2.18E-13	1.60E-14	7.3	4.57E+05	3.51E-04	6.0	6.7	1.6
KM95-005	LLNL10000	2.59E-13	1.40E-14	5.4	1.19E+05	1.08E+05	8.44E-03	KNSTD9919	2.36E-13	1.10E-14	4.7	7.45E+05	3.57E-04	6.2	6.9	0.6
KM95-006	LLNL10000	2.83E-13	9.80E-15	3.5	1.12E+05	1.01E+05	5.97E-03	KNSTD9919	3.66E-13	1.50E-14	4.1	6.88E+05	2.91E-04	6.1	6.8	0.5
KM95-007	LLNL10000	1.64E-13	5.80E-15	3.5	8.32E+04	7.52E+04	7.16E-03	KNSTD9919	2.36E-13	9.20E-15	3.9	5.50E+05	2.34E-04	6.6	7.3	0.8
KM95-008	LLNL10000	9.69E-13	1.70E-14	1.8	3.34E+05	3.02E+05	7.02E-03	KNSTD9919	1.31E-12	6.20E-14	4.7	2.08E+06	9.90E-04	6.2	6.9	0.4
KM95-009	LLNL10000	2.75E-13	7.30E-15	2.7	1.46E+05	1.32E+05	7.24E-03	KNSTD9919	5.47E-13	2.30E-14	4.2	9.91E+05	4.28E-04	6.8	7.5	0.5
KM95-010	LLNL10000	3.87E-13	1.10E-14	2.8	1.44E+05	1.30E+05	5.84E-03	KNSTD9919	4.15E-13	1.60E-14	3.9	8.84E+05	3.48E-04	6.1	6.8	0.4
KM95-011	LLNL10000	2.67E-13	8.60E-15	3.2	1.11E+05	1.00E+05	5.98E-03	KNSTD9919	5.11E-13	2.00E-14	3.9	6.79E+05	2.75E-04	6.1	6.8	0.5
KM95-012	LLNL10000	2.23E-13	8.30E-15	3.7	9.35E+04	8.45E+04	6.16E-03	KNSTD9919	2.13E-13	1.10E-14	5.2	5.92E+05	3.15E-04	6.3	7.0	0.6
KM95-013	LLNL10000	1.49E-13	1.60E-14	10.8	9.01E+04	8.15E+04	1.33E-04	KNSTD9919	1.93E-13	1.10E-14	5.7	4.41E+05	2.77E-04	4.9	5.4	1.0
KM95-014	LLNL10000	2.88E-13	3.60E-14	12.5	1.03E+05	9.29E+04	1.35E-04	KNSTD9919	2.33E-13	1.10E-14	4.7	6.48E+05	3.13E-04	6.3	7.0	1.1
KM95-015	LLNL10000	1.22E-13	8.00E-15	6.6	6.25E+04	5.65E+04	8.41E-03	KNSTD9919	2.01E-13	1.50E-14	7.4	4.54E+05	3.56E-04	7.3	8.0	1.4
KM95-016	LLNL10000	3.56E-12	7.20E-14	2.0	1.79E+06	1.61E+06	3.34E-04	KNSTD9919	4.05E-12	8.20E-14	2.0	8.34E+06	1.69E+05	4.7	5.2	0.2
KM95-017	LLNL10000	9.81E-13	2.40E-14	2.4	4.23E+05	3.82E+05	1.07E-04	KNSTD9919	2.16E-12	7.70E-14	3.6	2.28E+06	8.19E+04	5.4	6.0	0.3
KM95-018	LLNL10000	4.34E-13	1.10E-14	2.5	1.64E+05	1.48E+05	5.82E-03	KNSTD9919	4.04E-13	1.60E-14	4.0	9.61E+05	3.87E+04	5.9	6.5	0.4
KM95-019	LLNL10000	5.45E-13	1.20E-14	2.2	2.12E+05	1.92E+05	6.03E-03	KNSTD9919	7.68E-13	2.80E-14	3.6	1.38E+06	5.09E+04	6.5	7.2	0.4
KM95-020	LLNL10000	2.71E-13	7.90E-15	2.9	1.02E+05	9.21E+04	5.34E-03	KNSTD9919	3.39E-13	1.40E-14	4.1	7.68E+05	3.25E+04	7.5	8.4	0.6
KM95-021	LLNL10000	2.34E-13	7.00E-15	3.0	1.05E+05	9.45E+04	6.34E-03	KNSTD9919	3.87E-13	2.10E-14	5.4	7.56E+05	4.20E+04	7.2	8.0	0.7
KM95-022	LLNL10000	1.94E-13	1.40E-14	7.2	8.44E+04	7.63E+04	7.62E-03	KNSTD9919	3.21E-13	2.22E-14	6.9	4.48E+05	3.18E+04	5.3	5.9	0.7
KM95-023	LLNL10000	1.02E-13	8.70E-15	8.5	1.21E+05	1.10E+05	1.80E+04	KNSTD9919	3.12E-13	2.30E-14	7.4	5.61E+05	4.60E+04	4.6	5.1	0.9
KM95-024	LLNL10000	7.21E-13	1.70E-14	2.4	3.56E+05	3.22E+05	9.50E+03	KNSTD9919	9.99E-13	3.70E-14	3.7	2.19E+06	8.16E+04	6.1	6.8	0.3
KM95-025	LLNL10000	2.18E-13	6.70E-15	3.1	8.04E+04	7.27E+04	5.06E-03	KNSTD9919	2.57E-13	1.40E-14	5.4	5.61E+05	3.13E+04	7.0	7.7	0.7
KM95-026	LLNL10000	2.06E-13	9.30E-15	4.5	8.03E+04	7.26E+04	6.04E-03	No Data	No Data	No Data	No Data	No Data	No Data	No Data	No Data	No Data
KM95-027	LLNL10000	4.79E-13	1.40E-14	2.9	1.92E+05	1.73E+05	6.98E-03	KNSTD9919	6.13E-13	2.30E-14	3.8	1.22E+06	4.62E+04	6.3	7.0	0.4
KM95-028	LLNL10000	2.43E-13	7.80E-15	3.2	7.58E+04	6.86E+04	4.38E-03	KNSTD9919	2.42E-13	1.20E-14	5.0	4.99E+05	2.54E+04	6.6	7.3	0.6
KM95-029	LLNL10000	2.43E-13	7.90E-15	3.2	1.20E+05	1.08E+05	7.01E-03	KNSTD9919	3.59E-13	1.90E-14	5.3	7.86E+05	4.27E+04	6.6	7.3	0.6
KM95-030	LLNL10000	2.81E-13	5.60E-14	19.9	1.23E+05	1.12E+05	2.47E+04	KNSTD9919	1.90E-13	2.54E-14	13.4	4.14E+05	5.62E+04	3.4	3.7	1.0
KM95-031	LLNL10000	2.07E-13	7.50E-15	3.6	7.10E+04	6.42E+04	4.92E+03	KNSTD9919	3.09E-13	1.40E-14	4.5	4.90E+05	2.31E+04	6.9	7.6	0.7
KM95-032	LLNL10000	1.23E-13	6.70E-15	5.5	7.48E+04	6.76E+04	9.51E+03	KNSTD5000	1.53E-13	2.10E-14	13.7	1.73E+05	2.73E+04	2.3	2.6	0.5
KM95-033	LLNL10000	5.30E-13	1.60E-14	3.0	2.16E+05	1.96E+05	8.23E+03	KNSTD9919	9.10E-13	7.00E-14	7.7	1.80E+06	1.39E+05	8.3	9.2	0.8
KM95-034	LLNL10000	1.97E-13	2.00E-14	10.2	8.61E+04	7.78E+04	1.06E+04	KNSTD9919	2.55E-13	1.10E-14	4.3	5.69E+05	2.58E+04	6.6	7.3	1.1
KM95-035	LLNL10000	3.45E-13	1.00E-14	2.9	1.94E+05	1.75E+05	8.37E+03	KNSTD5000	4.64E-13	2.10E-14	4.5	1.04E+06	4.79E+04	5.3	5.9	0.4
KM95-036	LLNL10000	4.27E-13	4.10E-14	9.6	2.10E+05	1.90E+05	2.04E+04	KNSTD9919	5.71E-13	1.90E-14	3.3	1.23E+06	4.17E+04	5.8	6.4	0.7
KM95-037	No Data	No Data	No Data	No Data	No Data	No Data	No Data	KNSTD9919	4.31E-13	1.90E-14	4.4	1.14E+06	5.13E+04	No Data	No Data	No Data
KM95-038	LLNL10000	1.07E-13	8.20E-15	7.7	9.06E+04	8.19E+04	1.25E+04	KNSTD9919	1.81E-13	2.10E-14	11.6	4.38E+05	5.33E+04	4.8	5.3	1.0
KM95-039	LLNL10000	4.09E-13	1.20E-14	2.9	1.96E+05	1.77E+05	7.70E+03	KNSTD9919	6.94E-13	2.60E-14	3.7	1.35E+06	5.12E+04	6.9	7.6	0.4
KM95-040	LLNL10000	3.67E-13	9.80E-15	2.7	2.25E+05	2.03E+05	9.05E+03	KNSTD5000	9.83E-13	4.55E-14	4.6	1.44E+06	6.77E+04	6.4	7.1	0.5
KM95-041	LLNL10000	1.24E-13	8.90E-15	7.2	5.85E+04	5.29E+04	6.91E+03	KNSTD9919	2.38E-13	1.39E-14	5.8	4.41E+05	2.69E+04	7.5	8.3	1.2
KM95-042	LLNL10000	1.49E-13	9.40E-15	6.3	8.09E+04	7.32E+04	7.83E+03	KNSTD9919	2.07E-13	1.70E-14	8.2	3.71E+05	3.18E+04	4.6	5.1	0.7
KM95-043	LLNL10000	1.28E-13	1.00E-14	7.8	5.01E+04	4.53E+04	6.02E+03	KNSTD9919	2.20E-13	1.46E-14	6.6	3.80E+05	2.61E+04	7.6	8.4	1.3
KM95-044	LLNL10000	2.12E-13	1.20E-14	5.7	7.54E+04	6.81E+04	6.16E+03	KNSTD5000	1.39E-13	1.00E-14	7.2	3.93E+05	2.91E+04	5.2	5.8	0.7

Table R2, cont.

KM95-045	LLNL10000	1.25E-13	9.00E-15	7.2	8.10E+04	7.32E+04	9.48E+03	KNSTD9919	1.87E-13	1.15E-14	6.1	5.00E+05	3.25E+04	6.2	6.8	1.0
KM95-046	LLNL10000	1.57E-13	1.10E-14	7.0	6.29E+04	5.69E+04	6.25E+03	KNSTD9919	2.08E-13	1.70E-14	8.1	4.47E+05	3.71E+04	7.1	7.9	1.1
KM95-047	LLNL10000	1.96E-13	3.50E-14	17.8	9.46E+04	8.55E+04	1.80E+04	KNSTD9919	2.44E-13	1.90E-14	7.8	3.11E+05	2.54E+04	3.3	3.6	0.8
KM95-048	LLNL10000	1.72E-13	8.50E-15	4.9	7.51E+04	6.79E+04	5.85E+03	KNSTD9919	2.37E-13	2.02E-14	8.5	4.25E+05	3.72E+04	5.7	6.3	0.8
KM95-049	LLNL10000	3.77E-13	1.70E-14	4.5	1.78E+05	1.61E+05	8.88E+03	KNSTD9919	7.10E-13	3.07E-14	4.3	1.09E+06	4.75E+04	6.1	6.8	0.5
KM95-059	LLNL10000	1.32E-13	8.90E-15	6.7	6.64E+04	6.00E+04	7.24E+03	KNSTD9919	1.91E-13	2.42E-14	12.7	3.57E+05	4.64E+04	5.4	6.0	1.1
KM95-060	LLNL10000	2.13E-13	3.00E-14	14.1	9.09E+04	8.22E+04	1.37E+04	KNSTD9919	2.16E-13	1.80E-14	8.4	4.88E+05	4.15E+04	5.4	5.9	1.1
KM95-061	LLNL10000	2.27E-13	1.70E-14	7.5	1.16E+05	1.05E+05	1.01E+04	KNSTD9919	2.95E-13	1.90E-14	6.4	5.92E+05	3.90E+04	5.1	5.6	0.7
KM95-062	LLNL10000	1.72E-13	2.10E-14	12.2	7.18E+04	6.49E+04	1.02E+04	KNSTD9919	1.49E-13	1.10E-14	7.4	4.50E+05	3.40E+04	6.3	6.9	1.2
KM95-063	LLNL10000	1.55E-13	1.20E-14	7.7	8.21E+04	7.42E+04	8.71E+03	KNSTD9919	2.19E-13	2.40E-14	11.0	3.55E+05	4.02E+04	4.3	4.8	0.8
KM95-064	LLNL10000	1.96E-13	1.90E-14	9.7	8.58E+04	7.76E+04	9.64E+03	KNSTD9919	1.44E-13	1.00E-14	6.9	4.52E+05	3.21E+04	5.3	5.8	0.8
KM95-066	LLNL10000	2.40E-13	2.30E-14	9.6	1.14E+05	1.03E+05	1.19E+04	KNSTD9919	3.46E-13	2.30E-14	6.6	6.95E+05	4.69E+04	6.1	6.7	0.9
KM95-067	LLNL10000	4.86E-13	1.60E-14	3.3	1.91E+05	1.72E+05	7.43E+03	KNSTD9919	5.88E-13	2.20E-14	3.7	1.22E+06	4.62E+04	6.4	7.1	0.4
KM95-068	LLNL10000	5.48E-13	1.90E-14	3.5	5.10E+05	4.61E+05	1.87E+04	KNSTD9919	1.62E-12	1.05E-13	6.5	2.65E+06	1.73E+05	5.2	5.7	0.4
KM95-069	LLNL10000	1.86E-13	8.20E-15	4.4	9.49E+04	8.58E+04	7.68E+03	KNSTD5000	1.05E-12	1.00E-13	9.5	5.45E+05	5.31E+04	5.7	6.4	0.8
KM95-070	LLNL10000	2.24E-13	1.20E-14	5.4	9.67E+04	8.74E+04	7.41E+03	KNSTD5000	3.10E-13	1.40E-14	4.5	6.27E+05	2.94E+04	6.5	7.2	0.7
KM95-071	LLNL10000	6.35E-13	2.70E-14	4.3	2.59E+05	2.34E+05	1.13E+04	KNSTD9919	4.85E-13	2.30E-14	4.7	1.47E+06	7.00E+04	5.7	6.3	0.4
KM95-072	LLNL10000	3.38E-13	1.20E-14	3.6	1.39E+05	1.25E+05	6.67E+03	KNSTD9919	4.21E-13	1.90E-14	4.5	1.08E+06	4.95E+04	7.8	8.7	0.6
KM95-073	No Data	No Data	No Data	No Data	No Data	No Data	No Data	KNSTD9919	3.84E-13	1.50E-14	3.9	1.12E+06	4.49E+04	No Data	No Data	No Data
KM95-074	LLNL10000	1.11E-13	1.00E-14	9.0	6.21E+04	5.61E+04	8.88E+03	KNSTD9919	1.38E-13	1.03E-14	7.4	3.30E+05	2.63E+04	5.3	5.9	1.0
KM95-075	LLNL10000	1.22E-13	1.10E-14	9.0	6.33E+04	5.72E+04	8.49E+03	KNSTD9919	1.24E-13	1.34E-14	10.8	2.89E+05	3.27E+04	4.6	5.1	0.9
KM95-076	LLNL10000	1.19E-13	1.20E-14	10.1	5.67E+04	5.13E+04	8.21E+03	KNSTD9919	1.59E-13	1.20E-14	7.5	3.78E+05	2.97E+04	6.7	7.4	1.3
KM95-077	LLNL10000	1.29E-13	1.00E-14	7.8	6.33E+04	5.72E+04	7.55E+03	KNSTD9919	2.71E-13	1.90E-14	7.0	3.97E+05	2.90E+04	6.3	6.9	1.0
KM95-078	LLNL10000	1.44E-13	1.10E-14	7.6	5.75E+04	5.20E+04	6.30E+03	KNSTD9919	1.97E-13	1.30E-14	6.6	3.72E+05	2.55E+04	6.5	7.2	1.0
KM95-079	LLNL10000	1.42E-13	1.90E-14	13.4	6.44E+04	5.82E+04	1.05E+04	KNSTD9919	1.93E-13	1.25E-14	6.5	4.05E+05	2.73E+04	6.3	7.0	1.3
KM95-080	LLNL10000	1.86E-13	7.80E-15	4.2	5.54E+04	5.01E+04	5.06E+03	KNSTD9919	1.87E-13	1.70E-14	9.1	3.85E+05	3.59E+04	7.0	7.7	1.1
KM95-081	LLNL10000	1.07E-13	1.20E-14	11.3	7.17E+04	6.48E+04	1.20E+04	KNSTD9919	1.95E-13	1.60E-14	8.2	4.03E+05	3.52E+04	5.6	6.2	1.3
KM95-082	LLNL10000	1.37E-13	1.10E-14	8.0	5.67E+04	5.12E+04	6.63E+03	KNSTD9919	1.91E-13	1.23E-14	6.4	3.71E+05	2.47E+04	6.5	7.2	1.1
KM95-083	LLNL10000	1.28E-13	9.00E-15	7.0	6.37E+04	5.76E+04	7.26E+03	KNSTD9919	2.36E-13	1.73E-14	7.3	3.36E+05	2.61E+04	5.3	5.8	0.9
KM95-084	LLNL10000	1.07E-13	1.10E-14	10.3	5.38E+04	4.86E+04	8.53E+03	KNSTD9919	2.12E-13	1.25E-14	5.9	3.33E+05	2.13E+04	6.2	6.8	1.3
KM95-086	LLNL10000	1.46E-13	1.20E-14	8.2	5.67E+04	5.13E+04	6.47E+03	KNSTD9919	2.44E-13	1.42E-14	5.8	3.69E+05	2.24E+04	6.5	7.2	1.0
KM95-087	LLNL10000	1.32E-13	7.50E-15	5.7	5.97E+04	5.40E+04	6.05E+03	KNSTD9919	1.85E-13	1.36E-14	7.3	3.62E+05	2.77E+04	6.1	6.7	0.9
KM95-088	LLNL10000	1.18E-13	7.80E-15	6.6	7.00E+04	6.33E+04	8.30E+03	KNSTD9919	2.82E-13	2.14E-14	7.6	3.87E+05	3.12E+04	5.5	6.1	0.9
KM95-089	LLNL10000	1.48E-13	1.00E-14	6.8	6.76E+04	6.11E+04	6.81E+03	KNSTD9919	1.38E-13	1.20E-14	8.7	3.35E+05	3.01E+04	5.0	5.5	0.8
KM95-090	LLNL10000	1.60E-13	1.10E-14	6.9	6.53E+04	5.91E+04	6.33E+03	KNSTD9919	2.45E-13	1.59E-14	6.5	3.58E+05	2.42E+04	5.5	6.1	0.8
KM95-091	LLNL10000	1.09E-13	8.70E-15	8.0	5.05E+04	4.56E+04	6.94E+03	KNSTD5000	1.48E-13	1.10E-14	7.4	2.65E+05	2.12E+04	5.2	5.8	1.0
KM95-092	LLNL10000	1.67E-13	6.90E-15	4.1	4.83E+04	4.37E+04	5.02E+03	KNSTD9919	2.15E-13	1.50E-14	7.0	4.46E+05	3.20E+04	9.2	10.2	1.4
KM95-093	LLNL10000	1.26E-13	1.00E-14	7.9	5.40E+04	4.89E+04	6.64E+03	KNSTD5000	2.25E-13	2.50E-14	11.1	3.20E+05	3.66E+04	5.9	6.6	1.2
KM95-094	LLNL10000	9.51E-14	9.60E-15	10.1	3.47E+04	3.13E+04	5.99E+03	KNSTD5000	1.07E-13	8.50E-15	7.9	1.96E+05	1.69E+04	5.7	6.3	1.3
KM95-095	LLNL10000	1.34E-13	1.30E-14	9.7	5.55E+04	5.01E+04	7.40E+03	KNSTD5000	1.04E-13	8.80E-15	8.5	1.68E+05	1.58E+04	3.0	3.4	0.6
KM95-096	LLNL10000	1.05E-13	1.70E-14	16.2	3.99E+04	3.60E+04	8.71E+03	KNSTD5000	6.48E-14	7.80E-15	12.0	1.22E+05	1.62E+04	3.1	3.4	0.9
KM95-097	LLNL10000	1.28E-13	1.20E-14	9.4	5.44E+04	4.92E+04	7.27E+03	KNSTD5000	1.14E-13	9.70E-15	8.5	1.94E+05	1.80E+04	3.6	4.0	0.7
KM95-098	LLNL10000	1.51E-13	1.40E-14	9.3	6.52E+04	5.89E+04	7.85E+03	KNSTD5000	3.33E-13	2.50E-14	7.5	3.29E+05	2.57E+04	5.1	5.6	0.9
KM95-099	LLNL10000	1.29E-13	1.40E-14	10.8	5.28E+04	4.77E+04	7.68E+03	KNSTD5000	2.89E-13	2.40E-14	8.3	2.78E+05	2.42E+04	5.3	5.8	1.1
KM95-100	LLNL10000	4.42E-13	2.10E-14	4.7	1.98E+05	1.79E+05	1.03E+04	KNSTD9919	2.83E-13	1.30E-14	4.6	6.71E+05	3.18E+04	3.4	3.8	0.3
KM95-101	LLNL10000	4.59E-13	1.70E-14	3.7	2.25E+05	2.04E+05	9.66E+03	KNSTD9919	8.78E-13	3.70E-14	4.2	1.27E+06	5.41E+04	5.6	6.2	0.4
KM95-102	LLNL10000	2.69E-13	9.90E-15	3.7	9.89E+04	8.95E+04	5.66E+03	KNSTD9919	4.28E-13	3.60E-14	8.4	6.79E+05	5.78E+04	6.9	7.6	0.8
KM95-103	LLNL10000	2.20E-13	7.20E-15	3.3	9.06E+04	8.19E+04	5.53E+03	KNSTD9919	2.24E-13	1.20E-14	5.4	5.39E+05	2.98E+04	6.0	6.6	0.6
KM95-104	LLNL10000	1.86E-13	6.00E-15	3.2	9.59E+04	8.67E+04	7.02E+03	KNSTD5000	3.82E-13	2.62E-14	6.9	5.83E+05	4.13E+04	6.1	6.7	0.7

Table R2, cont.

KM95-105	LLNL10000	1.94E-13	6.60E-15	3.4	8.38E+04	7.58E+04	5.98E+03	KNSTD5000	2.21E-13	1.22E-14	5.5	5.30E+05	3.02E+04	6.3	7.0	0.7
KM95-106	LLNL10000	1.86E-12	4.60E-14	2.5	8.85E+05	8.00E+05	2.07E+04	KNSTD5000	1.98E-12	6.56E-14	3.3	4.24E+06	1.41E+05	4.8	5.3	0.2
KM95-107	LLNL10000	2.88E-12	7.30E-14	2.5	1.19E+06	1.07E+06	2.78E+04	KNSTD9919	3.01E-12	5.60E-14	1.9	5.71E+06	1.06E+05	4.8	5.3	0.2
KM95-108	LLNL10000	1.38E-12	4.20E-14	3.1	8.43E+05	7.62E+05	2.46E+04	KNSTD5000	1.92E-12	6.93E-14	3.6	4.10E+06	1.48E+05	4.9	5.4	0.3
KM95-109	LLNL10000	1.29E-12	3.10E-14	2.4	7.44E+05	6.72E+05	1.77E+04	KNSTD5000	1.69E-12	7.24E-14	4.3	3.57E+06	1.53E+05	4.8	5.3	0.3
KM95-110	LLNL10000	2.28E-12	1.10E-13	4.8	1.35E+06	1.22E+06	5.99E+04	KNSTD5000	3.05E-12	1.02E-13	3.4	5.79E+06	1.95E+05	4.3	4.7	0.3
KM95-112	LLNL10000	2.53E-12	6.40E-14	2.5	1.18E+06	1.06E+06	2.77E+04	KNSTD9919	2.43E-12	8.30E-14	3.4	5.42E+06	1.85E+05	4.6	5.1	0.2
KM95-113	LLNL10000	2.08E-13	1.40E-14	6.7	8.74E+04	7.91E+04	7.30E+03	KNSTD9919	2.74E-13	1.54E-14	5.6	4.39E+05	2.55E+04	5.0	5.6	0.6
KM95-114	LLNL10000	1.88E-13	1.60E-14	8.5	9.07E+04	8.20E+04	9.31E+03	KNSTD9919	2.05E-13	1.33E-14	6.5	5.02E+05	3.34E+04	5.5	6.1	0.8
KM95-115	LLNL10000	2.04E-13	1.40E-14	6.8	8.35E+04	7.55E+04	7.12E+03	KNSTD9919	2.20E-13	2.41E-14	10.9	4.40E+05	4.89E+04	5.3	5.8	0.9
KM95-116	LLNL10000	1.66E-13	1.20E-14	7.3	7.62E+04	6.89E+04	7.46E+03	KNSTD9919	4.03E-13	2.78E-14	6.9	4.65E+05	3.30E+04	6.1	6.8	0.9
KM95-117	LLNL10000	1.42E-13	1.20E-14	8.4	7.47E+04	6.75E+04	8.85E+03	KNSTD9919	2.80E-13	2.10E-14	7.5	4.50E+05	3.49E+04	6.0	6.7	1.0
KM95-130	LLNL10000	1.39E-13	8.70E-15	6.3	6.63E+04	5.99E+04	6.71E+03	KNSTD5000	2.02E-13	1.50E-14	7.4	3.35E+05	2.62E+04	5.1	5.6	0.8
KM95-131	LLNL10000	1.65E-13	6.90E-15	4.2	5.97E+04	5.40E+04	5.26E+03	KNSTD5000	2.84E-13	1.60E-14	5.6	4.12E+05	2.42E+04	6.9	7.6	0.9
KM95-132	LLNL10000	1.21E-13	9.20E-15	7.6	6.82E+04	6.17E+04	8.46E+03	KNSTD5000	3.09E-13	2.20E-14	7.1	4.17E+05	3.13E+04	6.1	6.8	1.1
KM95-133	LLNL10000	1.64E-13	9.70E-15	5.9	9.08E+04	8.21E+04	7.98E+03	KNSTD5000	7.73E-13	5.40E-14	7.0	6.08E+05	4.35E+04	6.7	7.4	0.9
KM95-134	LLNL10000	1.31E-13	8.70E-15	6.7	6.71E+04	6.06E+04	7.34E+03	KNSTD5000	1.07E-13	8.10E-15	7.6	3.34E+05	2.68E+04	5.0	5.5	0.8
KM95-135	LLNL10000	1.94E-13	1.20E-14	6.2	8.27E+04	7.47E+04	6.72E+03	KNSTD5000	2.17E-13	1.40E-14	6.5	4.56E+05	3.02E+04	5.5	6.1	0.7
KM95-136	LLNL10000	1.41E-13	1.00E-14	7.1	9.30E+04	8.41E+04	9.13E+03	KNSTD5000	1.77E-13	1.70E-14	9.6	3.25E+05	3.28E+04	3.5	3.9	0.6
KM95-138	LLNL10000	2.34E-13	1.20E-14	5.1	9.22E+04	8.34E+04	6.72E+03	KNSTD9919	2.90E-13	1.50E-14	5.2	4.25E+05	2.31E+04	4.6	5.1	0.5
KM95-139	LLNL10000	1.13E-13	8.10E-15	7.2	6.72E+04	6.08E+04	8.63E+03	KNSTD9919	1.71E-13	1.79E-14	10.5	3.85E+05	4.20E+04	5.7	6.3	1.1
KM95-140	LLNL10000	2.51E-13	5.90E-14	23.5	7.11E+04	6.43E+04	1.80E+04	KNSTD9919	2.88E-13	1.50E-14	5.2	4.04E+05	2.20E+04	5.7	6.3	1.8
KM95-141	LLNL10000	1.94E-13	6.50E-15	3.4	6.91E+04	6.25E+04	4.75E+03	KNSTD9919	2.50E-13	1.30E-14	5.2	4.28E+05	2.31E+04	6.2	6.9	0.6
KM95-142	LLNL10000	9.25E-14	8.30E-15	9.0	7.02E+04	6.35E+04	1.17E+04	KNSTD9919	2.04E-13	1.92E-14	9.4	3.57E+05	3.65E+04	5.1	5.6	1.2
KM95-143	LLNL10000	1.63E-13	1.80E-14	11.0	8.98E+04	8.12E+04	1.19E+04	KNSTD9919	2.40E-13	1.91E-14	7.9	4.93E+05	4.03E+04	5.5	6.1	1.0
KM95-144	LLNL10000	1.42E-13	1.20E-14	8.4	6.09E+04	5.50E+04	7.10E+03	KNSTD9919	1.57E-13	1.20E-14	7.7	3.10E+05	2.49E+04	5.1	5.6	0.9
KM95-145	LLNL10000	1.37E-13	1.20E-14	8.8	5.07E+04	4.58E+04	6.20E+03	KNSTD9919	1.57E-13	1.60E-14	10.2	2.79E+05	2.93E+04	5.5	6.1	1.0
KM95-146	LLNL10000	2.19E-13	7.20E-15	3.3	8.20E+04	7.42E+04	5.18E+03	KNSTD9919	3.04E-13	1.80E-14	5.9	5.14E+05	3.12E+04	6.3	6.9	0.6
KM95-147	LLNL10000	6.46E-13	1.70E-14	2.6	2.50E+05	2.26E+05	7.47E+03	KNSTD9919	7.42E-13	2.40E-14	3.2	1.56E+06	5.08E+04	6.2	6.9	0.3
KM95-149	LLNL10000	2.07E-13	1.20E-14	5.8	9.47E+04	8.56E+04	7.17E+03	KNSTD9919	2.81E-13	1.60E-14	5.7	6.92E+05	4.01E+04	7.3	8.1	0.8
PTD92-01	LLNL1000	1.42E-13	3.77E-15	2.7	4.90E+04	4.43E+04	4.55E+03	KNSTD9919	3.06E-13	1.87E-14	6.1	3.27E+05	2.11E+04	6.7	7.2	0.9
PTD92-02	LLNL1000	4.75E-13	1.26E-14	2.7	1.85E+05	1.68E+05	6.36E+03	KNSTD9919	9.65E-13	3.91E-14	4.1	1.14E+06	4.69E+04	6.2	6.6	0.4
PTD92-03	LLNL1000	2.62E-13	9.33E-15	3.6	1.01E+05	9.17E+04	5.73E+03	KNSTD9919	4.24E-13	3.58E-14	8.4	6.78E+05	5.78E+04	6.7	7.2	0.8
PTD92-04	LLNL1000	2.65E-13	6.84E-15	2.6	1.01E+05	9.13E+04	5.09E+03	KNSTD9919	4.43E-13	3.19E-14	7.2	6.92E+05	5.05E+04	6.8	7.4	0.7
PTD92-05	LLNL1000	5.51E-13	1.50E-14	2.7	2.27E+05	2.05E+05	7.39E+03	KNSTD9919	8.58E-13	4.13E-14	4.8	1.31E+06	6.35E+04	5.8	6.2	0.4
PTD92-07	LLNL1000	1.91E-13	5.00E-15	2.6	6.87E+04	6.22E+04	4.73E+03	KNSTD9919	3.06E-13	3.46E-14	11.3	4.02E+05	4.63E+04	5.8	6.3	0.9
PTD92-08	KNSTD	2.42E-13	6.71E-15	2.8	1.11E+05	1.00E+05	5.33E+03	KNSTD9919	3.61E-13	1.77E-14	4.9	7.00E+05	3.50E+04	6.3	7.0	0.5
PTD92-09	KNSTD	4.77E-13	2.05E-14	4.3	2.19E+05	1.98E+05	9.88E+03	KNSTD9919	8.83E-13	3.21E-14	3.6	1.34E+06	4.91E+04	6.1	6.8	0.4
PTD94-01	LLNL3000	3.71E-13	7.89E-15	2.1	1.46E+05	1.32E+05	5.31E+03	KNSTD9919	2.79E-13	1.29E-14	4.6	7.43E+05	3.49E+04	5.1	5.9	0.4
PTD94-02	LLNL3000	2.62E-13	6.43E-15	2.5	9.90E+04	8.95E+04	4.99E+03	KNSTD9919	2.24E-13	1.11E-14	4.9	5.55E+05	2.82E+04	5.6	6.5	0.5
PTD94-03	LLNL3000	1.81E-13	4.80E-15	2.7	6.11E+04	5.53E+04	4.47E+03	KNSTD9919	2.36E-13	1.10E-14	4.6	3.50E+05	1.74E+04	5.7	6.6	0.6
PTD94-04	LLNL3000	1.84E-13	6.63E-15	3.6	6.66E+04	6.02E+04	5.06E+03	KNSTD9919	2.75E-13	1.32E-14	4.8	4.25E+05	2.15E+04	6.4	7.4	0.7
PTD94-05	LLNL3000	2.87E-13	6.73E-15	2.3	1.14E+05	1.03E+05	5.24E+03	KNSTD9919	3.78E-13	1.82E-14	4.8	7.01E+05	3.46E+04	6.2	7.1	0.5
PTD94-06	No Data	No Data	No Data	No Data	No Data	No Data	No Data	KNSTD9919	5.11E-13	2.62E-14	5.1	6.75E+05	3.53E+04	No Data	No Data	No Data
PTD94-07	LLNL3000	2.11E-12	5.22E-14	2.5	8.86E+05	8.01E+05	2.06E+04	KNSTD9919	2.71E-12	6.42E-14	2.4	4.64E+06	1.10E+05	5.2	6.1	0.2
PTD94-08	LLNL3000	1.68E-13	6.74E-15	4.0	5.90E+04	5.33E+04	5.04E+03	KNSTD9919	3.58E-13	1.53E-14	4.3	3.97E+05	1.82E+04	6.7	7.8	0.8
PTD94-09a	LLNL3000	1.85E-13	4.26E-15	2.3	6.73E+04	6.09E+04	4.70E+03	KNSTD9919	4.10E-13	1.51E-14	3.7	5.17E+05	2.01E+04	7.7	8.9	0.8
PTD94-09b	LLNL3000	1.51E-13	3.49E-15	2.3	5.77E+04	5.22E+04	5.05E+03	KNSTD9919	3.20E-13	1.31E-14	4.1	4.00E+05	1.79E+04	6.9	8.0	0.9
PTD94-09c	LLNL3000	1.71E-13	3.94E-15	2.3	6.01E+04	5.44E+04	4.58E+03	KNSTD9919	3.45E-13	1.37E-14	4.0	3.91E+05	1.68E+04	6.5	7.5	0.7

Table R2, cont.

PTD94-10	LLNL3000	2.27E-13	6.11E-15	2.7	8.33E+04	7.53E+04	4.88E+03	KNSTD9919	2.09E-13	1.01E-14	4.8	5.20E+05	2.60E+04	6.2	7.2	0.6
PTD94-11a	LLNL3000	1.28E-13	3.89E-15	3.0	4.19E+04	3.79E+04	4.58E+03	KNSTD9919	1.21E-13	6.73E-15	5.5	2.75E+05	1.66E+04	6.5	7.6	1.0
PTD94-11b	LLNL3000	1.57E-13	4.67E-15	3.0	5.50E+04	4.98E+04	4.72E+03	KNSTD9919	2.33E-13	9.60E-15	4.1	3.39E+05	1.54E+04	6.2	7.1	0.8
PTD94-13	LLNL3000	1.60E-13	4.57E-15	2.9	5.56E+04	5.03E+04	4.67E+03	KNSTD9919	9.46E-14	3.40E-15	3.6	3.56E+05	1.43E+04	6.4	7.4	0.8
PTD94-14	LLNL3000	3.36E-13	7.97E-15	2.4	1.31E+05	1.19E+05	5.36E+03	KNSTD9919	2.76E-13	9.95E-15	3.6	8.55E+05	3.16E+04	6.5	7.5	0.4
PTD94-15a	LLNL3000	1.26E-13	4.08E-15	3.2	4.12E+04	3.73E+04	4.64E+03	KNSTD9919	1.26E-13	6.41E-15	5.1	2.92E+05	1.62E+04	7.1	8.2	1.1
PTD94-15b	LLNL3000	1.27E-13	3.92E-15	3.1	4.20E+04	3.80E+04	4.63E+03	KNSTD9919	1.24E-13	7.62E-15	6.2	3.04E+05	1.99E+04	7.2	8.4	1.2
PTD94-15c	LLNL3000	1.31E-13	6.25E-15	4.8	4.40E+04	3.98E+04	5.00E+03	KNSTD9919	1.43E-13	6.57E-15	4.6	3.17E+05	1.60E+04	7.2	8.3	1.1
PTD94-16	LLNL3000	1.55E-13	4.30E-15	2.8	5.61E+04	5.08E+04	4.89E+03	KNSTD9919	2.01E-13	2.11E-14	10.5	3.58E+05	3.87E+04	6.4	7.4	1.1
PTD94-17	LLNL3000	1.76E-13	7.71E-15	4.4	5.86E+04	5.30E+04	4.93E+03	No Data	No Data	No Data	No Data	No Data	No Data	No Data	No Data	No Data
PTD94-18a	LLNL3000	1.05E-13	2.94E-15	2.8	4.01E+04	3.63E+04	5.56E+03	KNSTD9919	1.28E-13	1.00E-14	7.8	2.50E+05	2.14E+04	6.2	7.2	1.3
PTD94-18b	LLNL3000	1.65E-13	4.73E-15	2.9	5.84E+04	5.28E+04	4.77E+03	KNSTD9919	2.50E-13	1.61E-14	6.4	3.94E+05	2.64E+04	6.8	7.8	0.9
PTD94-18c	LLNL3000	1.24E-13	3.80E-15	3.1	4.16E+04	3.76E+04	4.70E+03	KNSTD9919	1.43E-13	6.21E-15	4.4	2.76E+05	1.37E+04	6.6	7.7	1.0

*Reported isotopic ratios have not been corrected for backgrounds. Blanks are reported in Table R3.

†Values have been scaled from their original, measured values to reflect the currently-accepted ^{10}Be standard value (07KNSTD; Nishiizumi et al., 2007) that was developed after these samples were analyzed (1996-2001).

Table R3. Data for the 33 blanks included in the analysis.

Blank Name	Be Carrier (g)*	Al Carrier (g)*	Measured $^{10}Be/^{9}Be$ Ratio†	$^{10}Be/^{9}Be$ Ratio Unc.	Measured $^{26}Al/^{27}Al$ Ratio†	$^{26}Al/^{27}Al$ Ratio Unc.
B48-2	0.211	1.931	4.060E-14	5.900E-15	2.301E-14	8.700E-15
B49-H	0.239	1.980	1.770E-14	1.000E-14	1.052E-14	4.800E-15
B49-L	0.258	1.978	2.430E-14	5.800E-15	2.182E-15	2.200E-15
B50	0.233	1.726	2.890E-14	7.000E-15	7.837E-15	2.700E-15
51B	0.242	1.880	3.320E-14	1.800E-14	5.853E-15	3.000E-15
52B	0.251	1.983	1.720E-14	3.300E-15	7.738E-15	2.900E-15
53B	0.252	1.985	3.940E-14	3.000E-15	7.025E-14	8.900E-15
54B	0.254	1.994	2.100E-14	3.300E-15	1.577E-14	5.000E-15
55B	0.250	1.881	3.340E-14	3.800E-15	4.266E-15	1.600E-15
56B	0.253	1.995	3.020E-14	1.200E-14	1.290E-15	8.400E-15
58B	0.302	2.018	8.910E-14	2.500E-14	2.650E-15	1.400E-15
59B	0.299	1.904	2.690E-14	5.300E-15	1.100E-15	0.000E+00
60B	0.301	1.995	4.400E-14	6.500E-15	2.450E-15	1.500E-15
61B	0.300	1.960	4.100E-14	6.000E-15	1.350E-15	1.350E-15
62B	0.286	1.880	3.520E-14	4.900E-15	1.480E-14	5.300E-15
63B	0.298	2.003	4.820E-14	1.700E-14	1.900E-14	1.100E-14
64B	0.301	1.937	2.780E-14	6.900E-15	3.050E-15	2.200E-15
65B	0.304	2.017	2.430E-14	6.000E-15	3.700E-15	2.200E-15
66B	0.303	1.994	2.440E-14	4.900E-15	3.250E-15	1.900E-15
67B	0.300	1.993	3.470E-14	7.500E-15	3.850E-15	2.300E-15
69B	0.250	1.696	5.130E-14	3.800E-15	8.300E-15	3.700E-15
72B	0.249	2.031	2.940E-14	6.900E-15	8.900E-15	2.800E-15
146BLANK	0.248	1.993	1.726E-14	9.800E-16	2.473E-15	1.749E-15
152BLANK	0.301	2.984	1.906E-14	2.216E-15	2.997E-15	1.341E-15
160BLANK	0.254	2.641	2.028E-14	1.800E-15	2.208E-15	7.826E-16
160BLANKX	0.253	2.512	2.341E-14	2.274E-15	No Data	No Data
162BLANK	0.252	3.012	2.303E-14	4.430E-15	3.682E-15	1.451E-15
188BLANK	0.252	3.017	1.762E-14	2.887E-15	2.024E-15	2.024E-15
188BLANKX	0.253	3.015	2.136E-14	2.600E-15	1.485E-15	1.485E-15
191BLANK	0.260	3.018	1.525E-14	1.933E-15	4.492E-15	2.248E-15
192BLANK	0.316	2.878	3.668E-14	3.206E-15	2.427E-15	1.717E-15
193BLANK	0.256	2.499	2.431E-14	1.942E-15	1.034E-15	1.034E-15
193BLANKX	0.252	2.393	2.888E-14	1.280E-15	1.397E-15	1.397E-15
		MEDIAN:	2.735E-14	MEDIAN:	3.250E-15	
		STDEV:	9.546E-15	STDEV:	5.603E-15	

*All blanks were prepared using SPEX Be and Al carrier with a concentration of 1000 μg mL^{-1}.

†For each isotope, there was one blank (58B for Be, 53B for Al, listed in gray above) that was higher than any other blank by more than 1σ. We considered these measurements outliers and did not include them in our calculation of a background value.

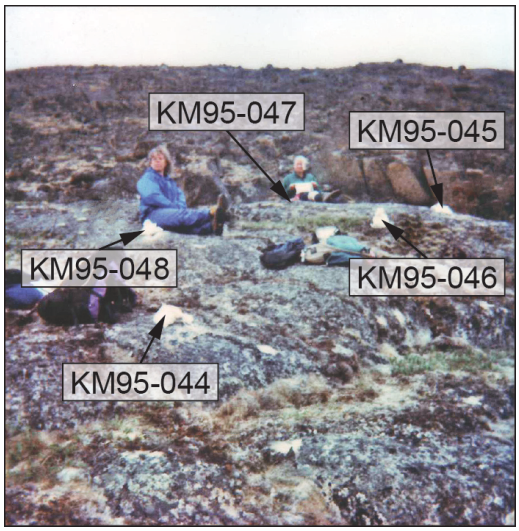

Figure R1. Photograph of molded bedrock outcrop near Pangnirtung (204 m a.s.l.) where five samples (KM95-044 through KM95-048) were collected from the same surface.

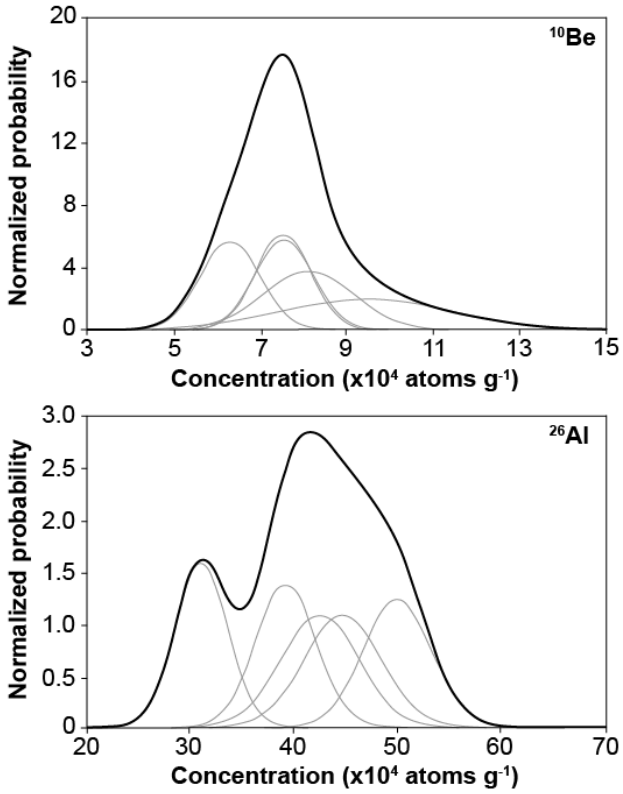

Figure R2. Probability density functions of ^{10}Be concentrations (top) and ^{26}Al concentrations (bottom) of the five samples from the same gneiss outcrop. Thin gray lines represent the measured isotopic concentrations and 1σ analytic uncertainties for each sample; thick black line represents the summed probability.

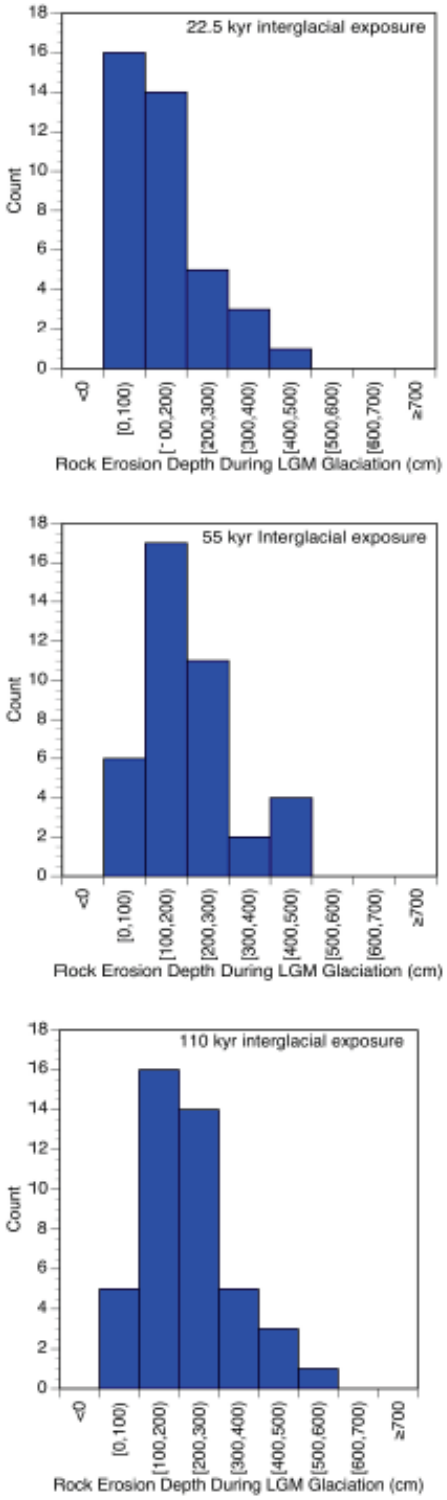

Figure R3. Histograms of erosion depths needed to remove nuclides from a single previous period of exposure for the bedrock samples in our analysis that contain inherited nuclides. We assessed three different durations for the previous interglacial period: 22.5 ky (top panel), 55 ky (middle panel) and 110 ky (bottom panel).